Measuring the Physical Properties of Distant Galaxies and Black Holes in the Era of Surveys

Author:
Shaun C. READ

Supervised by:
Dr Daniel J.B. SMITH &
Prof Elias BRINKS

Centre for Astrophysics Research
School of Physics, Astronomy and Mathematics
University of Hertfordshire

Submitted to the University of Hertfordshire in partial fulfilment of the requirements of the degree of Doctor of Philosophy.

March 2019

Abstract

In the era of deep and wide-field surveys (e.g. SDSS, LSST, LOFAR, SKA), we have access to an ever-increasing volume of multi-wavelength data for millions of galaxies both locally and at high redshifts. However, inferring the intrinsic properties of the whole population of galaxies requires robust statistical techniques and an understanding of observational bias.

In this thesis, I present a study of the Far-Infrared Radio Correlation (FIRC) – a relation which is widely used to infer star-formation rates from otherwise featureless radio sources. Using LOFAR 150 MHz, FIRST 1.4 GHz, and *Herschel* infrared luminosities derived from the new LOFAR/*H*-ATLAS catalogue, we investigate possible variation in the monochromatic (250μm) FIRC at low and high radio frequencies. Although the average FIRC at high radio frequency is consistent with expectations based on a standard power-law radio spectrum, the average correlation at 150 MHz is not. We see evidence for redshift evolution of the FIRC at 150 MHz, and find that the FIRC varies with stellar mass, dust temperature and specific star formation rate, whether the latter is probed using MAGPHYS fitting, or using mid-infrared colour as a proxy. We can explain the variation, to within 1σ using a Bayesian partial correlation technique. This work was published as Read et al. (2018) in the *Monthly Notices of the Royal Astronomical Society*.

Identifying an opportunity to increase in the efficiency of black-hole mass estimations, we perform photometric reverberation mapping using the `Javelin` photometric damped random walk model for the QSO `SDSS J144645.44 +625304.0` at $z = 0.351$ and estimate the Hβ lag of 72^{+5}_{-1} days and black hole mass of $10^{8.28^{+0.12}_{-0.07}}\mathrm{M}_{\odot}$. An analysis of the reliability of photometric reverberation mapping conducted using many thousands of simulated light curves shows that we can recover any input lag less than a third of the duration of our observing campaign to within 4 per cent on average given our target's observed signal-to-noise of > 20 and cadence of 14 days. We use our suite of simulated light curves to deconvolve artefacts from the QSO's posterior lag distribution, increasing the signal-to-noise by a factor of ~ 3. We exceed the signal-to-noise of the Sloan Digital Sky Survey Reverberation Mapping Project (SDSS-RM) campaign with a quarter of the observing time resulting in a ~ 310 per cent per cent increase in SNR efficiency over SDSS-RM.

Finally, I present a study of the radio luminosity star-formation rate relation directly with the LOFAR Two Metre Sky Survey (LoTSS) DR1, in an effort to understand the mass dependency of the $L_{150\,\mathrm{MHz}} - \mathrm{SFR}$ slope reported by Gürkan et al. (2018). Building on our previous study of the FIRC, we develop a fast, generalised algorithm to recover *Complete And Noiseless Distributions from Incomplete Data* (`CANDID`). We find that the mass dependency is real and in agreement with previous estimations in the literature when we include the effects of selection biases present in the LoTSS DR1 sample. We also propose that type-Ia supernovae may contribute to a $L_{150\,\mathrm{MHz}}$ excess and construct a joint distribution of our LoTSS observations and the Horizon AGN simulation to test this.

Declaration

I declare that no part of this work is being submitted concurrently for another award of the University or any other awarding body or institution. This thesis contains a substantial body of work that has not previously been submitted successfully for an award of the University or any other awarding body or institution.

The following parts of this submission have been published previously and/or undertaken as part of a previous degree or research programme:

1. Chapter 2: this has been published as Read et al., 2018, *Monthly Notices of the Royal Astronomical Society*, **480**, 5625.
2. Chapter 3 has been submitted to the journal *Monthly Notices of the Royal Astronomical Society* as part of Read et al. submitted, 2019

Except where indicated otherwise in the submission, the submission is my own work and has not previously been submitted successfully for any award.

Acknowledgements

My thanks go to Dan Smith, who's unwavering enthusiasm and support has guided me throughout the course of this PhD. The quality of this thesis is largely dependent on his effort to keep me focused and intrigued with the subject area, despite my doubts.

Of course, addition thanks must go to my post-graduate colleagues at the University of Hertfordshire, in particular Garreth Martin, without whom, my curiosity would not have been as grounded in reality.

I also acknowledge my parents who continue to show patience and interest in my work despite my intermittent ability to do the same.

All research enclosed in this thesis was performed in collaboration with Dan Smith.

Contents

Chapter 1

Introduction

1.1 Galaxies, Classifications, and Evolution

The question of how galaxies form and evolve has been at the centre of astronomy ever since they were first identified by Hubble (1925, 1926) as being extragalactic in origin. Directly after their identification, Hubble (1926, 1927) classified these extragalactic objects into a two-staged system resembling a tuning fork based on their optical morphology, shown in Fig 1.1. Early-type galaxies (also known as ellipticals), categorised by their smooth and featureless elliptical surface brightness profiles, are positioned on the Hubble tuning fork in order of their observed ellipticity. Late-type galaxies are positioned on the opposite side of the tuning fork and are distinct from ellipticals in that they possess stellar discs with spiral arms (with or without central stellar bars), hence their alternative name: spirals. Spiral galaxies are ordered by the prominence of their spiral arms and the tuning fork becomes a continuous sequence with the addition of an intermediate class of lenticular (S0) galaxies (Sandage, 1975). These galaxies possess a disc structure but no spiral arms – a combination of both early- and late-type. Other galaxy morphological classification systems exist (e.g. de Vaucouleurs 1959), but the simple Hubble tuning fork is most widely recognised and the terms early- and late-type are still in use today (Baldry, 2008; González Delgado et al., 2016; Yu and Ho, 2019).

The fact that galaxies do not all look the same and can be classified on a continuous morphological scale suggests one of two things:

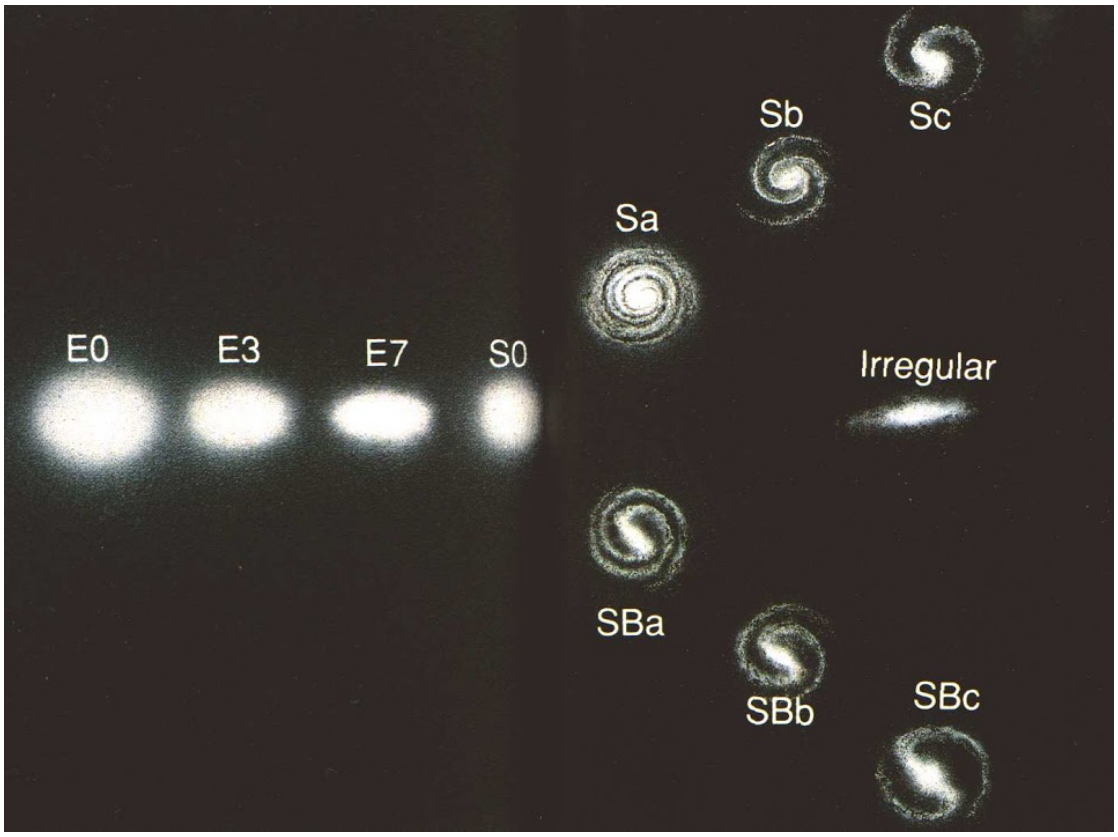

FIGURE 1.1: The Hubble tuning fork galaxy classification scheme taken from Hubble et al. (1958). Elliptical, "E", galaxies are positioned on the left and the unbarred/barred spiral "S(b)" galaxies are found on the two right-hand sequences. Irregular galaxies are presented off of the sequence on the right since they tend to be highly star-forming (Kennicutt, 1998b)

1. Present-day galaxies have evolved from a progenitor class via two or more pathways. If these evolutionary tracks give rise to two different observed galaxy morphologies, they would have to mix in order to generate the continuous sequence we see today.

2. Galaxies broadly evolve from one end of the Hubble tuning fork to the other. This would require one galaxy type to contain an older stellar population than the other.

Massive, bluer stars exhaust their fuel quickly (see Sparke and Gallagher 2007 and references therein). Therefore, bluer galaxy colours imply the existence of a younger stellar population and redder colours indicate the presence of an evolved population of stars.

When selecting galaxies in optical wavelengths, a bimodal distribution in colour and stellar mass (as measured by optical magnitude as a proxy) appears as shown in Fig 1.2, (Baldry et al., 2004; Bell et al., 2004; Balogh et al., 2004; Pozzetti et al., 2010; Whitaker et al., 2011; Caputi et al., 2017). A "blue cloud", containing galaxies readily classified as spirals with ongoing star-formation, was identified by Strateva et al. (2001); Hogg et al. (2003); Balogh et al. (2004);

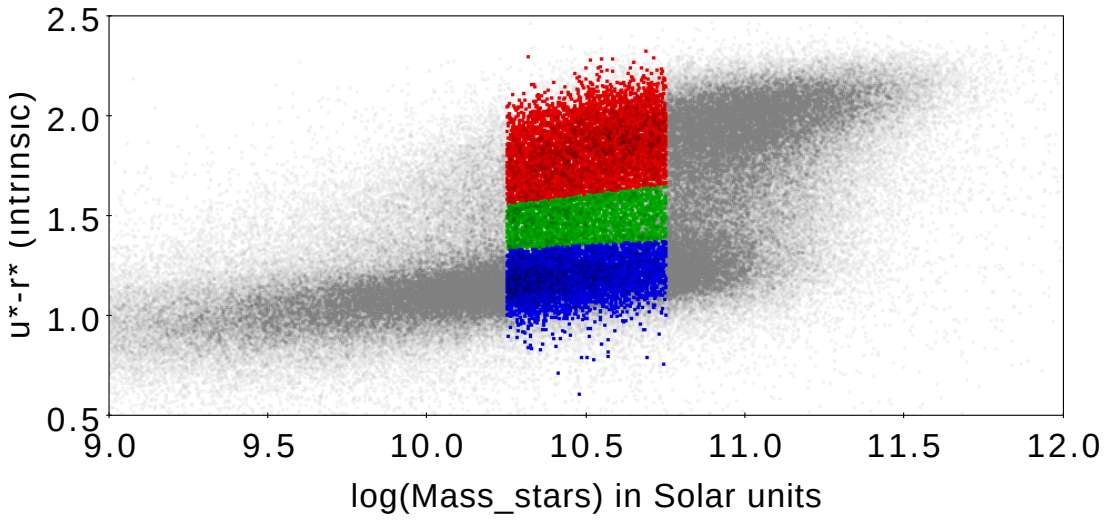

FIGURE 1.2: The galaxy Colour-Mass diagram from Bremer et al. (2018). Highlighted are their subsets of blue star-forming, green valley, and red quiescent galaxies. There is a distinct bimodality in the total distribution of colour versus stellar mass, plotted in grey.

Baldry et al. (2004). In contrast, the "red sequence", first identified by Baum (1959), contains those galaxies with far less ongoing star-formation as inferred from their optical colours – though the red sequence also contains a mix of galaxy types as shown by Cortese (2012), where a sample of red disc galaxies are shown to still be forming stars at a rate comparable to blue star-forming discs of the same stellar mass (also see Salim and Rich 2010). Furthermore, when selecting galaxies based on their optical magnitude, there appear to be relatively few galaxies situated between the red sequence and blue cloud (Strateva et al., 2001; Brammer et al., 2009; Trayford et al., 2016). Using the large increase in galaxy numbers provided by the Sloan Digital Sky Survey (SDSS; York, 2000), Strateva et al. (2001) showed that so-called "green valley" galaxies are much rarer than either red or blue galaxies, implying that there are two physically distinct types of galaxy, similar to those classified by morphology on the Hubble tuning fork.

Although never intended to be taken as true temporal evolution (Hubble, 1927), the Hubble tuning fork designations early- and late-type have been mistakenly interpreted as literal, with the elliptical early-types evolving into late-type spirals (Baldry, 2008). However, if late-type stellar populations (generally bluer) are generally much younger than early-type populations (generally redder) then this implies that the second option of galaxy evolution is more likely: ellipticals evolve from spirals. Moreover, if there are few "green" galaxies, this implies that the transition from star-forming to passive is fast: less than 2 Gyr (Martin et al., 2007; Trayford et al., 2016; Bremer et al., 2018).

The standard hierarchical evolution model (Fall and Efstathiou, 1980; Bosch, 2002; Agertz et al., 2011), shown in Fig 1.3, dictates that stable star-forming discs form from condensing gas within a dark matter halo which go on to develop spiral arm instabilities. In addition to the secular evolution of spiral galaxies (where star-formation is increased or decreased by the increased or decreased inflow of halo gas, Bouché et al. 2010; Lilly et al. 2013), spiral galaxies can merge in dense environments. If the masses of the two galaxies is roughly of the same order, a major merger occurs, destroying the disc, removing the gas, and creating a passive elliptical (Toomre, 1977; Negroponte and White, 1983; Di Matteo et al., 2007; Hopkins et al., 2009; Ferreras et al., 2009; Conselice et al., 2009; Taranu et al., 2013; Naab et al., 2014; Deeley et al., 2017). If this is true we should see more early-type galaxies where there are more mergers. Indeed, Dressler (1980) found that the prevalence of elliptical and lenticular galaxies increases sharply with increasing cluster density whilst the number of spirals simultaneously decreases.

However, morphology becomes more difficult to classify with increasing redshift (due to the smaller angular size of more distant galaxies) and Hubble type only correlates with average intrinsic properties such as star-formation rates and colour (Roberts and Haynes, 1994). Indeed, the main reason that the Hubble tuning fork classifies local galaxies by star-formation rate and colour at all is because the merger rate in the local universe is low (3 per cent: Patton et al., 1997) and star-formation is on the decline (Madau et al., 1998). As we look towards higher redshifts, Hubble type classification is less useful since a large proportion of galaxies at $z > 3$ are irregular and do not fall into a classical morphological type (Conselice, 2001). Therefore, we must increasingly rely on intrinsic, whole-galaxy properties such as colour and luminosity with increasing look-back times.

Observational studies of galaxy evolution are unable to observe the evolution of a single galaxy over cosmic time and have access only to snapshots of populations of galaxies, distributed over redshift. Therefore, we have to rely on statistical tools applied to large numbers of galaxies observed over wide ranges of redshifts to infer and quantify the paths of galaxies moving within the parameter space of physical properties (such as SFR, luminosity, stellar mass). The star-formation history, whether integrated over the whole population or for individual star-forming galaxies, is important for characterisation of the evolution mechanisms of galaxies over cosmic time.

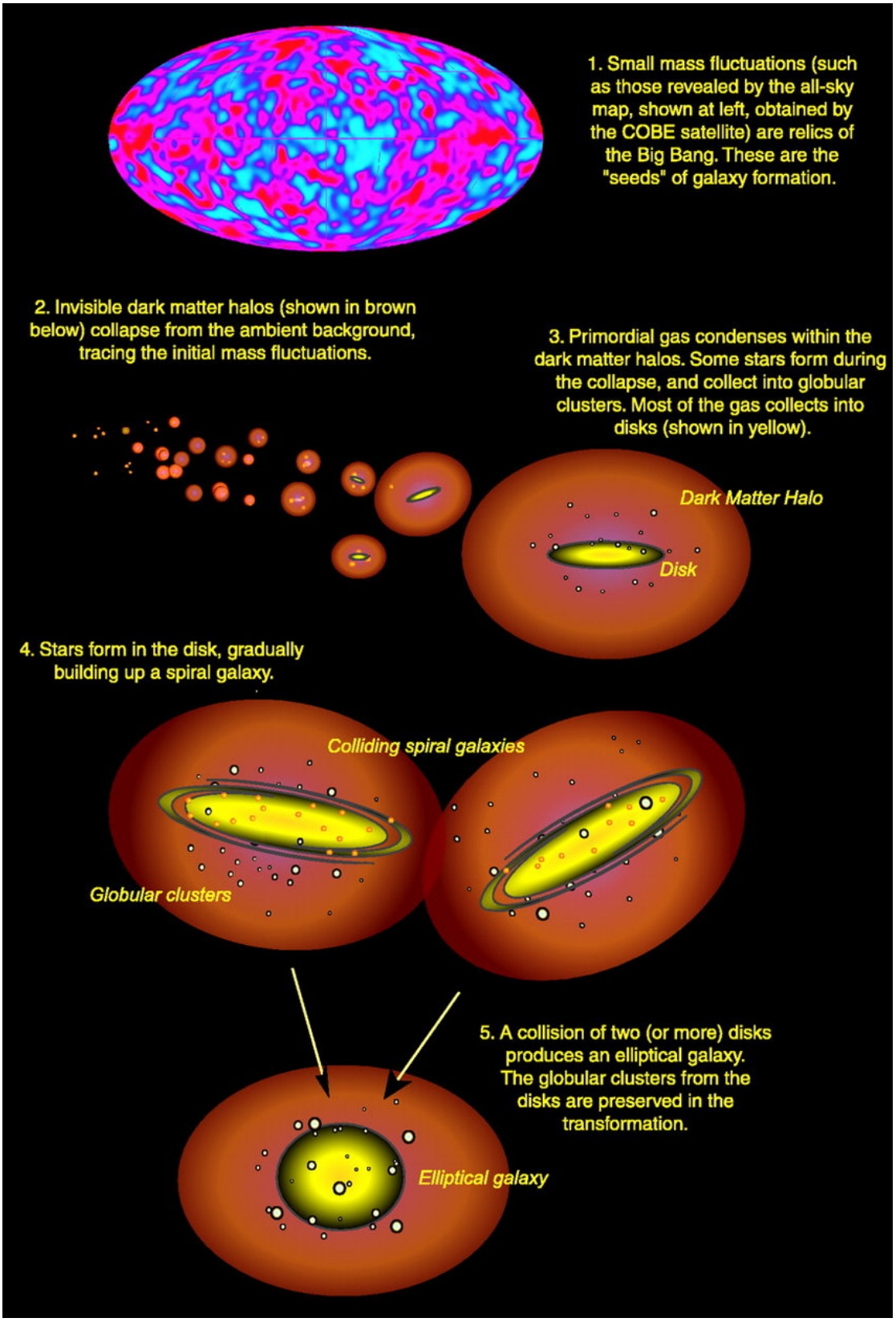

FIGURE 1.3: A schematic illustration from Abraham and van den Bergh (2001) of the formation of galaxies in the hierarchical assembly model.

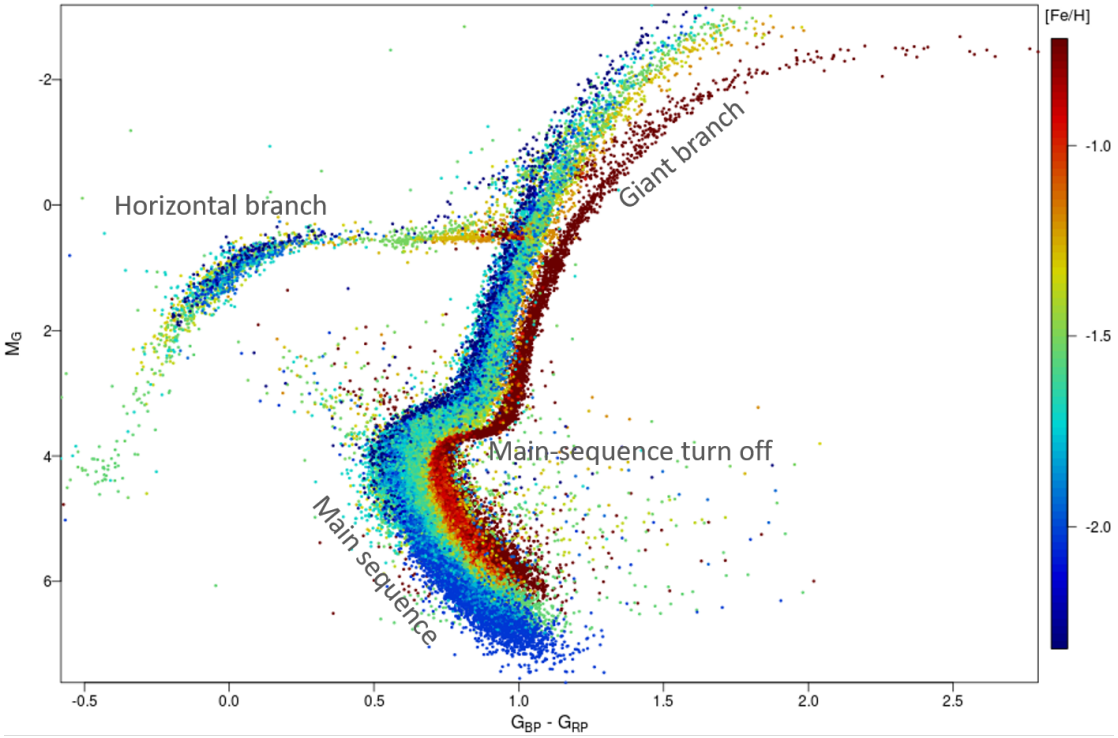

FIGURE 1.4: The colour-magnitude diagram as measured from the Gaia Data Release 2 (Prusti et al., 2016; Brown et al., 2018), taken from Babusiaux et al. (2018). Points indicate individual stars from 14 globular clusters. The colour of the points indicate metallicity as shown in the colorbar. Both the main-sequence and the main-sequence turn-off are clearly visible and vary with the metallicity of the stars. The x-axis is the colour calculated from the Gaia blue and red photometric passbands. The y-axis is the absolute magnitude in the Gaia total passband which spans from 330nm to 1050nm.

1.2 Measuring Star-formation Rates and Star-formation Histories

For nearby galaxies, where we can resolve individual stars, it is possible to construct a colour-magnitude diagram (Rosenberg, 1910; Hertzsprung, 1911; Russell, 1914), shown in Fig 1.4. The colour-magnitude diagram of an evolving stellar population contains several features whose shape and position are indicative of stellar age. Stars burn their hydrogen gas on the main sequence until it is exhausted, at which point a star turns off of the main sequence on to the red giant branch (Salpeter, 1955; Kurucz, 1979; Girardi et al., 2000; Bressan et al., 2012). Since more massive stars have bluer colours and shorter main-sequence lifetimes, the colour of the bluest stars (and the shape of the red giant branch) can be used to derive the age of that stellar population. Likewise, if there is another burst of star-formation triggered by infalling gas, then this will also be reflected in the colour-magnitude diagram after a delay of approximately 10^8 years.

Therefore, the position of stars on the colour-magnitude diagram can be used to infer the star-formation history of the galaxy using many simulations of stellar evolution given different initial conditions. The stellar birth function, SBF (the number of stars born per unit mass, time, and metallicity), can be fit to the data given a sufficiently accurate stellar evolution model (Tosi et al., 1989, 1991; Bertelli et al., 1992; Tolstoy and Saha, 1996; Hernandez et al., 1999; Olsen, 1999; Hernandez et al., 2000a,b; Harris and Zaritsky, 2001; Dolphin, 2002; Dolphin et al., 2003; Yuk and Lee, 2007; Walmswell et al., 2013; Gennaro et al., 2015; Bernard et al., 2015; Williams et al., 2015). The initial mass function, IMF, can be recovered from the SBF by marginalising over the metallicity at time $t = 0$ and is given by

$$\xi(m)dm \propto \left(\frac{m}{M_\odot}\right)^{-\alpha} \left(\frac{dm}{M_\odot}\right), \tag{1.1}$$

where m is mass and α sets the slope of the IMF (which can itself be a function of mass). For instance the Salpeter (1955) IMF sets the slope as a constant 2.3, whereas Kroupa (2001) specifies that α has a piece-wise form that decreases in magnitude at masses below $0.5\,M_\odot$ – see Figure 1.5.

The IMF is integral to the inference of star-formation histories since the observed spectrum of a galaxy is sensitive to the mass distribution of stars at every star-burst.

The instantaneous rate of star formation and its history cannot be directly observed when a galaxy is too distant to resolve individual stars. Instead, we must rely on indirect relations that have been calibrated to nearby galaxies based on their integrated properties. Population synthesis methods form the backbone of all ongoing-star-formation rate and star-formation history estimations. As in the resolved scenario, a grid of stellar evolution tracks can be produced for a range of metallicities, and ages. The observed luminosity in a particular waveband or a large portion of the stellar spectrum can be simulated from such a grid of initial values using stellar atmosphere models and libraries of stellar spectra. Adding together the observed luminosities over the entire population of stars, weighted by an input initial mass function (IMF), results in the integrated luminosity for the grid of initial values and star-formation histories. The resulting series of templates can then be fit to observations to infer the star-formation history, galaxy age, and metallicity for a given galaxy. Many synthesis model grids are currently used in this way (Bruzual A. and Charlot, 1993; Bertelli et al., 1994; Leitherer and Heckman, 1995; Fioc and Rocca-Volmerange, 1997; Leitherer et al., 1999; Bruzual and Charlot, 2003; Bruzual, 2007;

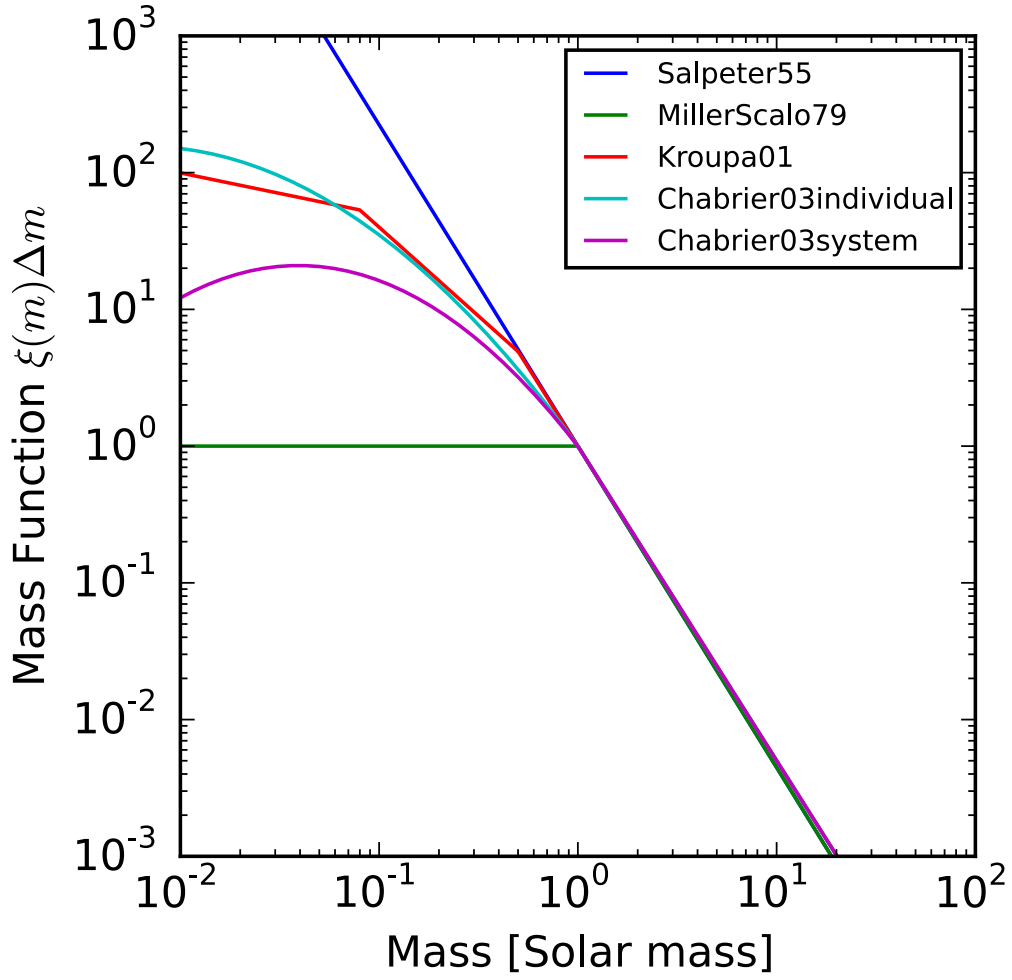

FIGURE 1.5: The form of the IMFs described by Salpeter (1955); Miller and Scalo (1979); Kroupa (2001); Chabrier (2003).

Leitherer et al., 2010). Models can be fit to galactic spectra or photometric data by marginalising over a library of templates, thereby retrieving the best fit parameters such as stellar mass, star-formation history, and metallicity (Reichardt et al., 2001; Panter et al., 2003; Heavens et al., 2004; Koleva et al., 2009; da Cunha et al., 2008, 2011). Furthermore, using model grids can provide uncertainties on these parameters.

However, it is difficult to extract these properties from observed data alone since degeneracies exist whereby the same observation can be due to different properties. In addition, the discrete nature of observations (i.e. broad and narrow band filters) cannot sample the entire spectrum, and so can give rise to further degeneracies since key emission/absorption features can be missing. Indeed, the more wavelengths sampled, either by spectroscopy or photometry, the more the characteristics of the underlying physical processes are constrained. For example, the optical colour of galaxies is due to a combination of dust reddening, stellar metallicity, and stellar age.

To break the metallicity-age-dust degeneracy here, infrared observations are required in addition to optical measurements. Inferring star-formation histories from finitely observed spectra is therefore fraught with difficulties since many different histories can give rise to the same observations.

Spectroscopic or photometric fitting of stellar templates ideally requires optical and infrared observations over a large range of wavelengths (Hayward and Smith, 2014). For a large sample of galaxies where it is impractical to fit or where there is insufficient data (such as detections in radio surveys with no optical counterpart), it is necessary to use star-formation relationships based on flux measurements made at one or more wavelengths (typically calibrated at low redshift, where they can be validated more easily against resolved colour-magnitude diagrams). The relations must be calibrated to stellar population synthesis models assuming some simple star-formation history and the recovered star-formation rate will only be accurate for that star-formation history. Therefore, the relationships can be derived from stellar population synthesis models but will contain some significant scatter due to differing intrinsic star-formation histories, especially for merging systems (Smith and Hayward, 2015).

1.2.1 Star-formation Rate Indicators

The stellar ultraviolet continuum between $1250-2500\,\text{Å}$ is dominated by the emission from unobscured young OB stars given that star-formation has recently started (Walborn and Fitzpatrick, 1990; Walborn, 1971; Massey et al., 1995; da Cunha et al., 2008). Using stellar population synthesis methods, it is possible to relate UV luminosity to star-formation rate assuming an IMF and that the SFR has remained steady on time-scales longer than the lifetimes of the OB stars themselves (which stay on the main sequence for less than 10^8 years). However, UV wavelengths are inaccessible from Earth and so nearby galaxies require observations to be made above the atmosphere. Furthermore, UV emission is highly susceptible to extinction due to dust and the relation between UV flux and star-formation rate is sensitive to the form of the IMF. For example, using a Salpeter IMF (Salpeter, 1955) will produce a near flat UV continuum between $1500-2800\,\text{Å}$ and gives a SFR-L_{UV} relationship that is accurate for a continuous star-formation rate over a period of 10^8 years:

$$SFR(M_{\odot}\text{yr}^{-1}, UV) \approx 1.4\times10^{-28} L_{\nu}\,/\text{ergs}^{-1} \tag{1.2}$$

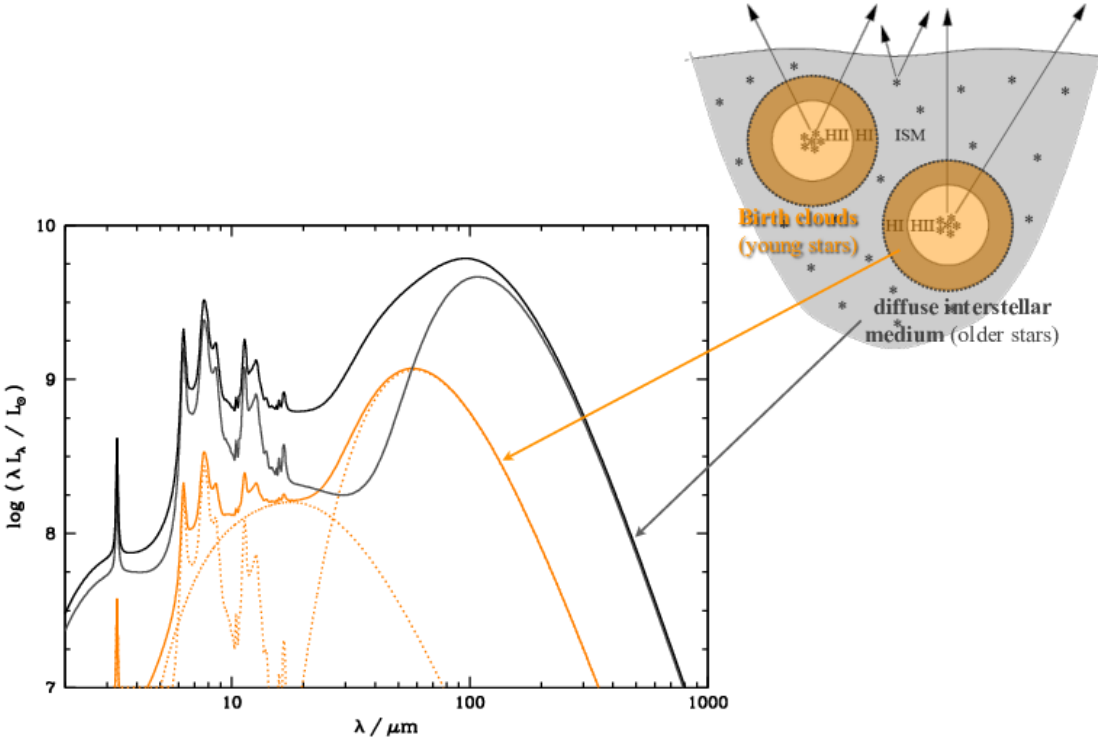

FIGURE 1.6: The schematic illustration (Charlot and Fall, 2000) of the two component model used by the SED fitting code MAGPHYS (da Cunha et al., 2008, 2011). The emission from the diffuse interstellar medium, heated by older stars, is shown in black. The emission from the birth clouds is shown in orange.

The UV continuum is only a portion of the Spectral Energy Distribution (SED) of a star-forming galaxy. The hydrogen recombination lines absorb and re-emit the massive-stellar light below the Lyman limit and so provide a reliable tracer for star-formation for stars above $10M_{\odot}$ which corresponds to a lifetime (and hence SFR time-scale) of 10^7 years (Kennicutt, 1998b; Charlot and Longhetti, 2001; Kennicutt et al., 2009; Hao et al., 2011; Murphy et al., 2011):

$$SFR(M_{\odot}\mathrm{yr}^{-1}, H\alpha) = 7.9 \times 10^{-42} L_{H\alpha}/\mathrm{ergs}^{-1} \tag{1.3}$$

The biggest disadvantage for Hα recombination line and continuum SFR indicators is dust extinction. UV photons are easily absorbed by dust along the line of sight and so SFR estimates based on UV measurements can significantly underestimate the true SFR when the effect of extinction has not been taken into account. OB stars are born within the dense molecular clouds surrounded by the ISM (Charlot and Fall, 2000), as shown in Fig 1.6, and so the effect of dust is significant. However, energy must be conserved and the UV light from these young stars is reprocessed by the dust into the infrared, producing an infrared SED peaking at mid- to

far-infrared wavelengths. The dust temperature increases with decreasing distance of the dust from the young stellar population. Therefore, different components of dust emit in different wavelength ranges, and so an infrared SED with a shorter peak wavelength indicates hotter temperatures. The form of the SED is then a composite modified-blackbody (a black-body with a wavelength-dependent emissivity $\varepsilon = \nu^{\beta}$, where β is the emissivity index), where each component of hot or cool dust contributes a different modified-blackbody at a different peak wavelength.

The stellar birth clouds typically disperse on time-scales of 10^7 years (Charlot and Fall, 2000; da Cunha et al., 2008) and so light from stars older than this will be predominantly reprocessed in the cooler ambient ISM. The total infrared output of dust can be therefore approximated by two grey-body SEDs (da Cunha et al., 2008, 2011) shown in Fig 1.6.

Different wavelengths of stellar light probe differently aged populations of stars and show whether they are obscured by dust. A star-formation history can be fit to an entire spectrum and therefore an approximate star-formation history and rate can be fit using discrete photometric observations taken over a range of wavelengths. This is the essence of SED fitting. SED fitting codes such as AGNFITTER (Calistro-Rivera et al., 2016) and CIGALE (Burgarella et al., 2005) use a self-consistent energy balance criterion, where the total energy radiated from stars and any central Active Galactic Nucleus (AGN) is equal to the energy observed in the UV and infrared components. This allows linking of stellar, dust, and AGN physics in a consistent and holistic manner. By modelling all sources of emission simultaneously, it is possible to arrive at a deeper understanding of the intrinsic properties of galaxies than one would by modelling them in isolation.

The star-formation rate indicators discussed above probe recent stellar birth either through dust reprocessing or directly via UV and optical. The same massive young stars whose UV and optical emission can directly trace recent star-formation end their lives in supernova explosions. The charged cosmic rays that are accelerated in the resultant shock-fronts become trapped in the galaxy's magnetic field emitting radio continuum synchrotron radiation for periods of around 10^8 years (Blumenthal and Gould, 1970; Condon, 1992; Longair, 2011). Towards longer wavelengths, the thermal radiation due to dust black-bodies and HII free-free emission diminishes and the emission due to synchrotron radiation dominates the galaxy SED at radio frequencies (Condon, 1992). When considering only supernovae-related emission, radio synchrotron traces

only the very massive young stars and is unaffected by the extinction that plagues UV and optical measurements. As such, observed radio luminosity can trace recent stellar death as opposed to the recent stellar birth that is traced by emission at other wavelengths. However, a coherent physical model for the radio synchrotron emission due to this process depends on many star-formation parameters and magnetic field assumptions (Condon, 1992; Lacki et al., 2010; Lacki and Thompson, 2010; Schober et al., 2017). So in order to estimate star-formation rates, it is necessary to bootstrap from the correlations between radio luminosity and emission for which we have star-formation models. This is most easily seen in the Far-Infrared Radio Correlation (FIRC van der Kruit, 1971; de Jong et al., 1985; Condon et al., 1991; Yun et al., 2001; Bell, 2003; Bourne et al., 2011) where the far-infrared is already calibrated to the star-formation rate as described above. This method has its own disadvantages, such as large variation in the slope of the correlation with many parameters including redshift (see Chapter 2, Read et al. 2018 for more details).

Each indicator has its own advantages, sensitivities, redshifts for which they are accessible, and SFR time-scales. For that reason, a complete cosmic SFR density over large ranges of redshift can best be traced with more than one indicator, each compensating for the other's weaknesses. The search for a perfect star-formation rate indicator is still ongoing...

1.3 Star-formation in Galaxies and Mechanisms for their Evolution

1.3.1 The Galaxy Main Sequence of Star-formation and Quenching

Deep and wide-field multi-wavelength surveys yield large samples of galaxies with which to calibrate and then study star-formation over cosmic time. Together with the improvements seen in stellar population synthesis models (e.g. Bruzual, 2007; Yuk and Lee, 2007; Walmswell et al., 2013; Gennaro et al., 2015; Bernard et al., 2015; Williams et al., 2015; Leitherer et al., 2010), they have allowed refinement of star-formation rate diagnostics (e.g. Kennicutt et al., 2009; Murphy et al., 2011; Hao et al., 2011; Kennicutt Jr and Evans II, 2012) and estimation of stellar masses and attenuation. With the advent of these large-scale surveys, most notably SDSS, it became clear that the galaxies selected in the optical are bimodally distributed in a number of properties such as star-formation rate, stellar mass, and colour (Baldry et al., 2004; Brinchmann et al., 2004; Salim et al., 2005) as shown in Fig 1.2.

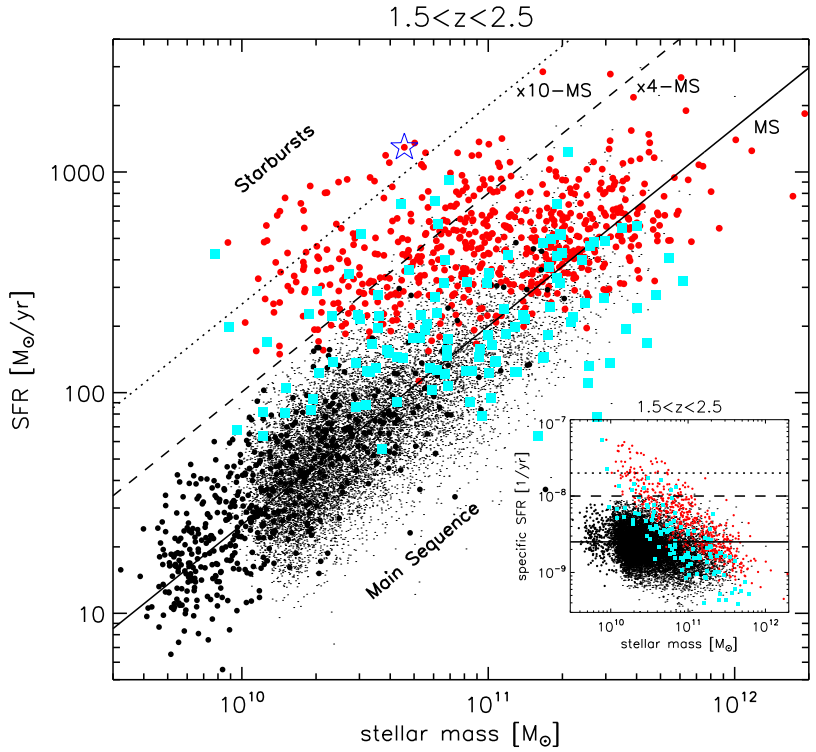

FIGURE 1.7: Star-formation rate versus stellar mass for star-forming galaxies (black) at redshifts between $1.5 < z < 2.5$ from Rodighiero et al. (2011). Star-bursts are shown in red. The solid black line indicates the main sequence at $z = 2$ identified by Daddi et al. (2007), while the dotted lines show the main sequence with difference normalisations. The inset axes show the main sequence in the plane of specific star-formation rate (sSFR) versus stellar mass.

In addition, a "main sequence" of galaxies that are currently forming stars is seen in the plane of star-formation rate and stellar mass (Fig 1.7 Guzmán et al., 1997; Brinchmann and Ellis, 2000; Noeske et al., 2007b,a). The main sequence is consistently detected across redshift (Noeske et al., 2007a; Speagle et al., 2014; Caputi et al., 2017) with an unchanging finite width of ≈ 0.3 dex, implying that its width and slope arise from self-regulating physical star-forming processes.

The bulk of star-formation took place at redshifts above $z = 1$ (Lilly et al., 1996; Madau et al., 1996; Hopkins and Beacom, 2006; Noeske et al., 2007c,a) and the normalisation of the main sequence increases towards higher star-formation rates with higher redshifts. Indeed, the current star-formation rate is approximately $1/20$ of the star-formation rate at $z = 2$ (Daddi et al., 2007; Hopkins and Beacom, 2006; Behroozi et al., 2013; Madau and Dickinson, 2014). The comparison of star-formation rate density estimates, making use of indicators from infrared to UV, paints a picture of a peak in star-formation density at $z = 2$ in Madau and Dickinson (2014, Fig 1.8) and also in the normalisation of the main sequence (Speagle et al., 2014).

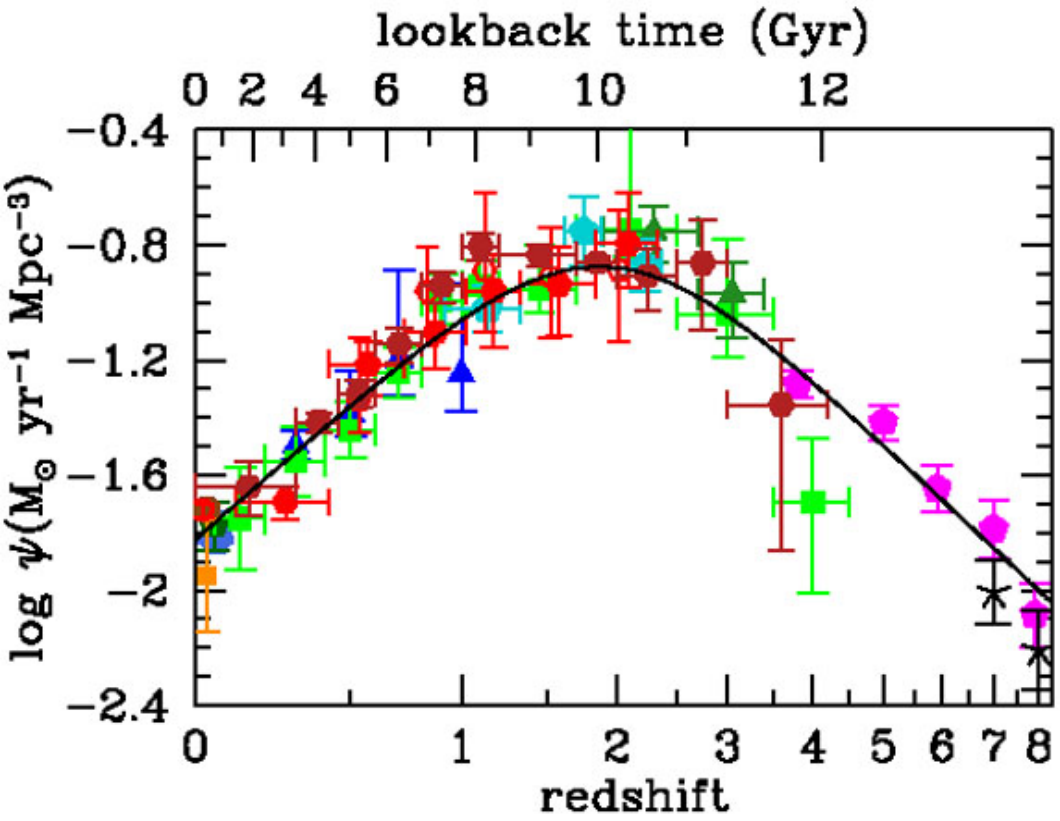

FIGURE 1.8: The cosmic star-formation history (Madau and Dickinson, 2014). The star-formation rate density over redshift as measured by UV (green, blue, and magenta points) and infrared (red and orange points). The UV data points have been corrected for dust attenuation using attenuation-reddening laws applied to spectral slopes of star-forming galaxies or from stellar population model fitting to the full optical-UV integrated SED.

The fact that there is a bimodal distribution of galaxies clearly separated in the planes of colour–magnitude and colour–colour (Tully et al., 1982; Baldry et al., 2004; Strateva et al., 2001), size–colour (Kelvin et al., 2014a,b), colour-structural concentration (Driver et al., 2006; Kelvin et al., 2012), and stellar mass–star-formation rate (Smethurst et al., 2015) suggests that the transition from late-type to early-type happens quickly, on the order of 2 Gyr (Bremer et al., 2018). We rarely observe galaxies within the "green valley" region between the star-forming and quiescent objects (Wetzel et al., 2012).

A plethora of mechanisms have been suggested to transform late-type galaxies into early-types.

Mergers will disrupt the stellar velocity distribution in a disc galaxy, heating the disc, increasing velocity dispersion and central concentration of gas, and eventually turning the galaxy into an early-type (Toomre, 1977). The removal of gas from the host galaxy by central black hole winds (Cicone et al., 2014) would freeze star-formation and cause the disc to fade on long time-scales. Since star-formation rate is proportional to cold gas density[1] (Schmidt, 1959; Kennicutt, 1998a; Lilly et al., 2013), strangulation, i.e. the disruption of inflowing gas, will also reduce the star-formation rate (Peng et al., 2015).

Faber et al. (2007) compared the luminosity functions of red and blue galaxies up to $z \sim 1$ using the DEEP2 (Davis et al., 2003) and COMBO-17 (Wolf et al., 2003) surveys. They found that the total stellar mass of blue galaxies has remained constant over this time with the number and mass of red galaxies rising significantly. It seems then, that blue galaxies must be "quenched" of their star-formation whereupon they transition to the red sequence and increase slowly in mass, perhaps by a series of mergers.

Bouché et al. (2010), Lilly et al. (2013), and Tacchella et al. (2016) have suggested that the main sequence of star-forming galaxies arises from a self-sustaining star-formation feedback loop. The ideal gas-regulated model (Bouché et al., 2010; Lilly et al., 2013) dictates that star-formation rate is proportional to the gas mass within the galaxy (Schmidt, 1959; Kennicutt, 1998a) and that the gas outflow rate is proportional to star-formation rate:

$$\dot{M}_* = \gamma^{-1} m_{gas}, \tag{1.4}$$

$$\dot{m}_{gas} = \lambda \dot{M}_*, \tag{1.5}$$

where the efficiencies γ and λ are assumed to be constant for a given halo mass.

Fig 1.9 shows the confinement of star-forming galaxies to a narrow region in sSFR-M_* space in the VELA hydrodynamic simulation suite (Ceverino et al., 2014; Zolotov et al., 2015; Tacchella et al., 2016). Galaxies travel along the main sequence, building stellar mass though accretion of inflowing gas. When the infall of gas is more efficient than star-formation within the galaxy, the galaxy becomes compact as gas falls to the centre triggering a star-burst. Quenching of star-formation then begins from the inside out as the centre depletes its gas reservoir. However, if the galaxy can be replenished with gas before it is depleted entirely, the quenching trajectory is reversed and the process can begin again, maintaining equilibrium. When the galaxy halo

[1] More precisely, the star-formation rate averaged over the galaxy is well correlated with the surface density of cold gas $\Sigma_{SFR} \propto \Sigma_{gas}^{\sim 1.4} / M_{\odot} yr^{-1} kpc^{-2}$ (Kennicutt, 1998a)

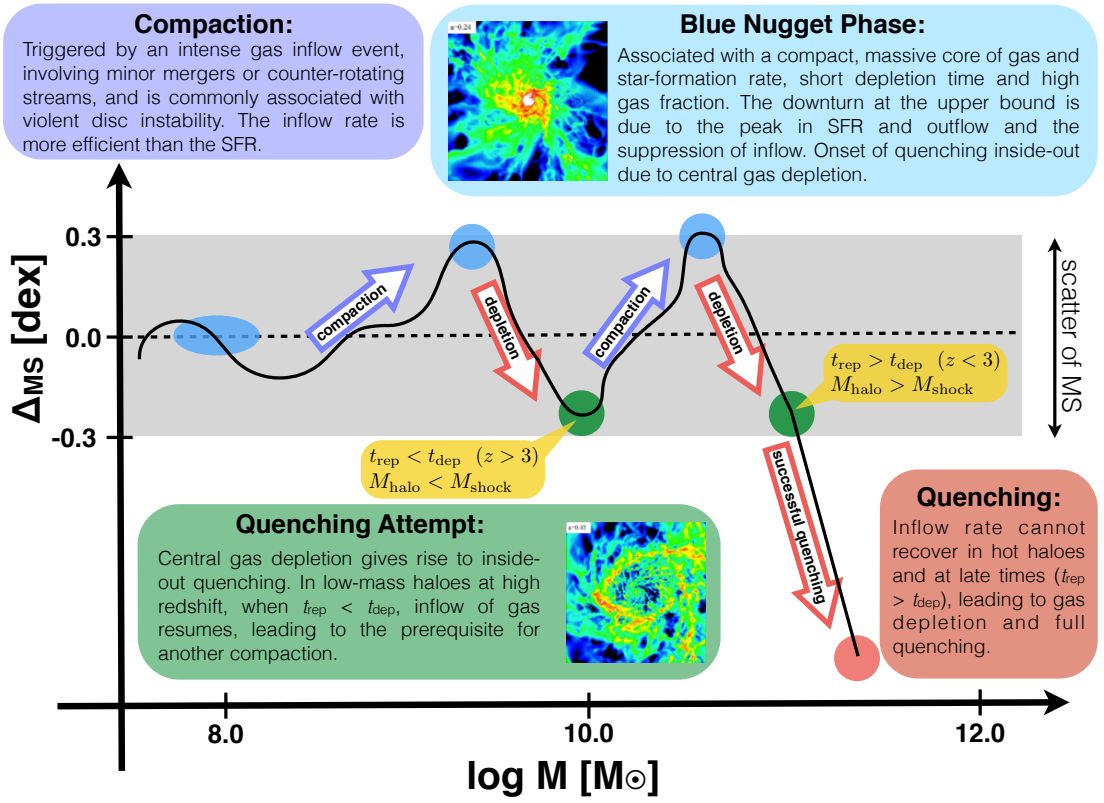

FIGURE 1.9: The main sequence confinement model by Tacchella et al. (2016). The offset from the star-forming main sequence in sSFR and stellar mass as a function of time. This diagram depicts the evolution of a typical star-forming galaxy (in the Tacchella et al. (2016) confinement model). The galaxy experiences a compaction phase where infall supplies gas to the galaxy faster than star-formation feedback can remove it. The galaxy's trajectory off the main sequence is opposed by gas outflow and SFR becoming more efficient in the centre. Quenching begins from the inside out after gas is depleted in the centre. The quenching can be halted in lower mass galaxies with rapid replenishment of gas. Eventually, when the halo mass passes the threshold for virial shock heating, long term quenching dominates and the galaxy moves off the main sequence.

becomes too hot (at about $10^{11.7}\mathrm{M}_{\odot}$), a stable shock (Dekel and Birnboim, 2006) can block the infall of gas and the efficiency of replenishment is substantially reduced allowing the galaxy to fall off the main sequence and be quenched into quiescence. The scatter in the main sequence in Tacchella et al. (comparable to the observed scatter of $\sim$0.3 dex 2016), therefore, is a result of the time that a galaxy spends oscillating in this feedback loop (equating to 1 Gyr at $z = 3$). The results from Tacchella et al. (2016) broadly match predictions for star-formation rate per unit mass over redshift given by Lilly et al. (2013), Speagle et al. (2014), and Schreiber et al. (2016).

1.3.2 A Galaxy Sequence?

However, all of these studies presume the existence of two separate classes of galaxies as evidenced by optical flux-limited surveys. Colour and sSFR cuts are applied and typically two resulting classes are compared. A body of literature is now hinting that rapid quenching is not required in general and that galaxies — with the exception of the 14 per cent of early-types, known as "slow-rotators", whose rotation is dominated by dispersion (Krajnovic et al., 2013) — form a continuous sequence instead of two distinct groups on the sSFR-M_* diagram (Eales et al., 2017). The dichotomy of quiescent and star-forming galaxies is brought into question when selecting galaxies based on their sub-millimetre or infrared colours.

In a volume limited survey, designed to contain all of the mass present in the local universe after 12 Gyr of galaxy evolution, Eales et al. (2017) present evidence for a single continuum from late-type to early-type. When selected in the infrared with the Herschel Reference Survey (Boselli et al., 2010), the sample forms a curved "galaxy" sequence in sSFR-M_* rather than a blue cloud and a red sequence. Furthermore, their morphological classifications smoothly transform from spiral to elliptical along the curved galaxy sequence (Eales et al., 2017, 2018a). If the population of galaxies is indeed unitary, then rapid quenching processes become less important. And indeed, Schawinski et al. (2014) report that the transformation from late-type to early-type morphology is not unimodal nor rapid. Instead, late-type galaxies maintain their disc structure as their star-formation rate fades slowly: the green valley is not a general rapid transition phase. Finding that the stellar metallicity is higher in quenched galaxies than in their progenitors, Peng et al. (2015) have argued that the dominant pathway for star-formation quenching is the strangulation of the gas supply and subsequent disc fading. Furthermore, fine structure such as lenses and rings cannot be expected to survive violent quenching events. The increase in the occurrence of these structures in the green valley relative to their blue and red counterparts serves to demonstrate that violent quenching pathways are less likely (Kelvin et al., 2018; Bremer et al., 2018).

1.4 Active Galactic Nuclei

Star-formation (through supernovae generated outflows) alone cannot explain the paucity of galaxies found at high luminosities where observationally-motivated simulations and theory over-predict their number density as seen in Croton et al. (2006, Fig 1.11) and Schaye et al.

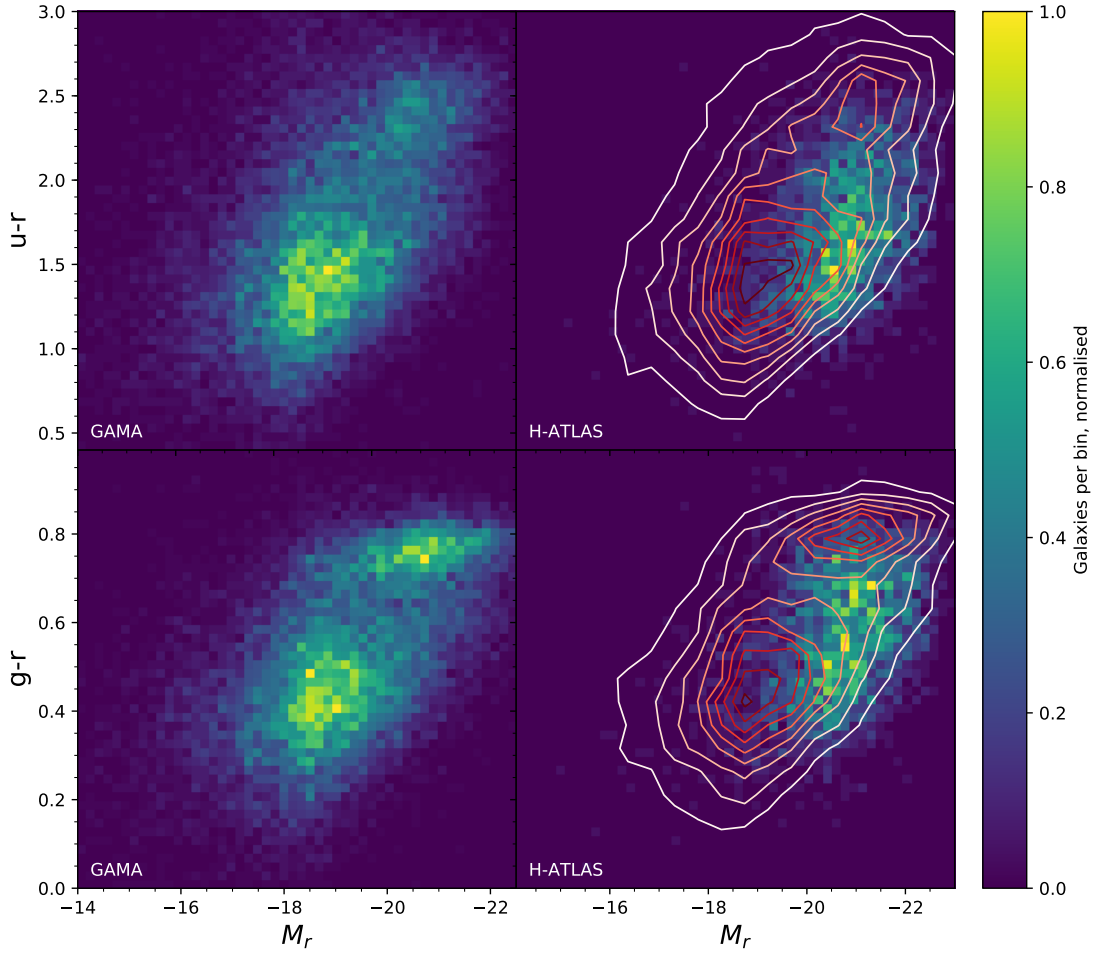

FIGURE 1.10: The green valley and green mountain as described by Eales et al. (2018b). The distribution of galaxies in the $g-r/u-r$ versus M_r planes selected from the GAs and Mass Assembly (GAMA Driver et al., 2011) or *H*-ATLAS. The contours on the *H*-ATLAS panels show the distribution of the GAMA-selected galaxies for comparison.

(2015). A much larger source of energy is required to heat the halo and quench star-formation by cutting off the supply of cool gas.

1.4.1 The Discovery and Unification of AGN

In 1901, Fath (1909) published the first spectroscopic detection of emission lines in the centres of NGC 1068 and Messier 81. Further spectroscopic measurements taken by Slipher (1917); Humason (1932); Mayall (1934, 1939) confirmed the existence of broad emission lines indicating the presence of high-velocity gas in the centres of spiral galaxies. Initially and tentatively, the broad emission lines were thought to be due to a high pressure gradient towards the nuclei of these galaxies. In 1943, the spectra for the original "Seyfert galaxies" NGC 1068, NGC 4151,

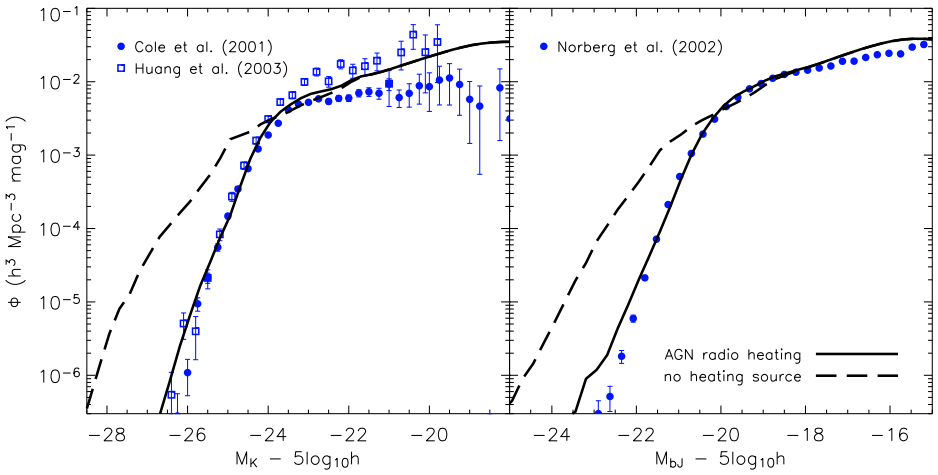

FIGURE 1.11: Comparison of measured galaxy luminosity functions to models from Croton et al. (2006). Points indicate observed data whereas the lines describe the models that include the heating due to AGN (solid line) and do not include the heating due to AGN (dashed line).

NGC 3516, and NGC 7469 were observed by Seyfert (1943) corroborating the growing consensus that there was a class of galaxies with nuclei that are physically different from normal spirals. With the influx of observations from radio telescopes came new insights into the nature of this emission source and the demand for its investigation. Curtis (1918) first observed an optical jet emitted from Messier 87 and the same structure was detected at 150 MHz associated with synchrotron emission by Baade and Minkowski (1954) with other jet structures observed some time after (e.g. Bridle and Perley, 1984; Keel, 1988; Fraix-Burnet, 1990; Liu and Xie, 1992). Quasi-Stellar Objects (Quasars/QSOs) were classified by their rapid variability in optical wavelengths and their small size (Sandage, 1965). After eight years, QSOs were finally accepted to be associated with host galaxies (Kristian, 1973) and located in the nuclei of their host.

Since then, many apparently different AGN have been identified by seemingly unrelated observations concerning emission line width, radio jet structures, optical variability, and high energy X-ray emission. Seyfert galaxies (Seyfert, 1943) were split into two types with Seyfert-I galaxies mostly able to identified by their broad permitted emission lines and Seyfert-IIs being classified only by their narrow forbidden emission lines. Khachikian and Weedman (1974) realised that the two sets of emission lines are superimposed, implying that different physical processes produced the two sets. The continuous nature of the Seyfert classification system was later suggested by Osterbrock (1981) where lower Seyfert numbers indicate the relative dominance of broad permitted lines, higher Seyfert numbers represent the relatively weaker broad lines in comparison to the narrow lines.

Broad emission lines indicate the presence of fast moving gas in the centre of Seyfert-I galaxies and the presence of strong forbidden narrow-lines in Seyfert-IIs requires the existence of a far harder source of ionising photons than supernovae in order to excite them. The energy output from young OB stars is insufficient to explain the Seyfert-II spectra, instead a heating source with a power-law spectrum or shock-heated gas must be responsible (Baldwin et al., 1981) – both of which imply energetic activity in the centre of these galaxies. Moreover, due to their high redshifts and luminosities, QSOs must be some of the most energetic objects in the universe ($> 10^{44}\,\mathrm{ergs}^{-1}$ in optical wavelengths). It seems that AGN must be powered by a highly energetic non-stellar energy source. The first attempt at unifying the different nuclear activities was suggested by Lynden-Bell (1969a) with a collapsed QSO model for explaining AGN energies. In this now accepted model, the accretion disc around a central black-hole provides the energy necessary to excite emission lines and produce variable continua. Furthermore, the magneto-hydrodynamical effects in the accretion disc are thought to power the jet seen in some radio AGN (Blandford and Znajek 1977; see also Sbarrato et al. 2014 and references therein).

In 1985, Antonucci and Miller (1985) measured the polarised spectrum from a standard Seyfert-II galaxy, NGC1068, and found that it resembled the expected spectrum of a Seyfert-I AGN. This was interpreted to mean that a Broad-Line Region (BLR) of fast moving gas had scattered the ionised light while the direct view of the central continuum emission was blocked by a dusty torus, matching the prediction of Antonucci (1984) for 3C234. The unification paradigm for AGN posits that all active galactic nuclei consist of essentially the same components. A central Super-Massive Black-Hole (SMBH) provides the gravitational potential to power the AGN (their existence supported by the detection of Keplerian motion in a nuclear disc by both stars in the Milky Way and gas e.g. Gillessen et al. 2009). The accretion disc surrounding the SMBH generates the continuum (Koratkar and Blaes, 1999) and a hot corona up-scatters the photons to produce high energy X-ray emission (Cao, 2009). The continuum emission is absorbed and reprocessed by a dusty torus providing the mid-infrared bump (Pier and Krolik, 1992; Contini et al., 2004; Fritz et al., 2006). A region of fast-travelling gas at small radii (BLR) produces the broad emission lines in Seyfert-Is and a region of ionised gas at larger radii producing the narrow-lines found in Seyfert-IIs.

Given this geometry, an AGN is classified as a Seyfert-II when the torus is oriented to block emission from the central region and the BLR (Antonucci, 1993; Netzer, 2015). The orientation unification model shown in Fig 1.12 also incorporates QSOs and blazars by jet orientation.

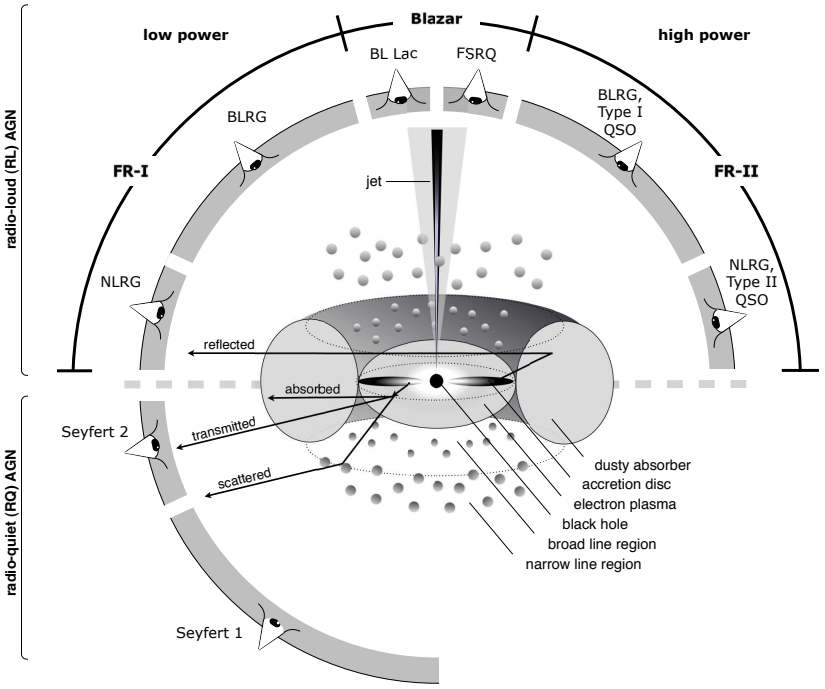

FIGURE 1.12: The schematic view of the orientation model of AGN unification taken from Beckmann and Shrader (2013). Different types of AGN are observed based on which universal components can be seen from different viewing angles. Radio-loud and radio-quiet AGN are also included, depicted by the presence (or not) of a jet.

QSOs are observed when a jet is pointed towards the observer, simultaneously producing a flat-spectrum (Urry and Padovani, 1995).

However, the orientation unification model cannot account for the presence (or not) of the radio jet itself: the presence of the jet must be governed by some intrinsic physical process. Best and Heckman (2012) summarises a description of two fundamentally different populations of AGN. Radiative-mode AGN are defined by their electromagnetic-dominated energy output. They can be further split into obscured and unobscured types, based on the viewing angle, producing the Seyfert classification system as detailed above. However, the energy output of jet-mode AGN is not dominated by electromagnetic (EM) energy and is instead mainly comprised of particle jets produced by advection-dominated flows (Narayan and Yi, 1995; Best and Heckman, 2012). In jet-mode AGN, the thin accretion disc found in radiative-mode AGN is replaced with a thick structure in which inflow is much shorter than radiative cooling time-scales and is therefore more radiatively inefficient. Radiatively-inefficient flows are capable of creating the relativistic jets which can be seen to extend to megaparsec scales. Radiatively-efficient flows, on the other hand, produce radiative-mode AGN, where the accretion rate is inferred to be much higher. The

ratio of AGN bolometric luminosity L_{bol} to its Eddington luminosity L_{edd} is canonically $\gtrapprox 0.01$ for these objects.

$$\frac{L_{bol}}{L_{edd}} = \frac{\varepsilon \dot{M} c^2}{4\pi G m_p c M_{BH}/\sigma_T} \approx \frac{9.1 \times 10^4 \varepsilon \dot{M}}{M_{BH}}, \tag{1.6}$$

where $\dot{M}$ is the accretion rate and ε is the accretion efficiency (theoretically motivated to be ~ 0.1: Best and Heckman 2012), and σ_T is the Thompson scattering cross-section. Radiatively-efficient AGN have higher radio luminosities (Best and Heckman, 2012) and more strongly ionise narrow emission lines with their higher EM output than in jet-mode AGN.

1.4.2 AGN and Star-formation: Co-evolution of AGN with their Hosts

With this much energy deposited from the AGN into the surrounding environment and host (Dunn and Fabian, 2006), it is reasonable to investigate whether AGN can influence the development of their hosts and neighbouring galaxies. Despite the disparity between relative masses and sizes, the mass of a bulge correlates surprisingly tightly with the mass of the central black-hole (e.g. Ferrarese and Merritt, 2000; Gebhardt et al., 2000; Merritt and Ferrarese, 2001; Tremaine et al., 2002; Wyithe and Padmanabhan, 2006; Wyithe, 2006; Hu, 2008; Gültekin et al., 2009; Woo et al., 2013).

Figure 1.13 shows the tight correlation between bulge stellar velocity dispersion and black-hole mass as measured by different methods over a wide dynamic range of masses and Hubble type. This shows that the central nucleus with gravitational influence over a few parsecs (Merritt, 2013) has influence on the stars on scales of kiloparsecs.

Could the central SMBH then contribute to feedback and regulation of star-formation? Upon measuring the ratio of star-formation to black-hole growth per unit volume over the last 10 Gyr Shankar et al. (2009); Heckman and Best (2014) find that the ratio remains roughly constant, with both growth rates experiencing a steep decline at high redshifts. The growth of black-holes and their hosts must therefore be linked, when averaging over volume.

There is a wealth of evidence that outflows are driven by radio-quiet AGN, based on blueshifted absorption lines in unobscured AGN (e.g. Crenshaw et al., 2003; Fabian, 2012), infrared emission from dust outflows driven by winds (e.g. Baron and Netzer, 2019) or radiation pressure (e.g. Ishibashi and Fabian, 2015); all implying fast outflows of gas with velocities of several tens of thousands of kms^{-1}.

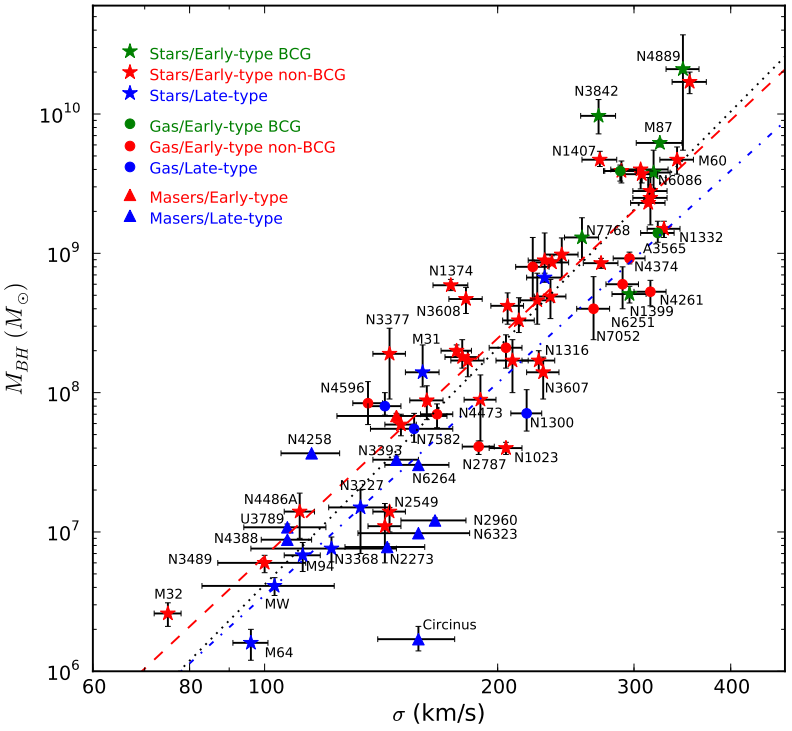

FIGURE 1.13: The $M_\odot$-σ relation as fit by McConnell and Ma (2013) for 72 galaxies of varying Hubble type with black-hole masses measured by a combination of Maser, gas, and stellar dynamics. A green marker indicates that the galaxy is Brightest Cluster Galaxy (BCG), a red marker indicates that the galaxy is designated as early-type, and a blue marker shows the late-types. The coloured lines indicate fits to the coloured points, with the black line depicting a fit to all data.

As for radio-loud sources, the evidence comes from the radio structures themselves. The jets and lobes observed at radio frequencies have been shown to expand, therefore performing thermodynamic work on their surrounding environment (Scheuer, 1974; Blandford and Rees, 1974; Kaiser et al., 1997; Begelman and Cioffi, 1989; Hardcastle and Worrall, 2000; Croston et al., 2004). Furthermore, the cooling time for the gas in a cluster environment is much shorter than the Hubble time, but cooling flows, which would provide gas for star-formation rate in excess of 1000 $M_\odot yr^{-1}$, are not seen (only around 10 per cent is observed, Peterson 2001; David et al. 2001; Tamura et al. 2001; Peterson et al. 2003). A candidate heating source to balance the cooling flow is the radio-AGN present in 70 per cent of Brightest Cluster Galaxies, BCGs, (Burns, 1990; Best et al., 2007; Best, 2007). To that effect, using a suite of simulated jet-mode AGN, Hardcastle et al. (2018) integrate over the kinetic energy output all radio loud AGN to arrive at a kinetic luminosity of 7×10^{31} W Mpc^{-3}. This value is comparable to the total cooling luminosity, 3×10^{31} W Mpc^{-3}. in local clusters (whose population is characterised by Böhringer

et al. 2014). This result implies that radio loud AGN can offset cluster cooling enough to be considered responsible for the continued quenched state of their massive elliptical hosts (Tadhunter, 2016). In addition, Seyfert galaxies are frequently positioned in the optical green valley (Smolcic, 2009; Pierce et al., 2010), which are assumed to be in the process of quenching; the AGN fraction peaks in the green valley (Martin et al., 2007).

AGN then undoubtedly contribute to the star-formation history of their host galaxies either by heating the surrounding gas to halt cooling flows which feed star-formation, or blow out the gas in a "fountain" to regulate star-formation (Croton et al., 2006; de Gouveia Dal Pino et al., 2018; Croton et al., 2016; Wada et al., 2016; Biernacki and Teyssier, 2018).

1.4.3 The Contamination of Star-forming Relations by AGN

Since most galaxies host a SMBH, and given an average duty cycle for AGN, it is reasonable to expect that most galaxies have or will play host to an active nucleus. If this is the case, and AGN emission is ubiquitous, then how can we trust that the star-formation indicators and fitted properties remain uncontaminated by non-star-forming processes?

It is hard to disentangle AGN and star-formation in an individual galaxy. Spatially fitting a nuclear component to a photometrically observed galaxy can remove some of the influence of the AGN (Belfiore et al., 2017; Sánchez et al., 2018; Spindler et al., 2018; Penny et al., 2018), and tools such as AGNFITTER (Calistro-Rivera et al., 2016) and CIGALE (Burgarella et al., 2005; Ciesla et al., 2015) are able to fit the SEDs of a star-forming component and an AGN component simultaneously, allowing the estimation of star-formation rates uncontaminated by AGN emission. However, spatially decomposing an individual galaxy is only successful at high resolutions and low redshifts. In addition, AGN/host decomposition by SED fitting requires measurements at many different wavelengths in order to properly partition the total SED.

With the aid of diagnostic diagrams such as mid-infrared diagrams (Stern et al., 2005; Jarrett et al., 2011; Stern et al., 2012; Coziol et al., 2015) which make use of increased emission supposedly from the dusty obscuring torus; emission line ratios such as BPT (Baldwin et al., 1981; Veilleux and Osterbrock, 1987); the offset from the star-forming correlation of radio luminosity with Hα and infrared emission; or a combination of stellar mass, radio luminosity, and $D_n(4000)$ strength (Best et al., 2005), it is possible to select a sample of galaxies where star-formation emission dominates by only using a small number of statistics, as shown in Fig 1.14.

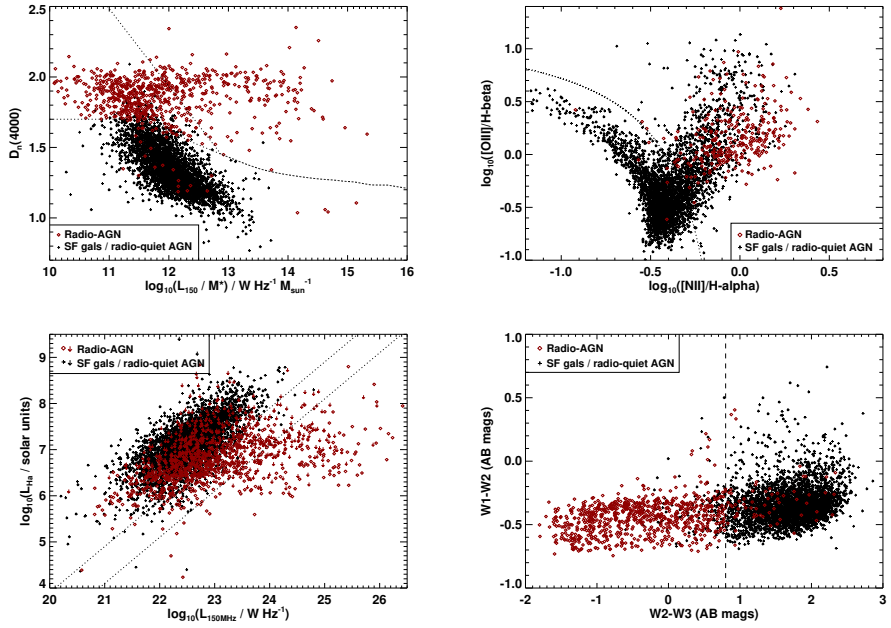

FIGURE 1.14: The Location of star-forming sources in the LOFAR Two-Metre Sky Survey (LoTSS, Williams et al. 2018b) DR1 taken from Sabater et al. (2018). *Upper left:* The 'D_{4000} versus $L_{150\,\mathrm{MHz}}/M_*$' method (Best et al., 2005). *Upper right:* The BPT emission line ratio diagnostic diagram (Baldwin et al., 1981). *Lower left:* The $L_{\mathrm{H}\alpha}$ versus $L_{150\,\mathrm{MHz}}$ relation. *Lower right:* The WISE W1–W2 versus W2–W3 colour-colour diagnostic diagram (MIRDD) (Wright et al., 2010; Jarrett et al., 2011). The radio AGN are labelled by red dots in all diagrams and the dotted lines represent each diagnostic's star-forming/AGN separation criteria.

However, low luminosity AGN are frequently not detectable by the diagnostics that are readily available and so their effect on the star-formation history and evolution of galaxies is unknown and probably conflated with that of a supposed "pure" star-forming sample (Read et al., 2018). Thus, in order to fully understand galaxy evolution and the impact of star-formation processes, it is of vital importance to characterise star-formation relations while accounting for the existence of low-level AGN emission.

1.5 Motivations and the Structure of this Thesis

The relative importance of different feedback mechanisms and quenching pathways are still very much debated. Radio star-formation rate relations are highly important to the upcoming radio surveys but they are a highly indirect measure of star-formation involving many areas of physics that are poorly-understood in star-forming galaxies. Indeed, it is vital that the shortcomings of the extrapolation of low redshift scaling relations to higher redshifts are well-known in order to understand the past evolution of galaxies.

There is therefore a need to develop methods to probe these relations and measure the properties of star-forming galaxies in order to understand the physics of star-formation and the evolution of galaxies.

In the age of large-scale surveys such as SDSS, LSST, SKA, which will provide truly huge amounts of data, it becomes possible to study and understand these complex scaling relations in multiple dimensions through sophisticated inference techniques. This thesis is a summary of the development, validation, and results of hierarchical models applied to scaling relations.

In the second chapter, we investigate the relation between radio luminosity at low frequency (which in principle should be cleanly related to SF) and infrared luminosity, in order to provide information about the use of the FIRC to calibrate radio star-formation rates. We find that the FIRC is untrustworthy as a star-formation rate indicator with large variations with mass, redshift, and dust temperature. The third chapter explores an untested photometric method to calibrate the black-hole mass – luminosity relation for reverberation mapping, which uses the delay between emissions from the central engine of the AGN and the outer Broad-Line Region to calculate the mass (Blandford and McKee, 1982). We validate the effectiveness of `Javelin`, the Bayesian reverberation mapping code, and then perform photometric reverberation mapping for a QSO to demonstrate its effectiveness. The fourth chapter concerns an investigation into the star-formation rate (as measured with Hα) radio luminosity relation (as measured by LOFAR at 150 MHz). Following the detection of a mass dependency in excess to that expected (Gurkan et al., 2018), we apply a new extreme deconvolution method to fit the joint distribution of star-formation rate, stellar mass, and radio luminosity as a function of redshift, emission line strength, and optical magnitude in an effort to remove selection biases from analysis. Finally, we conclude with a summary and exploration of future work.

We assume a standard ΛCDM cosmology with $H_0 = 71\,\mathrm{km\,s^{-1}\,Mpc^{-1}}$, $\Omega_M = 0.27$ and $\Omega_\Lambda = 0.73$ throughout and use the AB magnitude system unless otherwise stated.

Chapter 2

The Far-infrared Radio Correlation at Low frequency with LOFAR

2.1 Introduction

The far-infrared luminosities of star-forming galaxies have long been known to correlate tightly and consistently with synchrotron radio luminosity across many orders of magnitude in infrared and radio luminosities, independent of galaxy type and redshift (van der Kruit, 1971; de Jong et al., 1985; Condon et al., 1991; Yun et al., 2001; Bell, 2003; Bourne et al., 2011).

The existence of some relation should not be surprising since the basic physics relating emission in each waveband to the presence of young stars is well understood. Young stars heat the dust within their surrounding birth clouds, which radiate in the infrared (Kennicutt, 1998b; Charlot and Fall, 2000). The supernovae resulting from the same short-lived massive stars accelerate cosmic rays into the galaxy's magnetic field thereby contributing non-thermal radio continuum emission over $\approx 10^8$ years (Blumenthal and Gould, 1970; Condon, 1992; Longair, 2011). However, the fact that the Far-Infrared Radio Correlation (FIRC) has consistently been found to have low scatter (Helou et al., 1985; de Jong et al., 1985; Condon, 1992; Lisenfeld et al., 1996a; Wong et al., 2016) is surprising. Such tight linearity is consistent with a simple calorimetry model (Voelk, 1989), whereby cosmic ray electrons lose all of their energy before escaping the host galaxy and where all UV photons are absorbed by dust and re-radiated in the infrared. This results in synchrotron radiation being an indirect measure of the energy of the electron population and infrared luminosity being proportional to young stellar luminosity. Therefore, assuming

calorimetry, the ratio of these two measures will remain constant as they are both dependent on the same star formation rate. The FIRC can therefore be used to bootstrap a calibration between a galaxy's star formation rate and its radio luminosity (e.g. Condon, 1992; Murphy et al., 2011) – but only if there is no additional contribution from AGN.

The physics required to model the FIRC is complex. For example, the timescale of the electron synchrotron cooling that produces the radio emission is thought to be longer than the timescale for the escape of those electrons (Lisenfeld et al., 1996b; Lacki et al., 2010) for normal spirals, and starlight is only partially attenuated in the UV (Bell, 2003). Therefore, it is reasonable to suppose that the calorimetry interpretation must be at least partially inaccurate and that there should be some observable variation in the FIRC over the diverse population of star-forming galaxies. In particular, due to their strong magnetic fields, we expected starburst galaxies to be good calorimeters and therefore have a correlation with a slope that is much closer to one than other star-forming galaxies (Lacki et al., 2010).

However, since synchrotron emission depends strongly on magnetic field strength, the assumption about how this changes with galaxy luminosity is crucial to explain the correlation. Alternatives to the calorimetry model have also been proposed, e.g. (i) the model of Niklas and Beck (1997), where the FIRC arises as the by-product of the mutual dependence of magnetic field strength and star-formation rate upon the volume density of cool gas, and (ii) Schleicher and Beck (2016), where the FIRC is based on a small-scale dynamo effect that amplifies turbulent fields from the kinetic turbulence related to star formation. There are a number of reasons to expect the FIRC to vary with the parameters that control synchrotron and dust emission, but it seems that infrared and radio synchrotron must both fail as star formation rate indicators in such a way as to maintain a tight and linear relationship over changing gas density. The model detailed by Lacki and Thompson (2010) and Lacki et al. (2010) suggests that although normal galaxies are indeed electron and UV calorimeters, conspiracies at high and low surface density, Σ_g, contrive to maintain a linear FIRC. At low surface density, many more UV photons escape (and therefore lower observed infrared emission) due to decreased dust mass but at the same time, because of the lower gravitational potential, more electrons escape without radiating all their energy, decreasing the radio emission. Meanwhile, at high surface densities, secondary charges resulting from cosmic ray proton collisions with ISM protons become important (Torres, 2004; Domingo-Santamaria and Torres, 2005). Synchrotron emission from those electrons and positrons may dominate the emission from primary cosmic ray electrons. However, the

FIRC is maintained due to the increased non-synchrotron losses from bremsstrahlung and inverse Compton scattering at higher densities.

These conspiracies rely on fine tuning of many, sometimes poorly known, parameters in order to balance the mechanisms that control the linearity of the FIRC. If we expect variation over star-forming galaxies due to differences in gas density, stellar mass, and redshift (to name a few), then we should probe the FIRC over known star-forming sequences such as those found in colour-magnitude (Bell et al., 2004) and mid-infrared colour-colour diagrams (e.g. Jarrett et al., 2011; Coziol et al., 2015), and the star formation rate – stellar mass relation (Brinchmann et al., 2004; Noeske et al., 2007b; Peng et al., 2010; Rodighiero et al., 2011).

Naively, we might also expect some variation of the FIRC with redshift. At the very least, radio luminosity should decrease with respect to infrared luminosity due to inverse Compton losses from cosmic microwave background (CMB) photons (Murphy, 2009). The CMB energy density increases proportional to $(1+z)^4$ (Longair, 1994), so the ratio of infrared to radio luminosity should noticeably increase with redshift even at relatively local distances, assuming a calorimetry model and that CMB losses are significant.

However, this is one of the key areas of dispute between different observational studies. While many works find no evidence for evolution (e.g. Garrett, 2002; Appleton et al., 2004; Seymour et al., 2009; Sargent et al., 2010), there are exceptions (e.g. Seymour et al., 2009; Ivison et al., 2010; Michałowski et al., 2010b,a; Basu et al., 2015; Calistro-Rivera et al., 2017; Delhaize et al., 2017). Particular among those studies, Calistro-Rivera et al. (2017) find a significant redshift trend at both 150 MHz and 1.4 GHz when using the *Low Frequency Array* (LOFAR, van Haarlem et al., 2013) data taken over the Boötes field. The FIRC has been studied extensively at 1.4 GHz (de Jong et al., 1985; Condon et al., 1991; Bell, 2003; Jarvis et al., 2010; Bourne et al., 2011; Smith et al., 2014) but rarely at lower frequencies. These low frequencies are particularly important, since new radio observatories such as LOFAR are sensitive in the $15-200$ MHz domain, where at some point the frequency dependence of optical depth results in the suppression of synchrotron radiation by free-free absorption (Schober et al., 2017), causing the radio SED to turn over. As a result, there will be some critical rest-frame frequency below which we can expect a substantially weaker correlation between a galaxy's radio luminosity and its star formation rate.[1] Moreover, at the higher frequencies probed by *Faint Images of the Radio Sky at Twenty centimetres* (FIRST, Becker et al., 1995) (1.4 GHz), there may be a thermal

[1] This frequency at which a galaxy's radio SED turns over will depend heavily upon gas density and ionisation, and so we expect it to vary from galaxy to galaxy.

component present in the radio emission (Condon, 1992), which tends to make the correlation between infrared and higher radio frequencies more linear. However, due to the poor sensitivity of FIRST to star-forming galaxies with low brightness temperatures (galaxies with $T_{\rm bright} < 10$K will not be detected by FIRST), we cannot expect the thermal components of detected sources to help linearise the FIRC at 1.4 GHz. At low frequencies, these effects become less important and so the perspective they provide is useful in disentangling the effect of thermal contributions and lower luminosity galaxies on the FIRC. Given the potential ramifications for using low-frequency radio observations as a star formation indicator, this possibility must be investigated. Indeed, Gurkan et al. (2018) have found that a broken power-law is a better calibrator for radio continuum luminosity to star-formation rate, implying the existence of some other additional mechanism for the generation of radio-emitting cosmic rays.

Furthermore, lower radio frequencies probe lower-energy electrons, which take longer to radiate away their energy than the more energetic electrons observed at 1.4 GHz, and this results in a relationship between the age of a galaxy's electron population and the radio spectral index (Scheuer and Williams, 1968; Blundell and Rawlings, 2001; Schober et al., 2017). Therefore, even if the FIRC is linear at high frequencies due to some conspiracy, this will not necessarily be the case at low frequencies. An investigation of the FIRC at low frequency will test models of the FIRC which rely on spectral ageing to maintain linearity (e.g. Lacki et al., 2010).

Combined with the fact that radio observations are impervious to the effects of dust obscuration, this makes low-frequency radio observations a very appealing means of studying star formation in distant galaxies, providing that the uneasy reliance of SFR estimates on the FIRC can be put on a more solid footing. The nature of the FIRC conspiracies varies over the type of galaxy and its star formation rate (Lacki and Thompson, 2010). The detection of variation in the FIRC over those galaxy types, or lack thereof, will provide important information about the models that have been constructed (e.g. Lacki and Thompson, 2010; Schober et al., 2017). Several methods are used to distinguish galaxy types for the purposes of studying the FIRC, particularly to classify these into star-forming galaxies and AGN such as BPT diagrams (Baldwin et al., 1981), panchromatic SED-fitting with AGN components (Berta et al., 2013; Ciesla et al., 2016; Calistro-Rivera et al., 2016), and classification based on galaxy colours. Among these, galaxy colours provide a readily accessible method to distinguishing galaxy types or act as proxies for properties such as star formation rate. Diagnostic colour-colour diagrams are commonplace in galaxy classification; infrared colours in particular have been widely used to distinguish between star-forming galaxies and AGN (Lacy et al., 2004; Stern et al., 2005; Jarrett et al., 2011; Mateos

et al., 2012; Coziol et al., 2015). In order to investigate the potential difference in the FIRC over normal galaxies as well as in starbursts we use the mid-infrared diagnostic diagram, (MIRDD, Jarrett et al. 2011) . Constructed from the *Wide-field Infrared Survey Explorer* (WISE, Wright et al., 2010) $[4.6]-[12]$ and $[3.4]-[4.6]$ colours, SWIRE templates (Polletta et al., 2006, 2007) and GRASIL models (Silva et al., 1998) can be used to populate the MIRDD with a range of galaxy types spanning a redshift range of $0 < z < 2$. This MIRDD not only distinguishes AGN and SFGs but also describes a sequence of normal star-forming galaxies whose star formation rate increases to redder colours.

Past 1.4 GHz surveys such as FIRST and the *NRAO VLA Sky Survey* (NVSS, Condon et al., 1998) have been extremely useful in studying star formation, though there are inherent problems in using them to do this. NVSS is sensitive to extended radio emission on the scale of arcminutes. However, its sensitivity of ~ 0.5 mJy beam^{-1} and resolution of $45''$means that it is difficult to identify radio counterparts to optical sources and its flux limit means that it will preferentially detect bright or nearby sources. FIRST has both a higher resolution and a higher sensitivity than NVSS ($5''$ with ~ 0.15 mJy beam^{-1}). However, due to a lack of short baselines, FIRST resolves out the extended emission frequently present in radio-loud AGN and in local star-forming galaxies (Jarvis et al., 2010). This makes it difficult to remove galaxies dominated by AGN and to directly compare star-forming galaxies over different wavelengths. Meanwhile, LOFAR offers the best of both worlds: a large field of view coupled with high sensitivity on both small and large scales and high resolution (van Haarlem et al., 2013) at frequencies between 30 and 230 MHz. Operating at 150 MHz, LOFAR contributes a complementary view to the wealth of data gathered at higher frequencies. The sparsely examined low-frequency regime offered by LOFAR combined with its increased sensitivity and depth relative to other low-frequency instruments allows us to probe the FIRC in detail, and to test predictions of its behaviour relative to relations at higher frequencies that we measure with FIRST.

This study will analyse the nature of the FIRC at low and high frequencies and over varying galaxy properties. How does the FIRC evolve with redshift? Does it vary as a function of WISE mid-infrared colour? Do the specific star-formation rate (as fit by MAGPHYS) and stellar mass impact these questions? We answer these questions for our data set and compare these metrics with those found at higher frequencies and with literature results using different selection criteria.

This work uses the same base dataset as Gurkan et al. (2018). The same aperture-corrected fluxes

extracted from *Herschel*, LOFAR, and FIRST images are used here. Our investigation differs from theirs in that we concentrate on the observed variation of the FIRC over dust properties whereas Gurkan et al. (2018) focus on the direct characterisation of radio star-formation rates. In Section 2.2, we describe our data sources and the method of sample selection. In Section 2.3 we outline our methods for calculating K-corrections, luminosities, and the methods used to characterise the variation of the FIRC. We present and discuss the results of these procedures in Section 2.4, and summarise our conclusions in Section 2.5. For consistency with Jarrett et al. (2011), all magnitudes are in the Vega system.

2.2 Data Sources

The dataset we use here is the same as Gurkan et al. (2018) in that the infrared and radio aperture-corrected fluxes are drawn from the same catalogue. However, due to two effects listed below, our star-forming sample is selected using a different method. Firstly, a potential contamination of AGN will have a large effect on the detected variation of infrared-to-radio luminosity ratio over mid-infrared colours. We therefore require stronger signal-to-noise criteria (5σ detections in the BPT optical emission lines) than the one in use in Gurkan et al. (2018) (3σ). Secondly, using the Gurkan et al. (2018) star-forming selection criterion but with a 5σ requirement results in too few star-forming galaxies with reliable 5σ detections in the first three WISE bands. In order to increase our sample size but maintain robust classification we employ the methods detailed below.

2.2.1 Sample selection

To avoid introducing a possible bias by selecting our sample from far-infrared and/or radio catalogues, our sample is drawn from the MPA-JHU catalogue (Brinchmann et al., 2004) over the region of the *North Galactic Pole* (NGP) field covered by the LOFAR/*H*-ATLAS survey, which is described in sections 2.2.2 and 2.2.3. The MPA-JHU catalogue uses an optimised pipeline to re-analyse all SDSS (York, 2000) spectra, resulting in a sample with reliable spectroscopic redshifts, improved estimates of stellar mass, and star formation rate, as well as emission line flux measurements for each galaxy. We use their latest analysis performed on the SDSS DR7 release (Abazajian et al., 2009) to obtain optical emission line fluxes and spectroscopic redshifts for K-corrections.

To select our star-forming sample, we first obtain all optically selected 15,003 sources in the MPA-JHU catalogue with reliable (`ZWARNING = 0`) spectroscopic redshifts $z < 0.7$ in the region covered by our LOFAR/*H*-ATLAS data. Since we are interested in studying the FIRC, we wish to focus only on star-forming galaxies, and remove those sources with evidence for contamination by emission from an active galactic nucleus (AGN). Our priority is to seek an unbiased sample at the cost of such a sample not necessarily being complete. We do this using the BPT (Baldwin et al., 1981) emission line classification method, requiring fluxes detected at $\geq 5\sigma$ in $H\alpha$, $H\beta$, $[OIII]\lambda 5007$, and $[NII]\lambda 6584$, together with the star-forming/composite line defined by Kewley et al. (2001). 3,082 galaxies, with redshifts $z < 0.4$, are identified as star-forming in this manner.

To give us the largest possible sample of star-forming galaxies, we include those galaxies with 5σ detections in $[NII]\lambda 6584$, $H\alpha$, and $H\beta$, provided that the upper limit on the $[OIII]\lambda 5007$ flux in the MPA-JHU catalogue enables us to unambiguously classify them as star-forming. By using this method, we can be sure that they lie below the star-forming/composite line from Kewley et al. (2001) in Figure 2.1. We identify an additional 1,012 star-forming galaxies using this criterion, and they are shown in purple in Figure 2.1. In addition, we remove the 12 sources which lie within the QSO box defined in Jarrett et al. (2011). This provides us with our main sample of 4,082 star-forming galaxies with $z < 0.4$ for use in comparing the FIRC at high and low frequencies. We constructed the MIRDD (Jarrett et al., 2011) based on *WISE All Sky Survey* (WISE, Cutri, 2012) fluxes (with no *K*-correction applied) to identify the location of our galaxies compared to a range of sources of different types. Since we are binning across WISE colour spaces, we construct a second sample for the mid-infrared analysis only, requiring 5σ detections in the first three WISE bands (centred on 3.4 μm, 4.6 μm, and 12 μm). This results in a sub-sample of 2,901 sources for use in tracing the FIRC over the mid-infrared colour space depicted in Figure 2.2. Our sample sizes are shown in Table 2.1.

We do not use the catalogue of detected sources summarised by Table 2.1 for our analysis here. Such a catalogue will inevitably become contaminated with noise spikes. Instead, we employ averaging techniques described below in order to treat non-detections and detections in the same manner. We don't make any signal-to-noise cuts beyond those imposed on the BPT emission lines used in the star-forming classification. In addition, our samples are drawn from the MPA-JHU catalogue and so this imposes a strong optical prior on the location of a given source. This allows us to conduct forced aperture photometry, in order to estimate radio fluxes

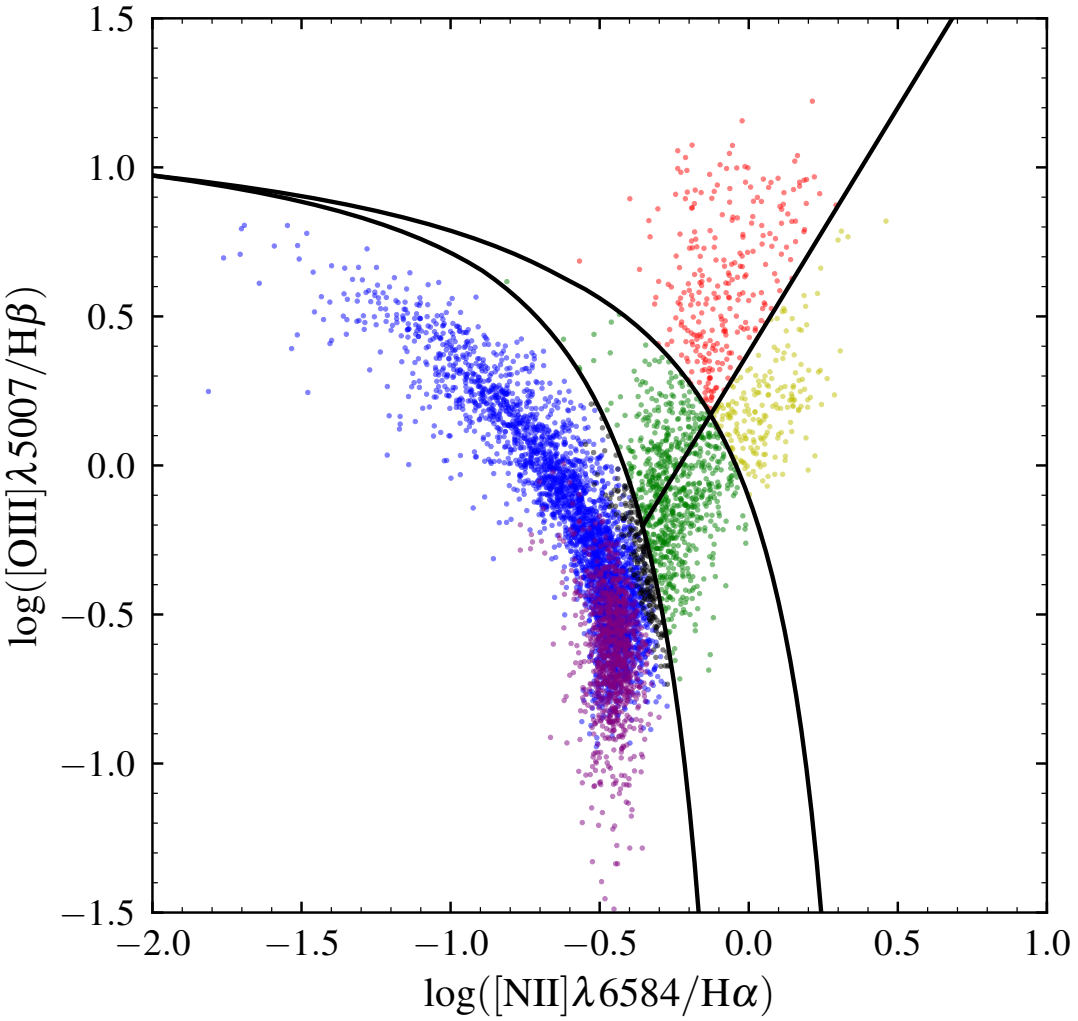

FIGURE 2.1: Emission line ratio diagnostic diagram. The coloured points represent Seyfert 2s (in red), star-forming galaxies (blue), transition objects (green), and LINERs (yellow). The black points are those galaxies whose 5σ upper limit on $[OIII]\lambda5007$ flux would not classify them as purely star-forming (not included in our sample). The purple points show those additional galaxies whose upper limits in $[OIII]\lambda5007$ still classifies them as star-forming. The upper and lower solid black lines used to distinguish between populations are from Kewley et al. (2001) and Kauffmann et al. (2003a) respectively.

(see Section 2.2.4), for our entire sample with a high degree of confidence that the aperture is correctly placed.

2.2.2 Infrared data

The far-infrared data used in this study come from the *H*-ATLAS survey (Eales et al., 2010; Valiante et al., 2016; Smith et al., 2017; Maddox et al., 2018; Furlanetto et al., 2018). *H*-ATLAS is the largest extragalactic *Herschel* survey, covering a total of 510 deg^2 in five infrared bands with the *Photoconductor Array Camera and Spectrometer* (PACS, Ibar et al., 2010; Poglitsch

TABLE 2.1: Number of star-forming galaxies within each sub-sample detected with *Herschel* at 250 μm , LOFAR at 150 MHz, and FIRST at 1.4 GHz.

		1. All SFGs	2. WISE detected SFGs
$> 3\sigma$	*Herschel*	3351	2673
	LOFAR	2436	2016
	FIRST	1438	1098
	both radio bands	1008	863
$> 5\sigma$	*Herschel*	2616	2209
	LOFAR	1876	1627
	FIRST	835	640
	both radio bands	533	455
total		4082	2901

et al., 2010) and *Spectral and Photometric Imaging Receiver* (SPIRE, Griffin et al., 2010; Pascale et al., 2011; Valiante et al., 2016) instruments (sampling wavelengths of 100, 160, 250, 350, and 500 μm). The *H*-ATLAS catalogues have a 5σ noise level of 33.5 mJy at 250 μm, which is the most sensitive band (Ibar et al., 2010; Rigby et al., 2011; Smith et al., 2011, 2012b, 2017). In this study, we focus on the *H*-ATLAS observations covering 142 deg^2 of the NGP field.

2.2.3 LOFAR data from LOFAR/*H*-ATLAS

LOFAR has observed the *H*-ATLAS NGP field at the sensitivity and resolution of the LOFAR Two-Metre Sky Survey (LoTSS Shimwell et al., 2017; Duncan et al., 2018; Williams et al., 2018b). Whilst the first implementation of the LOFAR/*H*-ATLAS survey Hardcastle et al. (2016) used a facet-calibration technique, this paper uses data calibrated by a significantly improved method. The new direction-dependent calibration technique uses the methods of Tasse (2014a,b). The calibrations are implemented in the software package KILLMS and imaged with DDFACET (Tasse et al., 2018) which is built to apply these direction-dependent calibrations. The LOFAR/*H*-ATLAS data were processed using the December 2016 version of the pipeline, DDF-PIPELINE2[2] (Shimwell et al., 2017, and in prep.). This reprocessing yields a higher image fidelity and a lower noise level than the process detailed by Hardcastle et al. (2016). It not only increases the point-source sensitivity and removes artefacts from the data, but also allows us to image at (slightly) higher resolution. The images used here (as in Gurkan et al. 2018) have a restoring beam of 6 arcsec FWHM, and 50 per cent of the newly calibrated LOFAR/*H*-ATLAS field has an RMS below ~ 0.25 mJy beam^{-1} and 90 per cent is below ~ 0.85 mJy beam^{-1}.

[2]See `http://github.com/mhardcastle/ddf-pipeline` for the code.

2.2.4 Photometry

Since we used optical data to select our sample, flux limited catalogues from the LOFAR, FIRST, or *H*-ATLAS surveys do not contain photometry for every source in our sample, since some of our sources are not formally detected (e.g. to $\geq 5\sigma$). Moreover, some sources are larger than the *Herschel* beam and so matched filter images are not preferred. Instead, the dataset used here (from Gurkan et al. 2018) follows Jarvis et al. (2010), Smith et al. (2014), and Hardcastle et al. (2016), by measuring LOFAR, FIRST, and *Herschel* flux densities using forced aperture photometry.

In order to have consistent flux densities across radio and infrared bands, we use 10 arcsec radius circular apertures, centred on each source's optical position, finding that this size of aperture is optimal since it is small enough to limit the influence of confusion noise, and large enough to mean that aperture corrections are small. The uncertainties on both LOFAR and FIRST flux densities were estimated using their respective r.m.s. maps: scaling the noise value in the image at the pixel coordinate of each source by the square root of the number of beams in the aperture. We do not correct for thermal contributions, whereby the thermal SED also contributes at radio frequencies, in FIRST or LOFAR. In the *Herschel* bands, we add the recommended calibration uncertainties of 5 per cent for PACS and 5.5 per cent for SPIRE, in quadrature (Valiante et al., 2016; Smith et al., 2017).

2.3 Methods

2.3.1 Low frequency luminosities

We calculate *K*-corrected 150 MHz luminosity densities for every source in our sample assuming that $S_\nu \propto \nu^\alpha$, with a spectral index of -0.71 (Condon, 1992; Mauch et al., 2013):

$$L_\nu = 4\pi d_L^2(z) S_{\nu,obs}(1+z)^{-\alpha-1}, \tag{2.1}$$

where the additional factor of $(1+z)^{-1}$ accounts for the bandwidth correction, and $d_L(z)$ is the luminosity distance in our adopted cosmology.

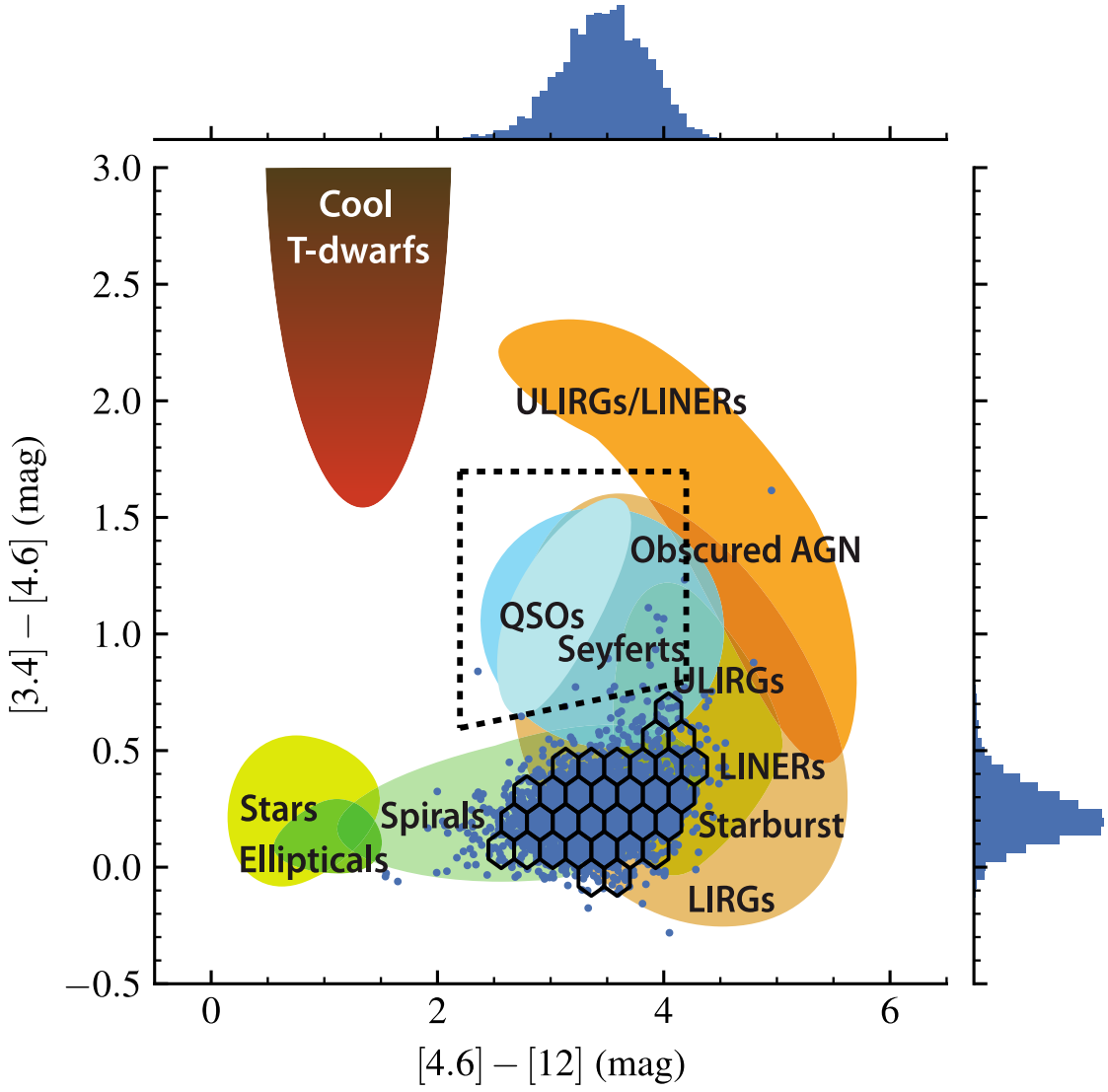

FIGURE 2.2: The mid-infrared sub-sample (5σ WISE detections, shown as blue points) overlaid on the Jarrett et al. (2011) MIRDD which uses the magnitudes at three WISE wavelengths $W1$ at 3.4 μm, $W2$ at 4.6 μm, and $W3$ at 12 μm. The coloured regions are as published in Wright et al. (2010), and intended to show the approximate locations of galaxies of a range of different types. The hexagonal bins over the region centred on $[4.6]-[12] \approx 3.5$, and $[3.4]-[4.6] \approx 0.25$ are used to trace q_{250} in later sections of this paper, and are shown here to provide context. The QSO box defined by (Jarrett et al., 2011) is depicted as a dashed box. Number counts over both colours are shown as blue histograms.

There is an additional uncertainty on the K-corrected luminosity densities due to assuming a constant spectral index; we attempt to account for this by bootstrapping based on the Mauch et al. (2013) distribution of star-forming spectral indices. For each galaxy we draw 1000 spectral indices from the prior distribution centred on -0.71 with an RMS of 0.38. The luminosity densities are calculated using Equation 2.1 with uncertainties estimated based on the standard deviation of the bootstrapped distribution, however we note that the K-corrections and their uncertainties derived for our sample are small since all sources are below $z = 0.4$.

2.3.2 Far-infrared luminosities

To estimate the intrinsic far-infrared luminosity densities, we assume an optically thin greybody for the dust emission:

$$S_\nu \propto \frac{\nu^{3+\beta}}{\exp(h\nu/kT) - 1}, \tag{2.2}$$

where T is the dust temperature, k is the Boltzmann constant, h is the Planck constant, and β is the emissivity index. The dust emissivity varies as a power law over frequency and its inclusion as the constant β attempts to summarise the varying dust compositions into a single galaxy-wide isothermal component. Taking $\beta = 1.82$ has been found to provide an acceptable fit to the infrared SEDs of galaxies in the H-ATLAS survey (Smith et al., 2013) and so we assume the same value for β here. We fit Equation 2.2 to the *Herschel* PACS/SPIRE fluxes at 100, 160, 250, 350, and 500 μm. We include the PACS wavelengths despite their reduced sensitivity since they have been found to be important in deriving accurate temperatures (Smith et al., 2013).

We use the Python package EMCEE (Foreman-Mackey et al., 2013) which is an implementation of the Goodman and Weare (2010) Affine Invariant MCMC Ensemble Sampler (AIMCMC). AIMCMC is known to sample from degenerate and highly correlated posterior distributions with an efficiency superior to traditional Metropolis techniques (Goodman and Weare, 2010). For each galaxy, 10 walkers are placed at initial temperatures drawn from a prior normal distribution centred at 30K with a standard deviation of 100K. We find that altering the width of the temperature prior does not affect our results.

The walkers sample the probability distribution set by the least squares likelihood function. At each temperature that the walkers sample, the resultant grey-body is redshifted to the observed

frame and propagated through the *Herschel* response curves. We ran the sampler for 500 steps with the 10 walkers and a burn-in phase[3] of 200 steps. Each galaxy therefore has 3000 informative samples to contribute to the probability distributions. In addition to the temperature for each MCMC step, we recorded the modelled intrinsic luminosity densities, modelled observed fluxes, and K-corrections for each each infrared wavelength. This allowed us to find the probability distributions for these parameters and hence their uncertainties in a Bayesian manner.

2.3.3 Calculating the FIRC

The FIRC is traditionally parametrised by the log of the ratio of infrared to radio luminosity, q (Helou et al., 1985; Bell, 2003; Ivison et al., 2010). However, the lack of PACS 60 μm coverage and small number of sources (<5 per cent) with WISE 22 μm fluxes in the H-ATLAS NGP field prohibits an accurate estimation of q based on total dust luminosity for a statistically significant sample. Therefore, we calculate a K-corrected monochromatic q_{250} in the SPIRE 250 μm band following Jarvis et al. (2010) and Smith et al. (2014).

$$q_{250} = \log_{10}\left(\frac{L_{250}}{L_{\rm rad}}\right) \tag{2.3}$$

The uncertainties on our monochromatic q_{250} estimates are found by propagating uncertainties from the K-corrected luminosity densities in the radio and 250 μm. We note that in all of the following sections, we calculate q_{250} using L_{rad} calculated at 150 MHz in the rest-frame.

Figures 2.3 and 2.4 show that for the galaxies for which we do have reliable dust luminosity estimates, there is still a tight and linear correlation between the infrared and the radio luminosities. We used MAGPHYS templates normalised using all WISE and *Herschel* bands to calculate the integrated dust luminosity between 8 and 1000 $\mu\,m$.

In addition to the individual q_{250} found for each galaxy we use a stacking method to evaluate trends across colour spaces, redshift, and temperature. Averaging q_{250} is fraught with problems such as underestimation caused by AGN contamination, undesirable influence by outlier sources, and amplification of those effects by using the average of the ratio of luminosity densities rather than the ratio of the average luminosity densities (luminosity stacking). We find that

[3]The burn-in phase allows the chain to become independent of the user defined starting point by discarding the first 200 steps.

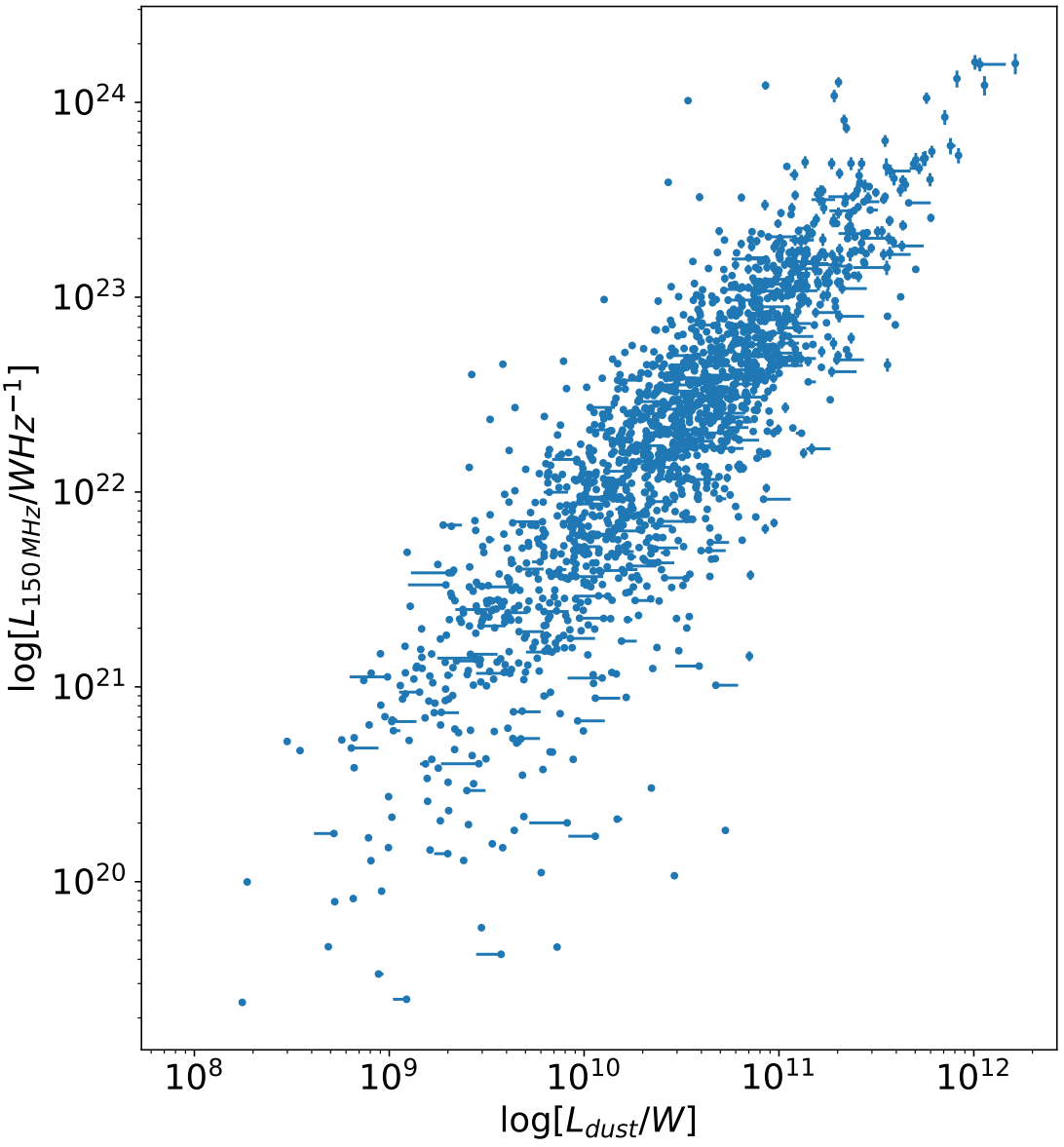

FIGURE 2.3: The FIRC using LOFAR at 150 MHz for galaxies detected at 3 σ in both total dust infrared and radio luminosities. The dust luminosity is calculated using the MAGPHYS infrared templates and is integrated between 8 and 1000 μm.

the distribution of q becomes wider when using the average ratio rather than the ratio of the averages, our results do not qualitatively change other than broadening the distribution of q. Indeed by using the average quotient, more low signal to noise objects are discarded before having the chance to contribute to the stack. To make matters worse, selection in either the radio or infrared band used to evaluate the FIRC introduces an inherent SED related bias (Sargent et al., 2010). Here we have mitigated the effects of such biases by selecting in an independent optical band. To mitigate the effect of outliers and AGN, the ratio of the median luminosity densities has previously been used (e.g. Bourne et al., 2011; Smith et al., 2014). Median averaging is sometimes

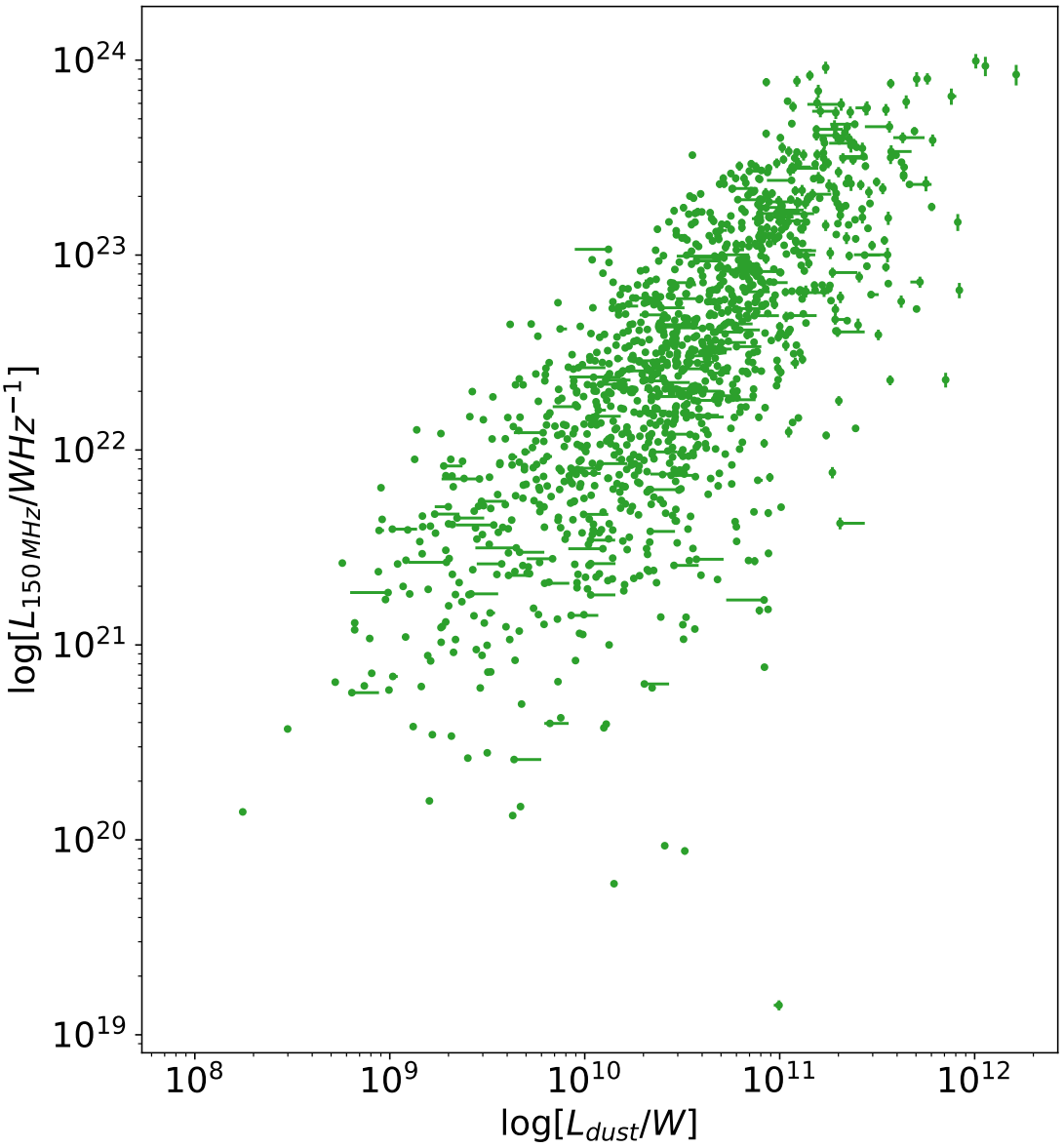

FIGURE 2.4: The FIRC using FIRST transformed to 150 MHz for galaxies detected at 3 σ in both total dust infrared and radio luminosities. The dust luminosity is calculated using the MAGPHYS infrared templates and is integrated between 8 and 1000 μm.

preferred since it is more resistant to outliers (e.g. residual low-luminosity AGN which may not have been identified by the emission line classifications), and since the median often remains well-defined even in the case of few individual detections (e.g. Gott et al., 2001). However, the distributions of luminosity density even in finite-width bins of redshift are skewed. We find that a median-stacked q_{250} calculated for the whole star-forming sample does not agree with the likewise-stacked q_{250} in bins of redshift (in that the median of the medians is not close the global median – this is not the case with the mean). If we use the mean-stacked q_{250}, we arrive at an agreement between the global and binned q_{250} across redshift. Due to this counter-intuitive

disagreement between measures of q_{250} and the importance of being able to quantify a change in the FIRC over redshift, we use the ratio of the mean luminosity densities (mean-stacked) to evaluate q_{250}. Although we may side-step issues regarding skewed distributions by using the mean, we are now potentially more affected by outliers and AGN. We will discuss the possible influence of AGN on our results in more detail in the coming sections.

To calculate our mean q_{250} values, we use a method similar to Smith et al. (2014) and take the quotient of the mean radio and 250 μm luminosity density for each bin. Uncertainties are estimated on each stacked q_{250} using the standard deviation of the distribution resulting from re-sampling this mean 10,000 times with replacement (bootstrapping). This bootstrapped uncertainty of q_{250} is representative of the distribution of the luminosity densities being stacked. To complement the parametrisation of the FIRC with q_{250}, we also fit the FIRC as a power-law with finite intrinsic width [4] to the data using Equation 2.4

$$L_{\rm radio} = kL_{250}^{\gamma}, \tag{2.4}$$

where k is the normalisation and γ is the slope of the FIRC. We take into account non-detections by re-sampling from each data point's uncertainty and discarding the negative-value realisations. We use EMCEE to fit the power-law with 6000 steps and 32 walkers. Fitting a power-law allows us to probe the physical mechanisms of radio continuum emission generation. A value of the slope close to one indicates that the conditions required for calorimetry are satisfied and the FIRC is linear. A super-linear slope might result from an escape-dominated scenario whereby cosmic rays escape before emitting in the radio. At sub-linear slopes, losses from cooling processes such as inverse-Compton dominate (Li et al., 2016).

We have discussed two methods of quantifying the FIRC (mean-stacked q_{250} and power-law fit). In addition, there are three types of uncertainty in the FIRC that we discuss in this analysis:

1. The uncertainty in q_{250}, calculated as the width of the bootstrapped distribution of stacked q_{250}.
2. The uncertainty in the slope of the FIRC, γ, quantified by MCMC fit.
3. The change in stacked q_{250}, γ, and other statistical results due to the presence of misclassified AGN.

[4] The intrinsic width of the power-law fit, $\log[\sigma]$, is defined as the logged fractional width of the Gaussian over the power-law line, which we define as: $L_{150\,\rm MHz} \sim (kL_{250\,\mu\rm m}^{\gamma})(1+\varepsilon)$, where $\varepsilon \sim \mathcal{N}(0,\sigma)$. We fit the parameter σ along with γ and k in our MCMC run.

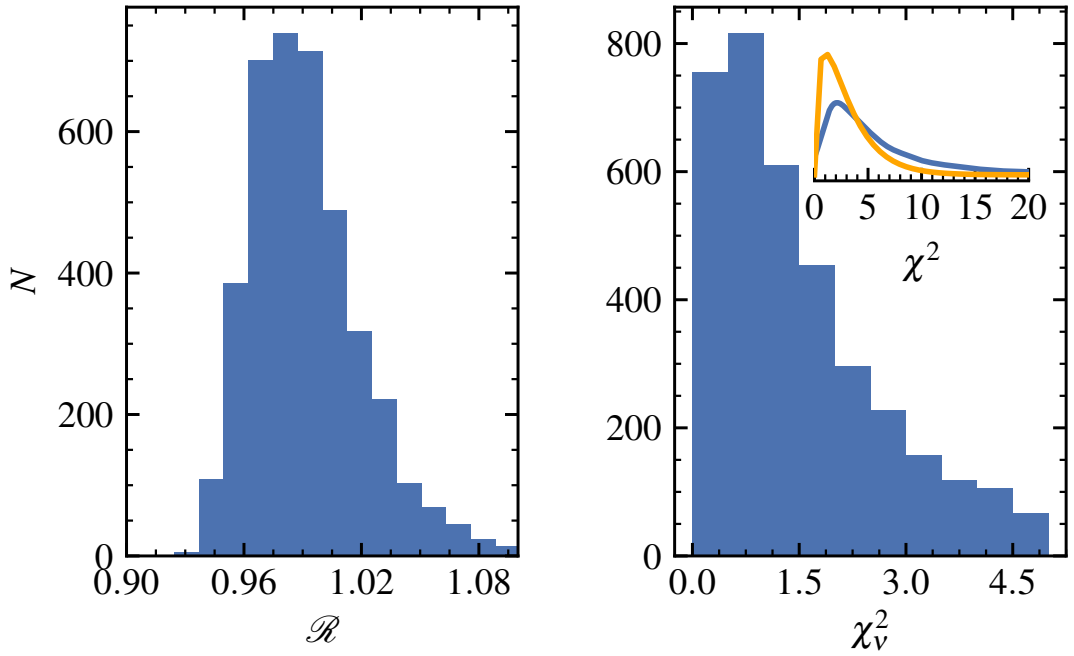

FIGURE 2.5: Fit diagnostics for our full star-forming sample. The Gelman-Rubin convergence statistic histogram is shown on the left indicating that all of our fits have converged. The reduced χ^2 distribution of the sample is shown on the right as the blue histogram. The distribution of χ^2 is also shown in the inset in blue, along with the χ^2 distribution expected for 3 degrees of freedom for comparison in orange.

We estimate the change in our results due to misclassified AGN in Section 2.4.5 where we run our analysis again, this time including the BPT-AGN. This test will be of limited use since BPT-AGN galaxies may not be similar in luminosity nor in temperature to those galaxies which host a low-luminosity AGN. We resort to this method since we are investigating the FIRC itself and so we cannot use the FIRC to distinguish low-luminosity AGN from star-forming galaxies.

2.4 Results & Discussion

2.4.1 Isothermal fits

Before proceeding to investigate the variation of the FIRC with redshift and other parameters, we undertake several checks to ensure that our temperature estimates and K-corrections are reliable. As a means of testing goodness-of-fit, we calculate the Gelman-Rubin $\mathscr{R}$ statistic for the sampled temperature and reduced χ^2 for each object. Figure 2.5 shows the distributions of $\mathscr{R}$ and reduced χ^2 for our full sample of star-forming galaxies.

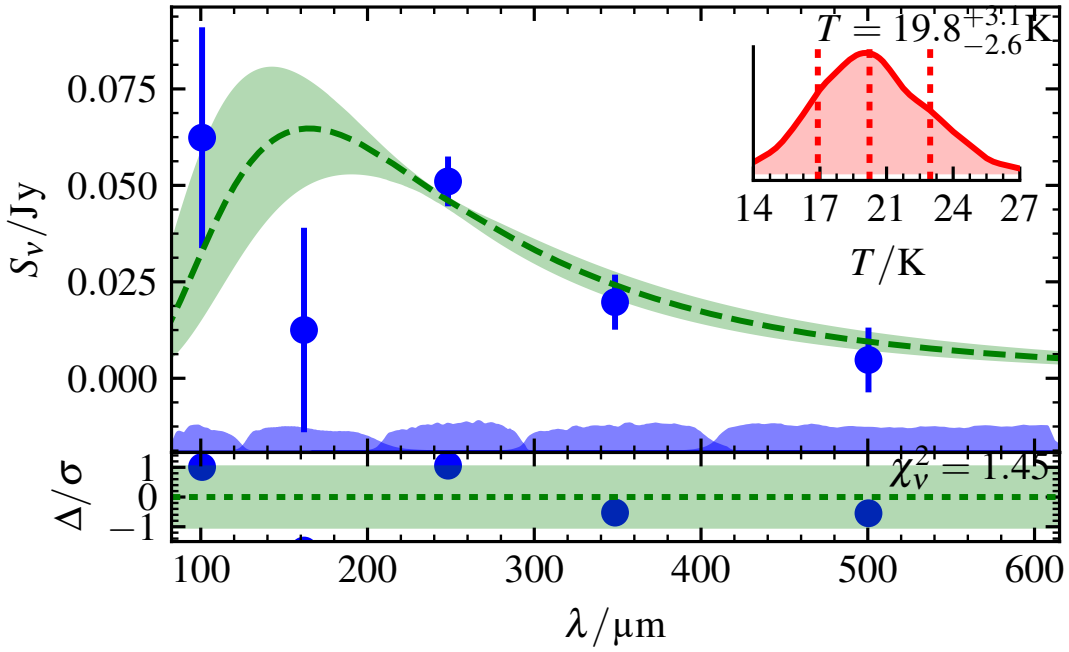

FIGURE 2.6: A sample isothermal fit to an SDSS star-forming galaxy at $\alpha_{J2000} = 12^h49^m46.1^s$, $\delta_{J2000} = 31°35'30''$. The probability distribution for temperature is shown in the top right with the 1-sigma equal-tailed credible interval as dashed lines around the median temperature of 19.8K with a reduced χ^2 of 1.45. The Herschel flux measurements and their uncertainties are shown as blue errorbars. The fit observed-frame isothermal greybody with its own 1σ credible interval is shown as the green curve. The differences between the estimated flux and the measurement are shown along the bottom axis. The filter transmission profiles are also shown in blue along the bottom for each wavelength.

An $\mathscr{R} \approx 1$ signifies that all chains are sampling from the same distribution and have therefore converged (see Gelman and Rubin, 1992, for a full description); all sources in our sample have $0.9 < \mathscr{R} < 1.1$ indicating that the fits have converged.

The χ^2 distribution of our sample, which we fit by least squares regression, has 3 degrees of freedom consistent with our 1-parameter model (normalisation is not fit and is instead optimised with χ^2 minimisation) when fitting with 5 bands of far-infrared observations. In addition, 83 per cent of our total sample have a reduced $\chi^2 < 2$. Conducting this experiment with only those sources with reduced $\chi^2 < 2$ does not affect the conclusions presented here.

Smith et al. (2013) found that median likelihood estimators in greybody fitting are less susceptible to bias with *H*-ATLAS data than the best fit. Therefore, in what follows we adopt the median likelihood value from the MCMC fits as a galaxy's effective temperature for use in Equation 2.2, along with uncertainties estimated according to the 16th & 84th percentiles of the derived distribution. Figure 2.6 shows an example fit.

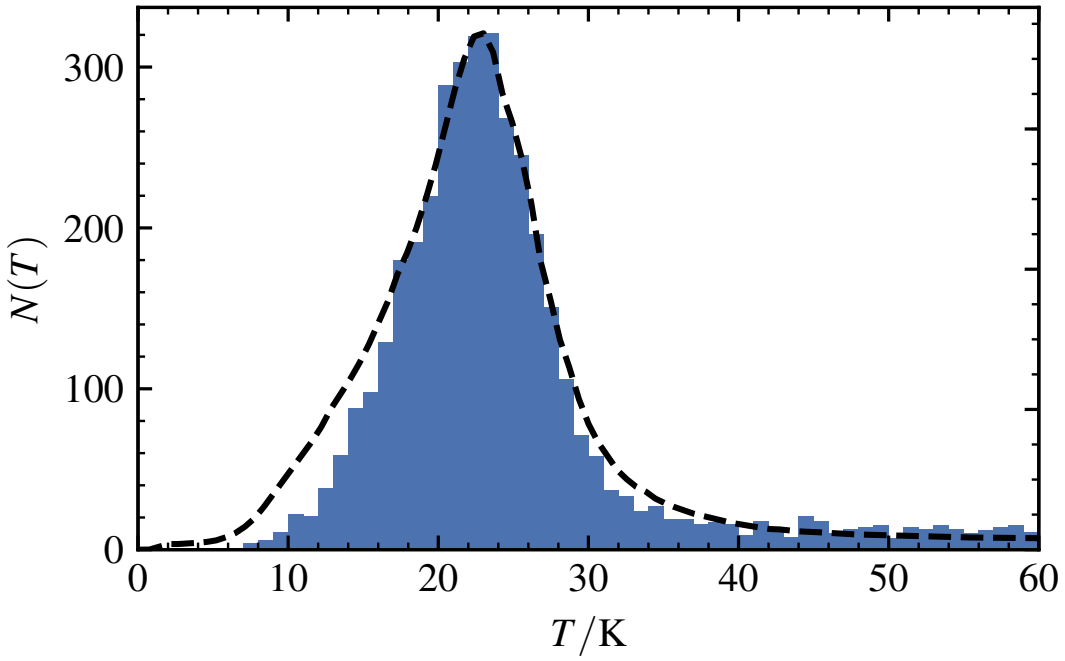

FIGURE 2.7: The distribution of median temperatures for our sample of emission-line classified star-forming galaxies (blue histogram), overlaid with the sum of temperature distributions for every galaxy obtained by MCMC (dashed line). No radio or infrared detection threshold is applied to arrive at this sample of galaxies.

Figure 2.7 shows that our sample of emission-line classified star-forming galaxies exhibits a dust temperature distribution centred around $\sim 23\,\mathrm{K}$ with a standard deviation of $\sim 10\,\mathrm{K}$. The total aggregated temperature probability distribution for all galaxies, also shown in Figure 2.7, is slightly wider than the median likelihood temperature histogram. This is due to the fact that the aggregated distribution includes the uncertainty from each galaxy rather than just reporting the average median likelihood temperature.

2.4.2 The global FIRC at different radio frequencies

To compare the values of q_{250} obtained at 150 MHz and 1.4 GHz, we extrapolate the FIRST luminosity densities to 150 MHz assuming a power-law with a spectral index of -0.71. For clarity, we label this transformed q_{250} as $q^{\mathrm{FIRST}}_{150\,\mathrm{MHz}}$ to distinguish it from the related quantity at its measured frequency, $q^{\mathrm{FIRST}}_{1.4\,\mathrm{GHz}}$. Though it isn't especially instructive due to the large range of redshifts included in our study, we find an average value of $q^{\mathrm{FIRST}}_{1.4\,\mathrm{GHz}} = 2.30 \pm 0.04$ (which is equivalent to $q^{\mathrm{FIRST}}_{150\,\mathrm{MHz}} = 1.61 \pm 0.04$) which is consistent with previous studies (Ivison et al., 2010; Smith et al., 2014) to within 1σ. We find that the average FIRC is not consistent between low and high radio frequencies, with $q^{\mathrm{LOFAR}}_{150\,\mathrm{MHz}} = 1.42 \pm 0.03$ and $q^{\mathrm{FIRST}}_{150\,\mathrm{MHz}} = 1.61 \pm 0.04$.

These values of aggregate q_{250} are inclusive of all our star-forming-classified sources. A spectral index calculated from detected sources will be unreliable and a bias towards flatter spectral indices would be introduced due to the differing sensitivities and depths of LOFAR and FIRST. Free-free absorption is also an issue at low frequency, where it flattens the radio SED, and so may have an effect on q_{250}, but we do not correct for its influence here. To check whether the difference in q_{250} between low and high frequency is due to spectral index we find the value of α which allows $q^{\mathrm{LOFAR}}_{150\,\mathrm{MHz}} - q^{\mathrm{FIRST}}_{150\,\mathrm{MHz}} = 0$ for sources detected at 3σ in both bands. The value for the spectral index that we find from the mean-stacked q_{250} of these sources is -0.58 ± 0.04 (Gaussian distributed) which is in agreement with Gurkan et al. (2018). We note that we do not use this value for the spectral index in our analysis because it will be biased by only considering the brighter sources that are 3σ detected. Instead we continue to use the value of -0.71 from Mauch et al. (2013) as originally stated.

We fit the slope of the FIRC to our star-forming sample for LOFAR and FIRST using Equation 2.4. We find that the FIRC measured with LOFAR is described by $L^{\mathrm{LOFAR}}_{150} = 10^{-0.77\pm0.19}$ $L^{0.97\pm0.01}_{250}$ with an intrinsic width of 0.89 ± 0.02 dex. This is slightly below the value of unity quoted for pure calorimetry. The FIRC measured with FIRST is described by $L^{\mathrm{FIRST}}_{150} = 10^{2.94\pm0.25}$ $L^{0.83\pm0.01}_{250}$ with an intrinsic width of 1.04 ± 0.03 dex. We show these fits graphically in Figure 2.8 and include supplementary fits to the FIRC over different ranges of mid-infrared colour and specific star-forming rates in Appendix A.2.

2.4.3 The evolution of the FIRC

As discussed in Section 2.1, there have been numerous studies of the redshift evolution of the FIRC. Figure 2.9 shows the evolution of 250μm and radio luminosity densities over our redshift range for context. To quantify the evolution of temperature and q_{250} with redshift we fit a straight line using the Bayesian method detailed in Hogg et al. (2010) and implemented with PyMC3 (Salvatier et al., 2016). We show these redshift relationships in Figure 2.10.

To calculate the effective temperature in each bin, the *Herschel* fluxes are mean-stacked and their uncertainties are derived from bootstrapping. Uncertainties on the mean redshift and mean fluxes are propagated through the MCMC fit to gain an effective temperature for each bin and its uncertainty. The uncertainty on the mean flux is small in bins with large numbers of sources, resulting in temperature uncertainties of order 2K. Due to significance cuts made with BPT line ratios, Figure 2.10 lacks the higher redshift galaxies present in the work of Smith et al. (2014),

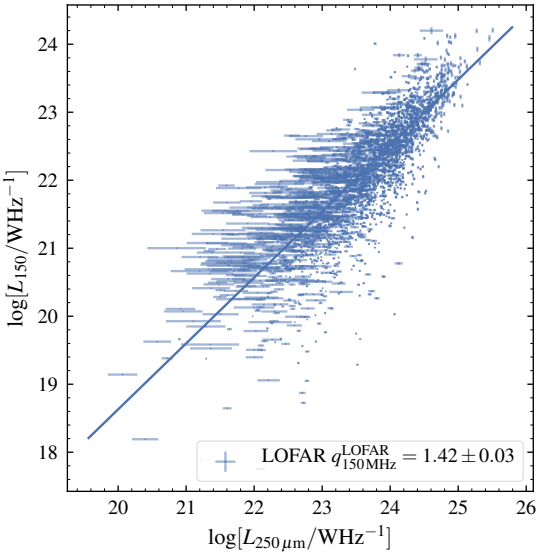

(a) The FIRC as measured with LOFAR at 150 MHz

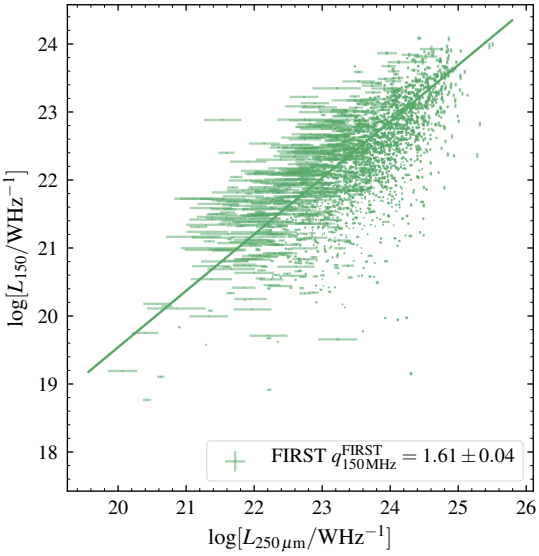

(b) The FIRC as measured with FIRST at 1.4 GHz

FIGURE 2.8: The Far-Infrared Radio Correlation for LOFAR (blue) and FIRST (green). The points shown are $> 3\sigma$ detected in radio and infrared fluxes, showing two clear but distinctly different correlations at 1.4 GHz and 150 MHz. The fit lines are power-law fits to the all sources in our star-forming sample including non-detections. For the purpose of comparison the FIRST 1.4 GHz luminosity densities have been transformed to 150 MHz assuming a power law with spectral index from Mauch et al. (2013).

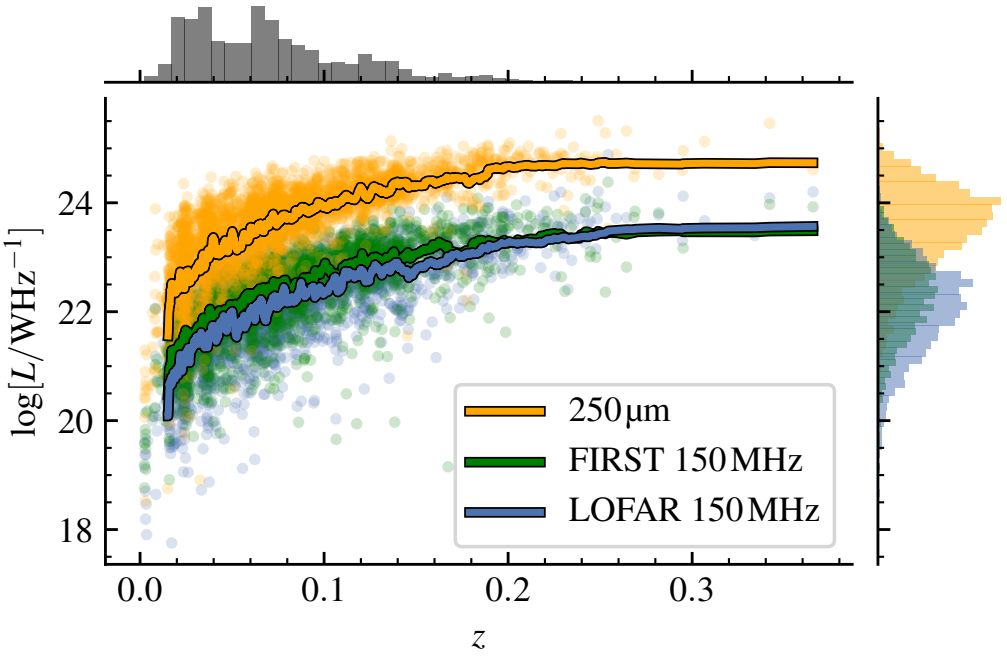

FIGURE 2.9: Distributions of Herschel SPIRE 250 μm (yellow), FIRST (green), and LOFAR (blue) luminosity densities over redshift for our main star-forming sample. A rolling mean (inclusive of all non-detections) with a window size of 200 points is plotted to guide the eye.

hence there is a large uncertainty above $z = 0.25$ (not shown). However, in the bins where the uncertainty on the dust temperature is small (< 2K), there is no statistically significant trend with redshift, consistent with Smith et al. (2014). With an MCMC trace of 50,000 samples for each fit, we find strong evidence of a decrease in q_{250} over our low redshift range for LOFAR (gradient $= -1.0^{+0.2}_{-0.3}$) but no such strong evidence of such a decline with FIRST (gradient $= -0.5^{+0.5}_{-0.3}$), despite being consistent with LOFAR to within 1σ. It is worth noting that using the median stacking results in gradients which are consistent with the gradients calculated using the mean to within 1σ. We discuss the difference between the mean and median results (and lack of impact on our results) further in Section 2.4.5. A lack of evolution seen with FIRST is in line with the 250 μm result from Smith et al. (2014), the 70 μm result from Seymour et al. (2009), and the 70 μm and 24 μm result from Sargent et al. (2010). Calistro-Rivera et al. (2017) detect an evolution at both frequencies in the Boötes field and our result is consistent with theirs at redshifts below 0.25 at both frequencies. However, it is important to note that Calistro-Rivera et al. (2017) find curved radio SEDs, suggesting that a constant slope between 150 MHz and 1.4 GHz is not realistic.

At 3 GHz, Molnár et al. (2018) find no evidence for evolution in the total infrared-radio correlation in disk-dominated galaxies up until $z \sim 1.5$ (though Delhaize et al. 2017 find such an

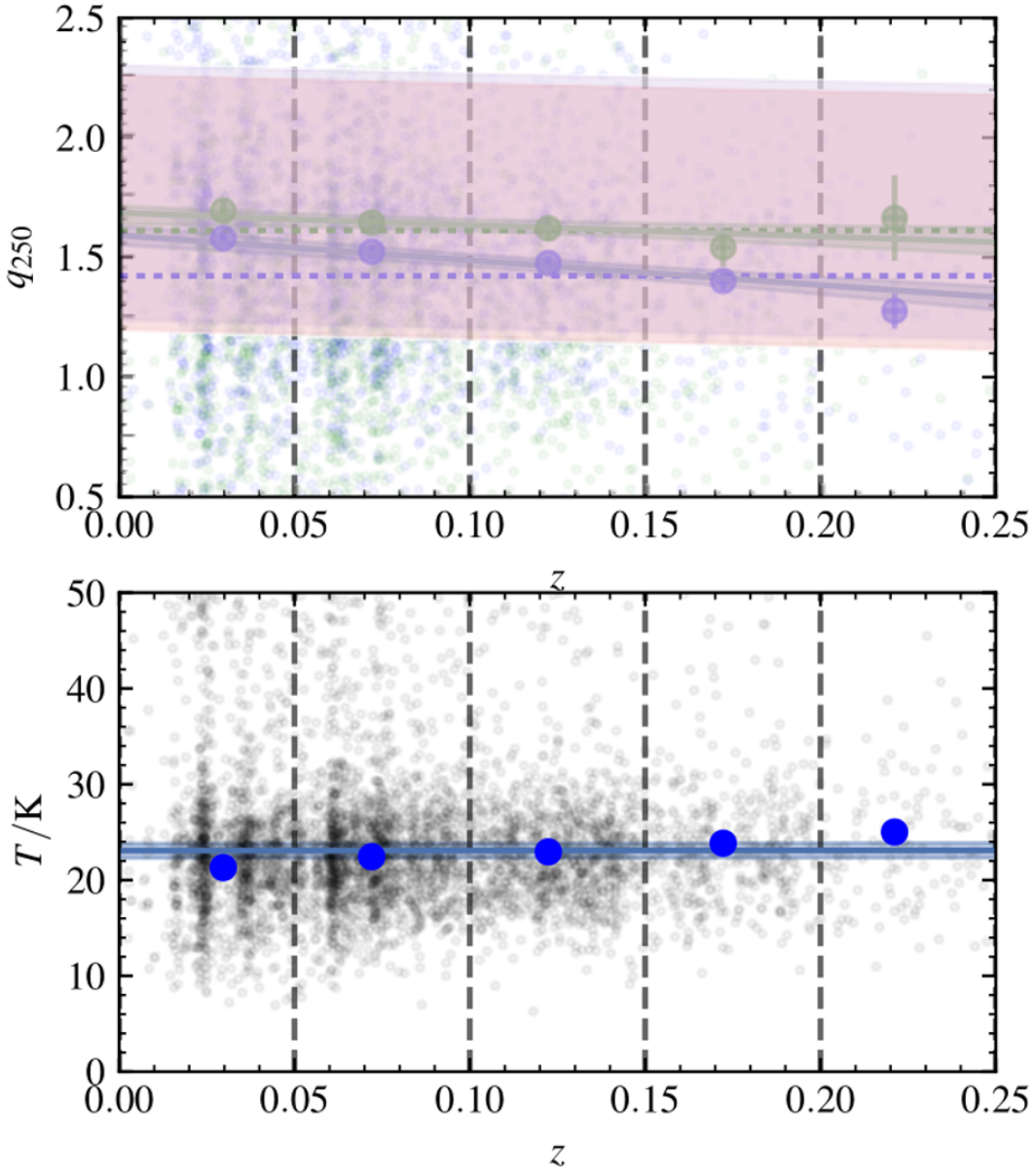

FIGURE 2.10: **Top:** Evolution of q_{250} over redshift measured with LOFAR at 150 MHz (blue) and FIRST transformed to 150 MHz (green). The dashed horizontal line in the upper plot is the mean-stacked q_{250} for all star-forming galaxies taken from Figure 2.8 for FIRST and LOFAR at 150 MHz. The coloured lines indicate the straight line fit to all galaxies in our sample binned in redshift for LOFAR and FIRST. The uncertainty of the relations from Calistro-Rivera et al. (2017) are also plotted as the orange (LOFAR, 150 MHz) and the purple (FIRST, 150 MHz) shaded regions. **Bottom:** The temperature in each bin, calculated by constructing an infrared SED from the average K-corrected flux of each source in every band and fitting Equation 2.2 to the result. The temperature and uncertainties are overlaid with a straight line fit to the data. The vertical dashed lines represent bin edges.

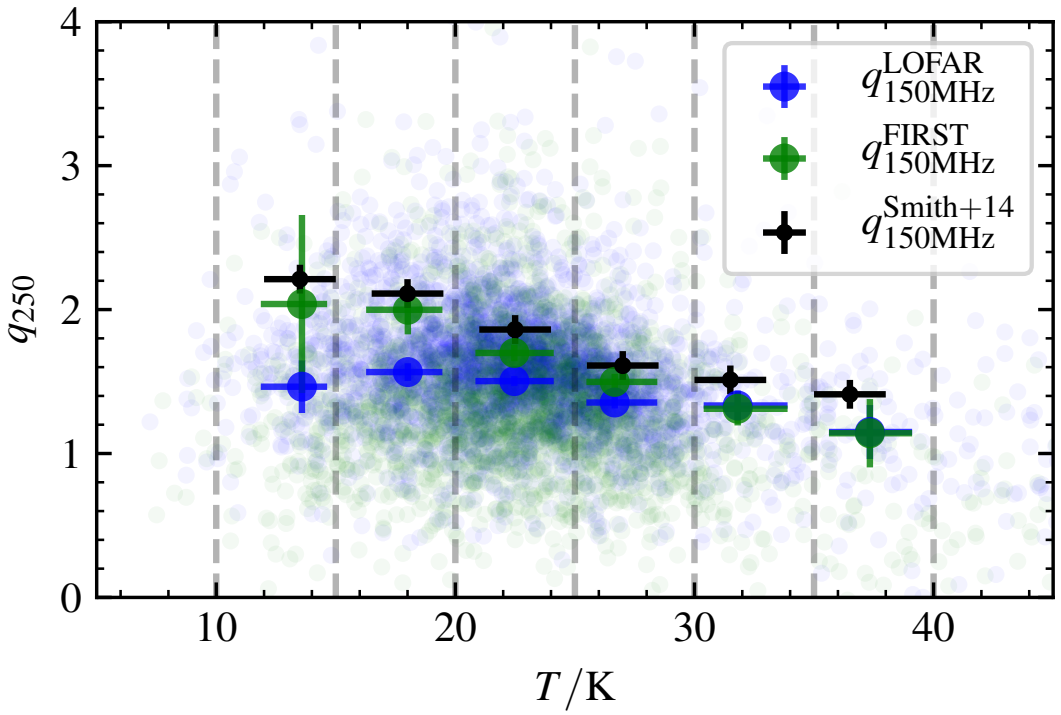

FIGURE 2.11: The temperature dependence of q_{250} compared between high and low frequency. The background dots are the individual q_{250} calculated from the LOFAR 150 MHz (blue) and FIRST (green) luminosity densities. The q_{250} calculated from stacked LOFAR and SPIRE luminosity densities described earlier is plotted in bold points with errorbars derived from bootstrapping the luminosity densities within the depicted dashed bins 10,000 times. The temperature uncertainties in each bin are calculated from the 16th and 84th percentiles. The same calculation from Smith et al. (2014) is shown as the black errorbars for comparison.

evolution in q using total infrared luminosity densities at redshifts ≥ 6). Together with Figure 2.10, we therefore find tentative evidence for a frequency dependence of the evolution of q_{250} over redshift. However, Molnár et al. (2018) also find that an evolution in q_{250} over redshift is present in spheroids and is consistent with other studies of star-forming galaxies in general. They suggest that AGN activity not identified with traditional diagnostics is the cause. Extending their conclusion to our star-forming sample may imply that the cause of the evolution found here is also low level AGN activity, with AGN prevalence increasing with redshift.

Figure 2.11 shows the evolution of q_{250} versus temperature. For comparison, $q_{150\,\mathrm{MHz}}^{\mathrm{LOFAR}}$, $q_{150\,\mathrm{MHz}}^{\mathrm{FIRST}}$ and the results of Smith et al. (2014) transformed to 150 MHz ($q_{150\,\mathrm{MHz}}^{\mathrm{Smith+14}}$) are shown together. Assuming a spectral index of -0.71, the trend of decreasing q_{250} with increasing temperature is found with both LOFAR and FIRST, agreeing within uncertainties when transformed to the same frequency at higher temperatures. Cold cirrus emission is not associated with recent star-formation and so the ratio of infrared to radio luminosity (and hence q) will be larger for galaxies

with colder integrated dust temperatures Smith et al. (2014). We discuss the deviation at lower temperatures in Section 2.4.5.

The origin of the evolution of q_{250}^{LOFAR} with redshift is uncertain but we show here that the dependence of luminosity density upon redshift cannot account for all of the evolution measured in q_{250}^{LOFAR}. The bottom panel of Figure 2.10 shows that the average dust temperature does not depend on redshift, when averaging across the whole sample. Therefore, if stacked 250 μm luminosity density is correlated with dust temperature (and Smith et al. 2014 show that same dependency at 250 μm) in our sample, then the dependency of stacked q_{250}^{LOFAR} upon redshift cannot only be due to a luminosity dependence on redshift.

2.4.4 Variation over the mid-infrared colour-colour diagram

In this section we focus solely on the sample of 2,901 star-forming galaxies with 5σ WISE detections in order to construct the MIRDD of Jarrett et al. (2011). This sample covers part of the star-forming region defined by Wright et al. (2010) as shown in Figure 2.2. When showing q_{250} variation of this sub-sample, we zoom in on this region.

We calculate the mean values of temperature and q_{250} as described in Section 2.3 over hexagonal bins in the WISE colour space. We show only those bins which contain more than 50 galaxies and have a stacked q_{250} with $SNR > 3$. When these conditions are applied, 33 and 29 contiguous bins remain for LOFAR and FIRST respectively, all with a high SNR in binned $q_{150\,\mathrm{MHz}}^{\mathrm{LOFAR}}$, $q_{150\,\mathrm{MHz}}^{\mathrm{FIRST}}$ of at least 7 and 3 respectively. Figure 2.12 shows the mean isothermal temperature in each bin. There is a clear and smooth increase in temperature towards redder $[4.6]-[12]$ and $[3.4]-[4.6]$ colours. The isothermal temperature of our sample increases towards the area populated mainly by starburst and Ultra-Luminous Infrared (ULIRG) galaxies. Our sample is positioned away from the Jarrett et al. (2011) AGN area, shown as a dashed box in Figures 2.12 and 2.13, although we note that radiatively inefficient radio-loud AGN may populate other regions of this plot (Gurkan et al., 2018).

The trend in temperature over mid-infrared colour is reflected in Figures 2.12 and 2.13, where the q_{250} measured using both FIRST and LOFAR decreases with redder WISE colours in a similar fashion to temperature. The higher sensitivity of LOFAR in comparison to FIRST is reflected in the much smoother relation between binned q_{250} and mid-infrared colours.

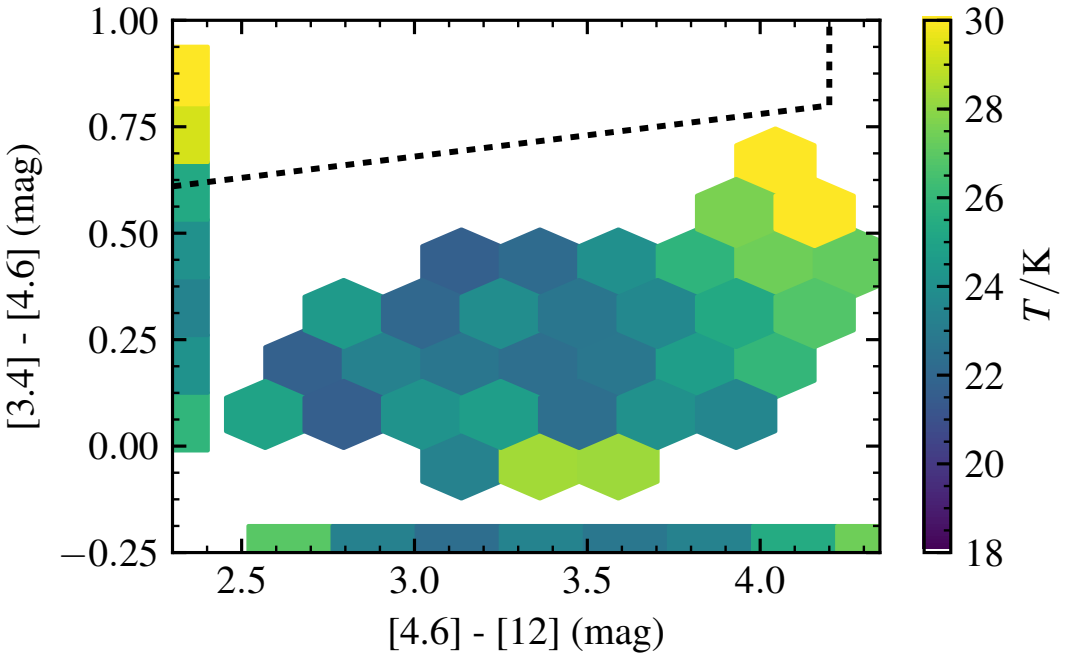

FIGURE 2.12: Mean isothermal temperature across the Jarrett et al. (2011) MIRDD. Bins are hexagonal and are coloured linearly between 18K and 30K described by the colour bar. All bins have an SNR in $q_{150\,\mathrm{MHz}}^{\mathrm{LOFAR}} > 7$ and contain more than 50 galaxies each. Also plotted are the marginal bins summarising horizontal and vertical slices of the entire plane. These slices also obey the two conditions set on the hexagonal bins. For reference, the box described by Jarrett et al. (2011) to contain mostly QSOs is marked by dotted lines.

Both the q_{250} parameter (for both frequencies) and the temperature change smoothly across mid-infrared colour. We interpret this smooth variation of the temperature over $[4.6]-[12]$ colour towards more heavily star-forming galaxies as tracing the specific star formation rate of a population of normal star-forming galaxies.

To quantify the observed trend with mid-infrared colour we use a Bayesian method to find the correlation coefficients of stacked q_{250} against both WISE colours. From Figure 2.13, q_{250} clearly correlates with both $[3.4]-[4.6]$ and $[4.6]-[12]$. However, since redshift is also highly correlated with $[3.4]-[4.6]$ and q_{250} is independently correlated with redshift, it is necessary to control for the effects of redshift using partial correlation (Baba et al., 2004) in order to quantify the effect of mid-infrared colour on q_{250}. We also control for isothermal temperature and stellar mass to see if all of the variation in q_{250} over mid-infrared colour can be accounted for by covariances with those parameters.

Our method consists of fitting a trivariate normal distribution to $[4.6]-[12]$ (x), $[3.4]-[4.6]$ (y), and q_{250} to obtain correlation-coefficient estimates (ρ_x and ρ_y). We estimate the correlation-coefficients for q_{250} without controlling for any other parameters ($\rho_{x\cdot\emptyset}$ and $\rho_{y\cdot\emptyset}$) and for the

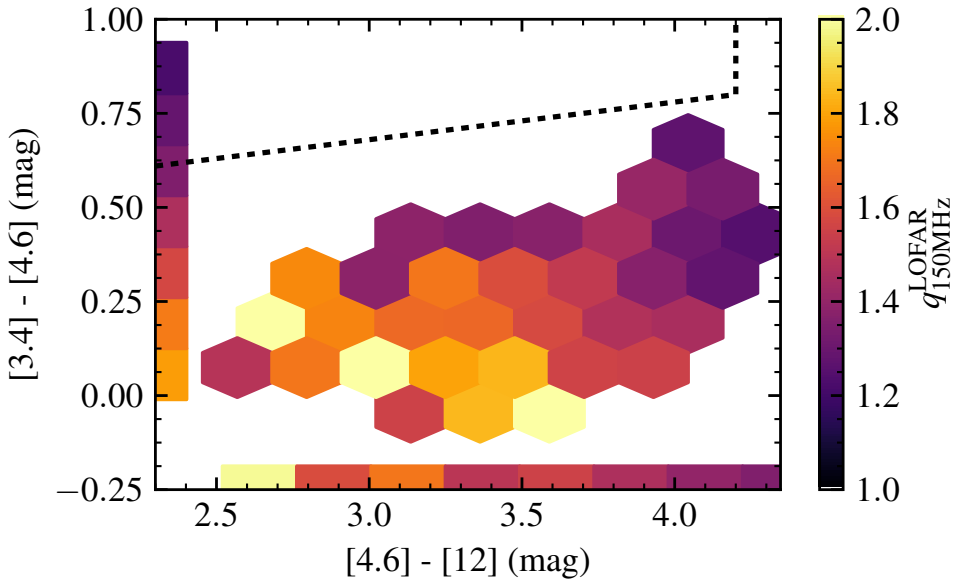

(a) LOFAR at 150 MHz

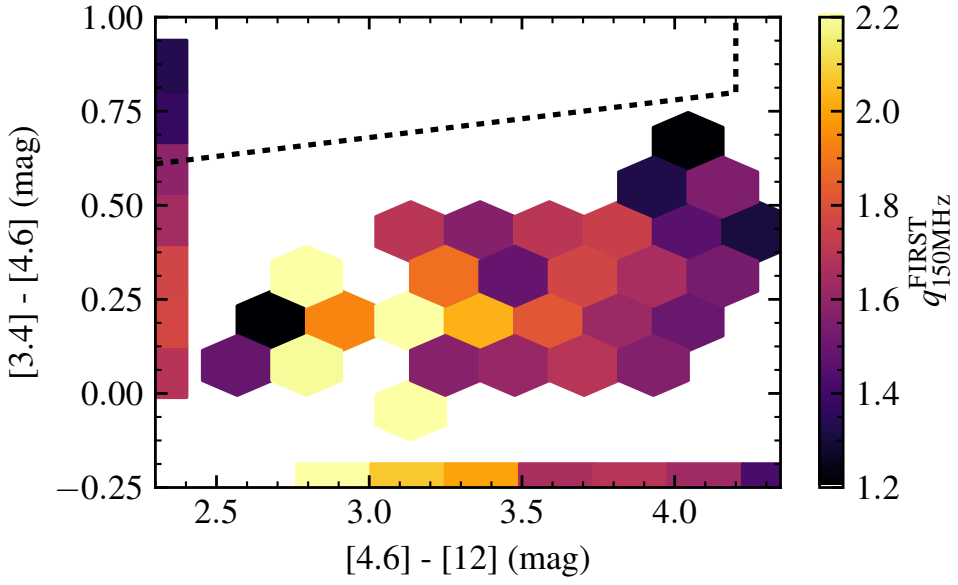

(b) FIRST transformed to 150 MHz assuming $\alpha = -0.71$

FIGURE 2.13: Mean-stacked q_{250} across the Jarrett et al. (2011) MIRDD. Bins are hexagonal and are coloured linearly according to the scale shown on the right. All bins have an SNR in $q_{250} > 3$ and contain more than 50 galaxies each. Also plotted are the marginal bins summarising the horizontal and vertical slices of the entire plane. These slices also obey the two conditions set on the hexagonal bins. For reference, the box described by Jarrett et al. (2011) to contain mostly QSOs is marked by dotted lines.

residuals in q_{250} obtained from fitting a linear relationship to q_{250} against z, T_{eff}, and M_*.We fit the correlation coefficients with an LKJ prior (Lewandowski et al., 2009) using the PyMC3 (Salvatier et al., 2016) model specification along with EMCEE Ensemble sampler used above. LKJ distributions represent uninformative priors on correlation matrices and their inclusion allows us to randomly sample correlation coefficients.

To represent the correlation of q_{250} over the two dimensions of WISE colour space, Figure 2.14 shows the the marginalised probability distributions for each correlation coefficient. The top panel of Figure 2.14 shows the effect of controlling for redshift, temperature, and stellar mass independently as well as a naive fit which accounts for no other influential variables. The bottom panel of Figure 2.14 shows the probability distribution of the correlation coefficients when controlling for redshift, temperature, and stellar mass at the same time. Initially, the distribution of q_{250} is highly correlated with both MIR colours (-0.5 ± 0.1 and -0.7 ± 0.1 for $[4.6]-[12]$ and $[3.4]-[4.6]$ colours respectively). Figure 2.14 as a whole shows that the variation of q_{250} with either WISE colour cannot be satisfactorily explained by a dependence on temperature, redshift, or stellar mass individually, but by all three at once. This results in correlation coefficients of 0.1 ± 0.2 and 0.2 ± 0.2 for $[4.6]-[12]$ and $[3.4]-[4.6]$ respectively.

Using the model described above, we find that the effects of stellar mass, dust temperature, and redshift upon q_{250} explain 16, 36, and 48 per cent of the total explainable correlation of q_{250} over the $[3.4]-[4.6]$ and 8, 71, and 21 per cent over $[4.6]-[12]$, respectively. However, the effects of these parameters on the variation of q_{250} are not independent of each other. Indeed, there are non-zero covariances between these parameters, e.g., the effect of stellar mass and dust temperature upon q_{250} at once is not equivalent to the sum of their independent effects.

Luminosity in $250\,\mu$m and both radio bands increases towards redder WISE colours and hotter temperatures, consistent with evidence of a luminosity-temperature relation found by Chapman et al. (2003), Hwang et al. (2010), and in the radio by Smith et al. (2014). Given that the temperature evolution over redshift in our sample is consistent with being flat to within the 1σ, we can conclude that such a luminosity-temperature relation is not simply due to redshift effects. This is more evidence of the trend in q_{250} tracing the specific star formation rate.

To test our assumption that the $[4.6]-[12]$ colour traces specific star formation rate, we use the specific star formation rates obtained from MagPhys fits (Smith et al., 2012a). Figure 2.15 shows a highly significant trend (both gradients are non-zero with a significance above 3σ) between MagPhys specific star formation rate and q_{250} for both FIRST and LOFAR (low

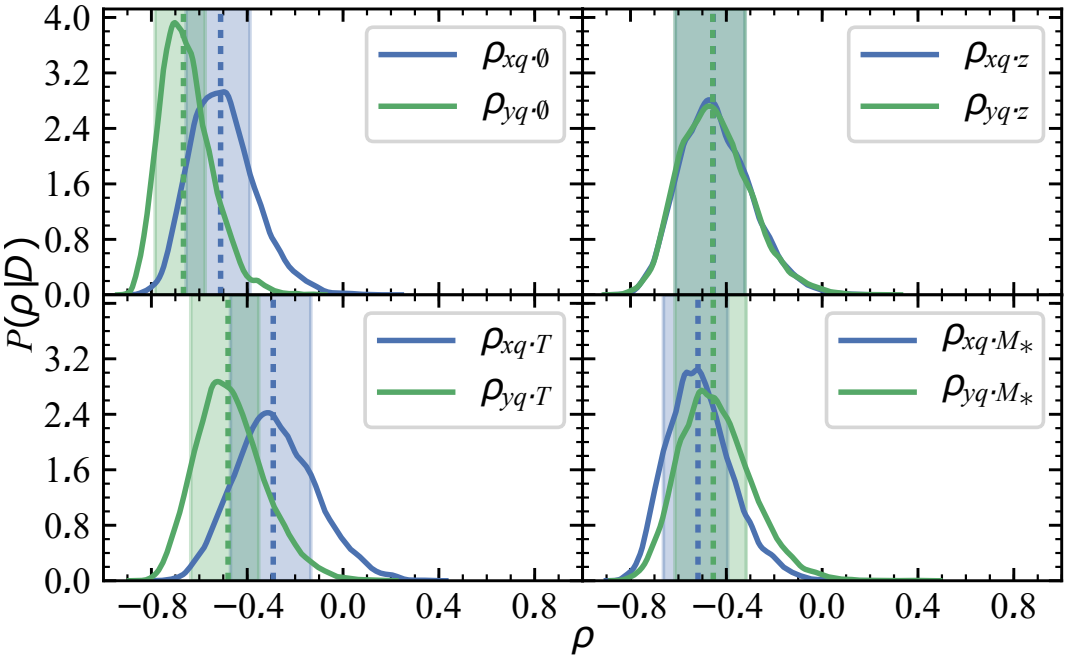

(a) Independent partial correlation coefficient PDFs

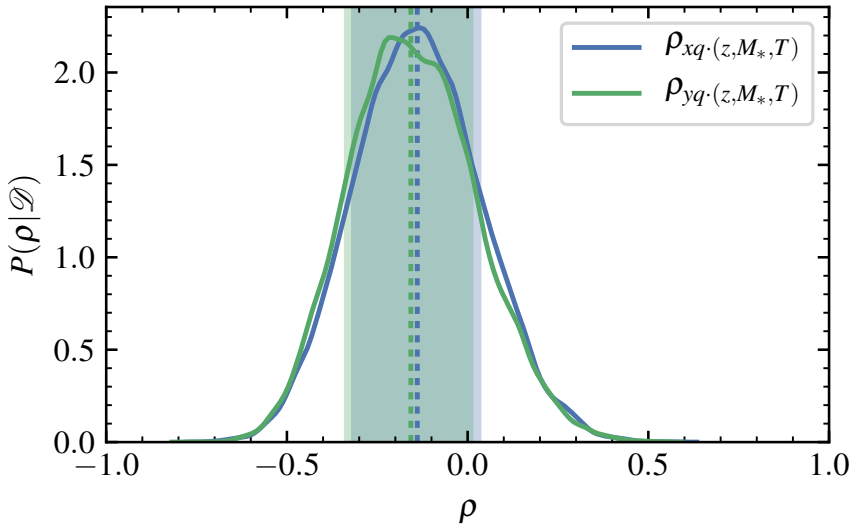

(b) Partial correlation coefficient PDF controlling for all variables at once.

FIGURE 2.14: The marginalised probability density, $P(\rho|\mathscr{D})$, distributions for the correlation coefficients (ρ) of $[4.6]-[12]$ (blue) and $[3.4]-[4.6]$ (green) against stacked $q_{250}^{\rm LOFAR}$. $\rho = (-)1$ corresponds to maximal (anti-) correlation, whilst $\rho = 0$ corresponds to no correlation. **Top left (a):** The correlation coefficient PDFs calculated assuming that $q_{250}^{\rm LOFAR}$ does not depend on other variables. **Top right (a):** The correlation coefficient PDFs after controlling for a linear dependence of $q_{250}^{\rm LOFAR}$ upon redshift. **Bottom left (a):** The correlation coefficient PDFs after controlling for a linear dependence of $q_{250}^{\rm LOFAR}$ upon effective temperature. **Bottom right (a):** The correlation coefficient PDFs after controlling for a linear dependence of $q_{250}^{\rm LOFAR}$ upon stellar mass. **Bottom panel (b):** The correlation distribution when controlling for all three parameters at once. The vertical lines mark the median value for the correlation coefficient with the shaded areas marking the $16-84$th percentile range. A Gaussian kernel was used to smooth the probability distributions.

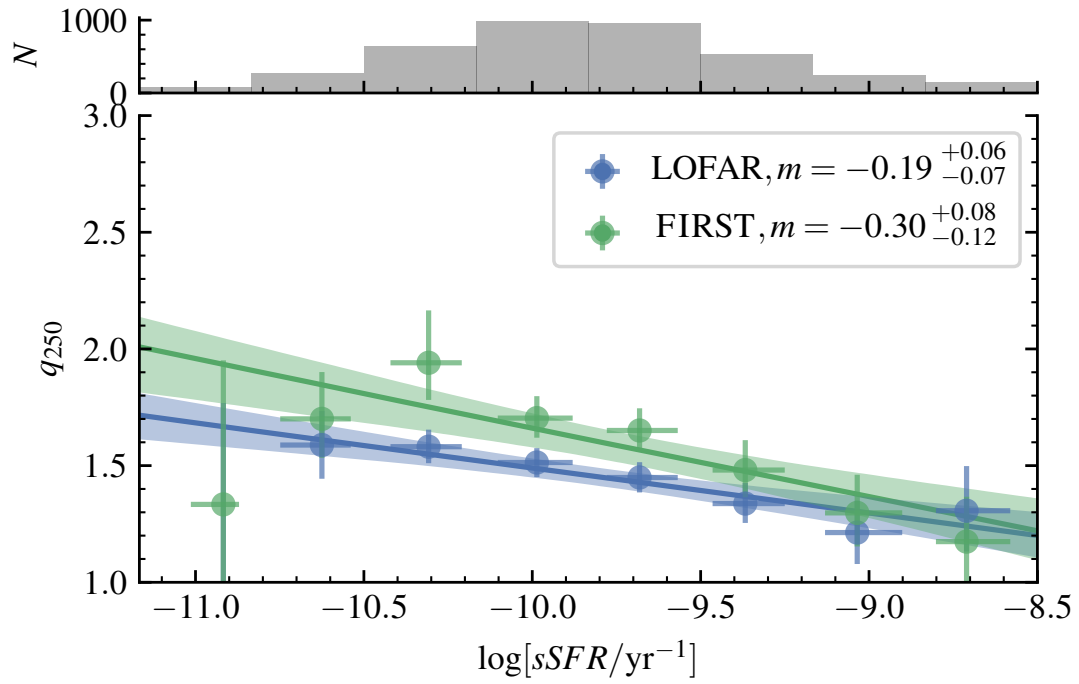

FIGURE 2.15: q_{250} for LOFAR (blue) and FIRST (green) at 150 MHz against the specific star formation rate in 8 bins of width 0.3 dex. The uncertainties on q_{250} are calculated via bootstrapping within each bin. The uncertainties on sSFR are calculated from the 16th and 84th percentiles in each bin. Straight line fits are shown as coloured lines with 1σ credible intervals shown as shaded regions. The top histogram shows the number of galaxies in each bin.

sSFR is discussed below). The gradients of the trend at high and low frequency are consistent to within 1σ.

Gurkan et al. (2018) have found that above a stellar mass of $10^{10.5} M_{\odot}$, a strong mass dependence of radio emission, inferred to be non-AGN in origin, emerges. We show here that the for the variation of q_{250} over the MIRDD to be explained, the effects of stellar mass and specific star-formation rate (for which isothermal temperature is an effective proxy) must be taken into account since they independently explain 25 and 38 per cent of the total correlation respectively.

2.4.5 Potential AGN contamination

BPT classification identifies AGN based on emission line ratios. However, star formation and AGN activity are not mutually exclusive (Jahnke et al., 2004; Trump et al., 2013; Rosario et al., 2013) and one ionisation process can mask the other. Indeed, the BPT diagram shows a population of Seyfert 2 objects seamlessly joined to the star-forming branch (Baldwin et al., 1981; Kewley et al., 2006). Obscured AGN SEDs are bright in the mid-infrared due to the re-radiated

emission from their obscuring structure (Antonucci, 1993; Stern et al., 2005). In particular, radiatively efficient QSOs and obscured AGN are expected to be detected by WISE and to be located in the reddest space on the WISE MIRDD (Jarrett et al., 2011).

2.4.5.1 Searching for hidden AGN

Whilst it may be difficult to exclude composite galaxies based purely on line ratios, spectra can be searched for AGN features and radio images inspected for signs of jets or compact cores. The angular resolutions of FIRST and LOFAR are too low to distinguish AGN cores from compact starbursts, but we can rule out obvious radio loud contamination. To look for signs of physical differences between the low and high q_{250} areas and to check for the impact of radio-mode AGN, we take two samples of galaxies. The first sub-sample, named "WISE-blue", we take from the region of highest q_{250} and bluer WISE colours. This region is described by the conditions $2.5 < [4.6]-[12] < 3.25$ and $0.0 < [3.4]-[4.6] < 0.4$ and so should correspond to lower-luminosity star-forming galaxies.

The second sub-sample, named "WISE-red", we take is described by the conditions $3.75 < [4.6]-[12] < 4.5$ and $0.2 < [3.4]-[4.6] < 0.6$, and is characterised by the lowest values of q_{250}. This is the area most likely to be contaminated by AGN, given its proximity to the QSO box defined in Jarrett et al. (2011) and low value of q_{250}. We note that we have removed the 12 sources which lie within the QSO box before conducting the analysis here.

We visually inspected the FIRST and LOFAR images of 100 randomly-chosen galaxies from the WISE-blue and WISE-red sub-samples for signs of cores and jets. However, although the sub-samples are selected based on their position in the MIRDD, they also correspond to different redshift ranges. The higher redshift sources are selected at redder WISE colours and therefore the most luminous radio sources are selected in the WISE-red sub-sample and, conversely, the WISE-blue sub-sample consists of some of the least luminous radio sources. As a result, the WISE-red sub-sample tends to have extended and brighter radio emission at 150 MHz than our WISE-blue sub-sample. Therefore, if there is any significant AGN presence, they are more likely to populate the WISE-red sample than in the WISE-blue sample. We find little evidence of AGN activity due to compact cores or jet structures in either sample. However, the extended emission due to the luminosity bias mentioned above makes it difficult to compare the two sub-samples. Figure 2.16 shows the rest-frame spectra, median-stacked using the method found in Rowlands et al. 2012, for the WISE-red sub-sample in red and the WISE-blue sub-sample in blue. Taking

the difference between the spectra of the two sub-samples indicates the potential AGN (WISE-red sub-sample) have brighter emission lines relative to their continuum and have strong $H\gamma$ and $[OIII]$ lines relative to the WISE-blue sub-sample. The $H\gamma$ line is found to have an equivalent width of 1 Å which is below what would be expected for broad-line AGN (Peterson, 1997). Given the increased infrared luminosity, this seems to indicate that the ionisation required to excite $H\gamma$ is generated by star formation. Moreover, if we position each median spectrum on the BPT diagram, they are both firmly within the star-forming region.

However, a significant fraction of the radio AGN population lack characteristic emission lines (Jackson and Rawlings, 1997; Sadler et al., 1999; Best et al., 2005; Evans et al., 2006) and hence cannot be identified using a BPT classification. Such Low Excitation Radio AGN (LERAGN) could explain the decrease in q_{250} with their additional contribution to radio luminosity. LERAGN have traditionally not been reconciled with the AGN unification model proposed by Antonucci (1993). However, there are significant differences between LERAGN and their standard high excitation counterparts (HERAGN) such as black hole masses (e.g. McLure and Jarvis, 2004; Smolcic, 2009), depending on sample selection (Fernandes et al., 2015). Hardcastle et al. (2006) have suggested that LERAGN are the consequence of different accretion mechanisms whereby LERAGN accrete in a radiatively inefficient mode. LERAGN will have excess radio luminosity for their $H\alpha$ star formation, and so lie beneath the star-forming FIRC. The radio-loud fraction of galaxies that are LERAGN or HERAGN has been found to correlate with stellar mass, colour, and star-formation rate (Janssen et al., 2012). However, 98 per cent of our star-forming sample have stellar masses below 10^{11} $M_{\odot}$, where Janssen et al. (2012) report a radio-loud fraction of LERGS below 0.001.

In addition, Gurkan et al. (2015) found that radio-loud AGN tend to have lower star formation rates than star-forming galaxies, and that radio-quiet AGN also exhibit SFRs that are offset from the star-forming galaxies.

We use star formation rates and stellar masses fit by MAGPHYS (da Cunha et al., 2008; Smith et al., 2012a) to test whether our sample exhibits this offset. Figure 2.17 shows our entire sample including BPT-classified AGN. Our BPT-classified AGN, in yellow, clearly lie below the star-forming SFR-mass relation found by Gurkan et al. (2015) whereas our star-forming sample (in green) lie on it. Furthermore, our sub-sample drawn from the WISE-red region (red) lie above the rest of the galaxies suggesting again that q_{250} decreases with increased specific star formation rate. Figure 2.17 shows the galaxies within the WISE-red sub-sample (red) are representative

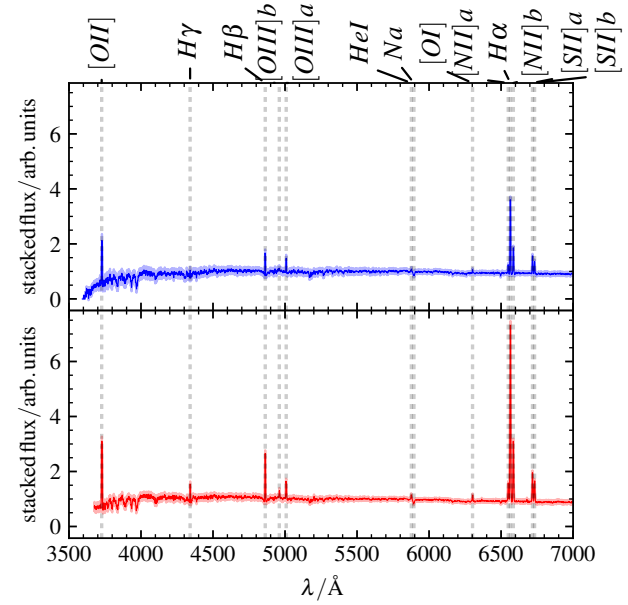

(a) Stacked spectra for each sub-sample

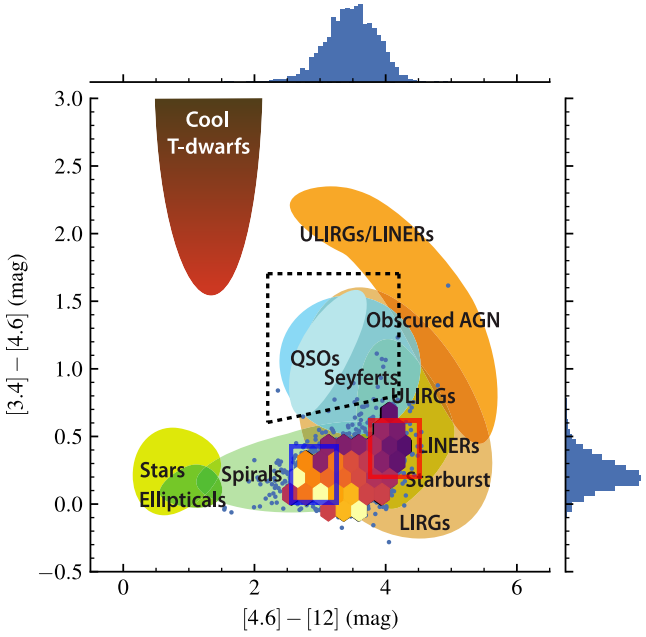

(b) Locations of the WISE sub-samples

FIGURE 2.16: The median-stacked rest-frame spectra of the WISE-blue (blue) and WISE-red (red) sub-samples (left) and their locations on the MIRDD (right). The spectra were blueshifted to their rest frame and interpolated to a common wavelength grid between 3500Å and 8000Å. Each spectrum was normalised based on the median interpolated flux between 5450 and 5550Å. The 1σ uncertainties in the median spectra are shown as light shaded regions around the median. The MIRDD is the same as in Figure 2.2 with the binned $q_{150\,\mathrm{MHz}}^{\mathrm{LOFAR}}$ taken from Figure 2.13 overlaid. Blue and red boxes indicate the boundaries for the WISE-blue and WISE-red sub-samples respectively.

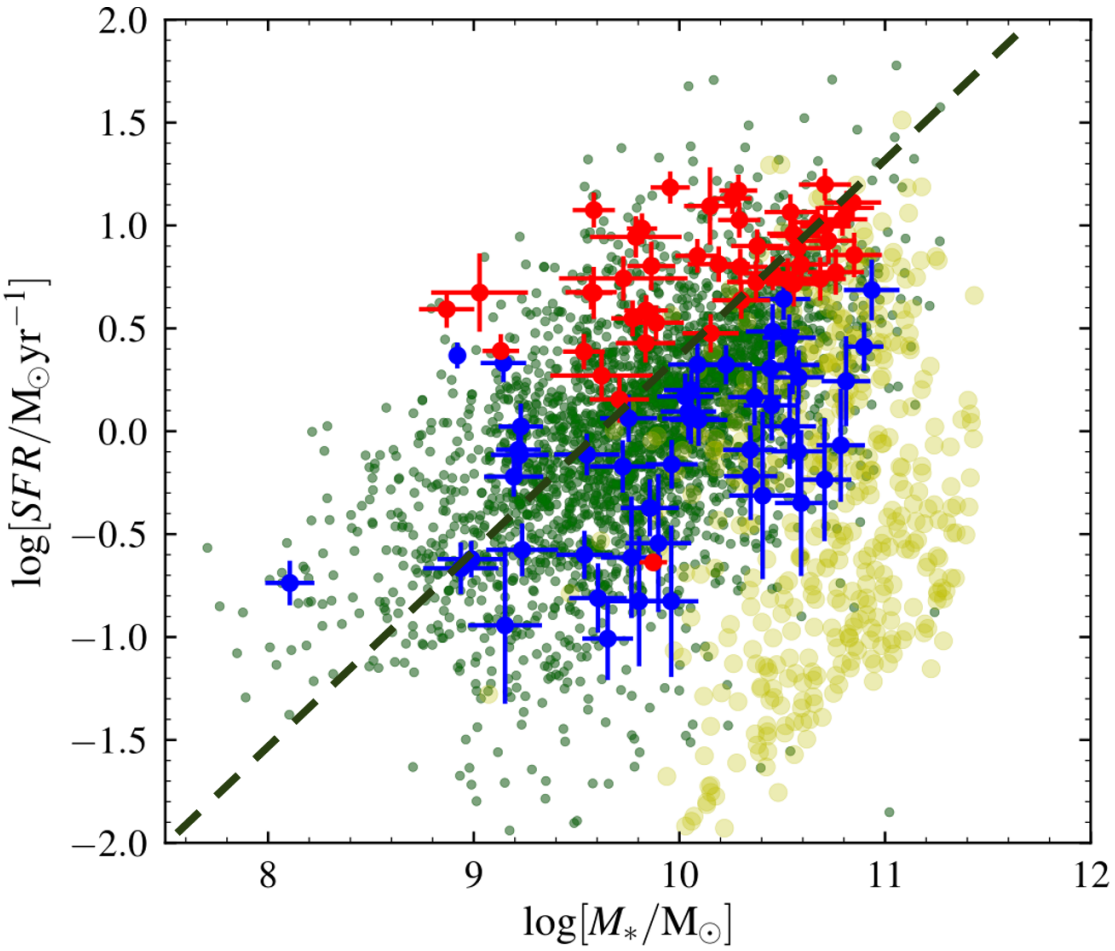

FIGURE 2.17: Stellar mass versus star formation rate for our sample. Our full sample is plotted in green. The 100 galaxies selected from both the WISE-red sub-sample (red) and the WISE-blue sub-sample (blue) are shown as the larger points with errorbars. For comparison, AGN classified by BPT are plotted in yellow. The straight line relation for star-forming galaxies from Gurkan et al. (2015) is shown as the dashed green line.

of starbursts given their increased star formation rate. The fact that our BPT-classified AGN are offset in star formation and stellar mass gives some reassurance that the effect of radio-quiet AGN is minimised in our WISE sample. Since using the mean instead of the median may well increase the effect of outliers/AGN, we test the effect of using the median on our results. We find that the discrepancy between q_{250} measured with LOFAR and FIRST, the evolution of q_{250} over redshift, and the variation of q_{250} over the MIRDD are not affected. In addition, we check for obvious outliers in the luminosity distributions for LOFAR and FIRST, finding no such source. This allows us to gain some degree of confidence that we are not plagued by outlying AGN. However, we note that the global value of q_{250} is increased by 0.2 dex for both LOFAR and FIRST when using the median.

2.4.5.2 Testing with the inclusion of known AGN

If we include the 447 5-sigma BPT-classified AGN and rerun our analysis, we find a large effect on both global q_{250} values and distributions over redshift, temperature, and specific star-formation rate (which we show in Appendix A.1). The AGN decrease the whole-sample q_{250} to 1.23 ± 0.01 and 1.25 ± 0.10 for LOFAR and FIRST respectively. The relative increase in radio luminosity is unsurprising and demonstrates that AGN can have a large impact on q_{250}.

We find that the addition of BPT-AGN affect q_{250} calculated in low temperature bins most severely but that the difference in q_{250} at high temperature is marginal and consistent with q_{250} calculated with our star-forming sample. The greatest effect is seen in the lowest temperature bin where there is a drop of 1.2 dex in q_{250}. Indeed, even when we include BPT-selected AGN we find that $q_{250} - T$ trend in Figure 2.11 is still consistent with Smith et al. (2014) at high temperatures.

The largest effect that the BPT-selected AGN have on q_{250} is found at very low specific star-formation rates. These are likely to be LERAGN since low specific star-formation rates imply that they are quenched. In fact, at $\log[sSFR/\mathrm{yr}^{-1}] > -10.5$ there are very few BPT-AGN; we find that a q_{250} evaluated in this regime with AGN included is in agreement with a q_{250} calculated with our star-forming sample.

The evolution of q_{250} with redshift at high and low frequency remains qualitatively the same (decreasing with redshift) with an average offset of ≈ 0.2. Moreover, when the problematic low temperature and low specific star-formation rate bins are removed from the calculation, the evolution of q_{250} over redshift at 150 MHz and 1.4 GHz is unaffected.

When BPT-AGN are included in the analysis, the variation in q_{250} over the WISE colour $[4.6] - [12]$ can be no longer be completely explained by the combined dependence on redshift, temperature, and stellar mass. The direction of this new correlation is not towards the location of QSO box at redder $[3.4] - [4.6]$ colour and actually inverts the correlation direction from negative to positive (see Figure A.3, for the equivalent Figure 2.14 with the addition of known AGN). This is likely due to the fact that we require 5σ detections in the MIRDD WISE bands and so only bright AGN are identified and positioned at bluer $[4.6] - [12]$ colours (since the $12\,\mu$m WISE band is less sensitive than $2.4\,\mu$m and $3.4\,\mu$m). As a result, no BPT-AGN are found towards the reddest colours on the MIRDD (see Figure A.5). If such a small number of included BPT-AGN can alter the correlation in the positive direction, it is unlikely that hidden AGN are the

root cause of the negative correlation found in our star-forming sample. Since the correlation of q_{250} with WISE colours in our star-forming sample is only just explained by these factors to 1σ, this could signal either a different misclassified population of objects in our supposed star-forming sample or a feature of star-formation itself. However, AGN which are not detected but have a BPT classification may be positioned differently on the WISE MIRDD and have different emission properties (see discussion above). We therefore cannot rule out low-level AGN contamination.

Based on the above analysis, q_{250} should only be marginally affected and therefore considered relatively trustworthy in galaxies with medium to high specific star-formation rates.

2.4.6 Reconciling with star-forming models

Through the model developed by Lacki and Thompson (2010), energy loss in starbursts is mainly due to bremsstrahlung and ionisation. This would increase q if it were not for the effect of secondary charge radiation. Though the exact contribution of secondary charges – resulting from cosmic ray proton collisions with ISM protons – that is needed for a consistent FIRC is model-dependent, their addition allows the high-Σ_g conspiracy to be maintained (i.e. a linear FIRC more or less unchanging over surface density, Σ_g). Our results show that q_{250} decreases with specific star formation rate and hence high gas density. Such a decrease in q_{250} is at odds with the expected behaviour that q_{250} should remain constant (especially at high specific star formation rates), derived from the standard model described by Lacki and Thompson (2010). However, there are numerous reasons why the high-Σ_g conspiracy could break down detailed by Lacki and Thompson (2010).

If the magnetic field is assumed to be dependent on volume density rather than surface density, synchrotron cooling becomes dominant and q will decrease with increasing density. The high-Σ_g conspiracy also depends on the assumption that the escape time for cosmic rays is the same in all starbursts and normal star-forming galaxies. If the vertical (with respect to the disk) cosmic ray diffusion scale height is constant instead, then the escape time would be two orders of magnitude smaller for starbursts than for normal star-forming galaxies. However, we expect this effect to be much stronger than the variation in q_{250} we see in our result and advective transport by galactic winds may dominate in spiral galaxies (Heesen et al., 2018). Indeed, the fact that the variation is smooth and can be adequately explained by a combination of three parameters, for normal and

highly star-forming galaxies, suggests that the same mass/temperature-dependent mechanism is responsible.

This work is based on the monochromatic q_{250} and is therefore not sampling all of the reprocessed light from recent star formation. It is therefore possible that a FIRC based on integrated infrared luminosity does not vary as the FIRC at 250 μm does. In a two-component model of the dust SED (Charlot and Fall, 2000), a warm but low-mass stellar birth cloud will outshine a cold but more massive ISM at 250 μm. If the warm stellar birth clouds are more dominant at higher isothermal temperature, then the FIRC will be a less accurate calibrator of star formation rate at lower temperatures, assuming a direct relation between synchrotron and recent star formation. Some of the variation of q_{250} with star formation rate could then be attributed to the effect of not using integrated dust luminosities.

There are many effects to consider when modelling the FIRC and the conspiracies listed in Lacki and Thompson (2010) depend on a subset of models. We cannot say precisely which effect will reconcile their standard model with this result.

2.5 Conclusions

We have used a catalogue of optically selected, BPT-classified star-forming galaxies from Gurkan et al. (2018) to study variation in the far-infrared radio correlation over redshift and other parameters. We calculate the monochromatic far-infrared radio correlation, parametrised as q_{250}, for 150 MHz and compare it to that found for 1.4 GHz, using forced aperture photometry. We obtained the photometry (fluxes were measured using 10 arcsec radius circular apertures centred on the optical positions) for all of these sources – including those which are not formal detections at LOFAR, FIRST, and *Herschel* wavelengths. To avoid introducing bias to our findings, we make no significance cuts on infrared or radio fluxes.

Knowing about possible variation in the FIRC is of great importance, since a constant FIRC underpins the use of radio luminosity estimates as a star formation rate indicator. Our main results are summarised as follows:

- q_{250} at 1.4 GHz for our sample is found to be consistent with previous studies (Jarvis et al., 2010; Ivison et al., 2010; Smith et al., 2014).

- The FIRC for 150 MHz is found not to be consistent with that for 1.4 GHz assuming a standard power law with spectral index of -0.71 (0.1 dex lower).

- We find evidence for a decreasing q_{250} with redshift at 150 MHz (gradient of $-1.0^{+0.2}_{-0.3}$). By comparing to the results of Molnár et al. (2018), we also find tentative evidence that the slope of this evolution becomes shallower with increasing frequency. An increase in radio luminosity of star-forming galaxies with redshift will be useful for high-redshift SFG detection, assuming that this evolution is maintained above $z = 0.5$, as has also been suggested by FIRC studies conducted with LOFAR at higher redshifts (e.g. Calistro-Rivera et al., 2017).

- We corroborate the q_{250}-temperature variation discovered by Smith et al. (2014) at high frequency. We find that this relation also applies at low frequency to within 1σ, but only at temperatures above 20K.

- We find that q_{250} varies across a two-dimensional mid-infrared colour-colour space, at both radio frequencies, and within the star-forming region defined by Jarrett et al. (2011). By using a hierarchical correlation model, we find that all of the correlation between q_{250} with $[4.6]-[12]$ and $[3.4]-[4.6]$ colours can be attributed to the combined effects of the correlations that we measure between q_{250} and stellar mass, redshift, and isothermal temperature, to within 1σ. We note that the variation is not explained by redshift, temperature, or stellar mass alone but by all three in conjunction.

- Using the indicative locations of different galaxy types within the WISE colour-colour plot from Jarrett et al. (2011) – e.g. spirals etc – we see that the trend to lower q_{250} appears to reflect the transition from spirals to LIRGs to starbursts. q_{250} decreases with redder $[4.6]-[12]$ colour and with increasing specific star formation rate. Indeed, the lowest values of q_{250} are seen in the region of the MIRDD occupied by the Polletta et al. (2007) starburst templates. Moreover, the region where LIRGs overlap with normal spirals ($3 < [4.6]-[12] < 4$) is the region where the largest gradient in q_{250} (relative to WISE colour) is seen.

- To test the possible influence of AGN contamination on our results, we re-ran our analysis but this time included the BPT-classified AGN. The only significant change in our results was at the lowest dust temperatures, and lowest specific star formation rates; the other regions of parameter space, and therefore our conclusions, are unchanged. We can be confident, therefore, that our results are robust to the inclusion of detectable AGN, and it is

tempting to attribute this variation to hitherto unknown physics of the FIRC. However, we cannot totally rule out the possibility that widespread low-level AGN have some influence (though we see no evidence of high ionisation and/or broad emission lines indicative of their presence in stacked rest-frame optical spectroscopy for subsets of our BPT-classified SFG sample). We also test for residual AGN contamination by analysing the radio images for WISE-red and WISE-blue sub-samples, finding no clear evidence for obvious AGN jet structure in either group. We also test that our choice of aggregate statistic (the mean) of the parameter q_{250} is not affected by outliers by performing the same analysis with the median. We find that the trends that we report of q_{250} over redshift, sSFR, temperature, and mid-infrared colours remain unaffected by the choice of aggregate statistic with only the global value of q_{250} changing.

Taken together, these results indicate that the monochromatic FIRC varies strongly across the full range of BPT-classified star-forming galaxies in a manner dependent upon their mid-infrared colours (which are widely used as an empirical probe of galaxies' star formation properties), even at fixed redshift.

We do not draw conclusions from our results alone about the efficacy of using the FIRC to calibrate radio star-formation rates, however Gurkan et al. (2018) used the same sample of galaxies, along with a full analysis of energy-balance derived stellar mass and star formation rate estimates, to investigate the low frequency radio luminosity star-formation rate relation directly. The broken power law relation between SFR and 150 MHz luminosity found in that work – which they suggest may indicate the presence of an additional mechanism for the generation of radio-emitting cosmic rays – is consistent with the possibility of residual low-level AGN contamination, and the FIRC behaviour we observe at low specific star formation rates. Indeed, this suggests that calibrations such as those proposed in Brown et al. (2017) may need to be more nuanced than they currently are.

Though our results underline the exquisite combined power of *Herschel* and LOFAR for studying star-forming galaxies (and in particular the high quality of the maps produced by the LoTSS pipeline), it will be of great interest to investigate the star-formation and AGN content of galaxies in more detail with even more sensitive, high resolution data in the coming years, as we enter the era of the Square Kilometre Array.

Chapter 3

Efficient Photometric Reverberation Mapping and the Efficacy of QSO Variability Modelling

3.1 Introduction

All active galactic nuclei (AGN) are believed to be powered by an accretion disk around a central super-massive black hole (SMBH) which is itself surrounded by a broad-line region (BLR) (Antonucci, 1993; Urry and Padovani, 1995; Ho, 2008; Heckman and Best, 2014). The mass of the SMBH has been observed to scale with the properties of its host galaxy (e.g. Magorrian et al. 1998; Silk and Rees 1998; Benson et al. 2003; Haering and Rix 2004; Croton et al. 2006; Guo et al. 2011; and Kormendy and Ho 2013 for a full review) and so it is essential that accurate masses for the SMBH can be derived in order to investigate the effect AGN feedback has on their host galaxies.

In the absence of a direct black-hole mass measurement, there exist scaling relations based on emission line widths (e.g. Hβ: Wandel et al. 1999 and Mg_{II}: McLure and Jarvis 2002) and luminosity at 5100 Å (e.g. Bentz et al. 2013). These relations are typically calibrated at low redshift and have not been extended to high redshift (Hiner et al., 2015; Barišic et al., 2017) despite wide-spread extrapolated use at high redshift (McLure and Dunlop, 2004; Vestergaard, 2004; Vestergaard and Peterson, 2006; Netzer et al., 2007; Runnoe et al., 2013; Feng et al., 2014;

Mejía-Restrepo et al., 2016). Therefore, it is also for the purposes of validating these scaling relations that more black-hole mass measurements at higher redshifts are needed.

Reverberation mapping (Blandford and McKee, 1982; Gebhardt et al., 2000; Ferrarese and Merritt, 2000; Peterson, 2004) is a powerful technique for estimating black hole masses. Assuming that the broad-line region is gravitationally dominated by the SMBH, it is possible to estimate the black hole mass from the time delay between continuum emission from the accretion disk and the reprocessed emission from the broad-line region, also known as the "lag", from the Keplerian motion equation:

$$M_{BH} = f\frac{R_{BLR}\sigma_{\rm disp}^2}{G}, \tag{3.1}$$

where the virial parameter f describes the structure and orientation of a broad-line region with radius $R_{BLR} = c\tau_{\rm lag}$ and an emission line width of $\sigma_{\rm disp}$. Assuming that the virial factor, f, is fully generated by the inclination, θ, of the disc, $f = 1/4\sin^2\theta$ and so at $\theta = 30^\circ$, $f = 1$ (McLure and Dunlop, 2001; Liu et al., 2017). The f can be determined on a case-by-case basis by modelling the BLR (Pancoast et al., 2011, 2014; Williams et al., 2018a), through gravitational redshift measurements (Liu et al., 2017), or through combinations of independent black-hole mass estimators. However, it is common to use an aggregated average for use in large data sets. Grier et al. (2013b), Onken et al. (2004), Park et al. (2012), and Graham et al. (2011) have measured values of $\langle f\rangle = 4.3 \pm 1.1$, 5.5 ± 1.8, 5.1 ± 1.3, and 2.8 ± 0.6 respectively from the independently measured stellar velocity dispersions.

So far, about 100 black hole masses have been measured using spectroscopic reverberation mapping techniques (Kaspi et al., 2000; Bentz et al., 2009a,b; Denney et al., 2010; Bentz et al., 2013; Barth et al., 2015; Grier et al., 2012; Shen et al., 2015b; Du et al., 2015, 2016a,b; Grier et al., 2017), which require long-term spectroscopic observations to recover their lags. Since BLR radii can span up to several hundred light days (Peterson, 2004; Bentz et al., 2014; Fausnaugh et al., 2017; Williams et al., 2018a) light curve observations need to take place over several months or years to match features in the continuum to the echoes from the BLR, with 3 times the observed-frame lag being the recommended baseline (Shen et al., 2015a). Cosmological time dilation increases the timescale of observed variability and so high-redshift QSOs require much longer observational campaigns than low-redshift QSOs. To compound this effect, higher-redshift QSOs are intrinsically more luminous than lower-redshift QSOs, which implies that they have longer lag time-scales than lower-redshift QSOs.

Fine et al. (2013) and then Brewer and Elliott (2014) have developed methods to recover lags from the stacked cross-correlations of photometric and spectroscopic observations to be used when individual lags are poorly constrained but there is a large sample of AGN. This method allows for the detection of emission-line lags for a population of AGN at very high redshift (Fine et al. 2013 use a sample of AGN with redshifts $z \lesssim 4.5$) and provides convincing evidence for the decreasing BLR radius for emission-lines with higher excitation energies. However, stacked reverberation mapping is a statistical technique and cannot provide more signal-to-noise for individual objects.

An extra source of inefficiency for spectroscopic campaigns is the need to disperse the light and subsequent decreased signal-to-noise especially at high redshift. In addition, there is an added difficulty of accurately flux-calibrating spectroscopic observations, especially as photometric RM requires the precise measurement of the ratio between continuum and emission line flux. Therefore, observing emission lines spectroscopically for reverberation mapping is expensive due to the required overhead, and restricted to bright or low redshift sources and so accurate photometric methods for reverberation mapping are highly sought after.

The variability of the BLR emission line can be captured within a redshifted narrow-band (or broad-band) photometric filter through the careful separation of the underlying, driving continuum (Haas et al., 2011; Chelouche and Daniel, 2012; Pozo Nuñez et al., 2012; Zu et al., 2016). This can be done either by modelling the variability as a damped random walk (DRW) (Zu et al., 2011, 2013, 2016) or by more empirical measures such as cross-correlation analysis, which are model-independent (White and Peterson, 1994; Rybicki and Kleyna, 1994; Peterson, 2004; Chelouche and Daniel, 2012; Shen et al., 2015a; Fausnaugh et al., 2017).

`Javelin` (Zu et al., 2013, 2011, 2016) is a parametric Bayesian tool which models the variability of the QSO itself rather than extracting peaks from empirical cross-correlation functions. Modelling the continuum emission as a DRW has some advantages over cross-correlation in that it allows for natural inclusion of Bayesian inference techniques for noisy data from which parameter values and uncertainties can be estimated (Zu et al., 2011, 2013). Stochastic DRW models of the accretion disk continuum emission are based on physical assumptions that can be tested by observations. The physical mechanism supporting the use of DRW models is the stochastic heating of the accretion disk by the central source and its subsequent variability due to thermal fluctuations (Kelly et al., 2009).

Although the sample of reverberation mapped QSOs is becoming more representative (in terms of luminosity and redshift) with time, the current sample is biased to low redshift QSOs which have very broad emission lines (Shen et al., 2015a). If photometric reverberation mapping can recover precise lag estimates for SMBHs, then fewer resources would have to be spent on spectroscopic campaigns in order to fill in the parameter space of black-hole mass, luminosity and redshift.

Photometric reverberation mapping has been performed on both individual targets below $z = 0.04$ (Haas et al., 2011; Edri et al., 2012; Pozo Nuñez et al., 2012; Ramolla et al., 2014; Pozo Nuñez et al., 2014; Carroll and Joner, 2015; Hood et al., 2015; Pozo Nuñez et al., 2015) and for a sub-sample of the SDSS-RM (Shen et al., 2015a) catalogue (Hernitschek et al., 2015; Zhang et al., 2017). However, the estimated uncertainties for these SDSS-RM sub-samples are typically larger than 100 per cent. Photometric reverberation mapping has also been applied to the continuum to measure the properties of the accretion disk (Mudd et al., 2017; Cackett et al., 2018), though not to estimate black hole masses.

This work sets out to demonstrate the efficacy and reliability of photometric reverberation mapping even for higher redshift targets. We aim to produce the first robust photometric reverberation mapped black-hole mass with a redshift above $z = 0.04$.

In Section 3.2, we carefully pre-select targets to give us the best possible chance of recovering precise lags. We specify that candidates must have redshifts that allow the use of a redshifted Hα photometric filter and have expected observed lags (from the lag-luminosity relation Bentz et al. 2013) such that they can be observed for $3t_{\rm lag}$ days over multiple semesters. We then detail our observations and the methods used to produce photometric light-curves for use with `Javelin`. Before fitting QSO variability models to our observations, we produce a suite of simulated light-curves in order to test how well `Javelin` can recover known lags for QSOs with the same cadence and signal-to-noise as our target observations. In Section 3.3 we present the fitted BLR lag and black-hole mass distributions for our observations. In order to test whether the slope is significantly affected by non-Gaussian errors, we also apply rigorous statistical analysis to the fitting of the Hβ lag-luminosity relation by not assuming Gaussian uncertainties for either our targets or for the Grier et al. (2017) catalogue. In Section 3.4 we compare the efficiencies of the SDSS-RM campaign (Shen et al., 2015a; Grier et al., 2017) and our own, in terms of signal-to-noise of the fitted lag. We also discuss future potential applications of

photometric reverberation mapping in upcoming surveys where such techniques can easily be applied. Finally, we summarise our conclusions and outlook in Section 3.5.

3.2 Methods

Our intermittent requirements make RM observations of small samples of high redshift targets unsuited to continuous observing campaigns. We observed our QSOs robotically with the Liverpool Telescope since it can accommodate our discontinuous observation campaign. We make use of the optical components of the infrared-optical (IO:O) suite of instruments available on the Liverpool Telescope since a range of $H\alpha$ filters are available in addition to the SDSS *ugriz* filters. This allows us to observe the Hβ emission lines of a wide range of high redshift QSOs, since their observed emission line will fall within the sensitivity of one of the available Hα filters.

3.2.1 Target selection

We select our targets to have $i_{AB} < 18$, spectroscopically-confirmed in the SDSS DR12 (York, 2000; Eisenstein et al., 2011) or BOSS (Dawson et al., 2013), and have Hβ emission lines with equivalent widths > 50 Å. We only select those QSOs whose redshifted $H\beta$ line will fall into one of the IO:O (Steele et al., 2004) $H\alpha$ photometric filters. Additionally, using the 5100 Å luminosities from Shen et al. (2011) and the $R - L_{5100}$ relation from Bentz et al. (2013), we pre-select targets that are likely to have observed lags $t_{lag}(1+z) < 95$ days. In order to derive the most reliable lag measurement, observed light curves should span 3 times the length the observed lag, as seen in the extensive simulations conducted by Shen et al. (2015a). We therefore imposed an additional criterion that the QSOs be observable for at least 3 times the length of their expected lag between the 14 months of the Liverpool Telescope (Steele et al., 2004) extended 2015B and 2016A semesters. Applying these constraints yields 10 targets which we submitted for observation.

Our targets, shown in Fig 3.1 as green points, are positioned between the redshift-luminosity locations of the high-redshift spectroscopic sample from Grier et al. (2017) and the low-redshift sample from Bentz et al. (2013).

SDSS ID	RA /°	Dec /°	z	i_{AB} /mag	λL_{5100} /log[ergs^{-1}]	$t_{H\beta}(1+z)$ /days	visibility /days	visibility /$t_{H\beta}(1+z)$	epochs Hα	epochs i-band	observed baseline /days	observed baseline /$t_{H\beta}(1+z)$
J082905.01+571541.6	127.2708	57.2615	0.350	17.9	44.24	61.4	250	4.1	0	0	0	0
J153601.07+162838.4	234.0044	16.4773	0.382	17.9	44.35	72.2	301	4.2	16	14	208	2.9
J112600.00+304005.3	171.5000	30.6681	0.361	17.9	44.41	76.1	231	3.0	0	0	0	0
J122519.30+372053.6	186.3304	37.3482	0.388	17.9	44.45	81.9	249	3.0	11	11	180	2.2
J154246.51+194626.1	235.6938	19.7739	0.398	17.9	44.46	83.1	305	3.7	0	0	0	0
J150243.09+111557.3	225.6795	11.2659	0.390	17.5	44.56	93.4	278	3.0	0	0	0	0
J153057.45+304322.0	232.7393	30.7228	0.378	17.6	44.57	93.5	314	3.4	17	19	189	2.0
J164224.30+444509.8	250.6012	44.7527	0.368	17.8	44.58	94.5	334	3.5	16	15	179	1.9
J153729.23+272250.7	234.3717	27.3807	0.388	17.9	44.57	95.0	312	3.3	0	0	0	0
J144645.44+625304.0	**221.6893**	**62.8844**	**0.351**	**17.8**	**44.57**	**91.7**	**337**	**3.7**	**31**	**30**	**329**	**3.6**

TABLE 3.1: Our pre-observation targets selected based on their luminosity, redshift and visibility. $t_{H\beta}(1+z)$ is the expected observed-frame lag derived from the Bentz et al. (2013) $t_{\rm rest} - L_{5100}$ relation, where L_{5100} is estimated from the SDSS spectrum. We quote the length of time each target is visible and the baseline of the observations in units of days and expected observed-frame lag.

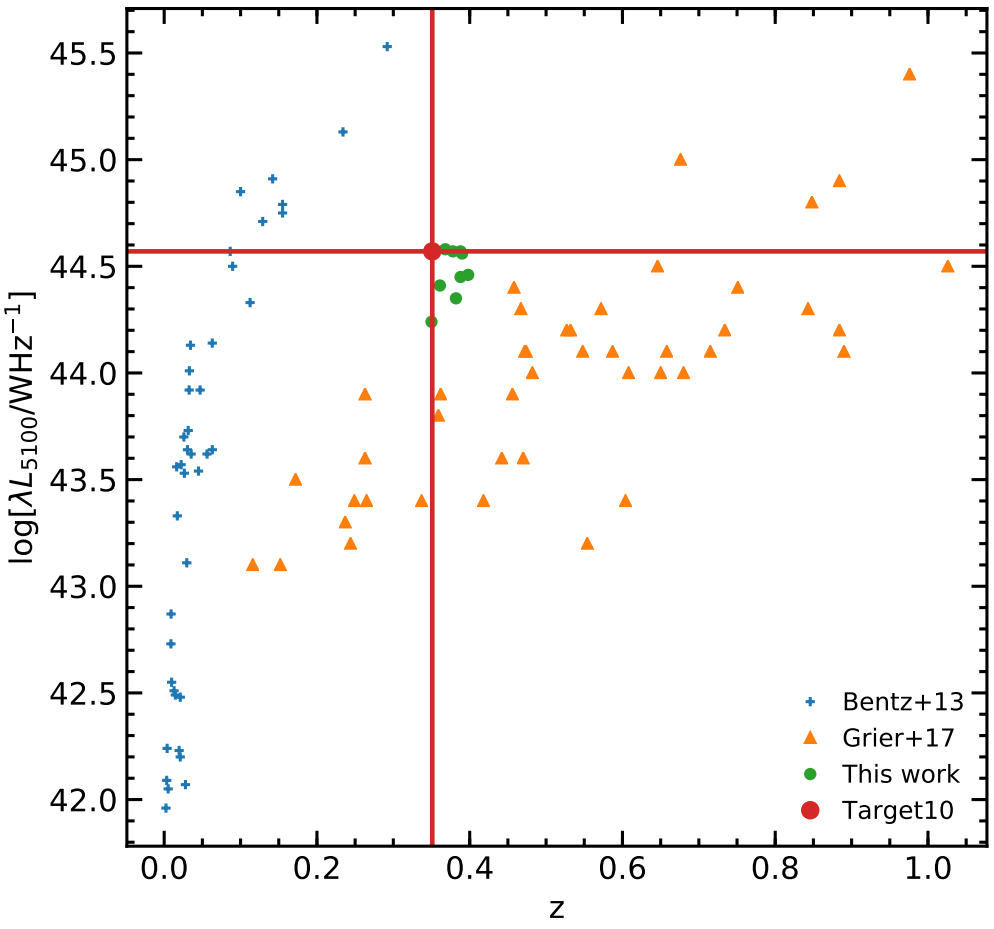

FIGURE 3.1: The distribution of luminosity versus redshift for the Bentz et al. (2013) sample, shown in blue, and the Grier et al. (2017) sample, shown in orange. Our dataset is shown in green with Target-10, highlighted with red lines, between the two datasets.

3.2.2 Observations

Since the expected continuum variability of QSOs is of order 10-70 per cent (Kaspi et al., 2007), we conservatively derive *i*-band exposure times, assuming an SNR > 20 (e.g. Bentz et al., 2013; Shen et al., 2015a) and seeing < 2 arcseconds, of 88s. This exposure time was calculated for our faintest target and so the SNR for the rest of our targets will be larger. Using the SDSS BOSS (Dawson et al., 2013) spectral observations of our targets (shown in Fig 3.2) we detect no bright spectral features that would interfere with our ability to measure the continuum accurately. We use the region between 6820 Å and 6960 Å to determine the median rest-frame L_{5100} in order to compare with other QSOs on the $L - t_{H\beta}$ diagram. This region is located in the wings of

the SDSS *i*-band filter that we used to measure the continuum variability. We do not expect any biases to arise from the difference between the luminosity used to measure the continuum variability and that used to measure the mean brightness of the QSO since the continuum is relatively flat between the regions in question. Accounting for the large equivalent widths of the Hβ lines and our experience of narrow-band imaging with the Isaac Newton Telescope (Smith and Jarvis, 2007), we use a 600s integration time for broad-line (i.e. narrow-band) observations to achieve SNR > 20 for all sources.

Our targets span a range of redshifts between 0.350 and 0.398. Therefore, for each source, we use the appropriate Hα photometric filter for which the redshifted Hβ line dominates. For Target-10, we use the Hα-6566Å narrow-band filter.

As seen in Table 3.1, we obtain the largest number of acceptable exposures with `SDSS J144645.44 +625304.0` (referred to as Target-10 hereafter). Indeed, Target-10 is the only QSO for which we have obtained a baseline of observations longer than the recommended $3t_{H\beta}(1+z)$ needed to recover a lag. Thus, in what follows, we only discuss the analysis of Target-10 and defer the rest to a future work.

3.2.3 Ensemble Photometry and Flux Calibration

In order to estimate lags between the broad-line region and the continuum-emitting region of the QSO, we must first calibrate the *i*-band and Hα photometric magnitudes to a common magnitude system. We are then required to calibrate our *i*-band photometry using the known SDSS DR12 AB magnitudes of sources in the observed field. We calibrate Hα photometry by propagating available SDSS spectra through the transmission curve for the same narrow-band Hα filter (6566 Å) used to observe the Hβ line in Target-10, accounting for the fibre aperture.

We perform aperture photometry using `Source Extractor` (Bertin and Arnouts, 1996) to estimate Petrosian magnitudes (Petrosian, 1976; Graham et al., 2005) for each detected source in the field for both *i*-band and Hα exposures. We use Petrosian magnitudes in order to calibrate each exposure to the SDSS catalogue and to easily avoid the effects of differing seeing between our observations without modelling the PSF. We consider only those sources which have SDSS CLEAN=TRUE and `Source Extractor` FLAGS= 0 for use as reference sources. We can then apply a similar ensemble photometry method to that detailed by Honeycutt (1992),

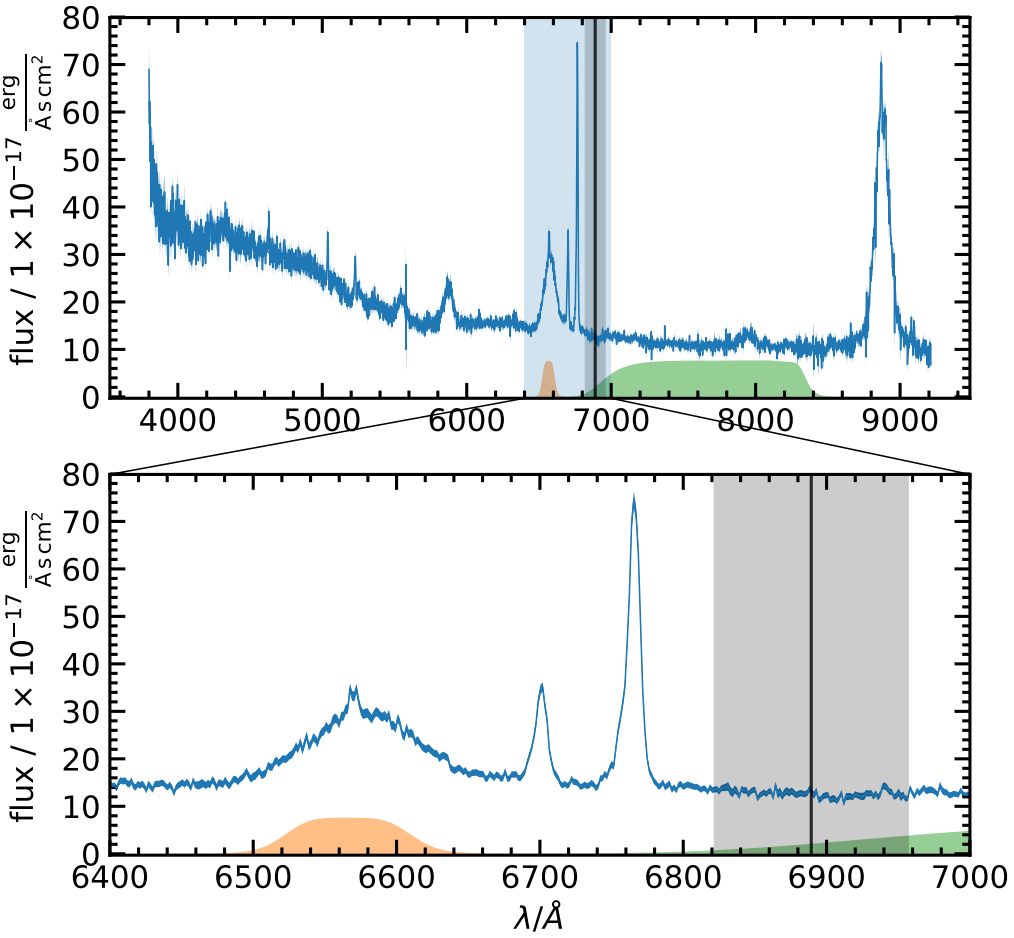

FIGURE 3.2: The SDSS-BOSS spectrum for Target-10. The transmission curve for the Hα filter used to measure the flux contained within the Hβ line is shown in orange and the SDSS i-band filter is shown in green. The region between 6820 Å and 6960 Å used to determine the median rest-frame L_{5100} for the SDSS spectrum is shown in grey. **Top:** The whole spectrum. **Bottom:** The region between 6400 and 7000 Å which contains both the broad Hβ line and the region used to measure the rest-frame L_{5100}

on the i-band exposures and calibrate those instrumental magnitudes to the SDSS absolute AB magnitude system.

To further improve our set of reference sources, we perform a number of checks. First, we perform the same aperture photometry extraction using `Source Extractor` that we used on our own i-band exposures on the SDSS i-band exposures that contain the candidate reference sources. If the Petrosian magnitude extracted from SDSS exposures by `Source Extractor` does not agree with the Petrosian magnitude quoted in the SDSS DR12 catalogue to within 0.05 mag, then we discard the source. This leaves the sources depicted in green in Fig 3.3. Ideally, we

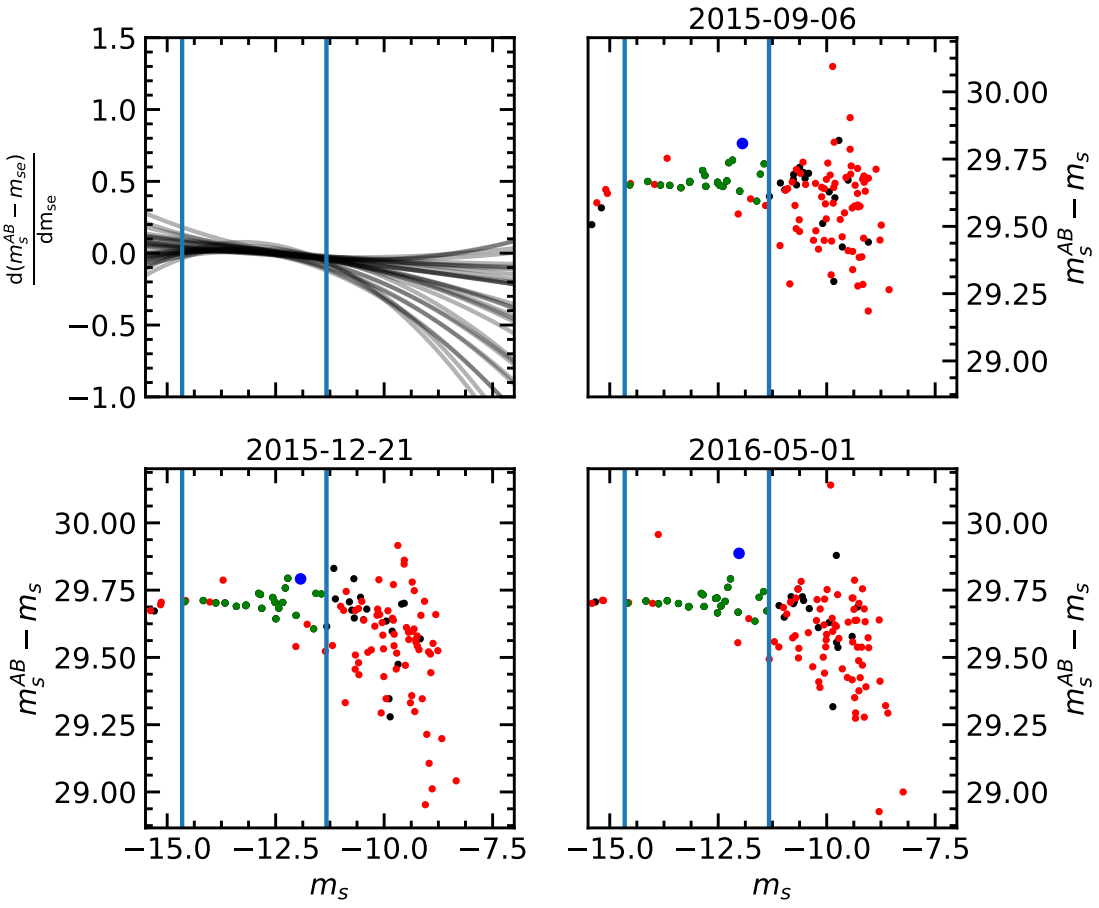

FIGURE 3.3: The selection of acceptable reference sources for Target-10 in the *i*-band. **Top left:** The derivative of the splines that were fit to the difference between SDSS AB Petrosian magnitude, m_{AB}, and `Source Extractor` instrumental Petrosian magnitude, m_s, for each exposure. **Other quadrants:** a sample of 3 exposures are shown in the other 3 quadrants of this figure. The region where the gradient of all splines is less than 0.05 mag, where acceptable sources can be found, is bounded by two vertical lines. All sources plotted here have SDSS CLEAN=TRUE & `Source Extractor` FLAGS= 0. Those sources whose extracted Petrosian magnitude extracted from the SDSS calibrated images is the same (not the same) as that extracted from the same image using `Source Extractor`, to within 0.05 mag, are shown in black (red). Those sources which are accepted for use as reference sources by spline fitting (see section 3.2.3) are shown in green. Target-10 is shown in blue.

would fit a single value of $m_s^{AB} - m_s$ across all instrumental magnitudes m_s to measure the *i*-band zeropoint. However, as shown for the three example exposures in Fig 3.3, the IO:O CCD can become saturated for many bright sources and faint sources are noisy. This results in non-linearity at both high and low magnitudes. We therefore employ a spline-based technique to select a contiguous range of `Source Extractor` magnitudes containing "well-behaved" sources, where we can fit a single flat *i*-band zeropoint. We fit a spline to $m_s^{AB} - m_s$ against m_s and find the range in which the gradient of the spline is 0 ± 0.05 mag. This range corresponds to the region where aperture photometry is the least affected by saturation and noise, and is shown in the first quadrant of Fig 3.3. We then select those candidate reference sources which have instrumental

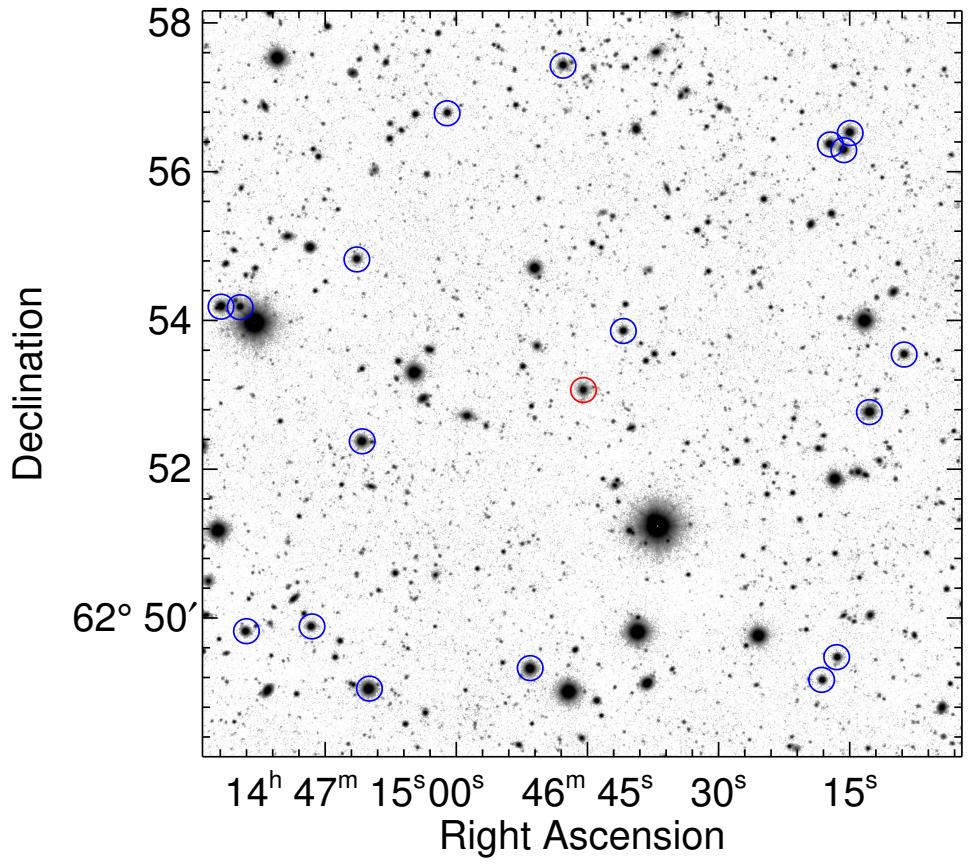

FIGURE 3.4: Stacked *i*-band exposures for Target-10. The QSO is circled in red and its accepted references are circled in blue.

magnitudes within that range. These sources, along with Target-10, are highlighted in Fig 3.4 and Fig 3.5.

In order to estimate the exposure zeropoints and their uncertainties to the greatest accuracy, we employ an ensemble photometry technique similar to Honeycutt (1992). We start out by fitting the instrumental magnitudes to SDSS AB magnitudes whilst also fitting a mean instrumental magnitude, $\hat{m}_r$, assuming that our reference sources are non-variable. This results in a log-likelihood given by

$$\ln \mathscr{L} \propto \sum_{e=1}^{N_e} \sum_{r=1}^{N_r} (m_{er} + \hat{z}_e - \hat{m}_r)^2 w_{er} + \sum_{r=1}^{N_r} \left(\frac{\hat{m}_r - m_r^{AB}}{\sigma_r^{AB}} \right)^2 \tag{3.2}$$

where m_{er} is the instrumental magnitude for reference source r in exposure e with weighting w_{er}, $\hat{m}_r$ is the magnitude of reference source r assuming that it does not vary over the course of observations, $\hat{z}_e$ is the zeropoint for exposure e, and m_r^{AB} is the AB magnitude of reference source r as measured by SDSS with its associated uncertainty σ_r^{AB}. We begin the fitting procedure by

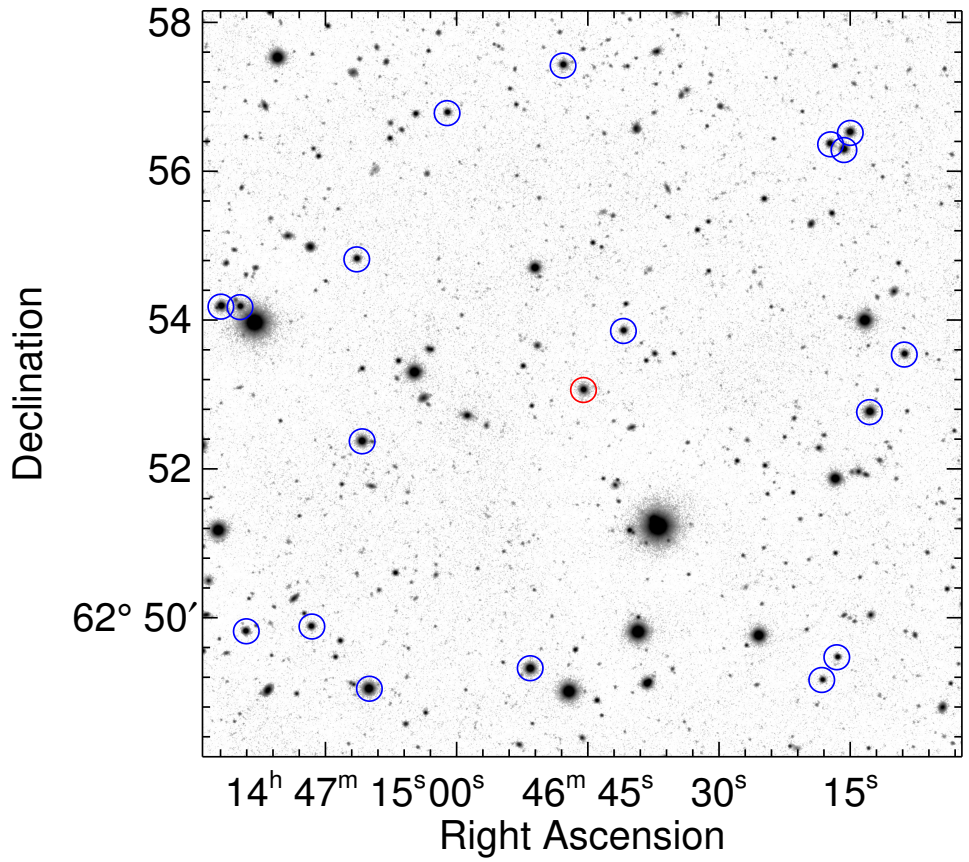

FIGURE 3.5: Stacked Hα exposures for Target-10. The QSO is circled in red and its accepted references are circled in blue.

setting the weight w_{er} for each reference source at each exposure to the instrumental magnitude uncertainty given by `Source Extractor`, $1/\sigma_{er}^2$. We then fit the quantities $\hat{m}_r$ and $\hat{z}_e$ using EMCEE (Foreman-Mackey et al., 2013) with 20 walkers until chain convergence is observed.

Some reference sources may indeed vary over the course of our observations. In addition, the instrumental uncertainty from `Source Extractor` may be underestimated by some factor. In order to reduce the offset to the zeropoint caused by the inclusion of varying sources, we scale the initial weighting by its probability in a fit Student-T distribution:

$$w_{er} \rightarrow \frac{p_{er}}{\sigma_{er}^2},$$
$$p_{er} = T(m_{er} - \hat{m}_r | \hat{\mu} = 0, \hat{\lambda}, \hat{\nu}) \tag{3.3}$$

where the inverse scale parameter, $\hat{\lambda}$, and number of degrees of freedom, $\hat{\nu}$, are both fit to the distribution of $m_{er} - \hat{m}_r$ assuming a mean of $\hat{\mu} = 0$. The Student-T distribution fit to the distribution of deviations of the instrumental magnitudes from their estimated mean (i.e. the

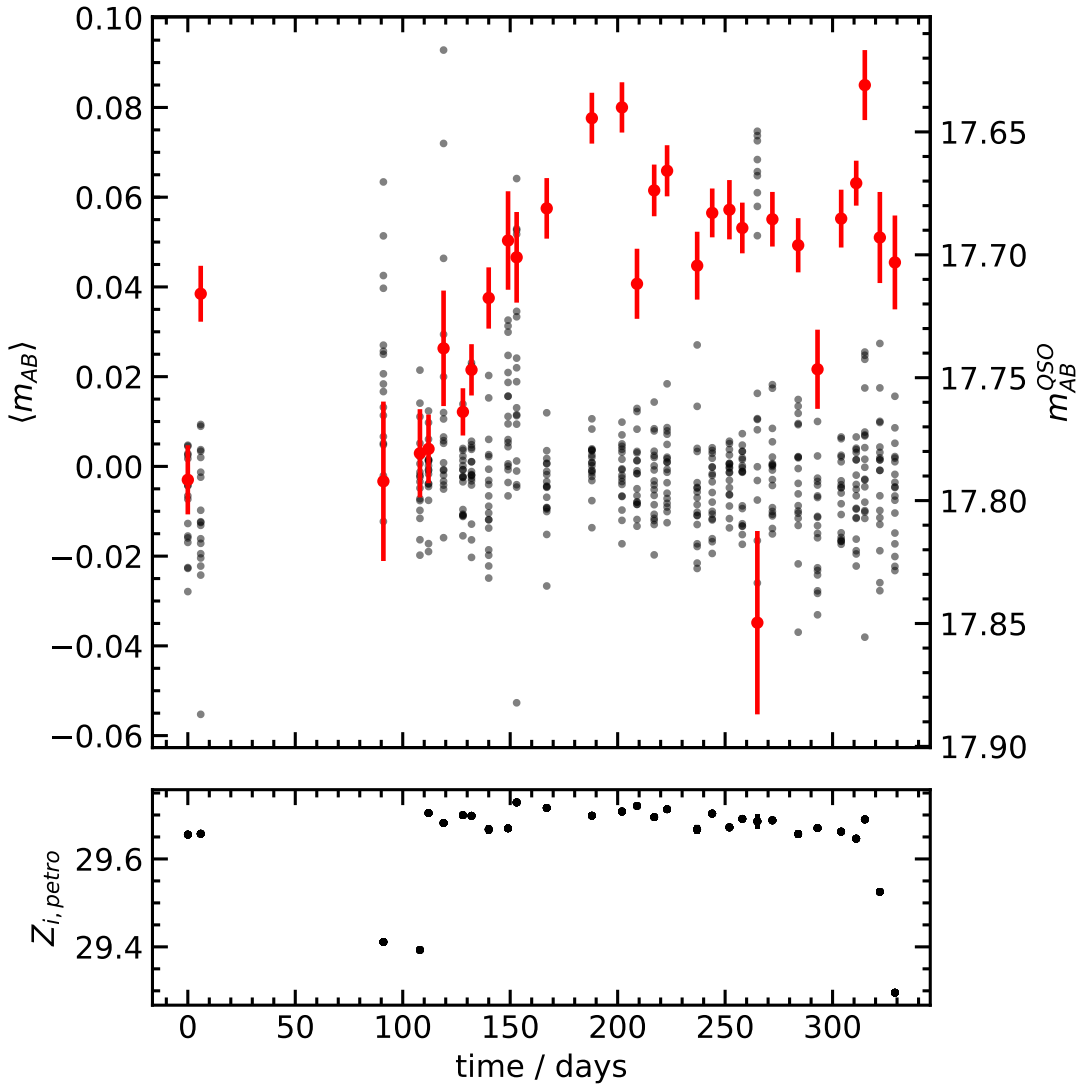

FIGURE 3.6: **Top:** The light curve for Target-10 is shown in red with its calibrated *i*-band AB magnitudes labelled on the right axis. The deviation from the mean magnitude for each of the reference sources for Target-10 *i*-band are also shown on the left axis. **Bottom:** The *i*-band AB zeropoint for each exposure calibrated to SDSS magnitudes using the Petrosian aperture.

distribution of the values of the black points in Fig 3.6), will update the weighting of each magnitude in each exposure and therefore assign very low weighting to sources which have larger variability over the course of our observations than others. We iteratively run this re-weighting procedure until each flux measurement in the light curve of the target QSO no longer changes within a tolerance of 0.001 mag. This typically takes 3-5 runs of MCMC inference, updating the weighting each time.

3.2.4 Light-curve Calibration

Fig 3.6 shows the resultant light curve for Target-10 in the *i*-band along with the deviation from the mean magnitude for its reference sources. The average uncertainty for the AB magnitudes for Target-10 is about 0.015 mag with the largest being 0.200 mag. The *i*-band magnitudes for Target-10 therefore have signal-to-noise ratio of between 25 and 120, exceeding than the necessary SNR$>$ 20 recommended by Bentz et al. (2013) and Shen et al. (2015a) to achieve reliable lags.

The SDSS DR12 catalogue lacks Hα photometry and our observed fields contain few sources for which SDSS has spectra (only one of which is not a QSO). Therefore, it is necessary to calibrate our Hα exposures to the magnitudes obtained from propagating SDSS spectra through IO:O Hα photometric filters. We derive zeropoints, relative to the "best" exposure (i.e. the exposure with the highest mean SNR for spectroscopic reference sources), for each of the Hα exposures by using the same ensemble photometry method detailed above. We make use of the SDSS spectroscopic catalogue to identify potential reference sources but find only one such source ($\alpha_{J2000} = 14^h46^m37^s, \delta_{J2000} = +62^\circ57'36''$) observed by the Baryon Oscillation Spectroscopic Survey (BOSS) spectrograph (Dawson et al., 2013).

Our calibration depends upon the accurate measurement of the reference's flux within the Hα filter. Given that we find that the source is resolved into two components as shown in Fig 3.7, the effect of seeing and aperture corrections cannot be neglected. We first fit a model consisting of two Gaussians to our best Hα exposure, then transform the model to the same seeing as the BOSS observation, and finally extract the flux contained within the BOSS 2 arcsecond aperture. The difference between the ensemble calibrated instrumental magnitude we obtain for our best exposure and the propagated BOSS spectrum is taken as our zeropoint, accounting for uncertainties in both magnitudes.

Fig 3.8 shows the the resultant light curve for Target-10 in the Hα waveband along with the deviation from the mean magnitude for its references sources. Due to the necessary intermediate step of calibrating differential magnitudes to the AB magnitude system via the spectral reference source at $\alpha_{J2000} = 14^h46^m37^s, \delta_{J2000} = +62^\circ57'36''$, the signal-to-noise ratio of the Hα magnitudes is unsurprisingly smaller than those in the *i*-band. We measure signal-to-noise ratios for the Hα fluxes of Target-10 range between 19.5 and 80.0.

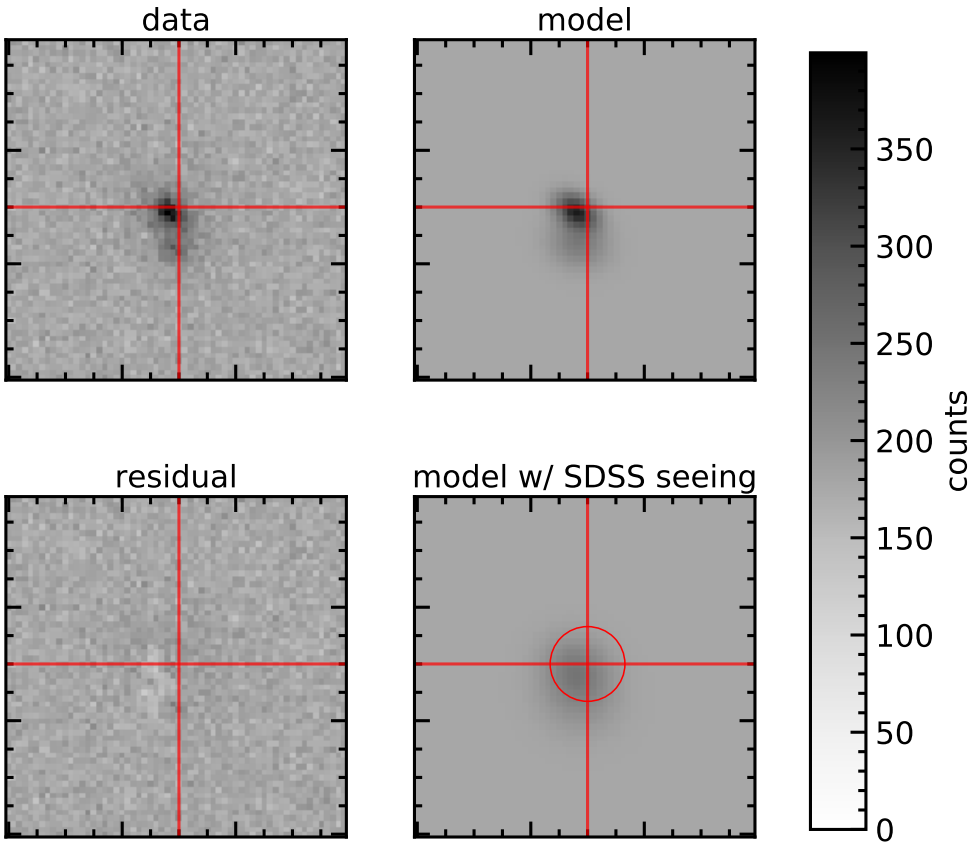

FIGURE 3.7: Modelling the spectral reference source at $\alpha_{J2000} = 14^h46^m37^s, \delta_{J2000} = +62°57'36''$ in Hα photometry. **Top left:** Our original exposure of the spectral reference source in Hα. **Top right:** The model of the spectral reference source using two Gaussian components and a background. **Bottom left:** The residuals from our two component model. **Bottom right:** The model convolved to the SDSS seeing for the spectrum observation using a difference-of-two-Gaussians kernel. Overplotted in red crosshairs is the location of the centre of the 2 arcsecond BOSS aperture and the aperture is shown in the bottom right panel.

The zeropoint for both i-band and Hα exposures can change by about 0.4 mag and the exposures where this occurs are the ones the highest uncertainty for the QSO magnitude. Upon inspection, it is clear that these exposures have increased cloud cover or worse-than-normal seeing. Our ensemble calibration method above takes into account the instantaneous deviation of reference sources from their inferred mean magnitudes and updates their weightings accordingly. We therefore do not exclude these exposures from further analysis.

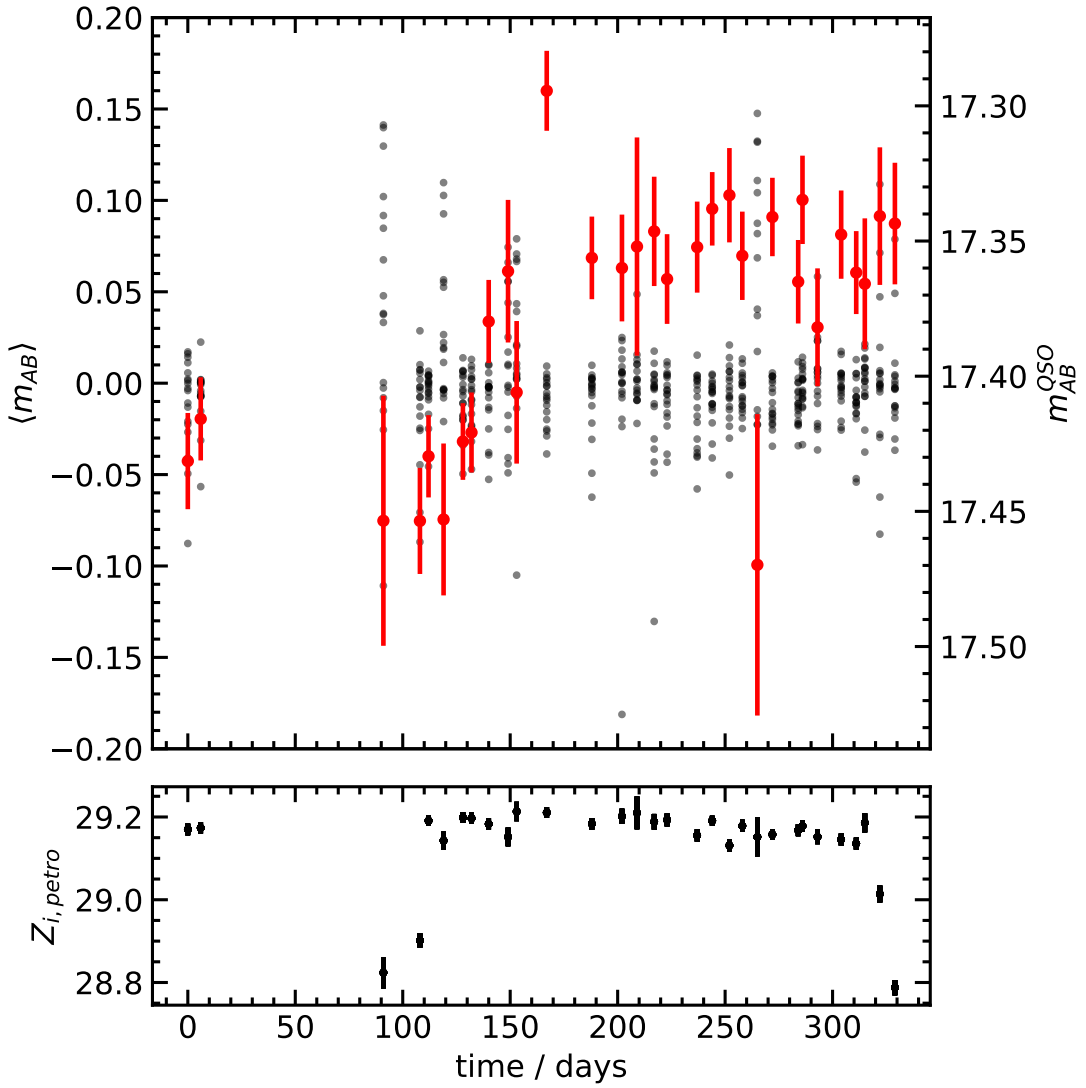

FIGURE 3.8: **Top:** The light curve for Target-10 is shown in red with its calibrated Hα AB magnitudes labelled on the right axis. The deviation from the mean magnitude for each of the reference sources for Target-10 Hα are also shown on the left axis. **Bottom:** The Hα AB zeropoint for each exposure calibrated to SDSS magnitudes using the Petrosian aperture.

3.2.5 `Javelin` reliability simulations

`Javelin` (Zu et al., 2013) can be used to model quasar variability with either spectroscopic (Zu et al., 2011) or purely photometric measurements (Zu et al., 2016). `Javelin` models the QSO continuum variability as a damped random walk (DRW). A random walk is defined such that the value of a data point in a time-series is only dependent on the previous state (i.e. a Markov chain). A damped random walk is the only "memory-less" Gaussian process and each step is generated by sampling from a Gaussian distribution, whose variance depends on the distance

between the previous state and the next state:

$$f_i = \alpha f_{i-1} + \varepsilon_i, \tag{3.4}$$

$$\alpha = e^{-|t_i - t_{i-1}|/\tau}, \tag{3.5}$$

$$\varepsilon \sim \mathcal{N}(\mu = 0, \Sigma = \sigma^2[1 - 2|t_i - t_{i-1}|/\tau]), \tag{3.6}$$

where f_i is the next flux to be generated at time t_i, τ is the time scale of the variability and σ is its amplitude. The damped random walk is therefore characterised by the exponential covariance kernel $S(\Delta t) = \sigma^2 e^{-|\Delta t/\tau|}$ and so on average, the light-curve of a pure DRW will always vary around a mean value.

`Javelin` supports a number of random walk covariance kernels which control the strength of the correlation between any two flux observations given the time between them. Zu et al. (2013) finds that the exponential covariance kernel is appropriate on time scales, τ, between months and years, and we therefore adopt their recommendation. Below a time scale of a few months, the correlation becomes stronger than can be accounted for by the exponential covariance kernel (Mushotzky et al., 2011; Zu et al., 2013). Since we have selected our targets to have expected lags – inferred from the lag-luminosity relation (Bentz et al., 2013) – in excess of 40 days, we deem the exponential covariance kernel appropriate for our targets.

Before modelling the QSO variablility of Target-10, we run a suite of simulations to ensure that `Javelin` can reliably recover lags given the noise properties of the Target-10 light curves and their cadence. This allows us to estimate the degree to which we can trust `Javelin` parameter estimations for a given QSO target and will reveal the nature of any artefacts which can occur due to the cadence of the input light curve. We perform such analysis with 151 200 simulated light curves constructed by varying the DRW parameters and noise level, for a given target's cadence.

The DRW model generates a continuum light curve from the random walk amplitude, σ and time-scale, τ, as shown in the upper panel of Fig 3.9. The resultant light curve is then smoothed with a top hat window of width w and scaled by line scale s to produce an emission line light curve, shown in the middle panel of Fig 3.9. To generate the mixture of line and continuum emission seen through a photometric filter, `Javelin` scales the continuum light curve by a continuum scale α and adds the resultant continuum to the emission line, as shown in the lower panel of Fig 3.9. The observations are then taken at the same cadence as that of Target-10 and

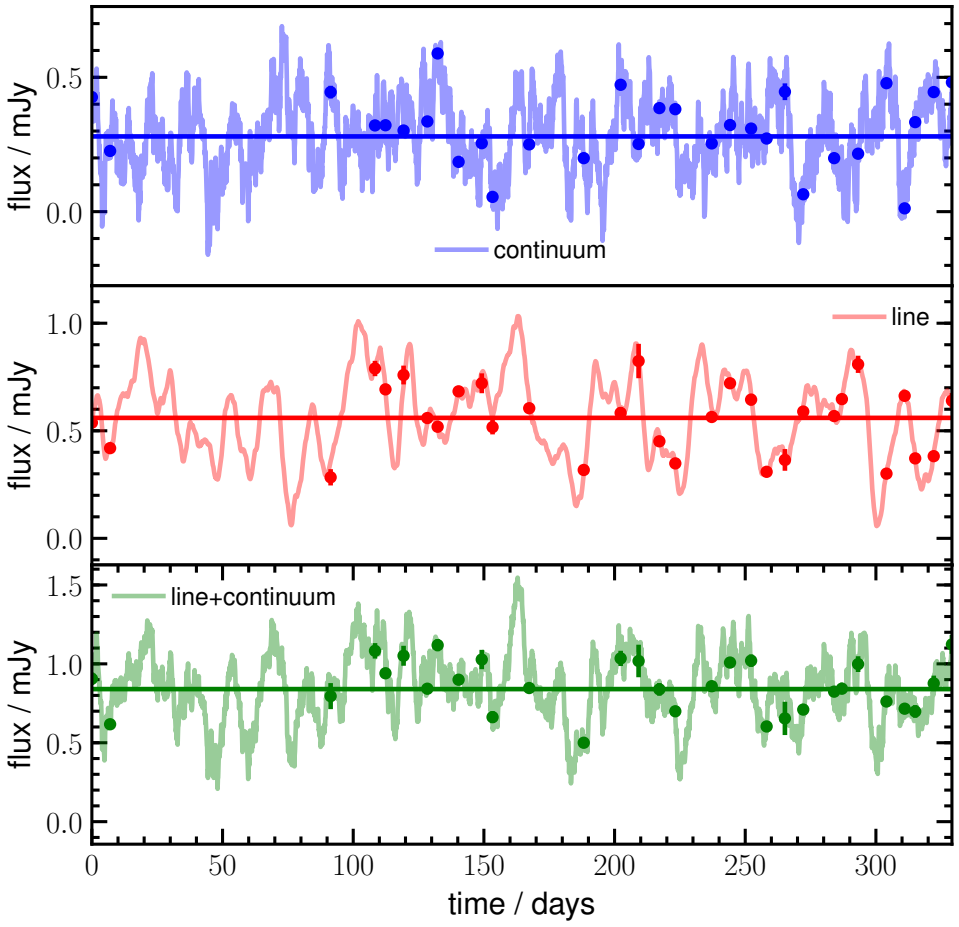

FIGURE 3.9: One of the 151 200 light curves generated from a grid of `Javelin` parameters based on Target-10. The continuum, pure line, and line with continuum light curves are shown in blue, red, and green respectively. The lines depict the intrinsic light curve generated by the simulated QSO using the damped random walk covariance kernel. The noisy observations, with the same signal-to-noise ratio as the calibrated Target-10 light curves are shown as points. The mean flux of each of the light curves is shown as a horizontal line.

assuming the same signal-to-noise (shown as dots in Fig 3.9). In order to test how dependent the lag estimate is upon the zeropoint obtained from the spectral reference calibration source, we also scale the resultant continuum+line light curve by a zeropoint offset between -0.4 and +0.4 mag, bringing the total number of parameters in our grid of simulations to 7. For Target-10, we use the ranges of parameters, guided by the posterior distribution for the `Javelin` fit to the Target-10 continuum, detailed in Table 3.2.

For each of these light curves, we run the following analysis to derive the best estimate for the lag. First, we infer the DRW parameters (amplitude, σ, and time-scale τ) of the *i*-band

parameter	lower value	upper value	N
$\log(t_{lag})$	1	2.5	10
$\log\sigma$	-2	-1.8	3
$\log\tau$	0.75	1.75	3
w	0.5	13	4
s	0.1	1.5	5
α	0.8	1.4	3
σ_z	-0.4	0.4	7
random seed	–	–	4

TABLE 3.2: The parameter ranges, on a linearly spaced grid, that create the simulated light curves for Target10. Each set of parameters was run 4 times with a different, pre-selected, random seed from which to generate the noisy light curves.

continuum with 200 walkers. We use the output probability distributions as a prior for the lag estimation using both i-band and Hβ light curves. We run `Javelin` with the default settings of a logarithmic prior which begins to penalise lag values larger than a third of the observation baseline, and a hard limit on lags longer than the baseline itself. MCMC chains must have converged before any reliable parameter estimation can be performed. The model is run until convergence is achieved, whereby MCMC is halted when the autocorrelation time for all parameters changes less than 1 per cent and the number of iterations is larger than 50 times the largest autocorrelation time estimate, as recommended by Foreman-Mackey et al. (2013)[1].

This analysis results in a large hyper-volume of probability distributions which we can marginalise over to give us the accuracy of lag estimates as a function of known input lags.

Due to the presence of more than one strong peak in the lag probability distributions, taking the median of an MCMC chain array may result in the parameter estimate being located in an area of low probability, between peaks, and not near a region of high probability. Therefore, any quoted estimate and its uncertainty could be misleading. We choose not to identify the primary peak by eye, but use a mode-finding method to identify the most probable solution within the highest-posterior-density (HPD) credible interval. The HPD interval is the narrowest interval that is guaranteed to contain the mode of the distribution. We fit a kernel-density-estimate (KDE) using the `FastKDE` (O'Brien et al., 2014, 2016) algorithm which calculates the kernel's parameters objectively (i.e. the hyper-parameters are informed entirely by the data and therefore it does not require user specification of bin width or kernel bandwidth), and choose the maximum value of that resultant KDE to be our best estimate for the `Javelin` parameters.

[1] `http://emcee.readthedocs.io/en/latest/user/autocorr/`

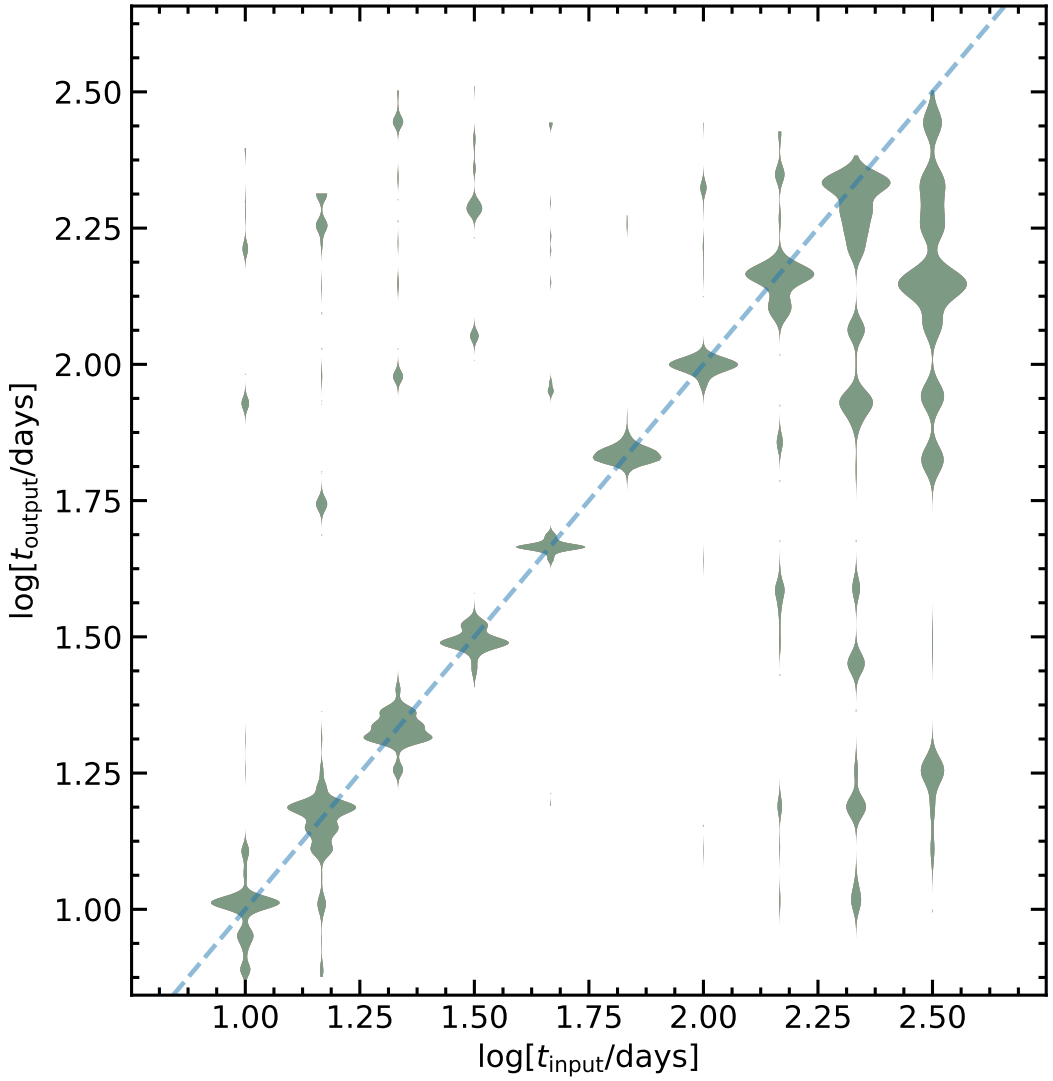

FIGURE 3.10: The comparison of input and output time lags for the simulated light curves. The violins at each input lag depict the distribution of `Javelin` best estimate lags, with their width indicating number density. These best estimates are determined by the KDE procedure described in Section 3.3.1. The 1:1 relation indicating perfect recovery of input lags is shown as the dashed line.

Fig 3.10 shows the distributions of the KDE best estimate of the Hβ lag based on the output `Javelin` probability distributions. The first observation we can make is that we can recover the lag to within 4 per cent as long as the input lag is below 145 days, given our observing campaign (of duration 330 days). Given that `Javelin` starts to penalise lag values larger than a third of the observation baseline it is perhaps not surprising that lags starting to approach the total length of the baseline itself are not as reliably recovered as those below a third of that length. We also observe that there are a number of hyperparameter combinations whose recovered lags are incorrect by $>$ 100 days. This occurs for combinations at all input lags and so we should not be surprised by spurious peaks in the probability distribution for Target-10 at higher lags. At all

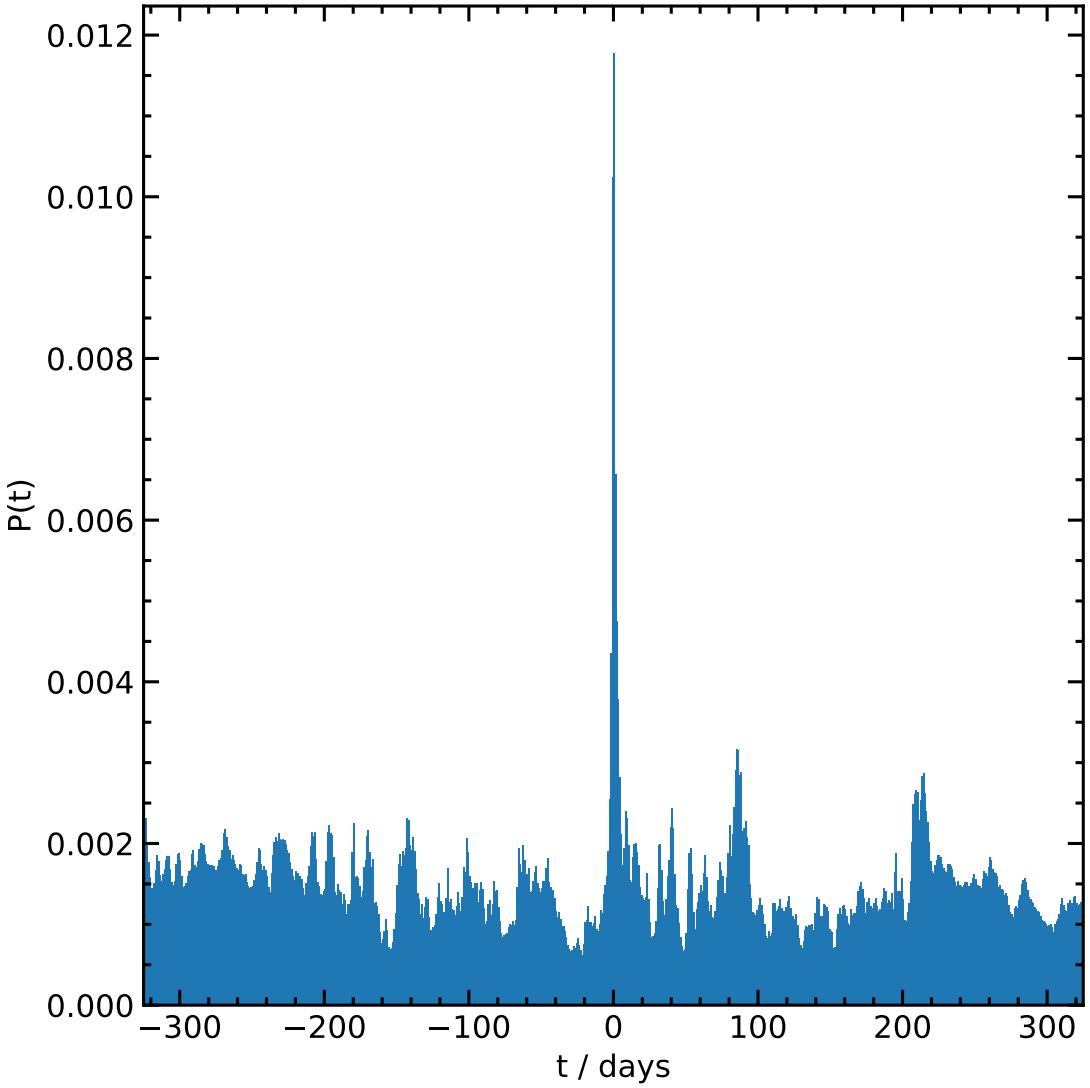

FIGURE 3.11: The median stacked lag probability distributions of all simulated light curves of lags between 10 and 316 days. The median stack shows only the spurious output values from the `Javelin`. The large peak particularly around 0-14 days can be attributed to the effects of cadence.

input lags, we find artificial (i.e. incorrect) peaks at negative lags and so we can be justified in disregarding the peaks below -100 days.

We find that there is always a large peak at around 0-14 days, which coincides with the average cadence of observations (14 days). This can be seen in Fig 3.11, where the distribution of artefacts resulting from fitting with `Javelin` contains a substantial peak at 0-14 days. We therefore attribute any peak seen at around this region to the artificial effect of cadence upon the `Javelin` fitting procedure.

The KDE method allows us to assess the most likely peak without referring to the unstable

maximum likelihood point, but it also implies a large uncertainty on the lag given that there are other regions of high probability which cannot be ruled out a priori. We can address the issue in three ways:

1. Use the output lag distribution for our reliability simulations to mitigate the effect of non-linear artefacts that arise from the `Javelin` fitting process.
2. Apply a prior to the lag distribution based on previous lag and luminosity measurements, and established relations i.e. (Bentz et al., 2013).
3. Limit analysis to the range of lags bounded by the minima surrounding the tallest peak.

We perform the only the first and the last steps detailed above since we want our lag measurement to inform the $t_{\rm rest} - L_{5100}$ relation, which cannot be done independently if our measurement is a result of an application of a prior based on the same relation.

3.3 Results

3.3.1 Lag estimation for Target-10

We perform the same `Javelin` fitting procedure for Target-10 as we did for our simulated light curves. Fig 3.12 shows the posterior predictive distribution for the observed light curves of Target-10 based on the burnt-in chain (i.e. with the first 1000 steps for the MCMC chain removed). The Hα predictive posterior light curve is the linear combination of continuum and emission line light curves where the emission line flux is only a fraction of the continuum. Manually identifying the time delay between them will be difficult.

In addition, the distribution of Hβ lags contains more than one convincing (SNR > 3) peak. However, since we have constructed a large suite of simulated light curves over a large range of DRW parameters, we can estimate the distribution of lag artefacts that results only from the `Javelin` fitting process and the properties of our data. We can then use the distribution to inform us as to which peak is the "real" one. First, we generate a set of simulated light curves (see Section 3.2.5) whose true lags fall within the dashed region shown in Fig 3.13 between 40 - 125 days and run `Javelin` to return the posterior lag distribution. This creates a distribution of lags without a peak corresponding to the true input lag, since the median at any point will suppress

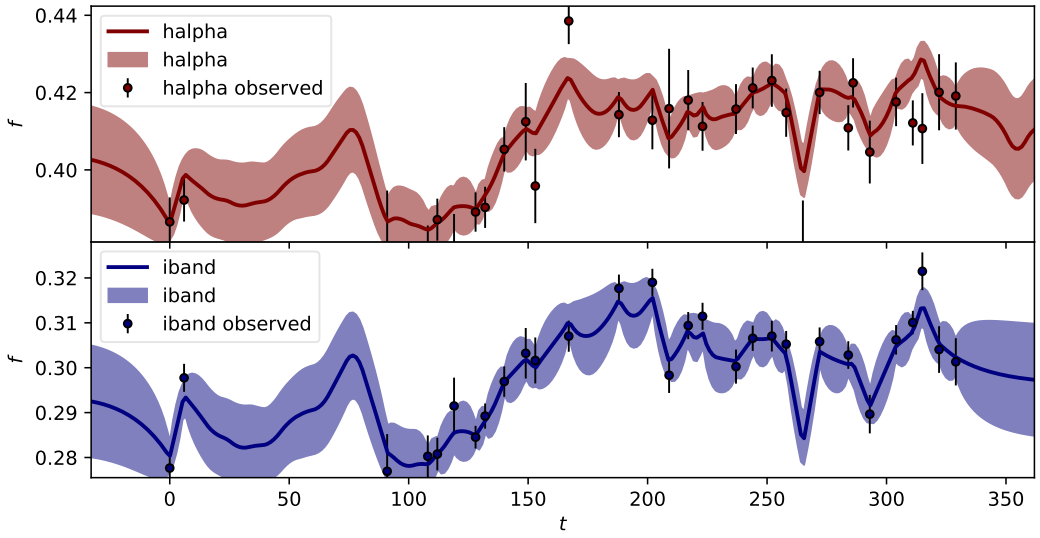

FIGURE 3.12: The posterior predictive light curves for Target-10 in mJy. **Top:** The redshifted Hα band light curve containing a mixture of Hβ line emission and continuum emission. **Bottom:** The *i*-band continuum emission. The shaded regions correspond to the 68 per cent density region covered by random draws from the `Javelin` posterior probability distribution. The black error bars denote the calibrated observations for each waveband.

such a peak. We scale the artefact distribution, an approximation of $1 - P(t_{H\beta})$, so that its median probability matches the median probability of the distribution of Target-10, $P(t_{H\beta} \mid \mathscr{D})$. Then we divide the Target-10 lag distribution by this artefact distribution, which has the effect of suppressing spurious peaks. The result is shown in Fig 3.13. There are some features of the artefact distribution that correspond to those found in the distribution for Target-10. In particular, the artefact peak at 63 days almost completely resolves the ambiguity of the double peak at 63 and 72 days for Target-10 by dramatically favouring the longer lag.

We partially follow the method of Grier et al. (2017) whereby we select the region bounded by the minima of the tallest peak (dashed lines in Fig 3.13) in the distribution that still contains artefacts. We then estimate the region of 68 per cent probability in the cases of artefact inclusion and deconvolution as shown in Fig 3.13. We recover an Hβ lag for Target-10 of 73^{+4}_{-13} days without taking into account any artefacts and an Hβ lag of 72^{+5}_{-1} days when we apply artefact deconvolution. Using a prior based on the fit $t - L_{5100}$ relation (Bentz et al., 2013) alone does not significantly favour either peak, at 63 and 72 days, over the other despite suppressing the PDF at very low and high lags. The best KDE estimate of the lag of Target-10 is consistent between both distributions but the uncertainty shrinks by a third when we use the artefact deconvolution method to simplify the posterior.

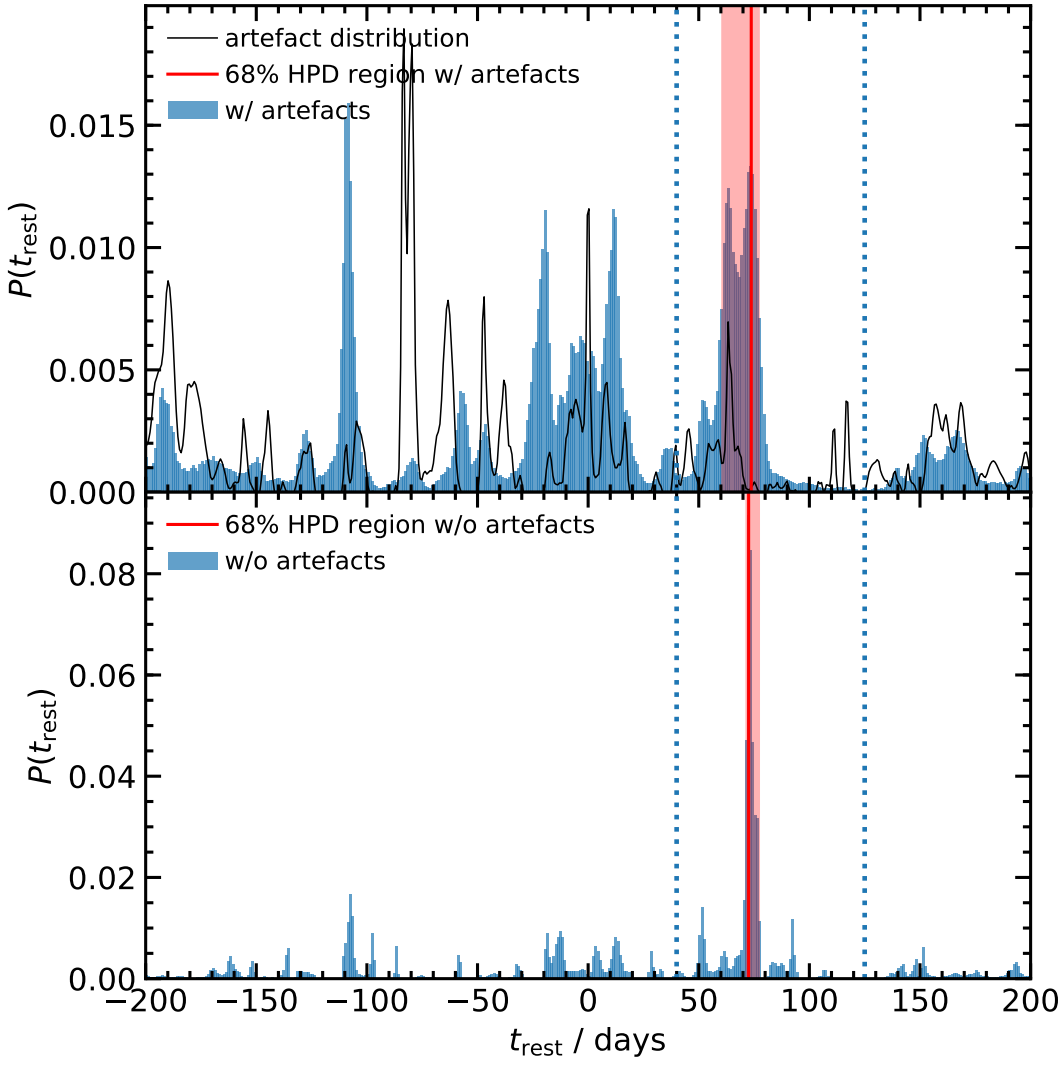

FIGURE 3.13: The probability distribution from `Javelin` for rest-frame lag of Target-10 before and after artefact deconvolution. **Top:** The full probability distribution for rest-frame lag as the blue histogram along with the artefact distribution in black derived from simulated light curves with rest-frame lags of 72 days. **Bottom:** The cleaned distribution of rest-frame lags for Target-10, where the artefact distribution is deconvolved from the output `Javelin` rest-frame lag distribution. The region marked by dashed lines indicates the region where we estimate the 68 per cent HPD interval (shaded red area), along with the mode (red line), which is determined by the position of the minima around the highest peak in the top panel (following the method performed by Grier et al. 2017).

3.3.2 Fits to the $t_{H\beta} - L_{5100}$ Relation

Using our derived time lag, we fit a power-law, with scatter, to the lag versus luminosity in linear space:

$$t'_{\rm rest}/1\,{\rm day} = 10^{K}[\lambda L_{\lambda}/10^{44}{\rm ergs}^{-1}]^{\alpha} \tag{3.7}$$

$$t_{\rm rest} \sim \mathcal{N}(\mu = t'_{\rm rest}, \sigma = t'_{\rm rest}\varepsilon) \tag{3.8}$$

where $t_{\rm rest}$ is the lag that would be observed without the effects of intrinsic scatter in the relation and $t'_{\rm rest}$ is the observed lag including that intrinsic scatter. The normal distribution is indicated as $\mathcal{N}$. Our fitting priors for the slope $\hat{\alpha}$, intercept $\hat{K}$, and scatter scale $\hat{\varepsilon}$ are:

$$\hat{\alpha} \sim \mathcal{N}(\mu = 0.5, \sigma = 0.75), \tag{3.9}$$

$$\hat{K} \sim {\rm Trunc.}\mathcal{N}(\mu = 1.5, \sigma = 1.0, a = 0, b = \infty), \tag{3.10}$$

$$\log[\hat{\varepsilon}] \sim \mathcal{N}(\mu = -2, \sigma = 1) \tag{3.11}$$

We do not fit a straight line in log space since the uncertainties in lag and luminosity along with the scatter are not strictly Gaussian in linear space and definitely not in log space. This subtlety may have a significant impact on the slope of the fit relation and therefore on its interpretation. We use this opportunity to test whether the correct treatment of non-Gaussian uncertainties makes a difference to resultant fit. We resample the uncertainty distributions of the lag estimations 1000 times per data point in order to fit the power law. In this way, we incorporate the probability distribution from `Javelin` naturally whilst also treating values from the literature correctly. We do not fit the power-law to the Grier et al. (2017) dataset since they reason that large selection effects due to limited monitoring cadence and duration may bias their lag measurements to lower values more so than the Bentz et al. (2013) sample. Instead, we use the Clean2+ExtCorr dataset from Bentz et al. (2013), which excludes two AGN due to potentially biased time lags and corrects the influence of internal extinction of one other. We recover the parameters listed in Table 3.3.

Fig 3.14 shows the fit lag-luminosity relation to the Bentz et al. (2013) Clean2+ExtCorr sample. There is no significant difference between the fits with and without Target-10 included. However, fitting in linear space produces a shallower relation (by ~ 0.013) than that of Bentz et al.

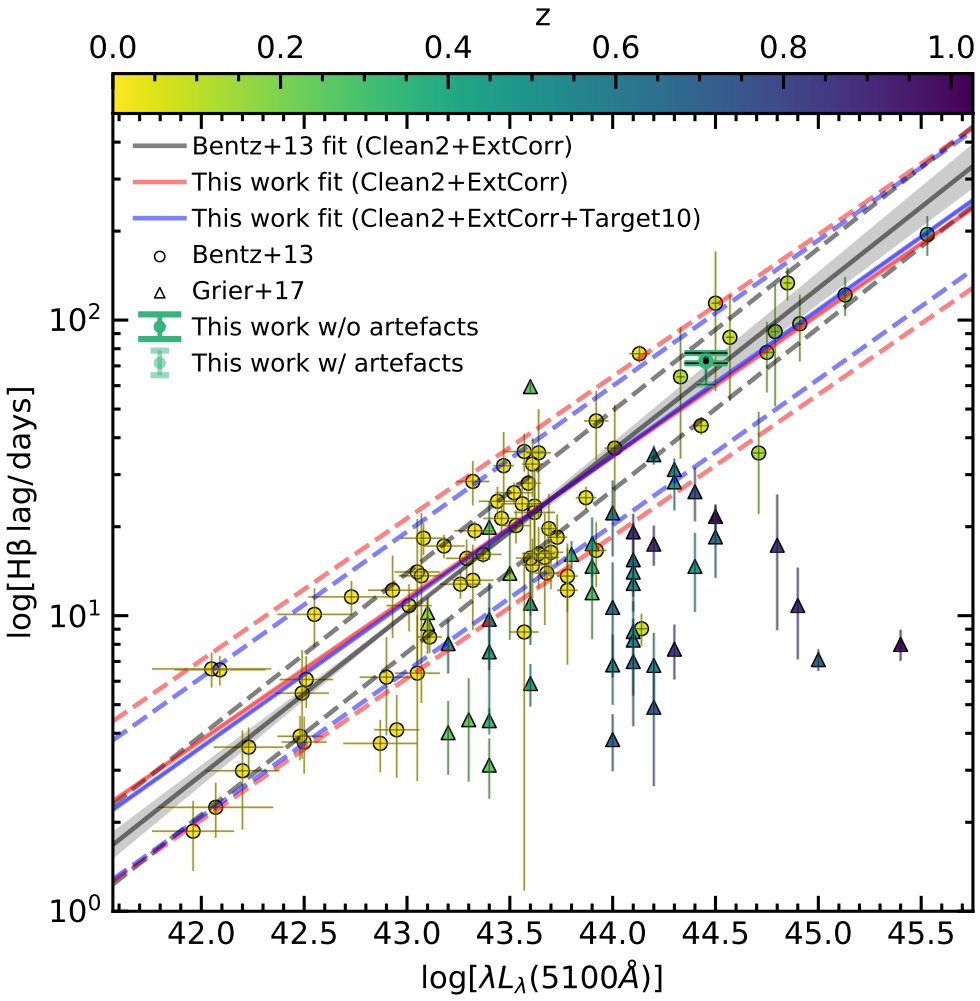

FIGURE 3.14: The rest-frame lag-luminosity relation shown for data from Bentz et al. (2013) (circles), Grier et al. (2017) (triangles), and Target-10. All points are coloured by redshift. The best estimate for the lag of Target-10 is shown as a bold green circle with and without the artefact deconvolution. The best fit line in log space to the Clean2+ExtCorr dataset by (Bentz et al., 2013) is shown in grey, the best fit line in linear space to the same data is shown in red. The best fit in linear space to the Clean2+ExtCorr dataset as well as Target-10 is shown in blue. The scatter estimated by MCMC in all best fit lines is indicated by dashed lines.

	$\hat{K}$	$\hat{\alpha}$	$\log[\hat{\varepsilon}]$
Clean2+ExtCorr+ Target10	$1.542^{+0.001}_{-0.002}$	$0.493^{+0.001}_{-0.001}$	$-0.542^{+0.005}_{-0.005}$
Clean2+ExtCorr	$1.539^{+0.001}_{-0.002}$	$0.480^{+0.001}_{-0.001}$	$-0.623^{+0.004}_{-0.005}$
Clean2+ExtCorr (Bentz+13)	1.559 ± 0.024	$0.549^{+0.028}_{-0.027}$	$\sim -1.016^{+0.169}_{-0.187}$

TABLE 3.3: Lag fit parameters for datasets with and without Target-10. The fit results from Bentz et al. (2013) are included but the scatter has been approximately converted to the power law model using $\varepsilon \approx 10^{\sigma} - 1$ for comparison.

	$\hat{K}$	$\hat{\alpha}$	$\log[\hat{\varepsilon}]$
Clean2+ExtCorr+ Target10	$8.048^{+0.002}_{-0.002}$	$0.535^{+0.001}_{-0.002}$	$-0.017^{+0.006}_{-0.004}$

TABLE 3.4: Mass fit parameters for datasets with Target-10.

(2013) and so, at extremes of luminosities, where there is a dearth of data, we find that our fit is significantly (2σ at 41.5 dex) different to the log-log straight line. Additionally, the uncertainty in our fit parameters is much reduced when compared to Bentz et al. (2013) and the scatter is larger (by about 0.5 dex). Our fit is compatible with that found in Bentz et al. (2013) in the well sampled regions. We also note that the impact of selection effects upon this and any fit of a t-L relation will be dependent on the cadence and duration of observations. This may go some way to explaining the seemingly excessive number of QSOs populating the space below the Bentz et al. (2013) data points. Furthermore, there may be an accretion rate dependency whereby the more fundamental relation is the plane of rest-frame lag, luminosity and accretion rate, as outlined by Du et al. (2016a). However, the explanatory power of this model is small for sources with the low accretion rates seen in the Grier et al. (2017) sample.

Propagating the posterior lag distribution for Target-10 through Equation 3.1, using the virial factor from Grier et al. (2013b) with a Gaussian distribution of $\langle f \rangle \sim \mathcal{N}(\mu = 4.3, \sigma = 1.1)$, we arrive at the distribution for black hole mass shown in Fig 3.15. The best estimates, with and without deconvolution of artefacts, for black hole mass are only separated by 0.01 dex.

Fig 3.16 shows the black-hole mass-luminosity relation for the Bentz et al. (2013) Hβ lags with line widths from the AGN Mass Catalogue (Bentz and Katz, 2015). The parameter fits for the mass-luminosity relation are detailed in Table 3.4. We find that Target-10 is in good agreement with the Bentz et al. (2013) Clean2+ExtCorr dataset.

We find that the scatter of the mass-luminosity relation (0.5 dex) is much larger than that of the lag-luminosity relation in log space. This is unsurprising since the former combines uncertainty from the virial factor $\langle f \rangle$ as well as the scatter in line widths shown in Fig 3.17, which shows the black hole mass against broad line velocity dispersion.

However, it is still useful to note that a black-hole mass predicted from the $t - L_{5100}$ relation can be wrong by more than 0.3 dex 50 per cent of the time[2].

[2]Calculated from the fit line in log-space (Figure 3.16) with a 1σ width of ~ 0.5 dex. $1 - P(-0.3 < t \leq +0.3) = 0.5$

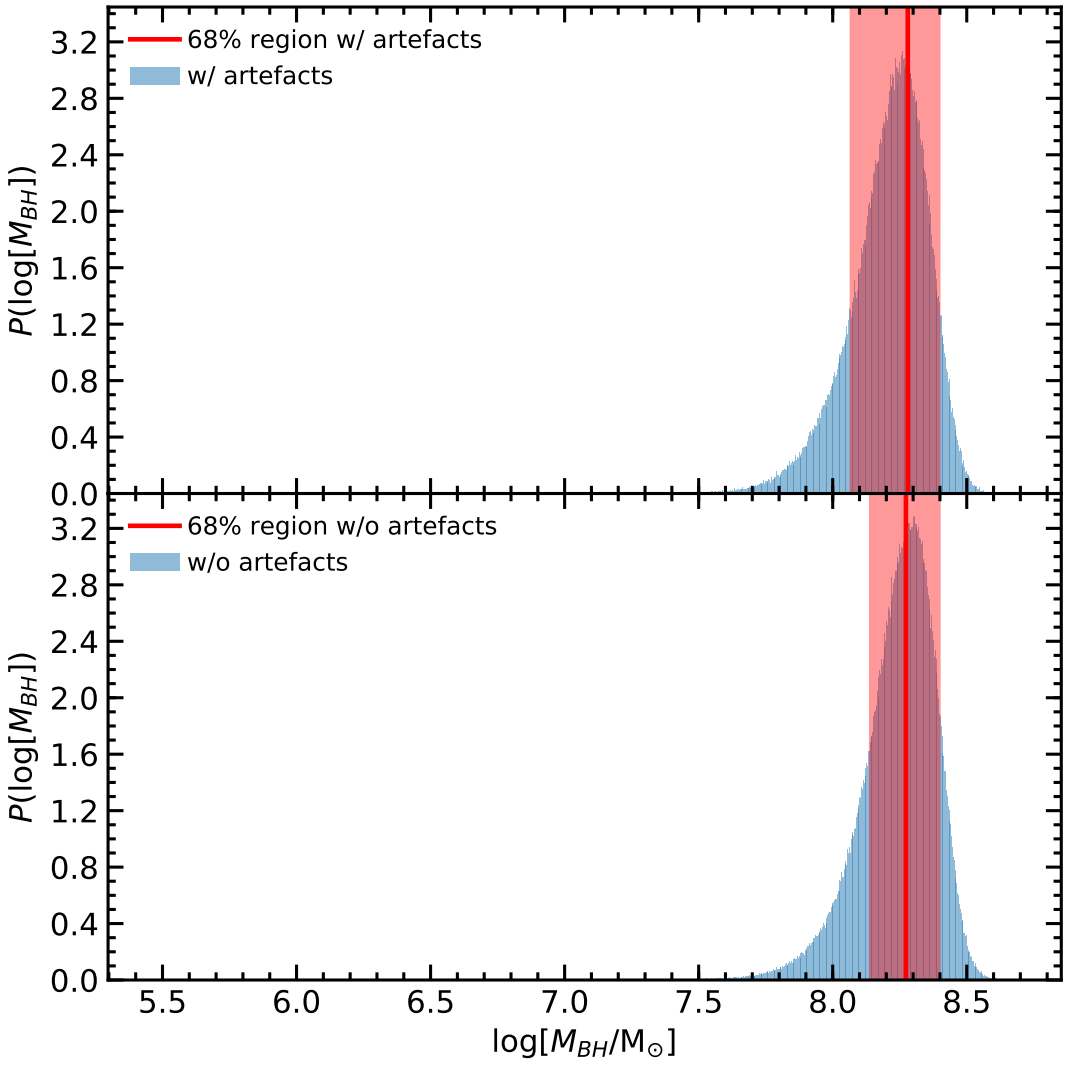

FIGURE 3.15: The probability distribution for black hole mass before and after deconvolution of the `Javelin` artefact distribution. **Top:** The probability distribution for the black-hole mass of Target-10 given the raw output from `Javelin`. **Bottom:** The probability distribution for the black-hole mass of Target-10 given the deconvolved lag distribution. Both distirbutions incorporate uncertainties on velocity dispersion and the virial factor. The 68 per cent HPD region is shown in red in both cases with the best estimate indicated by the solid line.

3.4 Discussion

3.4.1 Efficiency

This observing campaign totalled 17.4 hours (15.2 for Hα and 2.2 for *i*-band) in total, with 5.9 hours dedicated to Target-10. This is far shorter than the large majority of spectroscopic observing campaigns such as Shen et al. (2015a) where the typical epoch consists of at least eight 15 minute sub-exposures rather than our one 10 minute exposure with the Liverpool Telescope

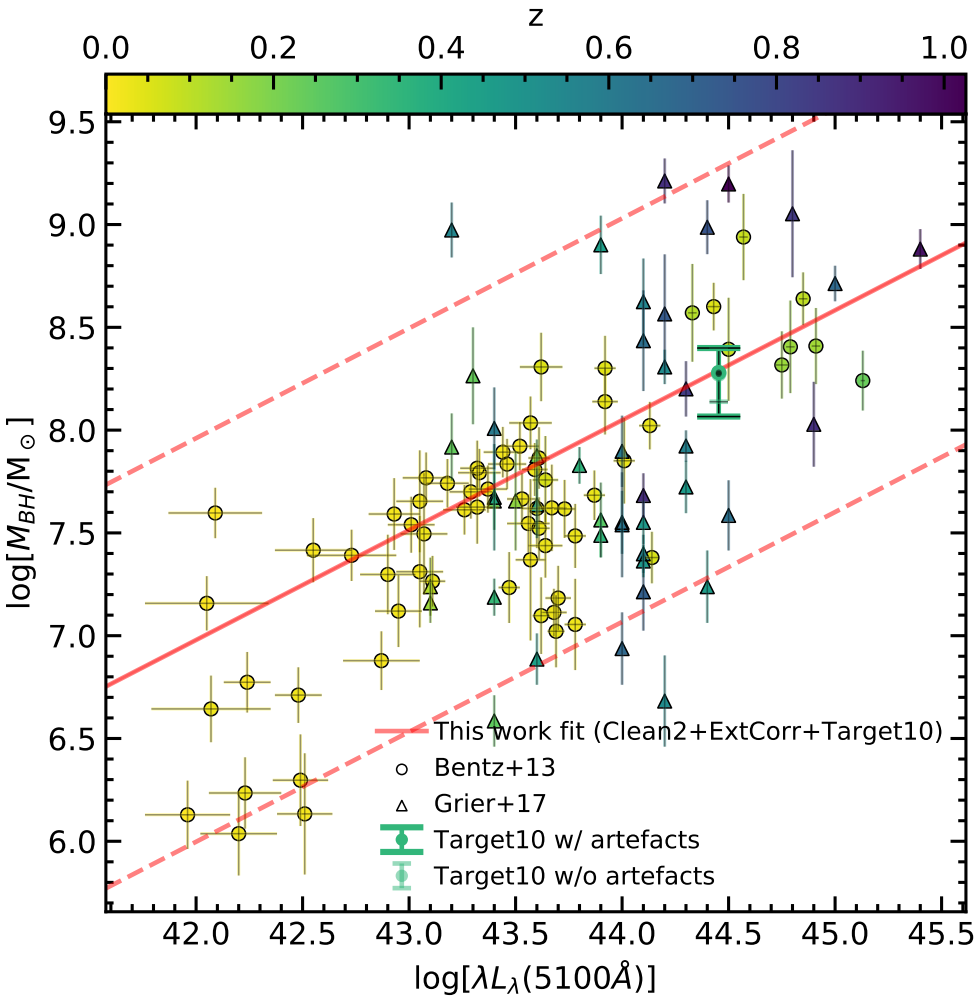

FIGURE 3.16: The black hole mass-luminosity relation shown for the sample from Bentz et al. (2013) (cirlces), Grier et al. (2017) (triangles), and Target-10. The black hole masses for the Bentz et al. (2013) sample are drawn from the AGN Mass Catalogue where possible and calculated using $f = 4.3 \pm 1.1$ (Grier et al., 2013a). The Grier et al. (2017) masses are scaled from $f = 4.47$ to $f = 4.3$. All points are coloured by redshift. The best estimate for the mass of Target-10 is shown in green with and without the artefact deconvolution. The best fit in linear space to the Clean2+ExtCorr dataset as well as Target-10 is shown in red. The scatter estimated by MCMC in all best fit lines is indicated by dashed lines.

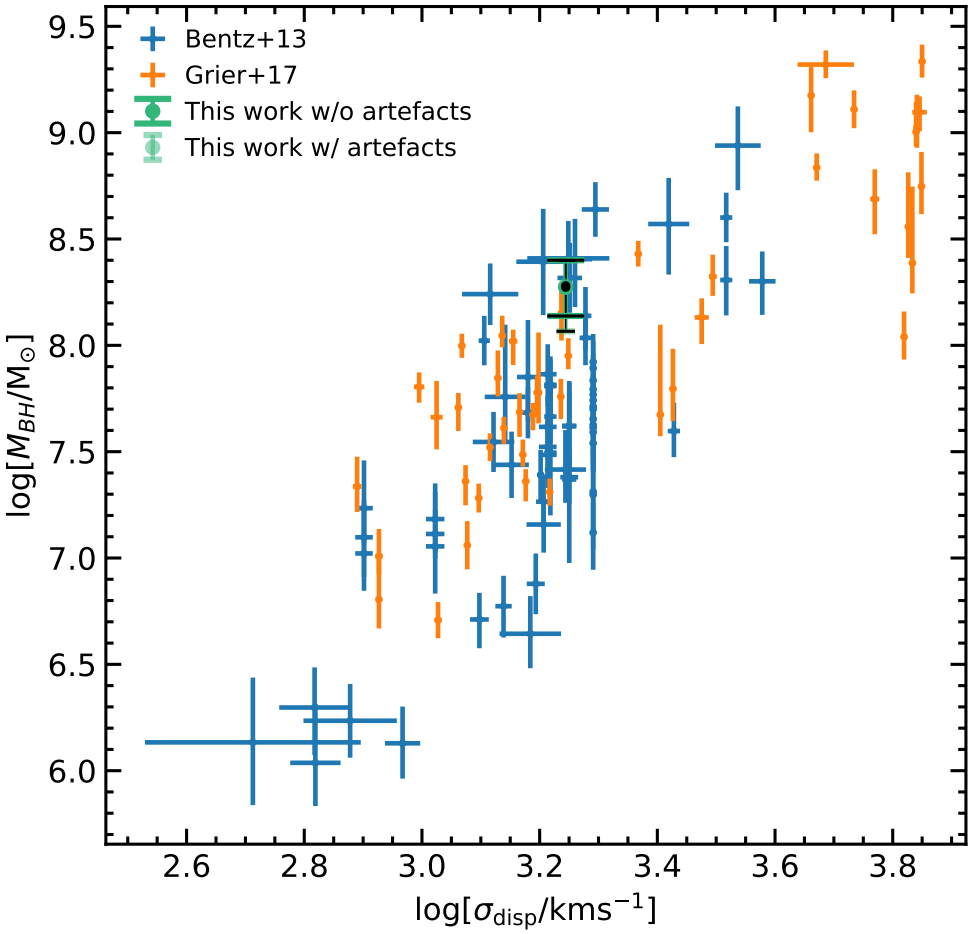

FIGURE 3.17: Estimated black hole mass versus the Hβ velocity dispersion. The Bentz et al. (2013) sample is shown in blue, Grier et al. (2017) sample is shown in orange, and Target-10 is shown in green with and without the Bentz et al. (2013) prior applied. The line widths for the Bentz et al. (2013) sample are retrieved from the AGN Mass Catalogue (Bentz and Katz, 2015).

per epoch. Grier et al. (2017) achieved an average uncertainty of 3 ± 2 days and a maximum SNR of 23.1 whereas Target-10 has an uncertainty of $+5/-1$ days (SNR$=$ 24.3), with much of the uncertainty attributed to artificial peaks having been mitigated using our simulations (see Section 3.3.1).

We define efficiency as the mean $\mathrm{SNR_{lag}}$ achieved for a given observing campaign divided by the total time required.

$$\varepsilon = \frac{\sum_{i=0}^{i=n} \mathrm{SNR_{lag}}}{n t_{\rm total} \pi (D/2)^2}, \tag{3.12}$$

This work	Selection SDSS-RM	$\varepsilon_{\mathrm{SDSS-RM}} \times 10^{-3}$	$\varepsilon_{\mathrm{This\,work}} \times 10^{-3}$	$\frac{\varepsilon_{\mathrm{This\,work}}}{\varepsilon_{\mathrm{SDSS-RM}}}$
$i_{AB} < 18$	all objects	4.4	18.1	4.1
	$i_{AB} < 18$	3.1		5.8
Target-10	$\min[f^{obs}_{5100} - f^{obs}_{5100,Target10}]$	1.3	460.2	363.7
	$\max[\mathrm{SNR}_{lag}]$	17.7		26.0

TABLE 3.5: The efficiencies, calculated with different selection criteria, for SDSS-RM (Shen et al., 2015b; Grier et al., 2017) and this work. The efficiencies are calculated using Equation 3.12. We compare the efficiencies on a per object basis as well as over the whole campaign. We compare our Target-10 to the most similar QSO in the Grier et al. (2017) catalogue (based on f_{5100}) and to their most precise lag estimation (in terms of SNR_{lag}). In all cases, photometric reverberation mapping is more efficient than spectroscopic reverberation mapping.

.

where n is the number of observed targets (detection or not), t_{total} is the total observing campaign observing time, and D is the primary mirror diameter. The mirror diameters are 2.5 m for SDSS-RM and 2 m for this work, which uses the Liverpool Telescope. This gives us the expected signal-to-noise for a given QSO per hour of observation per collecting area. In order to make a fair comparison, we include the SDSS spectrum integration time required to estimate velocity dispersions for each of our targets in the total time required to observe our targets as well.

We have achieved an efficiency of $\varepsilon = 18.1 \times 10^{-3}\mathrm{hr}^{-1}\mathrm{m}^{-2}$, whereas with spectroscopic reverberation mapping, SDSS-RM achieved $\varepsilon = 4.4 \times 10^{-3}\mathrm{hr}^{-1}\mathrm{m}^{-2}$, where our fraction of sources with detected lags (0.2) is the same as that of Grier et al. (2017). This is a 310 per cent increase in efficiency over the multiplexed SDSS-RM campaign. If we instead calculate the signal-to-noise per hour per square metre per object, SNR/t_{obj}, we find that on average we achieve 16 times more signal-to-noise per hour than Grier et al. (2017). Since the SNRs of the Grier et al. (2017) lags do not depend strongly on redshift, observed flux or luminosity, this is a fair comparison.

The efficiencies described above include targets that we have observed but not analysed and consider the whole observing campaign at once. If we only consider Target-10 compared to the most precise lag measured by Grier et al. (2017), for `SDSS J142103.53+515819.5`, our efficiency rises to 26 times more signal-to-noise per hour per square metre than Grier et al. (2017) Furthermore, if we consider the most similar target to our Target-10 in terms of observed flux (`SDSS J140759.07+534759.8`), their efficiency drops to $\varepsilon = 1.3 \times 10^{-3}\mathrm{hr}^{-1}\mathrm{m}^{-2}$.

3.4.2 Future Applications

Having shown that reverberation mapping using photometric methods with minimal spectroscopy, can be an effective means with which to measure black-hole masses, we can foresee a number of exciting applications for long term studies, which would require little extra effort to instigate.

The Liverpool Telescope (Steele et al., 2004) will soon be superseded by a new robotic successor, the Liverpool Telescope 2 (Copperwheat et al., 2014), with first light after 2020. The Liverpool Telescope 2 will benefit from a 4 metre diameter as opposed to the current Liverpool Telescope's 2 metres. Given the efficiency of photometric reverberation mapping with the current Liverpool Telescope, the application of these methods to its successor would be an effective use of time when applied robotically and make higher redshift measurements possible.

Photometric reverberation mapping lends itself well to large surveys, which often require that the instrument make repeated visits to the same field for calibration to standard stars. Selecting calibration fields to contain known QSOs would generate light curves with baselines as long as the survey's duration with a regular high-frequency cadence for little extra effort. The upcoming photometric surveys of the Javalambre Physics of the Accelerating Universe Astrophysical Survey (J-PAS, Benitez et al., 2014) and its companion calibration survey Javalambre-Photometric Local Universe Survey (J-PLUS) promise an opportunity for sustained long-term photometric reverberation mapping campaigns. Designed to accurately measure photometric redshifts for galaxies up to $z = 1$, with its unprecedented 56 narrow band filters, J-PLUS could easily observe the continuum and a wide range of emission lines for a sample of QSOs observed during calibration exposures. In addition, instruments such as the PAUCam (Castander et al., 2012; Padilla et al., 2016), providing 40 narrow-band filters in addition to the u,g,r,i,z, and y photometric filters, could also detect lags with higher SNR and a larger range of redshifts than IO:O. These observations could provide a far more detailed map of the broad-line region as inferred by Williams et al. (2018a), and also provide a large enough dataset to perform continuum reverberation mapping (Mudd et al., 2017) to estimate accretion disk sizes.

The Large Synoptic Survey Telescope (LSST, Marshall et al., 2017) will run a 10 year survey over 30 000 square degrees of sky with 6 broad-band photometric filters. LSST will observe the same regions of sky with a high frequency and 3 day cadence, making pure photometric reverberation (Zu et al., 2016) with large numbers of QSOs a realistic possibility. A QSO light curve dataset from LSST would probe the extremes of timescales where the damped random

walk model for QSO variability is thought to break down (Zu et al., 2013) whilst also providing opportunities for continuum mapping (Mudd et al., 2017).

Given that we can measure lags with 6 days uncertainty with current instrumentation, for baselines longer than $3t_{\rm rest}(1+z)$, these survey's long campaigns and high cadences, along with high precision photometry, will likely provide more than enough signal-to-noise for lag estimation for hundreds of QSOs/AGN covering a large range of lags and luminosities. Indeed, strategic application of photometric continuum mapping and multiple narrow band filters probing multiple broad-line region radii will yield much information regarding the geometry and mass of SMBHs.

3.5 Conclusions

We demonstrate an efficient method for purely photometric QSO reverberation mapping at high redshift ($z = 0.351$) using `Javelin` (Zu et al., 2016, 2013).

1. We observe 10 targets selected for their estimated signal-to-noise, observable time, and inferred Hβ emission line lag (according to the $t_{lag} - L_{5100}$ relation fit in Bentz et al. 2013).

2. Observing conditions ruled out the observation of 5 of our selected targets and 4 observed targets did not have the required baseline, recommended by Shen et al. (2015a), to observe their expected lag given their luminosity. We therefore proceed to discuss only `SDSS J144645.44 +625304.0` (referred to as Target-10).

3. We calibrate the Hα and *i*-band light curves, using an ensemble photometry method, to SDSS AB magnitudes. In order to achieve as accurate an Hα relative calibration zeropoint as possible, we use the only available SDSS-BOSS spectrum. This spectrum is observed to be resolved into two components in both our *i*-band and Hα exposures, and the SDSS *i*-band exposures. Therefore, we fit a two-component Gaussian model to the source in order to transform to the same seeing as the BOSS observation before fitting a zeropoint.

4. We find that the output lag probability distribution from `Javelin` is frequently affected by multiple peaks, some at negative lag values. By generating 151 200 simulated light curves

over a wide damped random walk parameter space (in the Zu et al. 2013 damped random walk model) using the same cadence and signal-to-noise measured in our calibrated light curves for Target-10, we identify artefacts in the lag probability distribution which occur due to cadence effects or the `Javelin` fitting procedure. We find that median estimate of the lag from the `Javelin` probability distributions often reports inaccurate values and large uncertainties for lags. We therefore use an HPD kernel method (Section 3.3.1) to automatically identify the most probable peak objectively. Using the HPD kernel method, we report the reliability of `Javelin` lag over 10 to 316 days. We are able to reliably recover the original input lag over all other nuisance parameter ranges for the simulated light curves with an average of 4 per cent deviation when the input lag is less than 145 days. When simulating light curves based on the signal-to-noise and cadence of Target-10, we find that an error of no more than 0.4 mag in Hα narrow-band zeropoint calibration is still able to recover the given input lag to within an average of 4 per cent.

5. Using simulated light curves with true lags around the suspected lag of Target-10, we compile a distribution of artefacts in the lag distribution produced by the `Javelin` fitting procedure. We deconvolve the artefact distribution from the lag distribution of Target-10 and measure Hβ lags and black hole masses with smaller uncertainties than without artefact deconvolution. We find that that the best estimate of the Hβ lag and black hole mass do not change beyond the 68 per cent HPD credible interval when the artefact deconvolution is applied. We recover an Hβ lag for Target-10 of 73^{+4}_{-13} days and an Hβ lag of 72^{+5}_{-1} days when we apply artefact deconvolution. Assuming an $\langle f \rangle = 4.3 \pm 1.1$, we measure a black hole mass for Target-10 of $10^{8.27^{+0.13}_{-0.15}}\mathrm{M}_{\odot}$ and a black hole mass of $10^{8.28^{+0.12}_{-0.07}}\mathrm{M}_{\odot}$ when we apply artefact deconvolution.

In conclusion, we find that by analysing the resulting probability distribution with more in-depth techniques, we can approach the precision demonstrated by spectroscopic reverberation mapping using photometric techniques. Furthermore, we can achieve this precision with a quarter of the total exposure time that the SDSS-RM programme required to achieve a higher average SNR with a smaller telescope. This results in a 310 per cent increase in efficiency over SDSS-RM. These simple yet powerful photometric methods can be readily applied to large surveys which require regular calibration in order to build a large baseline of known QSO observations.

Chapter 4

Characterising the Mass Dependency of the $L_{150\,\mathrm{MHz}}$-SFR Relation with LoTSS Using a New Generalised Method to Retrieve Complete Distributions from Incomplete Data

4.1 Introduction

An important part of testing and constructing models of galaxy evolution is reconstructing their star-formation histories and instantaneous star-formation rates over cosmic history. However, star-formation rate, whether instantaneous or averaged over time, is not an observable variable. Instead, it is only possible to estimate star-formation rates, for example using spectral template fitting (Reichardt et al., 2001; Panter et al., 2003; Bruzual and Charlot, 2003; Heavens et al., 2004; da Cunha et al., 2008; Koleva et al., 2009; da Cunha et al., 2011; Smith et al., 2014; Read et al., 2018) which rely on the star-formation histories of template SEDs being plausible and representative (other methods exist). More commonly, SFR is estimated by the use of indicators whose relation to SFR is either calibrated using template fitting or from simple physical models (e.g. Lacki and Thompson 2010; Schober et al. 2017) and then by empirical scaling

relations based on those calibrations such as the Far-infrared Radio Correlation (e.g. Condon, 1992; Murphy et al., 2011; Lacki et al., 2010), in the case of radio emission.

As discussed in Chapter 2, using radio emission as a star-formation rate tracer has many practical advantages over shorter wavelengths (improved resolution, dust is transparent, and huge surveys are easier to perform). Radio wavelengths are unaffected by dust extinction and hence would report the full unobscured star-formation rate given a sufficiently advanced model of its production in a given galaxy. Non-thermal radio emission is thought to be produced from the synchrotron losses of highly energetic cosmic rays as they travel through a galaxy's magnetic field.

In the absence of an AGN, the main source of non-thermal-producing cosmic rays is assumed to be in the shock fronts surrounding supernovae remnants where the charged particles are accelerated to cosmic ray velocities (Lynden-Bell, 1969a,b; Blumenthal and Gould, 1970; Drury, 1983; Condon, 1992; Schlickeiser, 2002; Longair, 2011). Since the rate at which type-II supernovae occur is proportional to the star-formation rate, albeit with a $\sim$ 1-100 Myr delay due to the lifetime of massive OB stars which end in supernovae, synchrotron emission should also be proportional to star-formation rate given no other sources of emission. However, the cosmic rays are thought to contribute to the synchrotron emission (whose intensity over time is frequency dependent) for 100 Myr after their acceleration, as the particles which did not achieve the escape velocity of the galaxy persist within the galaxy's magnetic field until their energy is lost (Blumenthal and Gould, 1970; Condon, 1992; Longair, 2011). Therefore, synchrotron emission reflects the integrated star-formation that occurred less than 100 Myr before the galaxy was observed, given no contamination from an AGN.

Variations in this time-scale due to differences in magnetic field strength or halo mass have the effect of dispersing the star-formation rate relation over star-forming galaxies even further. Indeed, the steeper the potential well, the longer the synchrotron-emitting particles can remain in the galaxy, preserving the calorimetry approximation (where the energy injected into the cosmic ray particles is all eventually emitted as synchrotron radiation from within the galaxy) more accurately than at low mass. The exact relation between synchrotron emission luminosity and star-formation rate is also co-dependent upon losses from ionisation, bremsstrahlung, inverse Compton scattering and galactic winds (Lacki et al., 2010; Schober et al., 2017). Thus, the slope and scatter of their relation depends upon the physical properties of magnetic field strength, gas density, interstellar radiation field, wind velocity, and ionisation degree to name a few. These

physical properties vary by orders of magnitude between normal star-forming galaxies and those which have experienced a recent starburst (Lacki et al., 2010).

In addition, AGN can dramatically contribute to the radio luminosity of a galaxy resulting in radio-loud sources in galaxies dominated by such central emission. The distribution of AGN radio luminosity spans several orders of magnitude (Sabater et al., 2018) and this implies that emission from low-luminosity AGN can contaminate the radio star-formation rate relations without being immediately detectable (Gurkan et al., 2018). Clearly, it is not practical to measure these components/properties for all galaxies and indeed it is not possible to do so for galaxies which lack an identified optical component, as will be the case for large numbers of galaxies observed with the SKA and its pathfinders such as LOFAR.

Therefore, it is important to produce a pragmatic radio star-formation rate tracer and quantify the inevitable deviations from it before applying it to radio sources without optically inferred star-formation rates.

Gurkan et al. (2018) investigated the 150 MHz luminosity – star-formation rate relation for SFGs in order to harness the potential of low radio frequency luminosity as a dust free star formation rate indicator (see Figure 4.1). They revealed that stellar mass appears to play a significant role in the slope and scatter of the relation between luminosity and SFR. Figure 4.2 shows the break in 150 MHz luminosity – star-formation rate relation over stellar mass. Since the calorimetry approximation breaks down in small low-mass systems due to shorter escape times, the radio luminosity of these star-forming objects should be smaller than that extrapolated from the higher-mass galaxies. In contrast, Gurkan et al. (2018) see more than an order of magnitude excess in radio luminosity at low star-formation rates. The slope of the $L_{150\,\mathrm{MHz}} - \mathrm{SFR}$ relation also appears to flatten out at low star-formation rates (especially at higher stellar masses) which could indicate a different cosmic ray generation pathway such as type-Ia supernovae, pulsars, or an amplification of galactic magnetic fields (Gurkan et al., 2018).

However, investigating the existence of a mass dependency in the star-formation rate radio luminosity relation requires knowledge of the covariation of stellar mass, luminosity, star-formation rate, and redshift together. To complicate matters further, these relations also depend on the galaxy's classification as star-forming or AGN or indeed, as in realistic cases, a mixture of the two (e.g. Cid Fernandes et al., 2004; Santini et al., 2012; Kirkpatrick et al., 2015; Delvecchio et al., 2017). Binning in star-formation rate over a relation that depends on two covariates, along with the inherent biases in the optically selected dataset, would result in heavily biased results

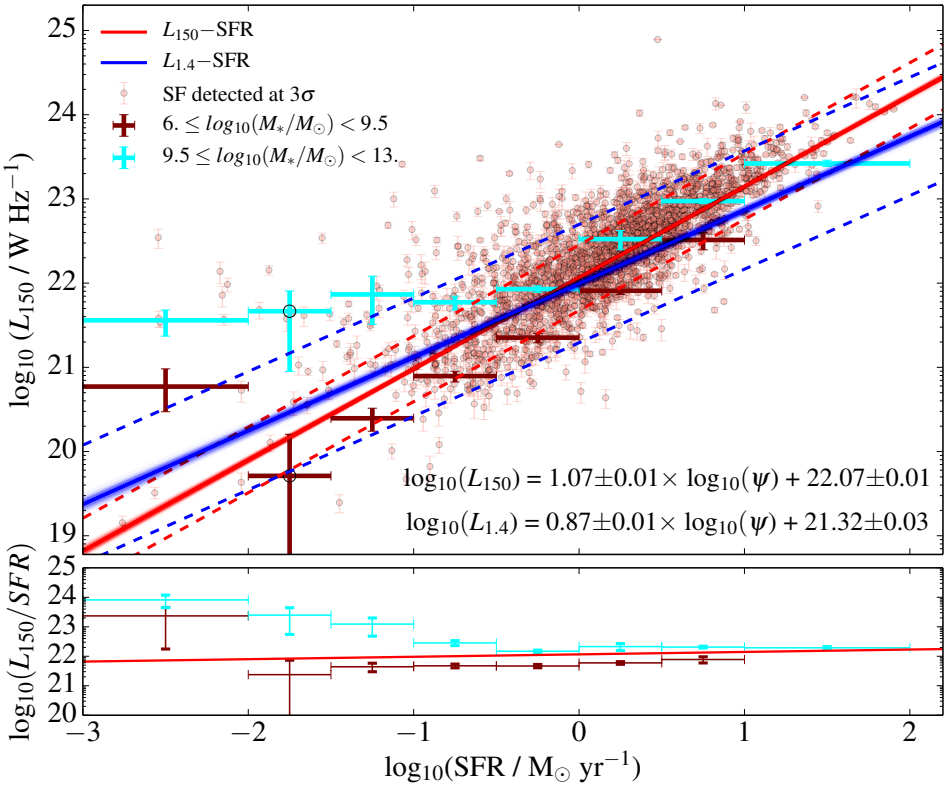

FIGURE 4.1: The radio luminosity stellar mass relation found by Gurkan et al. (2015). **Top:** The distribution of LOFAR 150 MHz luminosities of SFGs detected at 150 MHz as a function of their SFRs. The best fits obtained using all SFGs and LOFAR 150 MHz luminosities and errors on the best fit are shown as red shaded region and the blue shaded region shows the best fit to all data points of SFG obtained using 1.4 GHz and scaled to 150 MHz assuming $\alpha = 0.8$. The dashed lines around the best fits show the dispersion around the best-fit line implied by the best-fitting dispersion parameter σ. The results of the stacking analysis for two stellar mass bins are also shown for L_{150} as large cyan and maroon crosses. Open circles indicate the bins in which sources were not detected significantly. **Bottom:**: The $L_{150} - SFR$ ratios for two stellar mass bins are shown as cyan and maroon crosses, and the best fit divided by the SFR (red line) are shown.

(Towers, 2012). The degree to which the mass-dependency result of Gurkan et al. (2018) is affected by selection biases is unknown and is not easily corrected for *post hoc*. In practice, constructing an unbiased test for the mass dependency requires modelling the evolution of the luminosity and mass functions along with their star-formation rates whilst also accounting for optical selection effects.

Gaussian mixture models are adept at describing high-dimensional relations in astronomy which consist of more than one population or are heavily non-linear (Rasmussen, 2000; Hogg et al., 2010; Bovy et al., 2011; Melchior and Goulding, 2018). Their flexibility allows the use of Gaussian mixture models in semi-parametric or non-parametric models where the "true" functional

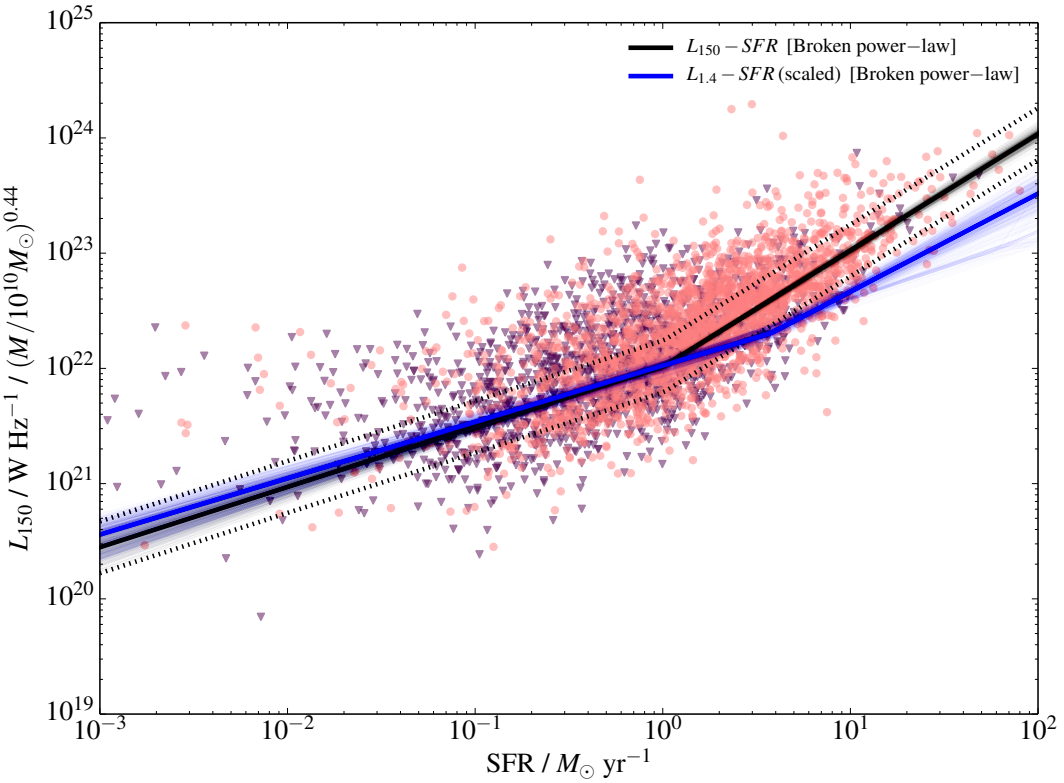

FIGURE 4.2: . Distribution of 150 MHz of SFGs as a function of their SFRs taken from Gurkan et al. (2018). Upper limits are indicated with purple triangles. The best fit obtained using all SFGs, and the uncertainties, are visualized by overplotting the lines corresponding to a large number of samples from the MCMC output. The dashed black lines show the 1σ intrinsic dispersion around the best-fit line implied by the best-fitting dispersion parameter σ. The same relation derived using high frequency observations is shown as the blue line, with fitting uncertainties displayed in the same way.

form is unknown or poorly defined (Rasmussen, 2000; Bovy et al., 2011; Lee and Scott, 2012). Modelling the entire parameter space non-parametrically allows for fast and unbiased conditioning (slicing at a certain value) and marginalisation (integrating over whole parameters) to estimate distributions for any number of lower dimensional models.

In the case of the $L_{150\,\mathrm{MHz}} - \mathrm{SFR}$ relation's mass dependency, it is vital to take into account redshift evolution. The main sequence is observed to evolve (Noeske et al., 2007a,b; Dutton et al., 2010; Schreiber et al., 2016) and so any test regarding the mass dependence will need to be performed by including redshift effects. Binning in this complicated scenario quickly devolves into low signal-to-noise estimations and the choice of bins in a high-dimensional parameter space can affect the result dramatically (Towers, 2012; Krislock and Krislock, 2014), and so we need to model the distribution holistically.

However, as with any astronomical sample, we cannot always representatively sample the entire distribution, due to limited survey volumes and limits on sensitivity. Luminosity functions are typically inferred by methods like the $1/V_{max}$ method (Kafka, 1967) with the incompleteness effects of a flux-limited survey usually corrected for with incompleteness weights (Johnston, 2011). Kelly et al. (2008) have proposed a non-parametric method of inferring complete luminosity functions from magnitude-limited survey data using Gaussian mixture models and MCMC inference techniques. This technique can, in theory, be extended to model other types of incompleteness such as an independent optical magnitude cut, by including an extra dimension into the fit (that of optical magnitude). However, Gaussian mixtures suffer from the "curse of dimensionality" in that the number of parameters needed to fit the distribution explodes as the number of measurement dimensions increases. The parameter space that an MCMC algorithm has to traverse becomes exponentially larger until independent and ensemble MCMC walkers can no longer efficiently sample the posterior (Foreman-Mackey et al., 2013). In addition, the uncertainties of the measurements are not taken into account in the method of Kelly et al. (2008) leading to a broader distribution than is justified by uncertain data.

The technique of *Extreme Deconvolution* (Bovy et al., 2011) provides an efficient way to infer the maximum likelihood parameters for multiple Gaussian components, modelling uncertain heteroscedastic measurements, and therefore infer complete distributions from noisy data. Building upon *Extreme Deconvolution*, Melchior and Goulding (2018) have devised a simple yet powerful extension, `PyGMMIS`, whereby they "impute" (or fill in) the missing data at every step using the current iteration of the maximum likelihood model. This allows the fitting of the complete distribution assuming that the unobserved part is not significantly different from an extrapolation of the observed model. However, measurement errors are frequently non-Gaussian, observations are nearly always incomplete, and the effect of data selection from other latent parameters (such as the effect of a optical magnitude limit in a a radio/optical catalogue) contrive to detract from the simplistic Gaussianity of the problem. Furthermore, with the volume of data used in this work, it becomes prohibitively expensive to run a `PyGMMIS` model at dimensions above 4, since it relies on rejection sampling to impute the missing dataset. There is not currently any method that incorporates solutions to all of these problems in one model fitting technique.

The goal of this work is to provide a test for the mass-dependency of the $L_{150\,\mathrm{MHz}} - \mathrm{SFR}$ relation whilst taking into account selection effects from optical photometric and spectroscopic selection, BPT classification, redshift trends, and modelling the effect of low SNR radio sources.

In order to achieve this it is necessary to combine the solutions to the problems of modelling multi-dimensional, missing, incomplete, non-Gaussian heteroscedastic data into one efficient algorithm.

We make use of the LOFAR Two-Metre Sky Survey (LoTSS DR1; Shimwell et al., 2017, 2018; Williams et al., 2018b) catalogue which includes an unprecedented $\gtrapprox 300,000$ detections and radio sensitivity at 150 MHz. A description of the available data from LOFAR, SDSS, and the resultant data products that we use is given in Section 4.2. In Section 4.3, we describe the methodology of our new PYTHON package, *Complete And Noiseless Distributions from Incomplete Data*, `CANDID`[1], which aims to fit the 9-dimensional distribution of local star-forming galaxies as well as any other N-dimensional incomplete dataset. We then verify our method by comparing the resultant total luminosity function with the literature in Section 4.4.1. In Section 4.4.2 we present the results of the mass dependency test. We then demonstrate that we can construct a joint model of star-forming galaxies between the Horizon AGN (Dubois et al., 2014) simulation and our LoTSS observations using our new method. We show that the effect of type-Ia supernovae on the $L_{150\,\mathrm{MHz}} - \mathrm{SFR}$ relation remains uncertain and warrants further investigation. Finally, we summarise our conclusions and future work in Section 4.5.

4.2 Data sources

The LOFAR Two-Metre Sky Survey, (LoTSS; Shimwell et al., 2017), is an ongoing high-resolution low frequency (120-168MHz) survey that will cover the whole northern sky. This work utilises the LoTSS DR1 catalogue (Shimwell et al., 2018; Williams et al., 2018b), which covers 424 square degrees centred on the Hobby-Eberly Telescope Dark Energy Experiment (HETDEX; Hill et al., 2008) Spring Field region (α_{J2000} =10h45m00s to 15h30m00s and δ_{J2000} = 45°00′00″ to 57°00′00″). The region contains over 300,000 5σ LOFAR-detected sources. The median RMS noise is $71\,\mu\mathrm{Jy\,beam^{-1}}$ at 150 MHz with 95 per cent of the area below $150\,\mu\mathrm{Jy\,beam^{-1}}$. The angular resolution is 6 arcseconds and cross-matching radio sources with detections in Pan-STARRS (Kaiser et al., 2002, 2010) and WISE (Wright et al., 2010), through the use of the likelihood ratio method (Sutherland and Saunders, 1992; Smith et al., 2011) and visual classification methods (Williams et al., 2018b), has yielded optical counterparts with a reliability of ≈ 99 per cent.

[1] to be made available at `https://github.com/philastrophist/candid`

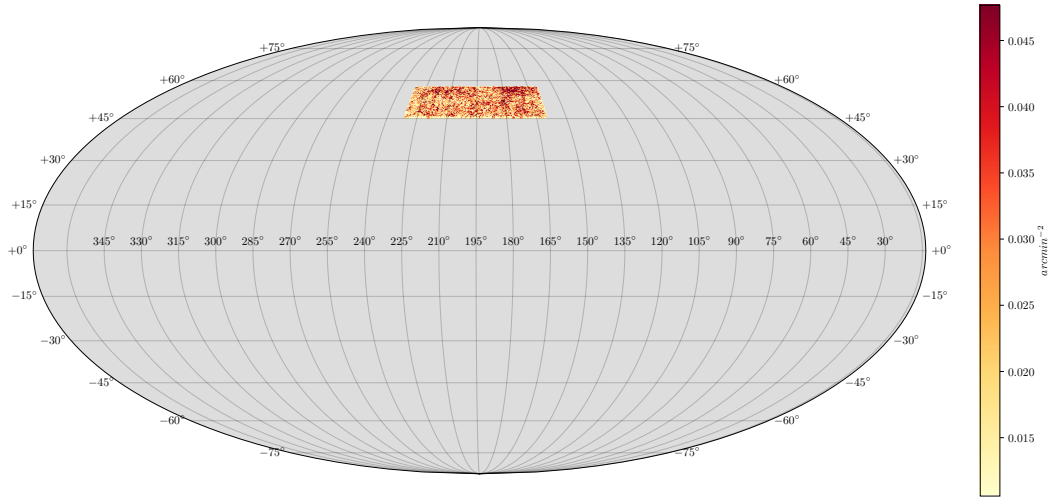

FIGURE 4.3: Source density of the optically identified radio sources over the sky showing the HETDEX region. Colour indicates the density of sources in arcminute^{-2}.

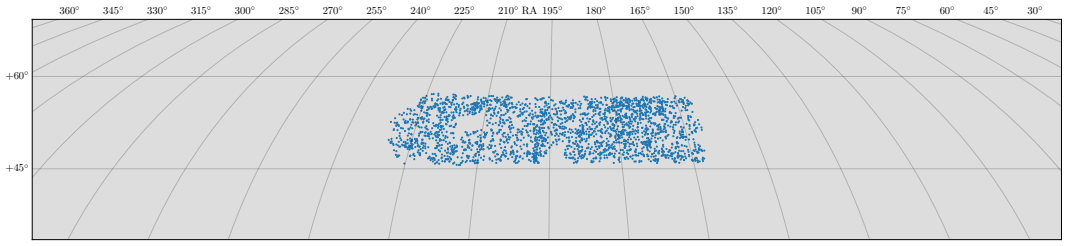

FIGURE 4.4: Our star-forming sample over the sky showing the HETDEX region. Each blue point represents an (r-band) optically identified source which meets our selection criteria.

We use a subset of this catalogue based on SDSS DR7 (York, 2000; Abazajian et al., 2009). The MPA-JHU value-added catalogue (Brinchmann et al., 2004) uses an optimised pipeline to re-analyse all SDSS (York, 2000) spectra, resulting in a sample with reliable spectroscopic redshifts, improved estimates of stellar mass, and star formation rate (Kauffmann et al., 2003b), as well as emission line flux measurements for each galaxy (Tremonti et al., 2004). We use their latest analysis performed on the SDSS DR7 release (Abazajian et al., 2009) to obtain optical emission line fluxes for classifications of SFG and AGN-dominated sources plus spectroscopic redshifts for K-corrections. There are roughly 43,000 galaxies with MPA-JHU information in the LoTSS–HETDEX area.

In order to probe star-formation rate relations at low radio luminosities, we perform forced aperture photometry on the SDSS optical positions of the cross-matched (Williams et al., 2018b) radio sources. We use the flux extracted from a 10 arcsecond radius aperture for all sources in our cross-matched catalogue. With this aperture radius, the aperture correction is negligible. We then convert the extracted 150 MHz flux to a luminosity using a spectral index of -0.71

(Hardcastle et al., 2016), defined in the sense that $S_\nu \propto \nu^\alpha$. Any analysis we perform later incorporates non-detections, with their large uncertainties, in the same way as detected sources. We make no distinction between non-detections and detections in radio flux.

To select our star-forming sample, we first obtain all 37,825 optically selected sources in the MPA-JHU catalogue with reliable (`ZWARNING = 0`) spectroscopic redshifts. Since we wish to focus only on star-forming galaxies, we remove those sources with spectroscopy and photometric evidence for contamination by emission from an active galactic nucleus (AGN). As noted by Gurkan et al. (2018), many sources that are not detected to within 3σ do not follow the star-forming luminosity-SFR relation. In addition, the offset of these source from the luminosity-SFR relation shows a strong mass-dependency with the radio-loud AGN classified by Best and Heckman (2012) positioned at the high mass end of the non-star-forming branch of the mass-luminosity diagram. Gurkan et al. (2018) reason that since the non-star-forming sources form a continuous sequence that reaches a much higher radio luminosity for a given mass than expected for SFGs, the intermediate sources in this diagram play host to low-luminosity AGN. Since we wish to probe the claim of a mass-dependency (and one that is non-linear) in star-forming galaxies, we take steps to reduce the contamination of low-luminosity AGN as much as possible. We construct a BPT diagram using the emission line fluxes in the MPA-JHU catalogue (Figure 4.5). We specify a strong 5σ significance cut for each BPT emission line flux and then select star-forming galaxies based on the Kauffmann et al. (2003a) SFG selection criteria, not including transition objects (shown in Figure 4.5). We select only those galaxies whose detected emission line ratios are classified as SFG to within 3σ.

Hardcastle et al. (2016) find that the *r*-band magnitude distribution of optically selected galaxies identified as AGN exhibits a sharp drop off, relative to SFGs, below $r = 17$. These galaxies were classified by their offset from the Far-Infrared Radio Correlation (FIRC) and so is independent from emission line classification. We therefore make a magnitude cut at 17 mag in the SDSS *r*-band.

We later incorporate the effects of selecting SFGs in this way into our model in order to offset any biases introduced by such a strong selection (see Section 4.3.4). We also remove those galaxies for which stellar masses or star-formation rates have not been estimated by the Brinchmann et al. (2004) MPA-JHU catalogue. In addition, we select only those galaxies whose redshifts are above 0.005, following (Brinchmann et al., 2004) in order to mitigate the effect of cosmic variance. This leaves 2575 galaxies which we call our main star-forming sample. The 2046 galaxies

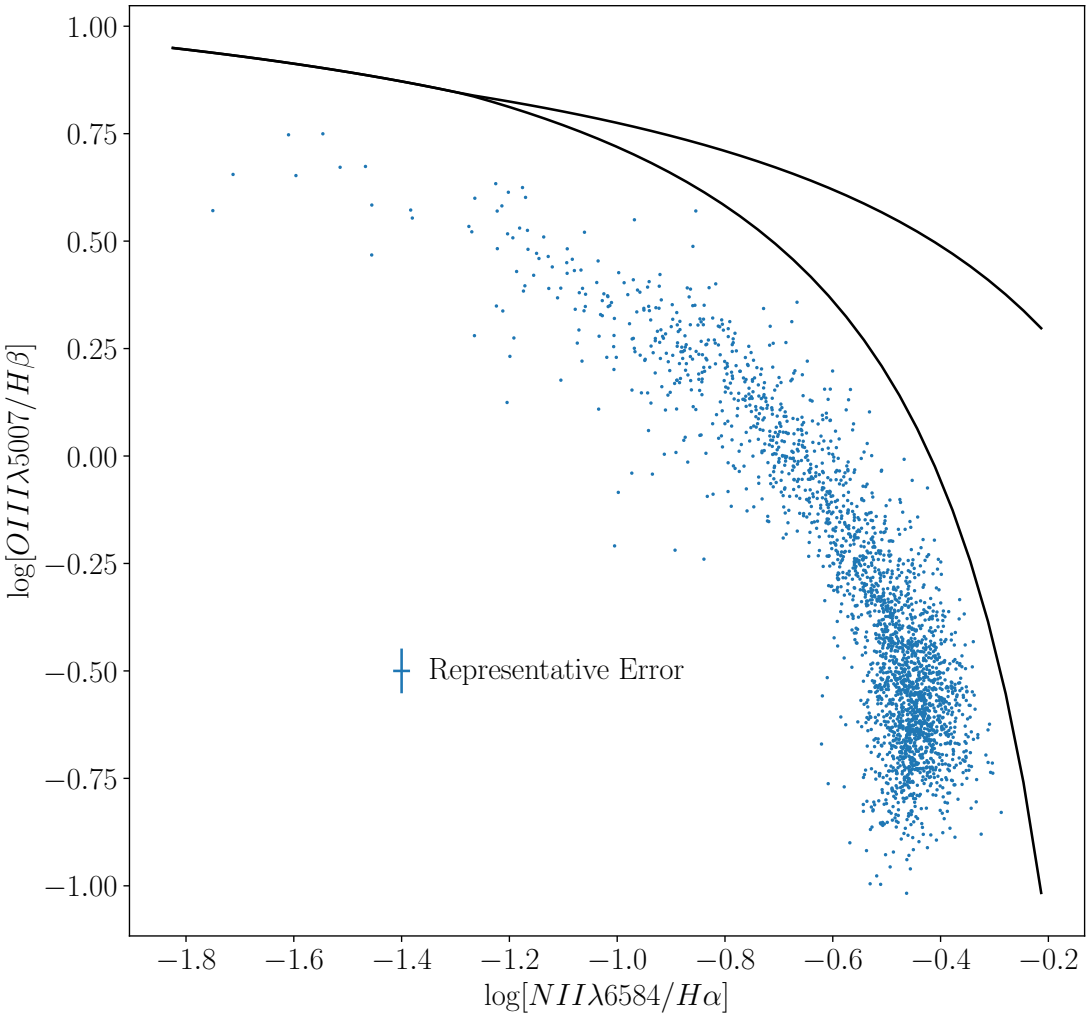

FIGURE 4.5: Emission line ratio diagnostic diagram for our star-forming sample. The upper and lower solid black lines used to distinguish between transition/AGN and SFG/transition populations are from Kewley et al. (2001) and Kauffmann et al. (2003a) respectively.

within our star-forming sample which also have 3σ detections in 150 MHz flux are shown in Figures 4.6 and 4.7.

4.3 Methods

4.3.1 The Hierarchical model

We follow the Gaussian Mixture Model (GMM) prescription of Kelly et al. (2008) for determining luminosity functions in the logarithmic space of luminosity and redshift. Evaluating the luminosity function in log-space allows us to recover the curve of the luminosity distribution with many fewer components. We extend the model of Kelly et al. (2008) to four dimensions

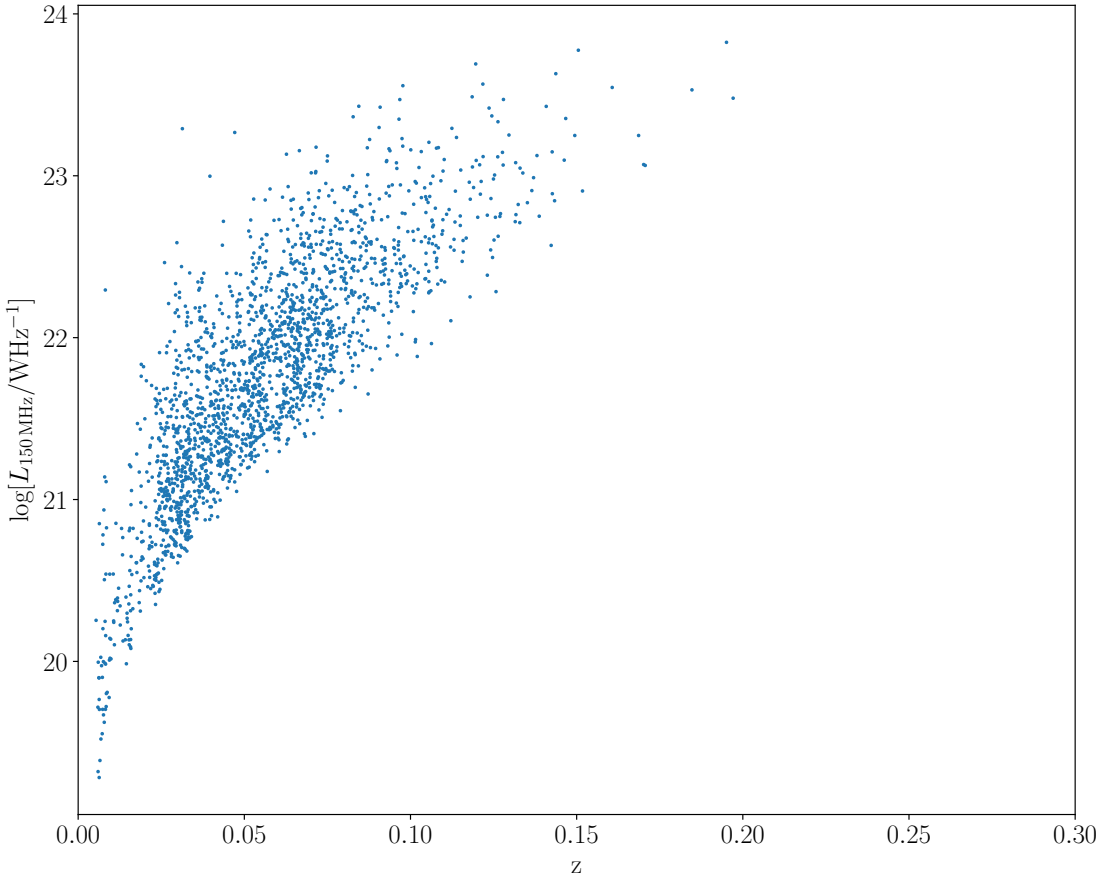

FIGURE 4.6: The luminosity distribution over redshift of the 2046 3σ LOFAR-detected sources in our star-forming sample.

Variable Name	Measurement Quantity	Fitting Quantity
Redshift	z	$\log[z]$
150 MHz	$S_{150\,\mathrm{MHz}}/\mathrm{Jy}$	$\log[4\pi d_L(z)^2 S_\nu (1+z)^{0.71-1}/\mathrm{WHz}^{-1}]$
Stellar Mass	$\log[M_*/\mathrm{M}_\odot]$	$\log[M_*/\mathrm{M}_\odot]$
SFR	$\log[SFR/\mathrm{M}_\odot\mathrm{yr}^{-1}]$	$\log[SFR/\mathrm{M}_\odot\mathrm{yr}^{-1}]$
r-band	m_r	$M_r = m - \mu(z)$
$4\times$ optical emission lines	$S/\mathrm{ergs}^{-1}\mathrm{cm}^{-1}$	$\log[4\pi d_L(z)^2 S/\mathrm{W}]$

TABLE 4.1: The transformations used to propagate our data measurements to the fitting regime. $d_L(z)$ is the luminosity distance and $\mu(z)$ is the associated distance modulus. The four BPT emission lines are grouped under one heading since they use the same transformation.

whereby we include the stellar mass and Hα star-formation rate estimates from MPA-JHU. In order to incorporate selection effects from r-band selection and BPT selection, we must model the complete distribution of each of these measured quantities. This requirement adds $H\alpha$, $H\beta$, $[OIII]\lambda 5007$, $[NII]\lambda 6584$ emission line fluxes from the MPA-JHU catalogue along with the r-band `CMODEL` magnitude. These additions bring the total number of physical quantities to 9 detailed in Table 4.1.

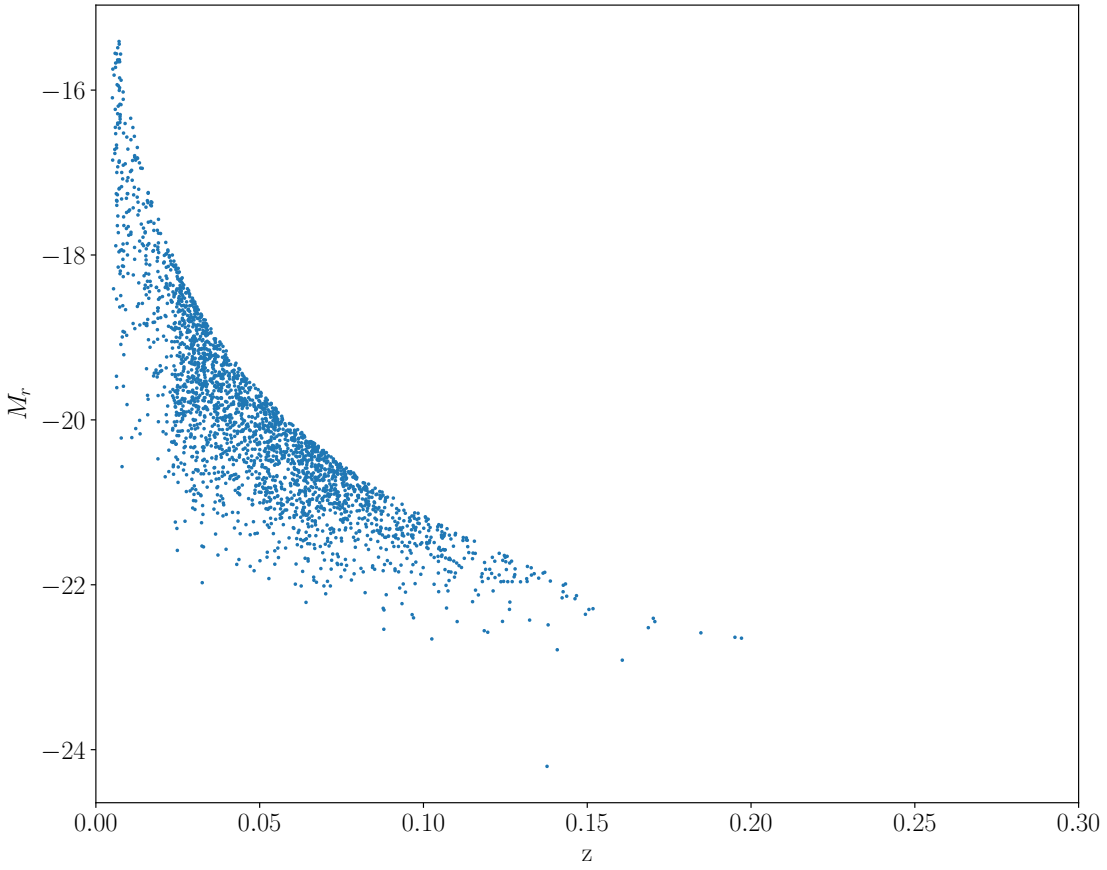

FIGURE 4.7: The r-band absolute magnitude distribution over redshift of the 2046 3σ LOFAR-detected sources in our star-forming sample.

In order to use all data available from the low radio luminosity sources, we resample each data point's ($\vec{x} = [S_{150\,\mathrm{MHz}}, m_r, \log M_*, \log SFR, S_{H\alpha}, S_{H\beta}, S_{[OIII]\lambda 5007}, S_{[NII]\lambda 6584}]$) uncertainties 15,000 times with the restriction that the flux quantities be positive. This allows us to transform our data points to the fitting regime without assuming Gaussianity.

Any fits to the data without taking optical selection criteria into account will produce incorrect results. We adopt an approach informed by the models of Kelly et al. (2008); Patel et al. (2013); Hinton et al. (2017); Melchior and Goulding (2018) whereby we add a new "selection probability" term, $P(S \mid \theta)$, to our likelihood. The unnormalised likelihood for a data point, i, with resamples, r, is then defined as

$$l_i(x_i \mid \vec{\theta}) \propto \sum_k \pi_k \prod_r \mathcal{N}(T(\vec{x_{ir}}) \mid \vec{\theta_k}) \tag{4.1}$$

$$\mathcal{L}_i(\vec{x}_i \mid \vec{\theta}) \propto \frac{l_i(x_i \mid \vec{\theta})}{P(S \mid \vec{\theta})}, \tag{4.2}$$

$$P(S \mid \vec{\theta}) = \int_{-\infty}^{\infty} P(S \mid \vec{D}, \vec{\theta}) l(\vec{D} \mid \vec{\theta}) d\vec{D}, \tag{4.3}$$

where $\mathcal{N}$ represents the normal distribution, $T(...)$ is the transformation from measured data to the fitting regime, $P(S \mid \vec{D}, \vec{\theta})$ denotes the probability of the resampled data point x_{ir} being observed and selected given some data $\vec{D}$, π_k is the weight of the kth component, and $\vec{\theta}$ represents the rest of the Gaussian model parameters. Thus the probability of selection requires integrating the mixture model over all possible data. Calculating this probability with selection effects cannot be done analytically and so must be approximated. Monte Carlo integration is the quickest way to estimate such an analytically intractable integral, whereby the integrand is sampled at random and the value of the integral is estimated from the mean of the samples:

$$\int f(x)dx = \lim_{N\to\infty} \frac{1}{N} \sum_{i=0}^{i=N} f(x_i), \tag{4.4}$$

$$P(S \mid \vec{\theta}) = \lim_{N\to\infty} \frac{1}{N} \sum_{i=0}^{i=N} P(S \mid \vec{D}_i, \vec{\theta}) \mathscr{L}(\vec{D}_i \mid \vec{\theta}), \tag{4.5}$$

when the samples D are drawn from an N-dimensional uniform distribution. However, the selection probability integral must be evaluated at each step in the inference chain. Sampling every time is prohibitively expensive, so we pre-compute the samples beforehand and transform them to the current form of the model as part of a likelihood evaluation. Our Gaussian mixture model lends itself to pre-computation since a single multivariate Gaussian can trivially be transformed into a mixture of Gaussians with different means and covariances. In addition, we further the efficiency of the likelihood evaluation by sampling using a Halton sequence (Halton, 1964). A Halton sequence is a quasi-random deterministic sequence based on co-prime numbers and drawing from an N-dimensional Halton sequence is to sample the N-dimensional $x \sim \text{Uniform}(0,1)$ while evenly spacing those draws. Halton sequences significantly increase the efficiency of Monte Carlo integration (Kocis and Whiten, 1997). To summarise, the integration method at each inference step is as follows:

1. Pre-compute samples:

   (a) Sample from the N-dimensional Uniform distribution using a Halton sequence.

$$x \sim \vec{U}(0,1) \tag{4.6}$$

(b) Transform samples to standard normal distribution using a multivariate cumulative distribution estimator:

$$y = \int_{-\infty}^{x} \vec{\mathcal{N}}(z \mid 0,1) d\vec{z} \tag{4.7}$$

$$y \sim \vec{\mathcal{N}}(0,1), \tag{4.8}$$

where y are now samples from the standard normal distribution, having integrated over all space with z.

2. Transform the uniform samples to samples from the model.

Given a model with n multivariate Gaussians with Cholesky lower diagonal matrices $\vec{L}$ (where the covariance matrix $\Sigma = L \cdot L^T$), transform the precomputed samples, y, into samples from the model, m:

$$\vec{m} = \vec{L} \cdot y^T \tag{4.9}$$

$$\vec{m} \sim \sum_k \pi_k \mathcal{N}(\theta_k) \tag{4.10}$$

3. Compute selection probability

Using the transformed pre-computed samples in the Monte Carlo integrations allows us to simplify Equation 4.5 to:

$$P(S \mid \vec{\theta}) = \lim_{N \to \infty} \frac{1}{N} \sum_{i=0}^{i=N} P(S \mid \vec{m}_i, \vec{\theta}) \tag{4.11}$$

where we only to need to evaluate the selection criteria and not the whole likelihood for each point (Hinton et al., 2017).

4.3.1.1 Priors

The prior for our model consists of 3 parts: the component weights, covariances, and means. We use the priors that Bovy et al. (2011) has set out. These priors are the standard conjugate priors of each variable, whereby the prior is from the same family as the likelihood and hence the posterior. We use a Wishart prior (conjugate to an inverse covariance matrix of multivariate normally distributed vector) on the covariance of each Gaussian.

$$\mathcal{W}(\Sigma_k^{-1} \mid \omega, W) = c(\omega, W) \mid \Sigma_k^{-1} \mid^{\omega-(d+1)/2} \exp[-\text{Trace}[W\Sigma_k^{-1}]], \tag{4.12}$$

where ω is the number of degrees of freedom, W is the scaling matrix hyperparameter for the prior, Σ_k is the covariance of the kth component, d is the number of dimensions, and $c(\omega, W)$ normalises the distribution. We also apply a Dirichlet prior to the weights given by

$$\mathscr{D}(\vec{\pi} \mid \vec{\gamma}) = b \prod_k \pi_k^{\gamma_k - 1}, \tag{4.13}$$

where γ_k is the hyperparameter that sets the prior weights of the components, π_k, and b normalises the distribution. In reality, we need only specify $k-1$ weights since all weights must sum to 1.

The prior on the means of each component is based on their distance from the mean of the data

$$\mathscr{N}(\mu_k \mid \hat{m}, \eta^{-1} V_k), \tag{4.14}$$

where μ_k is the mean of component k, $\hat{m}$ is the mean of the data, and η^{-1} is the scale applied to the covariance of the component in order to get the covariance of the prior on the mean. A stronger prior (increasing η) would mean a more compact, continuous distribution.

We assume a weakly-informative prior with $\gamma_k = 1$, $\omega = (d+1)/2$, and $\eta = 0$. This amounts to just penalising singular covariance matrices by restricting the minimum size of a component's covariance matrix.

4.3.2 Bayesian Parameter Estimation Tools

The hierarchical model described above is complicated, comprising $N_l = kd(d+1)/2 + kd + (k-1)$ parameters just for the likelihood and an additional $N_p = d + d(d+1)/2$ for any prior on the mean, covariance and weights that apply to all components. This rapidly becomes large ($N_l + N_p = 548$ with $d = 9$ dimensions and $k = 9$ components). In addition, we need to set $N_h = d(d+1)/2 + d + (k-1)$ hyper-parameters for the Wishart covariances, prior means, and Dirichlet weightings. Even though we only need to fit N_l parameters (i.e. we don't fit the prior), simple single chain Metropolis-Hastings (Hastings, 1970) will not suffice here. Even ensemble walker MCMC (such as `emcee`, Foreman-Mackey et al. 2013) will begin to devolve into a random walk with models of 100s of dimensions[2], and No-U-Turn samplers will struggle

[2] `https://statmodeling.stat.columbia.edu/2017/03/15/ensemble-methods-doomed-fail-high-dimensions/`

to move if the test point is not close enough to the peak of the distribution in such a high-dimensional space (Salvatier et al., 2016).

Instead we must consider Hamiltonian/Hybrid Monte Carlo (HMC, Duane et al., 1987), Gibbs sampling (Geman and Geman, 1984), or nested sampling (Skilling, 2004) if we want to sample large portions of the parameter space. HMC uses the gradient of the model to evolve its Hamiltonian and subsequently achieve higher acceptance ratios and faster convergence in very high dimensions. The gradient of the model can easily be estimated using `autograd` tools available for numerical analysis. `Theano` (Theano Collaboration Team 2016) derives gradients for our `PyMC3` (Salvatier et al., 2016) models. The disadvantage of this method is the computational intensity: gradient calculations as well as likelihood evaluations will add up.

Nested sampling is not MCMC. Instead of sampling the posterior like many of MCMC methods including HMC, Metropolis, and associated ensemble techniques, nested sampling initially samples from the prior. This allows nested sampling to generate samples from the entire posterior distribution[3]. In addition, nested samplers such as `PolyChord` (Handley et al., 2015) evaluate the Bayesian evidence and so with these samplers, we can compare models directly. However, nested samplers typically have a few hyperparameters governing the sampler itself which need to be tuned by the user. In addition, the analysis of the output of nested samplers is not as straight-forward as in other methods since weightings need to be applied to the generated samples (see Higson et al., 2019).

A much simpler approach, widely adopted, tried, and tested is the family of Expectation-Maximisation (EM) algorithms (Dempster et al., 1977).

EM assumes the existence of *latent* variables, i.e. hidden variables which generate observable ones. In the case of Gaussian mixtures, the latent variables are the *labels*, z_i for each data point i to its originating component. For example, data point x_i is said to be generated from component k if $z_i = k$.

The log-likelihood of a model, specified by parameters θ, with latent variables z_i generating observations x_i is as follows:

$$l(\theta) = \sum_i \log p(x_i|\theta) = \sum_i \log \sum_{z_i} p(x_i, z_i|\theta) \tag{4.15}$$

[3]In reality, the prior must be bounded, so frequently models which use improper priors cannot be sampled from unless the prior (and hence posterior) volume is restricted

We wish to infer information about the latent variables (in our case, these would be the position and shape of each component of our mixture model). However, Equation 4.15 is hard to optimise, since the labels z_i are not directly observable.

The EM algorithm guarantees the increase in the likelihood with each iteration by calculating the expectation value of "complete data log-likelihood", l_c, given a previous parameter set which attempts to fit the model (E-step, Equation 4.16), and then maximising its value by changing that parameter set (M-step, Equation 4.19). We follow Murphy (2012) in the derivation of the EM algorithm and derive the generalisation to resampled data in Appendix B. Here we only show the derivation of the general EM algorithm for explanatory purposes.

$$l_c(\theta) = \sum_{i=1} \log p(x_i, z_i|\theta) \tag{4.16a}$$

$$= \sum_{i=1} \log[p(z_i|\theta)p(x_i|z_i,\theta)] \tag{4.16b}$$

The complete data likelihood l_c cannot be computed since it is defined in terms of the hidden variables z_i (Equation 4.16), which cannot be observed. Instead, we can take the expectation of the complete data likelihood given our data and the previous parameter set, $\mathbb{E}[l_c(\theta)|\mathscr{D}, \theta^{t-1}]$, also known as the auxiliary function, $Q(\theta, \theta^{t-1})$. Assuming the latent labels are discrete (i.e. each data point originates from a single component), we may use the indicator function

$$\mathbb{I}(z_i, k) = \begin{cases} 1 \text{ if } z_i = k \\ 0 \text{ if } z_i \neq k \end{cases} \tag{4.17}$$

to filter the products in the likelihood for each component. Simplifying the log-likelihood in Equation 4.18, it becomes clear that we only need to calculate the responsibilities r_{ik} of the kth component for the ith data point and the likelihood of the data given each component individually, $\pi_k p(x_i|\theta)$.

$$Q(\theta, \theta^{t-1}) = \mathbb{E}[l_c(\theta)|\mathscr{D}, \theta^{t-1}] \tag{4.18a}$$

$$= \sum_i \mathbb{E}\left[\log\left[\prod_k (\pi_k p(x_i|\theta))^{\mathbb{I}(z_i,k)}\right]\right] \tag{4.18b}$$

$$= \sum_i \sum_k \mathbb{E}[\mathbb{I}(z_i,k)] \log[\pi_k p(x_i|\theta)] \tag{4.18c}$$

$$= \sum_i \sum_k p(z_i = k|x_i, \theta^{t-1}) \log[\pi_k p(x_i|\theta)] \tag{4.18d}$$

$$= \sum_i \sum_k r_{ik} \log[\pi_k p(x_i|\theta)] \tag{4.18e}$$

where we define responsibilities r_{ik} as the probability that data point x_i was drawn from component k.

The optimisation problem now becomes much easier to solve since maximising Q guarantees that l_c and hence $\mathscr{L}_i$ are also maximised (Dempster et al. 1977; Wu 1983; see also Murphy 2012 and references therein). Therefore, we iterate the procedure by first calculating r_{ik} given a set of mixture model parameters θ^{t-1} and then maximising $Q(\theta, \theta^{t-1})$ with respect to a new set of parameters θ

$$\theta^t = \text{argmax}_\theta Q(\theta, \theta^{t-1}), \tag{4.19}$$

where θ^t is the next parameter set in the iterative procedure. For a more detailed description of the derivation of the EM algorithm and the proof of likelihood increase, see Chapter 11.4 of Murphy (2012).

4.3.3 Expectation-Maximisation Iteration for Gaussian Mixture Models

For Gaussian mixture models, EM is a simple iterative procedure. The weights π_k, means μ_k, and covariances Σ_k for each component, k, are updated with the following simple recipe. First, the E-step consists of calculating the responsibilities, r_{ik}, of each Gaussian for each data point x_i. This is simply the probability that data point x_i belongs to component number k and is given

by:

$$r_{ik} = p(z_i = k|x_i, \theta) = \frac{p(x_i|z_i = k, \theta) \cdot p(z_i = k)}{\sum_{j=1}^{K} p(x_i|z_i = j, \theta) \cdot p(z_i = j)} \tag{4.20}$$

$$= \frac{\mathcal{N}(x_i|\mu_k, \Sigma_k) \cdot \pi_k}{\sum_{j=1}^{K} \mathcal{N}(x_i|\mu_j, \Sigma_j) \cdot \pi_j} \tag{4.21}$$

The parameters for the Gaussian mixture model can then be updated in the M-step with the following:

$$\pi_k \to \frac{1}{N} \sum_i r_{ik} \tag{4.22}$$

$$\mu_k \to \frac{\sum_i r_{ik} x_i}{\sum_i r_{ik}} \tag{4.23}$$

$$\Sigma_k \to \frac{\sum_i r_{ik}(x_i - \mu_k)(x_i - \mu_k)^T}{\sum_i r_{ik}} \tag{4.24}$$

where i is the data point index, k is the component index, π_k are the component weights, μ_k are the component means, and Σ_k are the component covariance matrices. These updates were derived by setting the derivative of Q with respect to each parameter to zero.

Since the likelihood is guaranteed not to decrease, EM can be theoretically be run until machine precision is reached. However, singularities can occur with covariance matrix updates and so it is useful to introduce a regularisation on the covariance matrices to penalise moving towards a singularity. In Bayesian formalism, this amounts to a broad prior on the shape of each of the Gaussian components. The EM algorithm can be adapted to include the prior described in Section 4.3.1.1 by modifying the M-step by adding a regularising covariance matrix:

$$\Sigma_k \to \frac{\sum_i r_{ik}(x_i - \mu_k)(x_i - \mu_k)^T + 2W}{1 + 2(\omega - (d+1)/2) + \sum_i r_{ik}}, \tag{4.25}$$

where ω and W are the number of degrees of freedom and the scaling matrix for a Wishart density distribution, $\mathcal{W}(\Sigma^{-1} \mid \omega, W)$ (Bovy et al., 2011).

4.3.3.1 Split-and-Merge

The problem of singularities can be generalised: a guarantee of likelihood increase is not a guarantee of reaching the global maximum (Wu, 1983). We therefore adopt the recommendations of Ueda et al. (2000); Bovy et al. (2011); Melchior and Goulding (2018) to include the "split and merge" algorithm. When the EM iterations seem to converge, we merge the components whose

data responsibilities/labels are the most similar. We sort the component pairs by:

$$J_{merge}(k,l) = \vec{r}_{ik}^{T}\vec{r}_{il}, \tag{4.26}$$

where $\vec{r}_{ik}^{T}$ is the vector of responsibilities for each data point for component k. After choosing which components to merge, we then find the component which least resembles the data.

In theory, the Kullback-Leibler (KL) divergence (Kullback and Leibler, 1951; Ueda et al., 2000), will inform us as to which component to split, since KL divergence describes the similarity between the data and the model. However, we follow the recommendations of Zhang et al. (2003) and sort by the largest eigenvalue, λ, of each component since KL divergence becomes badly affected by outliers as the number of dimensions increases (Zhang et al., 2003; Melchior and Goulding, 2018). Sorting by size works in practice, since the component most likely to be better described by two components is typically the largest one in the mixture (Melchior and Goulding, 2018). We sort the split candidates by the largest weighted eigenvalue

$$J_{split}(k) = \alpha_k \lambda_k, \tag{4.27}$$

and derive new means and covariances for each component along the axis of the eigenvector of the progenitor component:

$$\mu_{new,k} = \mu_k \pm \frac{1}{2}\vec{v}(\Sigma_k) \tag{4.28}$$

$$\Sigma_{new,k} = \mid \Sigma_k \mid^{1/d} \cdot \vec{I}, \tag{4.29}$$

where $\vec{v}(\Sigma_k)$ is the largest eigenvector of component k, $\mid \Sigma_k \mid$ is the determinant of that component's covariance matrix, d is the number of dimensions, and $\vec{I}$ is the identity matrix.

After we split-and-merge the optimal components as discussed above, we freeze the other untouched components and fit the altered ones. When convergence is achieved for those components, we then continue to fit the whole mixture model. If this new configuration does not converge to a more favourable likelihood, we then revert back to the original configuration and end the process.

4.3.3.2 Imputing the missing data

Our hierarchical model contains the effect of selection in optical wavelengths, in $P(S \mid x_i)$, and we must also take that into account in our EM algorithm. We adopt the imputation method of Melchior and Goulding (2018) to include a correction term in the updates to each of our Gaussian components. At each step in the EM algorithm, unobserved samples are "imputed" (or filled in) from the observed model. Using our transform technique to alter one pre-computed Gaussian into an arbitrary mixture of Gaussians, we then weight by the selection probability, $P(S \mid x_i)$, to arrive at the unobserved samples. We set the number of samples to a constant 1,000,000, and weight each sample by the scaling ratio $s = N_{data}/N_{model,obs}$ in order to replicate sampling of the model enough times as to observe N_{data} sources. In this way we can achieve accurate likelihoods and responsibilities for each component even if they are far away from observable regions. `PyGMMIS` (Melchior and Goulding, 2018) relies on rejection sampling to impute their missing values and so `PyGMMIS` becomes inefficient to the point of unsuitability at 9 dimensions.

Accordingly, Equations 4.22, 4.23, and 4.24 become

$$\pi_k \rightarrow \frac{1}{N_{total}} \left\{ \sum_{i \in T(D)} r_{ik} + \sum_{i \in I} s[1 - P(S|x_i)] r_{ik} \right\} \equiv \frac{1}{N_{total}} r_k \tag{4.30}$$

$$\mu_k \rightarrow \frac{1}{r_k} \left\{ \sum_{i \in T(D)} x_i r_{ik} + \sum_{i \in I} s[1 - P(S|x_i)] x_i r_{ik} \right\} \tag{4.31}$$

$$\Sigma_k \rightarrow \frac{1}{r_k} \left\{ \sum_{i \in T(D)} r_{ik}(x_i - \mu_k)(x_i - \mu_k)^T + \sum_{i \in I} s[1 - P(S|x_i)] r_{ik}(x_i - \mu_k)(x_i - \mu_k)^T \right\} \tag{4.32}$$

where N_{total} is the total number of sources predicted by the current model iteration, I is the set of 1,000,000 imputed samples drawn from that model and $T(D)$ is the set of data transformed to the fitting regime.

4.3.4 The Selection and Dispersion Functions

By weighting by the selection probability, $P(S|x_i)$, directly instead of just filtering out data points below a given limit, we can deal with selection effects that are not discrete (e.g. the SNR cut on emission line fluxes results in a fuzzy boundary in flux). To deal with fuzzy boundaries due to signal-to-noise cuts in emission line ratio, it is necessary to estimate the expected signal-to-noise of a given flux, $\mathrm{SNR}(S_\nu)$. Since we only want to estimate the mean SNR for a given flux, we fit to a binned dataset. For each emission line, we use the entire MPA-JHU dataset to fit a double sigmoid curve to the SNR and flux of the binned data. Our method is as follows:

1. Sort all sources into bins of emission line flux.
2. Estimate the distribution of emission line SNR in each bin using a normal distribution fit.
3. Estimate the proportion of sources in that bin with signal-to-noise above our emission line significance cut, $P(SNR > 5)$.
4. Fit a double sigmoid to $P(\mathrm{SNR} > 5 \mid S_\nu)$ in each bin:

$$P(\mathrm{SNR} > 5 \mid S_\nu) = \frac{1}{a + e^{-b(S_\nu + c)}} + \frac{1}{f + e^{-g(S_\nu + h)}} \tag{4.33}$$

   where a, b, c, f, g, h are the parameters to fit.

We use 500 bins in flux between the 1st and 99th percentiles of each emission line flux distribution.

The functional form of $P(\mathrm{SNR} > 5 \mid S_\nu)$ is unimportant so long as it estimates the probability that a given flux can be observed. Figure 4.8 shows that there is a good fit to the data for a double sigmoid relation between SNR and flux.

We also impose the same magnitude limit, redshift limits, and BPT selection that we used to select the data in our selection function as discrete cuts.

Since we are imputing our missing dataset in order to account of selection biases, the imputation must be as realistic as possible. Our observed data have uncertainties which are heteroscedastic (their variances are not constant) across our parameter space. Therefore, our imputed data samples must also exhibit the same scattering of intrinsic values as our observed measurements do. Without such a dispersion, the imputed dataset would have more weight than the observed

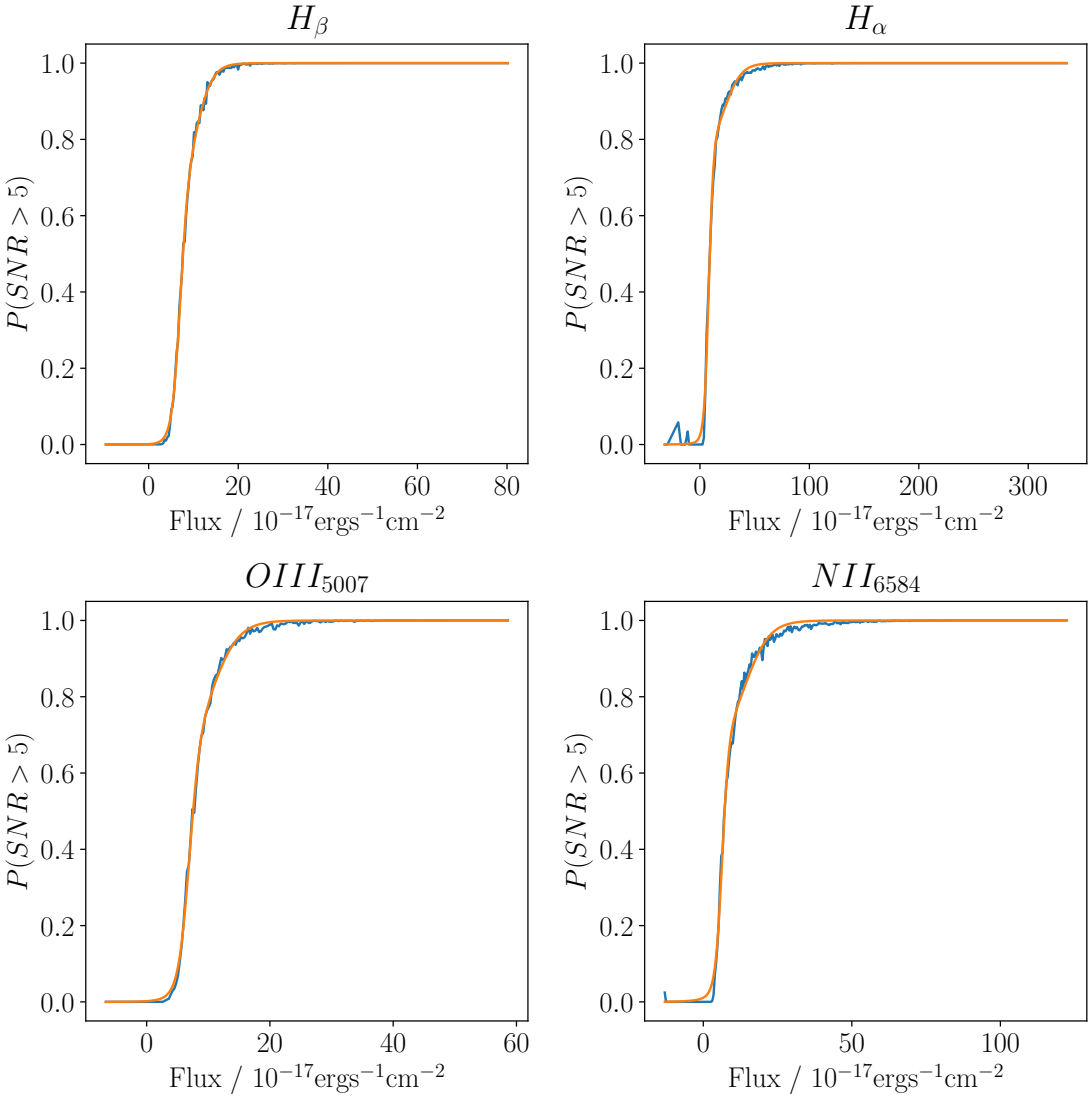

FIGURE 4.8: The fit detection curves for each emission line we use constructed using the entire MPA-JHU dataset. The blue line is the interpolated curve of the mean of the $P(SNR > 5|x_i)$ in each of the 500 flux bins. The orange line is the double sigmoid fit to the mean and standard deviations of the flux bins. Given our 5σ detection limit for each of the emission lines, the y axis represents the probability of being selected given no other selection criteria.

data in the EM algorithm and the resulting distribution would be too broad and shifted too far into the region of unobservability (Melchior and Goulding, 2018). The uncertainties of the data points only enter in the sums of the M-step and so we only need to estimate the *average* covariance for each imputed data point (Melchior and Goulding, 2018). Furthermore, we expect and assume that the uncertainties for each of our parameters is independent from that of the other parameters[4].

[4]This assumption does not need to be made since we can introduce correlated uncertainties when we resample the data points but we use it here since it simplifies the likelihood for now.

Parameter	Fit Curve
redshift	$\sigma_z = const.$
radio flux	$\log SNR_{150MHz} = a + b \log S_{150MHz}$
stellar mass	$\sigma_{\log M_*} = a + b \log M_*$
SFR	$\sigma_{\log SFR_*} = a + b \log SFR_*$
optical magnitude	$\log[\sigma_{m_r}] = a + b m_r$
emission line flux	$\log SNR = a + b \log S$

TABLE 4.2: The uncertainty interpolators for each parameter that will approximate the expected uncertainty $\sigma(x)$ for a given value x.

To estimate the expected uncertainty for a given parameter we fit a curve to the relation between the measurement and its error. We then have a functional form for expected error given a measurement value that we can interpolate over. After we have imputed the missing dataset in the fitting regime, we transform them to the measurement regime, where we disperse those values using a covariance matrix constructed from interpolating the data uncertainties. We then transform the resulting dispersed values back to the fitting regime, resulting in a distribution which resembles what would have been observed.

The interpolators for each parameter's expected uncertainty are given in Table 4.2 and the fits for those distributions are shown in Appendix C.

4.3.5 Convergence and Initial Conditions

Regular non-imputed Expectation-Maximisation procedures always converge monotonically to a local maximum. When imputing missing samples, the likelihood is not computed analytically and so there is the possibility for the likelihood to not increase monotonically.

Analytically calculated EM (such as that found in Bovy et al. 2011) can be run indefinitely and convergence can be detected by the difference between likelihoods at each step. However, since we are using estimated responsibilities and likelihoods, the EM steps will develop into a random walk when they converge and so $d\log(L)$ convergence tests cannot be applied. We therefore attempt to detect convergence every 100 steps by performing a student-T test for a straight line with increasing gradient, if the gradient ever becomes non-significant, we halt the EM procedure. When we detect convergence in this way, we also increase the number of samples in our imputed dataset by a factor of 5 and run for another 100 steps. This ensures the maximum-likelihood estimate is stable to our resolution (number of imputed samples) choice. Figure 4.9 shows the difference between the steps taken by an approximated EM algorithm versus the ones

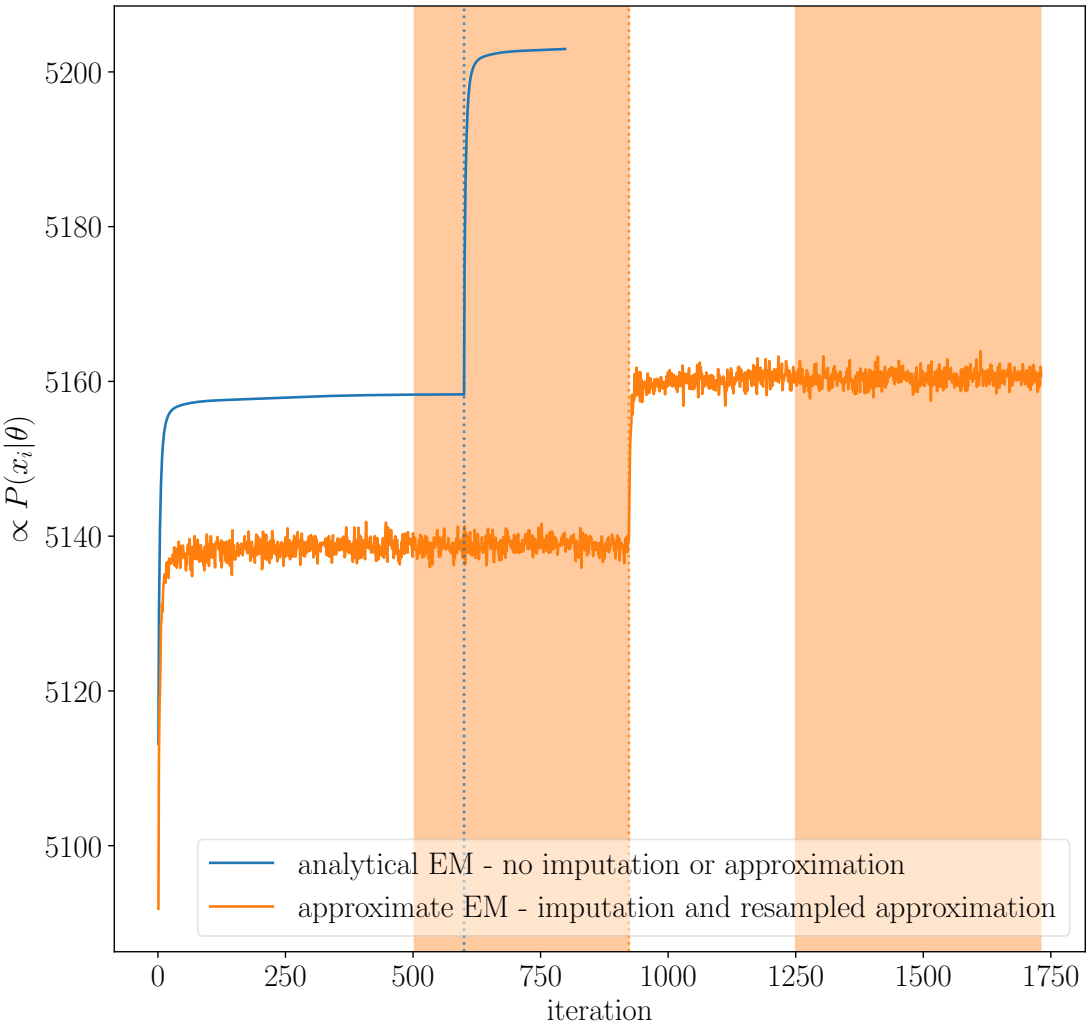

FIGURE 4.9: A demonstration of EM convergence. The curves represent the log-posterior (i.e. the log-likelihood plus the log-prior) of the Gaussian mixture model. Blue shows the iterations from an analytical model which does not attempt to estimate selection effects and the log-likelihood is calculated analytically. Orange shows the iterations from an imputed & approximated model where selection effects are estimated as well as the log-likelihood. The vertical lines show where a split-and-merge attempt has been successful in finding a taller peak in the distribution. The analytical model has converged within a set tolerance and convergence in the imputed model has been detected by the gradient test discussed in the text. The orange shaded region shows the area which was used to test the gradient before convergence.

taken by an analytical EM algorithm. The analytical algorithm converges faster since we do not need to wait to build up enough samples in order to test for convergence.

We perform the split-and-merge technique whenever convergence is detected and we proceed with this routine until split-and-merge no longer produces a significantly increased log-posterior. A significant increase, for an imputed EM algorithm, is when the distribution of likelihoods (extracted from the iterations deemed to be converged) exhibits a 1σ difference from the old

distribution. Figure 4.9 shows example runs for an imputed and non-imputed model along with the effect of the split-and-merge.

Using imputed samples also allows for the possibility of equally likely distributions of components that are not observable. For example, a component may have the same likelihood for the data if its mean is close to the observed data and covariance small as when its mean is far from the data and its covariance is large. Indeed, EM may force components outside of observable regions. We can detect this happening by adding a prior on the total number of galaxies given a known number of observations, from Kelly et al. (2008).

$$P(M|D,S) = C_{D-1}^{M+D-1} P(S \mid \theta)^D [1 - P(S \mid \theta)]^M, \tag{4.34}$$

where M is the number of missing galaxies in our model, D is the number of observed data points and C is the binomial coefficient for total number $M+D$ with D observations. This is equivalent to a negative binomial distribution given a logarithmic prior on the total number of galaxies, $P(\log[D+M]) \propto 1$ (Kelly et al., 2008). When EM moves towards a local minimum in which components can become evermore unobserved, the prior probability of the number of galaxies decreases and we can detect, halt, and reset if necessary.

In order to counter the problem of this type of local minima, we initialise each run of our EM at different starting point and build up a suite of models (see Section 4.3.6 below).

To assign initial starting positions for each component, we first fit a single multivariate Gaussian to the data and draw means from that distribution. Given those means and equal weights, we then assign a random covariance matrix drawn from the prior Wishart distribution. We then scale the covariance by a scalar factor until the selection probability is at least 0.8. In this way we can generate random starting positions whose components are mostly observed. We find that this is more effective than the methods proposed by Melchior and Goulding (2018) or Bovy et al. (2011), since it guarantees that the starting position for a given component will be at least 80 per cent observed.

In order to estimate the density distribution for a given dataset with a finite Gaussian mixture model, it is necessary to specify the number of components that comprise the mixture. Using the Bayesian Information Criterion ($\mathrm{BIC} = (N_p + N_l)\ln D - 2\ln \mathscr{L}_{max}$; Schwarz, 1978), it is possible to compare Bayesian models without computing their evidences. We fit models with different numbers of components to our data without specifying selection effects. After comparing the

BIC of our models fit to the observed data only, we determine that $K = 9$ is the best fit to the observed data, where K is the number of components.

4.3.6 Bootstrapping

In order to compute the full posterior distribution for data with uncertainties we bootstrap the fitting procedure. For 15,000 realisations of the dataset we draw once from each data point's nine-dimensional uncertainty distribution and seed the initial placement of the model Gaussians as described above in Section 4.3.5 using a different random seed. Once the iterative EM procedure has converged for each realisation we have a set of models whose variance reflects the variance of posterior given uncertain input data. We can then apply any function that we would apply to the maximum likelihood model to all models in our bootstrapped set. This enables us to retrieve the posterior predictive distribution given the uncertainty in the data points.

4.3.7 Summary

To summarise, `CANDID` aims to tackle the outstanding problem in astronomy of complete distribution approximation with imperfect data. In order to complete our objective we must deal with the following issues.

1. Heteroscedasticity

   It is common for each data point to have its own uncertainty distribution. Moreover, the size of the uncertainty distribution frequently changes across the parameter space. In the fitting of simple models, heteroscedasticity is incorporated naturally with the addition of a χ^2-like term into the likelihood. `CANDID` currently incorporates unequal uncertainties easily by bootstrapping the models with resampled measurements. In future work, we will use the resampled measurements within the EM-step rather than by bootstrapping.

2. Non-Gaussianity

   Assuming a Gaussian error distribution dramatically simplifies the posterior and hence the analysis. However, the Gaussian assumption is frequently incorrect and may lead to dramatically misleading results. For example, the uncertainty distribution of a flux measurement is easily approximated as Gaussian but given that the intrinsic value is strictly

positive, this assumption breaks down at low signal-to-noise. `CANDID` resamples the uncertainty distribution of each data point consistently such that flux variables remain strictly positive. The Gaussian mixture EM algorithm can readily be extended to incorporate resampled data points instead of directly solving for the convolution of the data uncertainty and model components (see Appendix B for a derivation of the EM algorithm for resampled data).

3. Incompleteness

   It is not possible to rerun the universe nor observe the entirety of a population in astronomy. Typically, incompleteness is addressed by methods such as $1/V_{max}$ or Monte Carlo simulations of point sources given an error map (Long and de Souza, 2017). However, when the number of dimensions grows, what is applicable to each variable individually becomes complicated when considering their covariation. `CANDID` aims to deal with incompleteness naturally by "imputing" the missing values from the approximated observed model given known selection criteria, following Melchior and Goulding (2018).

4. High dimensionality

   The "curse of dimensionality" firmly applies to Gaussian mixture models since each Gaussian component contributes $d(d+1)/2+d+1$ dimensions to the likelihood from its covariance matrix, mean vector and weight relative to the other components. Rejection sampling MCMC techniques start to fail at tens of parameters and interpolating ensemble MCMC (such as `emcee`) fails at hundreds of parameters. The EM algorithm is well suited to finding the peak of the posterior distribution. By dropping the need to sample the entire posterior distribution, we can iterate towards the maximum likelihood peak and then bootstrap, if need be, to sample its width.

4.4 Results and Discussion

Having fit a complete multi-dimensional model for the local star-forming galaxy population, we can extract distributions for parameters of interest such as luminosity functions. In order to extract these distributions, we average the models of our bootstrapped model suite with equal weight given to each model density. To compute posterior predictive distributions over our model (such as the $L_{150\,\mathrm{MHz}} - SFR$ relation), it is necessary to sample the bootstrapped suite and estimate the 1σ credible interval from the variance between the models relative to their

median. Each model predicts a different total number galaxies, N_{total}, and so when sampling from the bootstrapped suite we sample each model proportionally to the total number of galaxies it predicts.

4.4.1 Model Validation

We perform a series of checks to ensure that our model reflects the data and that the model remains physically motivated in the unobservable volumes of the parameter space. We have applied the selection criteria discussed above to our model to produce an "observed model". This is the model an observer would see if our "total model" is correct, given our selection function. The fraction of galaxies that each bootstrapped model predicts is observable is shown in Figure 4.10. The median fraction of observed galaxies is 20 ± 3 per cent, so that the total number of galaxies (given the 2515 observed star-forming galaxies) is $(12 \pm 2) \times 10^3$.

Figure 4.11 shows the averaged model from the bootstrapped suite. The total model, without selection effects applied, extends into regions of 0 probability of selection, where there are no data, and appears to be a reasonable extrapolation of the observed model. For example, the joint distribution of M_r and z is cut nearly in half by our apparent magnitude limit. The total model has filled in the missing region symmetrically to the observed data. The observed model should and does resemble the data over each parameter, when marginalising over all other parameters, except redshift.

The redshift distribution of the observed model, shown in Figure 4.12, succeeds in reproducing the sharp rise and then smooth decline in numbers with increasing redshift. Over all redshifts, the fraction of unobserved galaxies is high but increases towards higher redshifts as expected. In Figure 4.13, we compare the apparent r-band magnitude distribution of our model with the data. The total model has a peak at ~ 17.7 mag, which is also found by Brinchmann et al. (2004), which is shown by the line in Figure 4.13. The MPA-JHU catalogue is roughly complete in magnitude up until $m_r = 17.77$. Our observed model shadows their magnitude distribution and fills in the unobserved galaxies beyond $m_r = 17.77$. Since our model is not aware of a population above $m_r = 17.77$ directly, it has failed to incorporate the existence of the population of quiescent galaxies peaking at ~ 18.5 mag.

It is important that the model can reconstruct complex joint distributions of parameters such as the BPT diagram, where two ratios of luminosities are used to create a two-dimensional

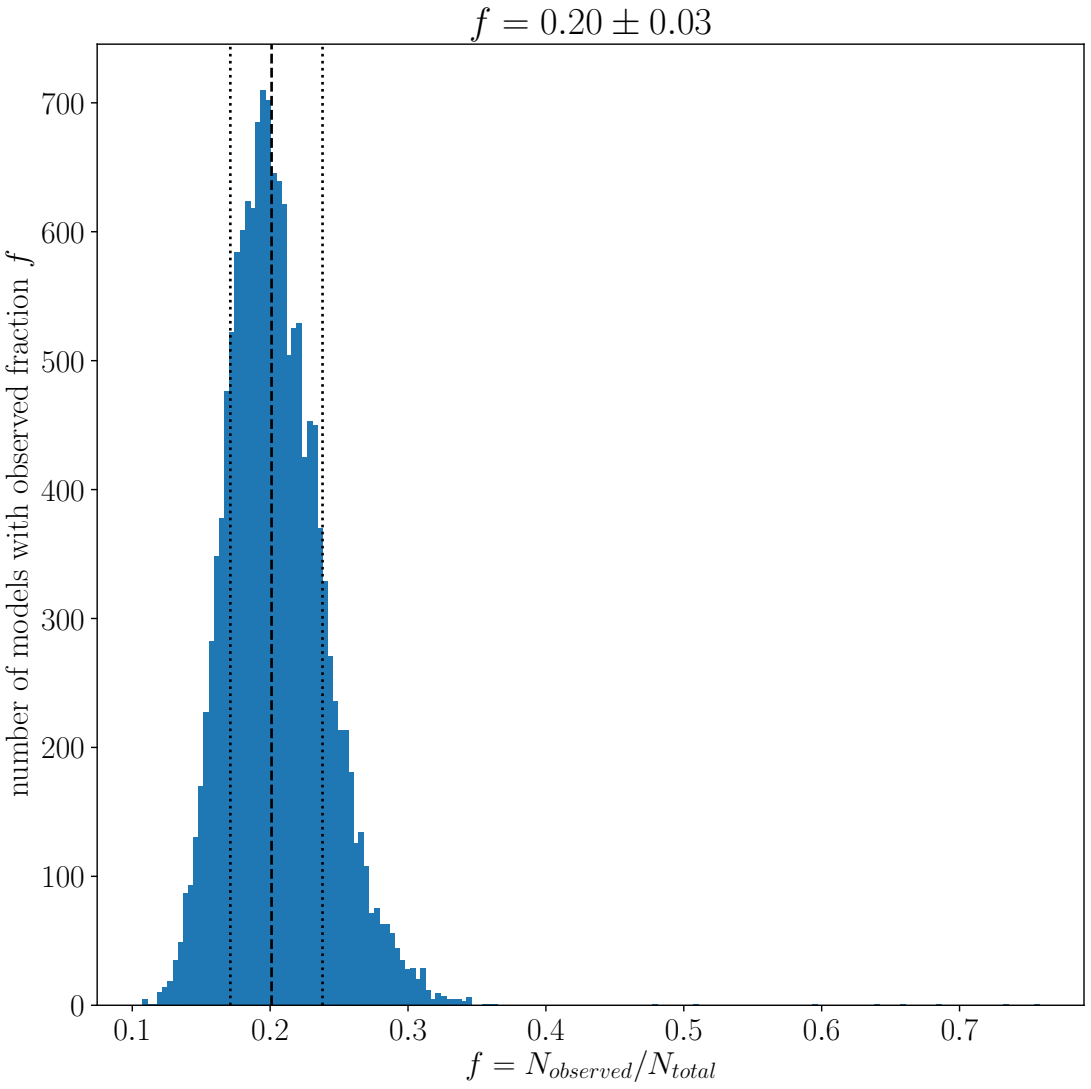

FIGURE 4.10: The bootstrapped distribution for fraction of galaxies that can be observed given the effects of our selection criteria described above. The histogram is constructed from the predicted total galaxy number from each bootstrapped model and the median fraction f along with its 1σ uncertainty are shown as black dashed lines.

classification for SFGs and AGN. Figure 4.14 shows that our observed model can reproduce the star-forming distribution in the BPT diagram. However, our model remains unaware of populations of star-forming galaxies beyond the Kauffmann et al. (2003a) SFG classification line and so it cannot reproduce it. By not selecting by BPT classification, we could, in principle, build a model which describes the whole SFG+AGN population. It would then be a simple task to classify the *model* after the fitting in order to estimate star-forming/AGN proportions across the parameter space. We defer this to a future work.

Finally, we compare the recovered luminosity function for our star-forming sample in Figure 4.15. The luminosity function we estimated using the $1/V_{max}$ method is in agreement with

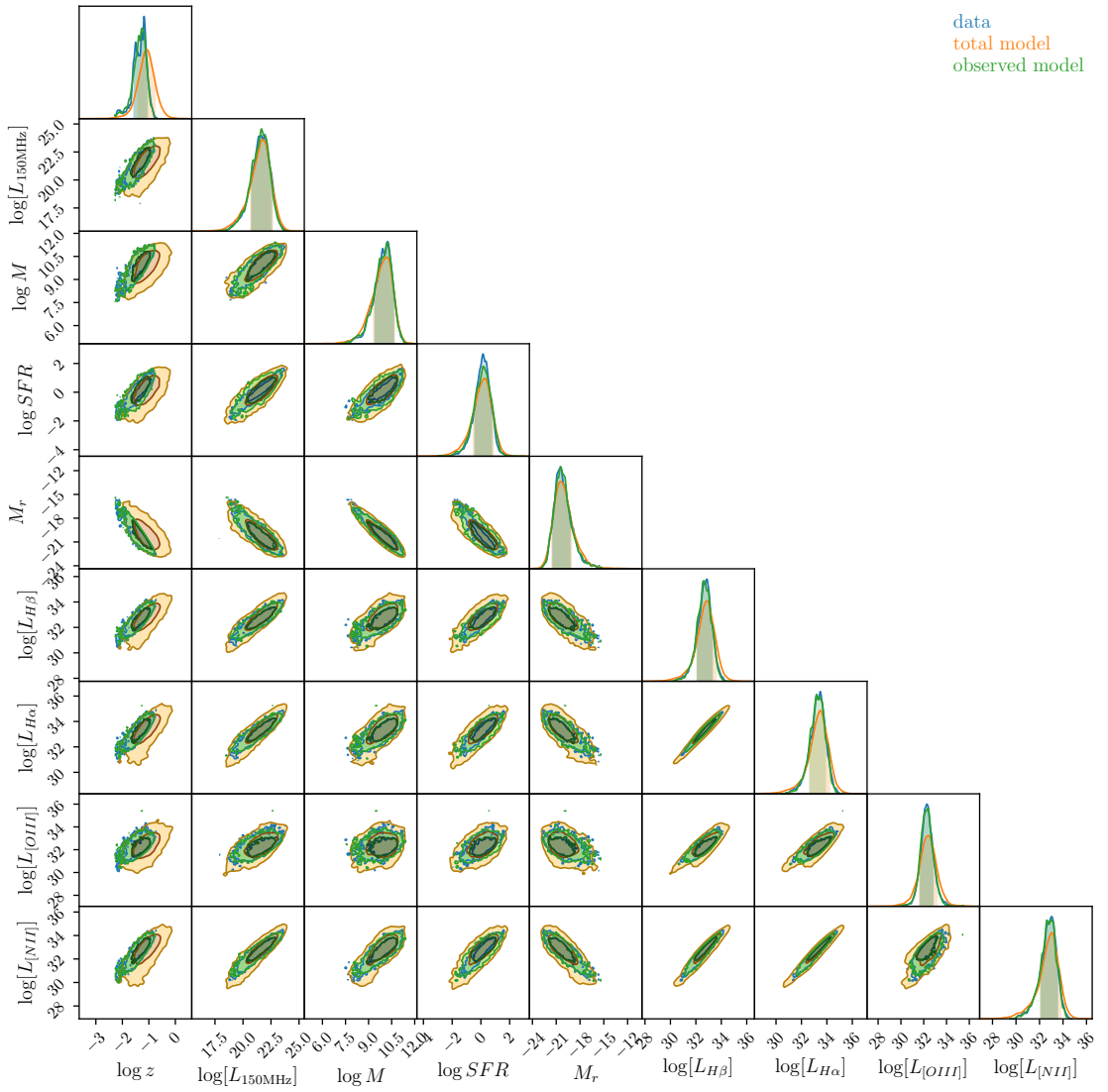

FIGURE 4.11: The complete distribution of the data (blue), total model (orange), and model with selection effects applied (green).

the luminosity of our observed model. The total model contains more galaxies per given luminosity than the observed model and so the luminosity function for a complete dataset should always be above or equal to that for a incomplete dataset. If the dataset were incomplete at random (i.e. no enforced selection criteria), we would expect the total model to have a constant density offset above the observed model. In our star-forming sample, no selection criteria were placed on the 150 MHz luminosities. Therefore, any variable offset in number between the total and observed luminosity functions will be due to indirect effects from the selection in the *r*-band or the emission lines. Since the model infers from observed data, any offset will be seen at low-luminosity where the apparent magnitude and emission line cuts remove the most galaxies.

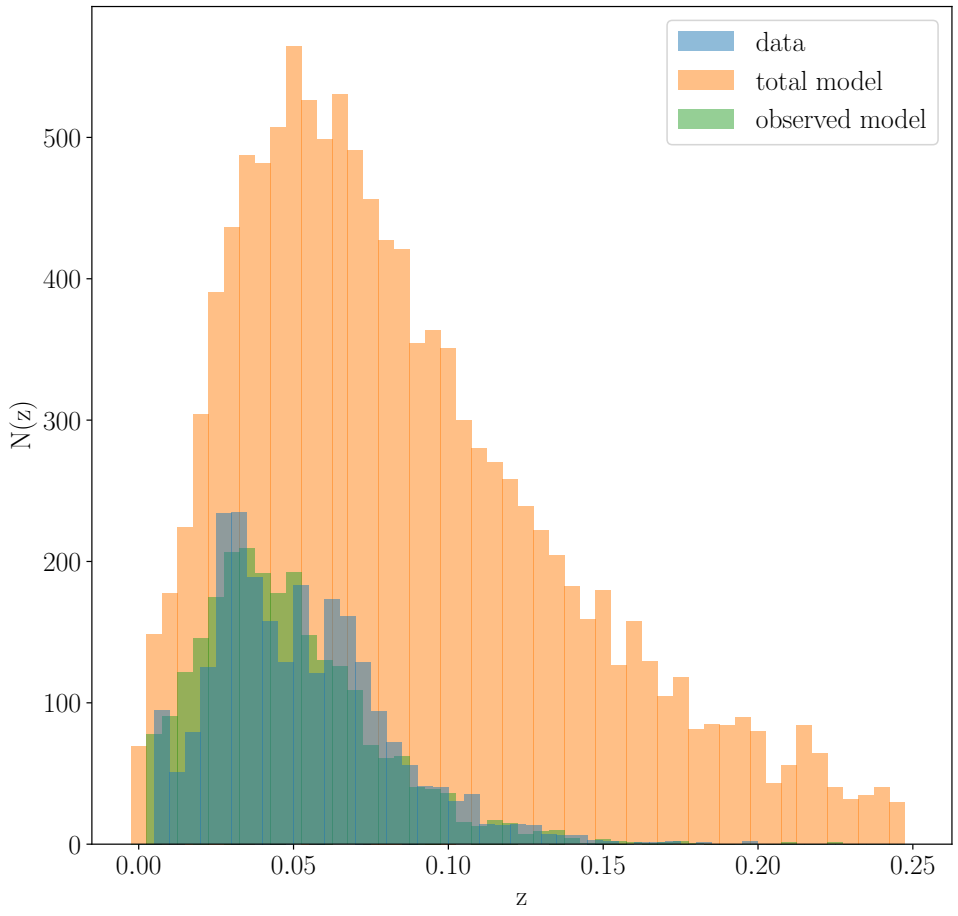

FIGURE 4.12: The redshift distribution for the data (blue), total unobscured model (orange), and model with selection effects applied (green).

Indeed, this is what we see at low radio luminosity, the observed luminosity function is consistently 0.1 dex below the total luminosity function until around $10^{20.5}$ WHz^{-1}, below which there is a hint of more unobserved galaxies. However, the width of the posterior predictive distribution of the luminosity function maintains that the difference between total and observed densities is consistent with a constant 0.1 dex to within 1σ until $10^{19.5}$ WHz^{-1}.

Our technique currently relies on bootstrapping to include low signal-to-noise low radio luminosities and build an uncertainty distribution for the whole model. However, bootstrapping will have the effect of broadening the posterior density where the signal-to-noise of our data is the smallest (at low radio luminosity). Bootstrapping will reconstruct a reliable posterior distribution whose width includes the posterior distribution that we would get by running EM on the

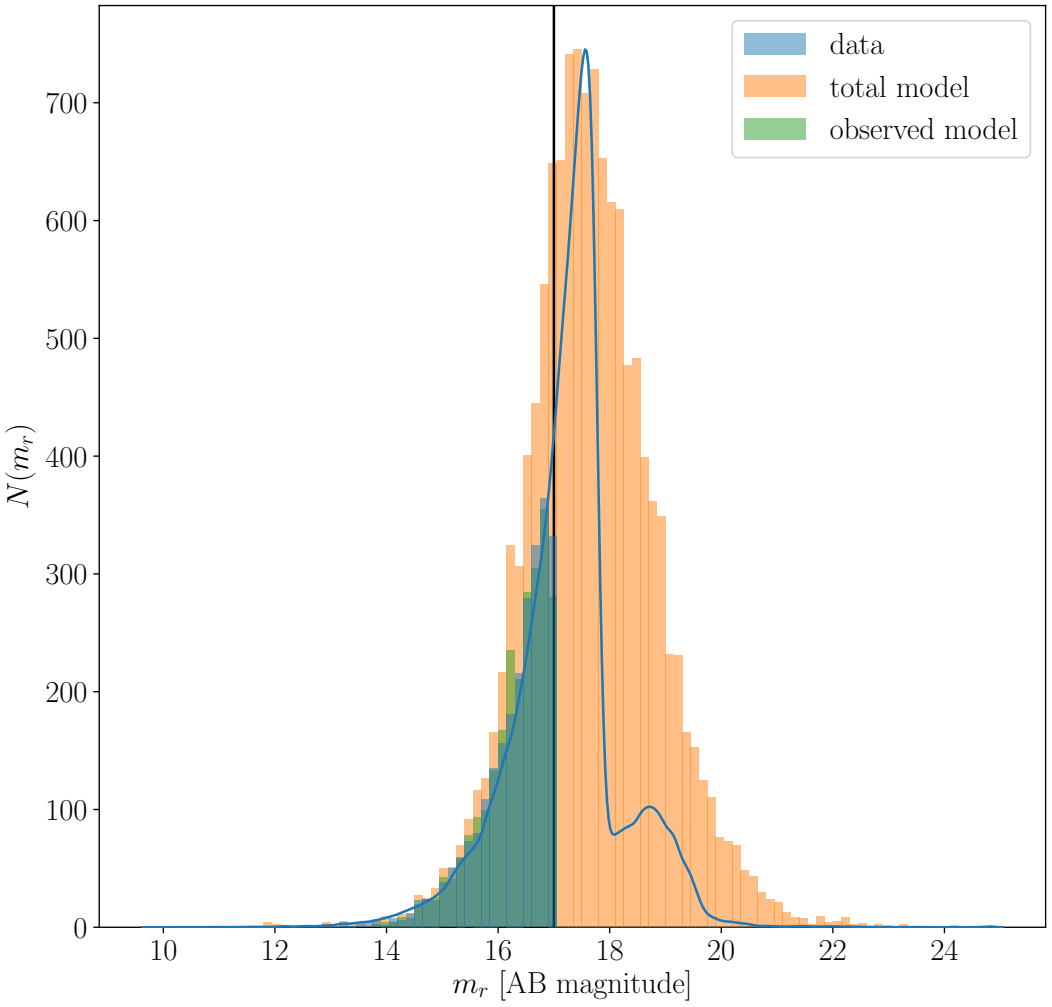

FIGURE 4.13: The apparent magnitude distribution for the data (blue), total unobscured model (orange), and model with selection effects applied (green). The magnitude distribution for all sources from the MPA-JHU catalogue, without any selection criteria applied, is shown as the blue line. The black line shows the magnitude limit in this work.

convolved likelihood (i.e. with measurement uncertainty incorporated at every EM step like in *Extreme Deconvolution*). Therefore, we may still perform statistical tests on our bootstrapped suite of models. Adding resampled measurements into `CANDID` will prevent such broadening and the subsequent posterior predictive distribution for the luminosity function will have a smaller width. This is the subject of future work.

We also observe that the slope of total and observed radio luminosity functions are consistent with that estimated from the LOFAR/*H*-ATLAS survey (Hardcastle et al., 2016) at high luminosities. However, the luminosity distribution is offset from Hardcastle et al. (2016) by $\sim$0.2 dex above $10^{23.5}$ WHz^{-1}. For the moment, we attribute this offset to a greater redshift range in the Hardcastle et al. (2016) sample and a less stringent optical magnitude cut (they use $r < 19$

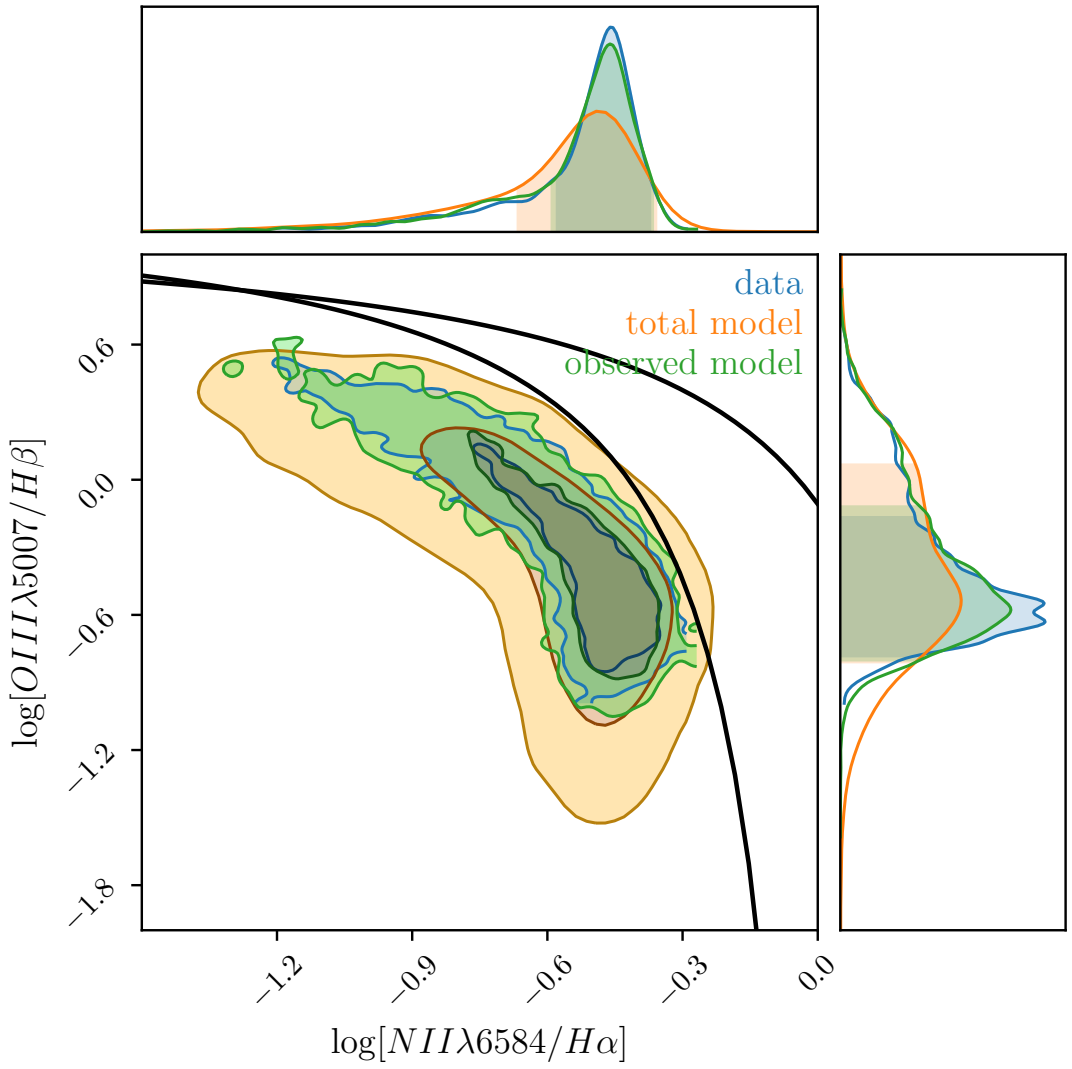

FIGURE 4.14: The BPT diagram for the data (blue), total model (orange), and the observed model with selection effects applied (green). The black lines from Kauffmann et al. (2003a) represent the boundaries between star-forming galaxies, transition objects, AGN.

whereas we use $r < 17$). Hardcastle et al. (2016) also find a steep ($\propto (1+z)^5$) redshift evolution in the luminosity function of SFGs and so the effect of a larger redshift range likely enhances this issue.

Above a luminosity of 10^{24} WHz^{-1} and below 10^{20} WHz^{-1} our model becomes very uncertain, with a posterior predictive width of ~ 0.5 dex.

4.4.2 The Mass Dependency of the SFR-150 MHz Luminosity Relation

Gurkan et al. (2018) found that the relation between 150 MHz luminosity and star-formation

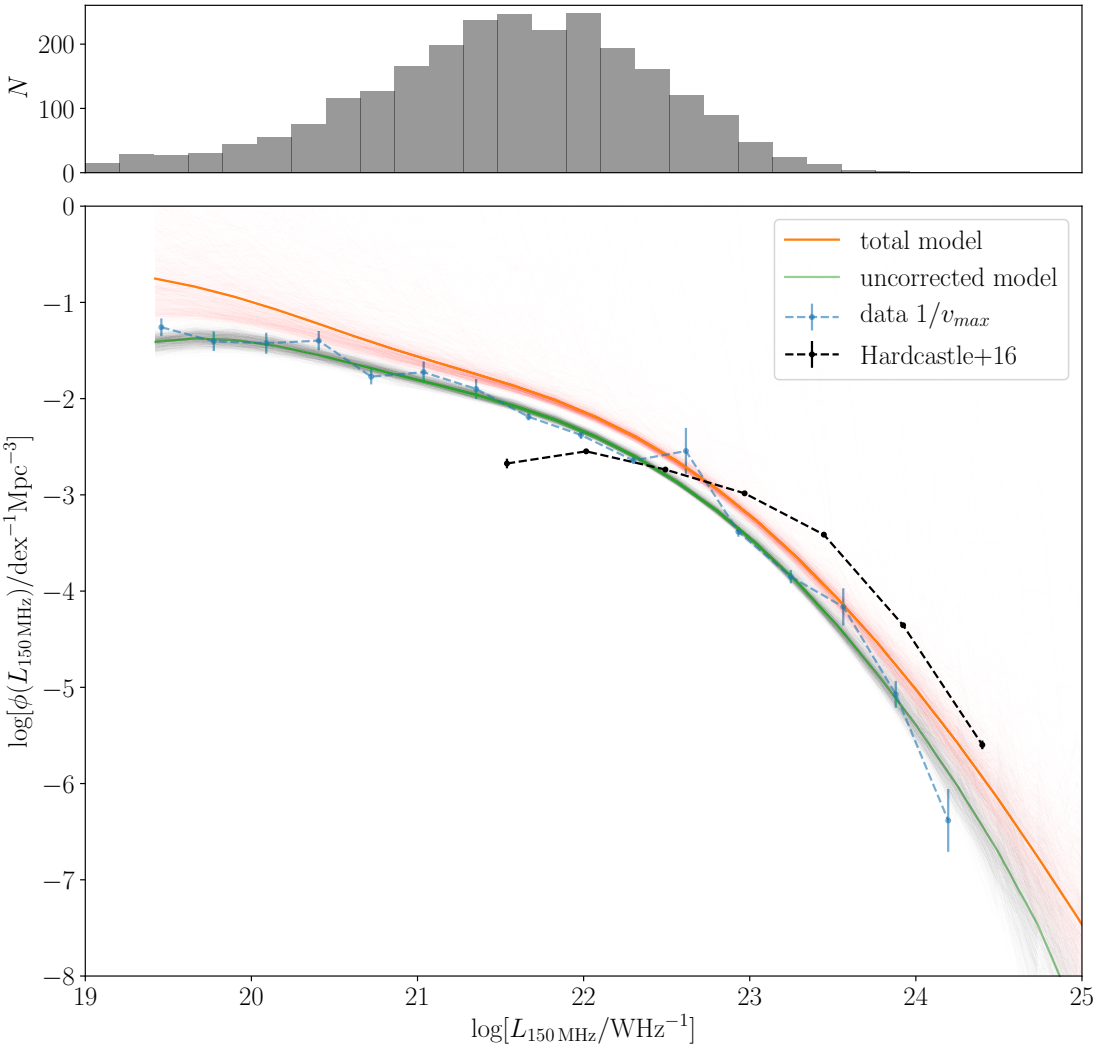

FIGURE 4.15: The luminosity function for our star-forming galaxies. The blue error bars are the $1/V_{max}$ estimations for the 150 MHz luminosity function given our star-forming sample. The orange lines show the total estimated luminosity function for our bootstrapped model suite, with the thick orange line representing their mean luminosity function. The green lines represent the model with our selection effects applied (the uncorrected model). The luminosity function, corrected for incompleteness from Hardcastle et al. (2016) is shown in black.

rate exhibits a mass dependency. High stellar mass galaxies are positioned above the $L_{150\,\mathrm{MHz}}$ − SFR relation for all galaxies whereas low stellar mass galaxies are found below. Furthermore, the slope of the $L_{150\,\mathrm{MHz}}$ − SFR relation exhibits an upturn at low star-formation rates for all masses. Here, we investigate whether these observed derivations from a single $L_{150\,\mathrm{MHz}}$ − SFR relation persist once selection effects have been taken into account. Figure 4.16 shows the $L_{150\,\mathrm{MHz}}$ − SFR relation for the Gurkan et al. (2018) dataset (as points) and our model (shown as continuous curves). We find that the slope of the $L_{150\,\mathrm{MHz}}$ − SFR relation is in agreement with the fit performed by Gurkan et al. (2018) to within 1σ, for the whole star-forming sample at every star-formation rate. Despite the fact that our model is offset in radio luminosity due to

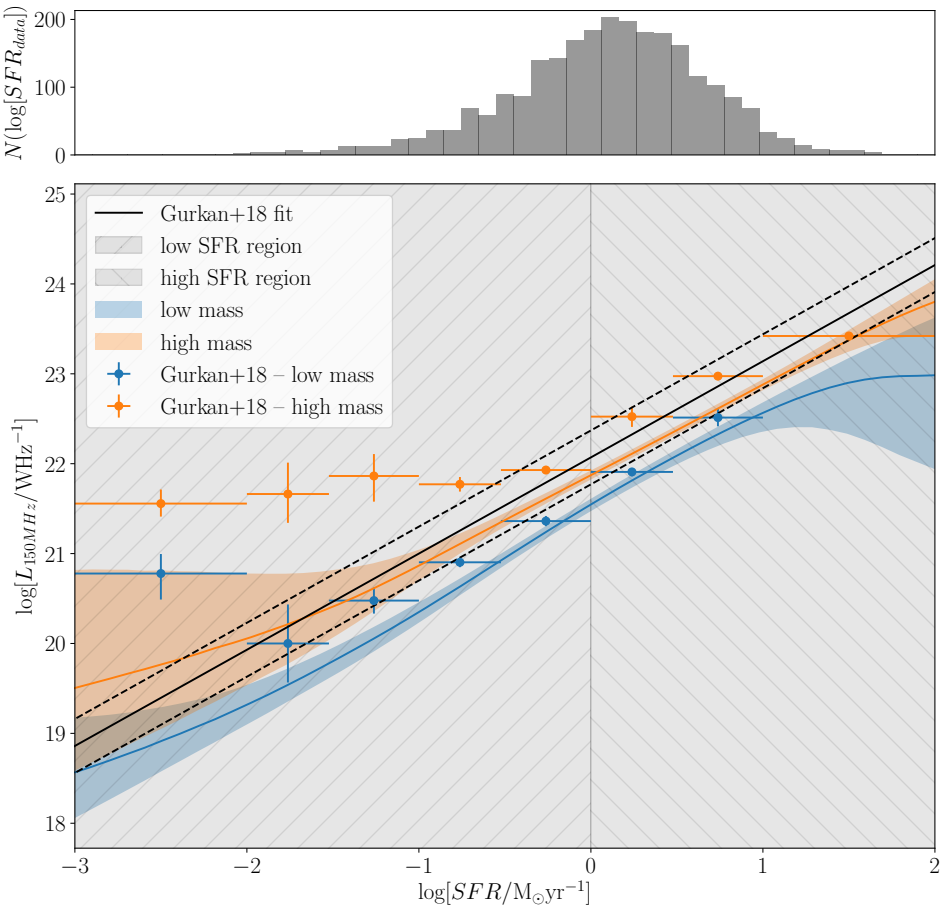

FIGURE 4.16: The L_{150}-SFR Mass dependency. The coloured curves show mean L_{150}-SFR relation for both the low (blue) and high (orange) mass galaxies calculated from the bootstrapped suite of models. The shaded areas represent the 1σ confidence region calculated from the bootstrapped suite of models. The hatched SFR regions mark the low and high SFR regions used to test for a decrease in slope in the L_{150}-SFR relation, as found by Gurkan et al. (2018). The fit to all data in Gurkan et al. (2018) is shown as a black line with the 1σ uncertainty region represented by dashed lines.

the reasons discussed above, we detect a systematic offset of $0.5^{+0.3}_{-0.2}$ dex between low and high mass galaxies in luminosity over all star-formation rates, shown in Figure 4.17, to 2.9σ.

Our inferred posterior predictive distributions have a large width (still within 1σ of Gurkan et al. 2018) and so the gradient of these lines, shown in Figure 4.18, is poorly defined at low star-formation rates.

Therefore, we perform a statistical test, comparing the slopes of the models in regions of low and high star-formation rates. We follow Gurkan et al. (2018) who divide their sample into

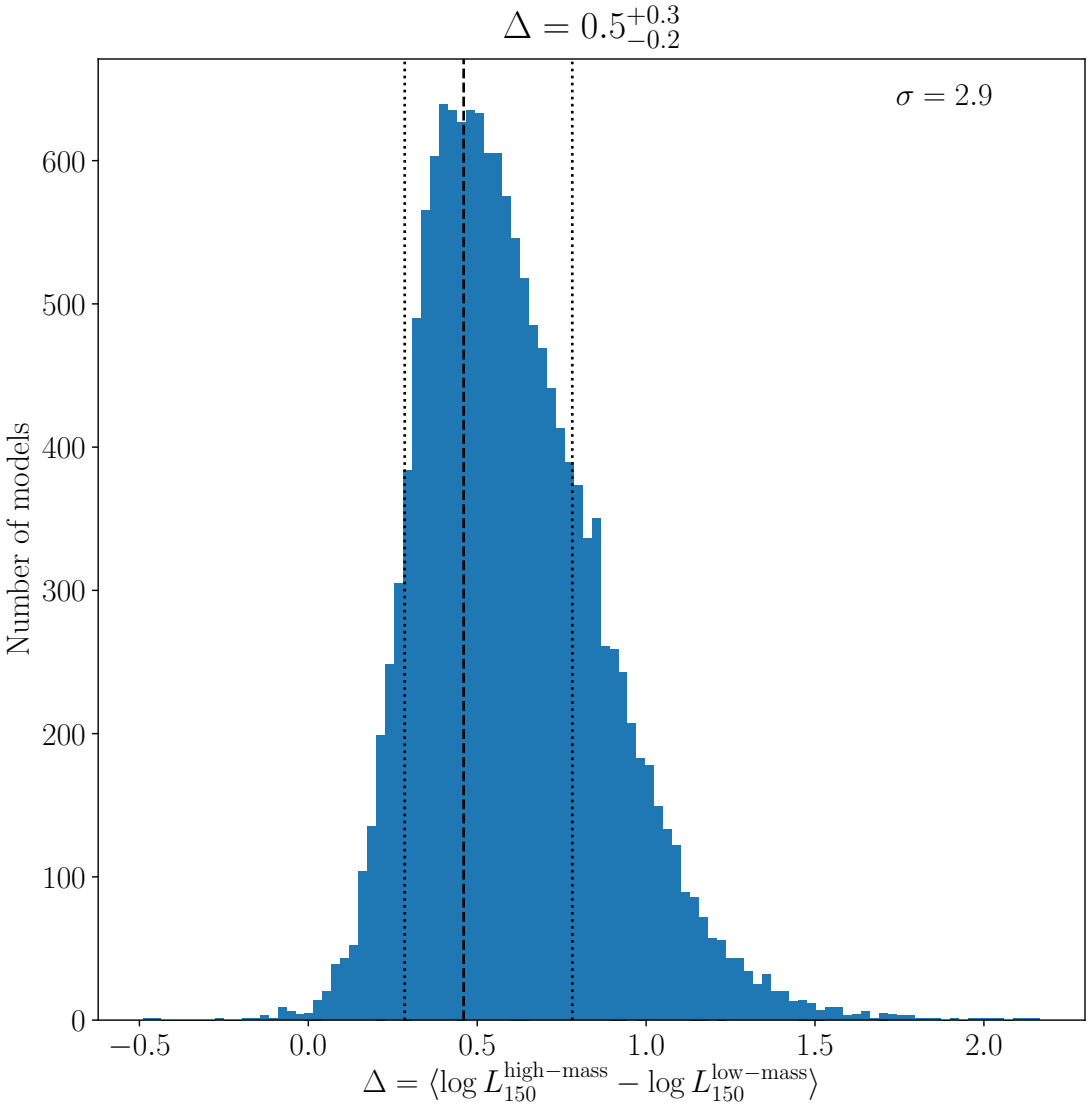

FIGURE 4.17: The distribution of offsets, Δ, between low and high stellar masses over all star-formation rates, from our suite of bootstrapped model. The significance of the offset is indicated in the top right and the 68 per cent highest-posterior-density (HPD) region is bounded by dotted lines with the peak of the distribution shown as the dashed line. The HPD was calculated using the method detailed in Section 3.3.1.

two mass bins: low ($6.0 \leq \log[M_*/M_\odot] \leq 9.5$) and high ($9.5 \leq \log[M_*/M_\odot] \leq 13.0$). In order to test for a lower slope at lower star-formation rates, we also divide our model into bins of low ($-3.0 \leq \log[SFR/M_\odot yr^{-1}] \leq 0.0$) and high ($0.0 \leq \log[SFR/M_\odot yr^{-1}] \leq 2.0$) SFR, shown in Figures 4.16 and 4.18 as hatched regions. This division corresponds to the position of the break in the $L_{150\,\mathrm{MHz}} - \mathrm{SFR}$ relation detected by Gürkan et al. (2018). The region we use for the low-SFR designation contains few galaxies but it is within this region that Gurkan et al. (2018) detect the excess in radio luminosity.

For each bootstrapped model, we calculate the mean difference between the high and low SFR

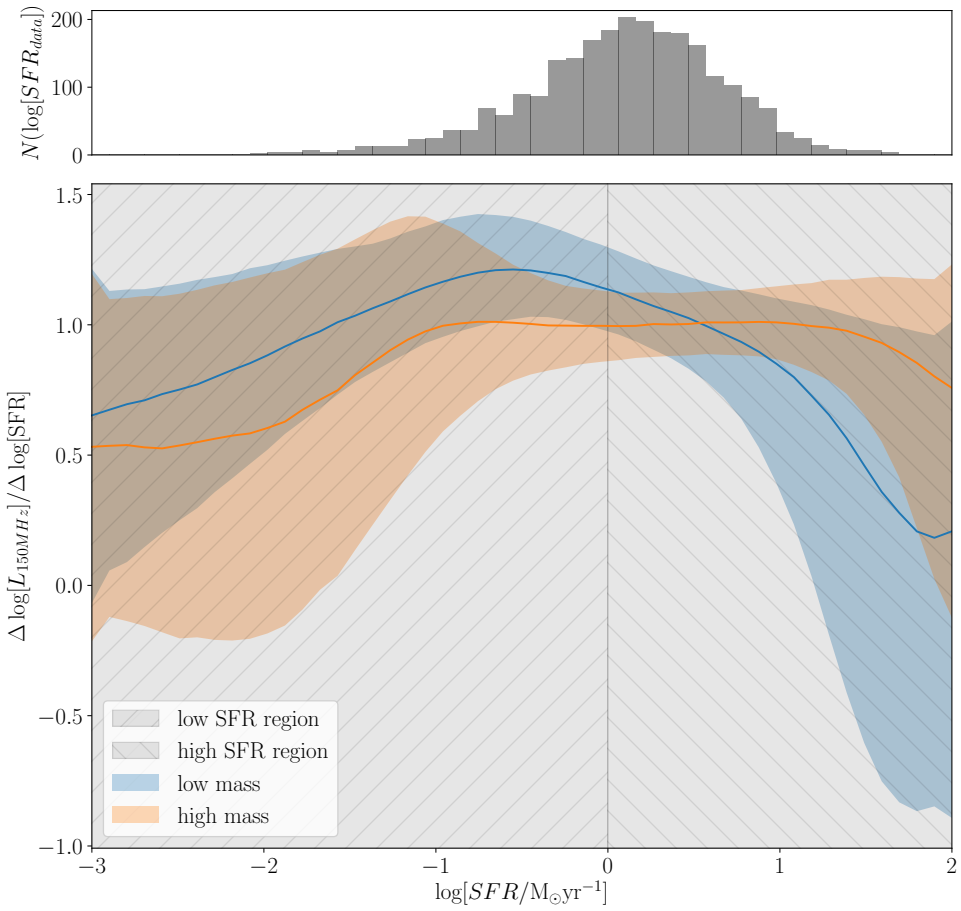

FIGURE 4.18: The gradient of L-SFR-Mass dependency. The lines show the mean gradient of the L_{150}-SFR relation for both the low (blue) and high (orange) mass galaxies calculated from the bootstrapped suite of models. The shaded areas represent the 1σ confidence region calculated from the bootstrapped suite of models. The hatched SFR regions mark the low and high SFR regions used to test for a decrease in slope in the L_{150}-SFR relation, as found by Gurkan et al. (2018).

regions. We then take the distribution of the differences (from all bootstrapped models) and calculate the significance of the slope difference.

Figure 4.19 shows the distribution of the gradient at each SFR given our suite of bootstrapped models and the cumulative probability distribution for the difference in slope. At both high and low masses, we find no strong evidence ($\sigma < 1$) that the difference in slope between SFR regions is larger at high than at low mass. The broadening of our posterior due to bootstrapping, will likely interfere with this test, and so we intend to investigate further, as detailed in Chapter 5.

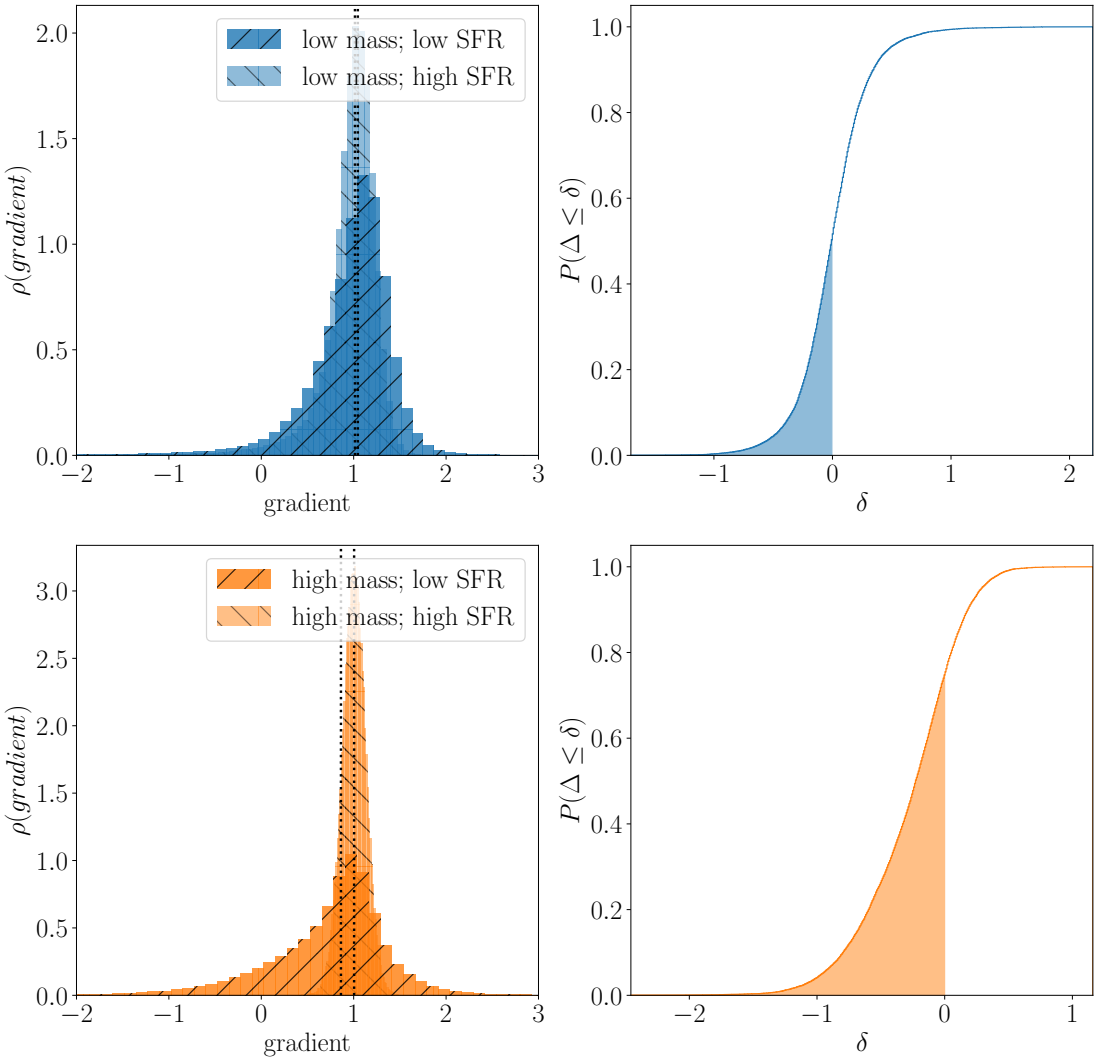

FIGURE 4.19: The probability density distribution of the gradient (left column) at high (dark colours) and low SFR (light colours) for both low (top panels, blue) and high (bottom panels, orange) mass galaxies, given the full bootstrapped suite of models. The dotted vertical lines indicate the median of each distribution. The hatching for each SFR region matches that found in Figures 4.16 and 4.18. The right column shows the cumulative probability distribution for the difference in slopes, Δ, at high and low SFR. The shaded regions in the right column show the probability mass for a slope difference between high and low SFR of less than zero.

4.4.2.1 Implications

An excess of radio luminosity at low star-formation rates indicates a deviation from the calorimetry approximation (Voelk, 1989), whereby all accelerated cosmic rays remain in the galaxy's magnetic field, emitting synchrotron radiation. The deviation is expected in that star-burst galaxies approximate calorimetry well (Lacki et al., 2010) with galaxies that are forming fewer stars emitting *less* synchrotron radiation for their star-formation rate. However, this is not what Gurkan et al. (2018) see. In contrast, they see an *excess* of 150 MHz luminosity regardless of

the mass of the galaxy. Assuming that this is a real phenomenon, either sources of synchrotron emission other than supernovae-accelerated cosmic rays are present to boost the emission at low star-formation rates or the galaxy's magnetic field is boosted. Gurkan et al. (2018) show that many of the BPT-unclassified high mass objects have much more radio luminosity for their mass with considerable overlap with the star-forming locus. The most luminous BPT-unclassified galaxies are classified as AGN by Best and Heckman (2012) indicating that low-luminosity contamination could be another source of the excess radio emission (if the AGN branch continues to overlap with SFGs at lower masses).

Another source of excess radio luminosity could be attributed to the large 10 arcsecond aperture they used to estimate total source flux. Gurkan et al. (2018) used this aperture in order to capture all dispersed flux from star-formation and hence reduce the aperture correction that would be required. However, confusion with nearby sources is possible and so other sources could be contributing to the flattening of the $L_{150\,\mathrm{MHz}} - \mathrm{SFR}$ slope. Since Gurkan et al. (2018) and this work both used the same aperture, this cannot be the source of the discrepancy.

However, our bootstrapping method likely broadens the posterior to a width where a change in slope is unlikely to be detected. We therefore cannot distinguish between the cases where selection effects play a role in increasing the average luminosity at low star-formation rates or that we simply cannot detect those effects with the present configuration of `CANDID`. We intend to improve our method by incorporating the uncertainties at each EM iteration rather than by bootstrapping the model.

4.4.2.2 Supernovae Contributions with Horizon AGN

At very low star-formation rates the energy injected into cosmic rays by type-II supernovae is reduced since these supernovae occur at the end of the lifetime of giant short-lived OB stars. In this case, energy injection from type-Ia supernovae will become more important, as their rate depends less on star-formation rate since they occur by chance in binary systems. Therefore, the rate of type-Ia supernovae depends more on the stellar mass of the galaxy with more massive galaxies having a greater frequency of both types of supernovae. The relative contributions of type-Ia and type-II change over stellar mass and star-formation rate. Horizon AGN (Dubois et al., 2014) provides us with an opportunity to estimate the luminosity excess due to type-Ia supernovae.

Here we conduct a simple experiment to be expanded upon in a future work. We employ the cosmological-volume hydrodynamical simulation, Horizon AGN (Dubois et al., 2014) based on the RAMSES (Teyssier, 2002) adaptive mesh refinement code. Horizon AGN simulates a volume with length $100h^{-1}$ cMpc with initial conditions set from the WMAP ΛCDM cosmology (Komatsu et al., 2011) using 1024^3 dark matter particles with a mass resolution of $8 \times 10^7 \mathrm{M}_\odot$. By incorporating AGN feedback, Horizon AGN is in good agreement with observed stellar mass and luminosity functions as well as the colour-magnitude diagram and colours of merging galaxies (Kaviraj et al., 2015, 2017). Horizon AGN provides the energy output from supernovae types Ia and II over the last 10 Myr (denoted here as E_{SN}) given a binary fraction. We adopt the binary fraction 0.55 from the Large Sky Area Multi-Object Spectroscopic Telescope (LAMOST Tian et al., 2018), though scope remains for running this analysis over a range of binary fractions (which we postpone to a future work).

This simple look at Horizon AGN supernovae energies is intended as a brief investigation into the fractional responsibility of supernovae type-Ia for the mass-dependency of the $L_{150\,\mathrm{MHz}} -$ SFR relation, in order to lay the groundwork for a future joint model of simulation and observation. As such, we fit only a simplistic model (1 Gaussian component) here and will investigate more complex (such as those detailed above) in the future. We fit a single component model independently to our data and to the Horizon AGN dataset using the same methods as described in 4.3, except that we confine our fit to the observed data without imputation. We defer complex imputed fitting to a future work.

Following Lamastra et al. (2013); Sparre et al. (2015) we renormalise the Horizon AGN star-formation rates to our observed star-formation rates by transforming the fit stellar-mass/star-formation rate distribution for Horizon AGN to our distribution for our data. Given that both are modelled by a single Gaussian component, this amounts to an assumption that our star-formation rate and stellar mass distributions are the same for the rest of the analysis. We can calculate the conditional distribution of the supernovae energy given some observation by generating samples from the the Horizon AGN model given a sample from our LoTSS model. By doing this for a large number of samples, we can build up a conditional distribution for the observed variable.

Figure 4.20 shows the relation between injected energy from type-Ia and type-II supernovae. For type-II supernovae, the star-formation rate traces the injected energy tightly, whereas for type-Ia supernovae the relation becomes dispersed. This is expected since type-II supernovae occur shortly after bursts of star-formation (100 Myr).

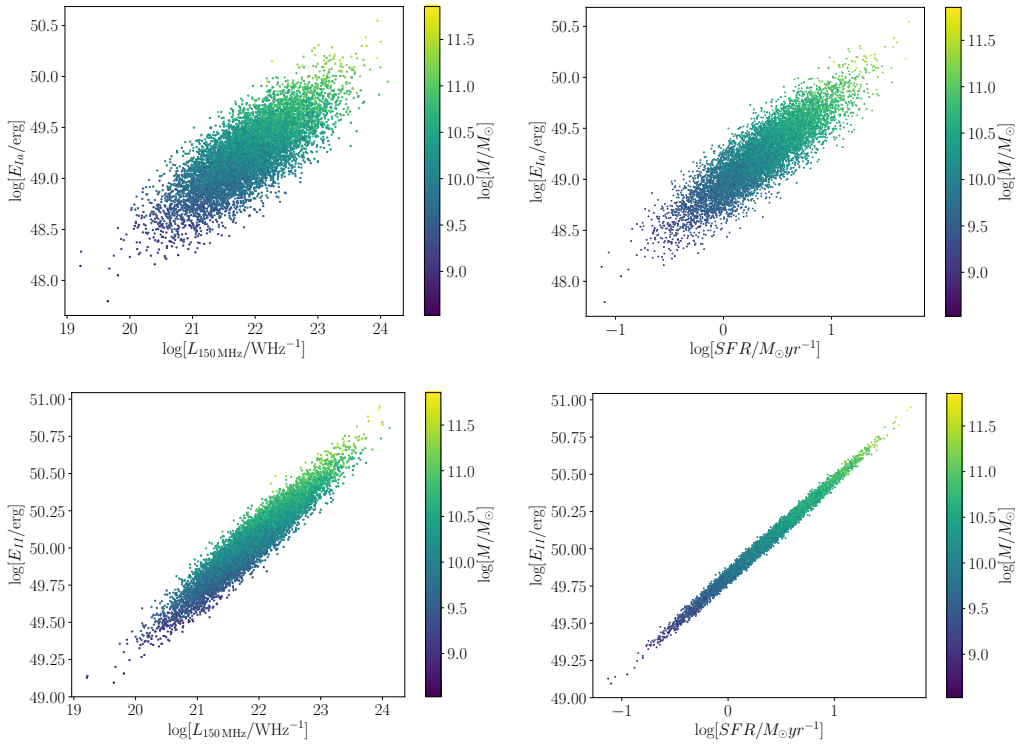

FIGURE 4.20: The energy injected by type-Ia (top row) and type-II (bottom row) supernovae over the last 10 Myr (as estimated in the Horizon AGN simulation) as a function of the 150 MHz radio luminosity of the HETDEX star-forming sample (left column) and as a function of the star-formation rate of the HETDEX star-forming sample (right column). The colour bar indicates the stellar mass of each galaxy. This plot assumes that the star-formation rate distribution of Horizon AGN and our dataset are the same as discussed in the text.

The energy-luminosity relations in both types of supernovae exhibit a strong mass dependence which varies across the width of the relation. This is a constrained simple model with limited applicability and with no selection effect incorporation. However, we show here that there is a more complex relationship between supernovae injected energy and luminosity/SFR than supernovae type-II can account for alone. Fitting a more complex model (as done above) would estimate the amount of mass-dependency that can be attributed to supernovae type-Ia & type-II and has the potential to explain our results from Section 4.4.2.

4.5 Conclusions

Using a star-forming sample, classified by BPT and observed by LoTSS DR1 in the HETDEX region, we have tested the existence of a stellar-mass dependency in the $L_{150\,\mathrm{MHZ}}-$SFR relation. To do this we have created the PYTHON package `CANDID` which, building upon the work of Kelly et al. (2008); Bovy et al. (2011); Hinton et al. (2017); Melchior and Goulding (2018) that

incorporates the treatment of individual non-Gaussian measurement error, along with the "imputation" of missing/incomplete data into a technique that reconstructs complete distributions of galaxy properties.

1. Using the 150 MHz aperture flux measurements from the LoTSS first data release (Shimwell et al., 2018) together with the MPA-JHU catalogue (Brinchmann et al., 2004), we construct a sample of star-forming galaxies based on the BPT classification scheme.

2. Whilst there are methods that exist to deal with missing and uncertain data (Kelly et al., 2008; Bovy et al., 2011; Hinton et al., 2017; Melchior and Goulding, 2018), we find that current methods do not incorporate the number of parameters needed, do not easily extend to high dimensions and cannot deal with non-Gaussian uncertainties. Most of all, however, they do not incorporate solutions to fit missing, uncertain, and non-Gaussian data in one technique.

3. Whilst building our hierarchical model, we find that traditional MCMC samplers such as Metropolis or affine ensemble (e.g. `emcee`; Foreman-Mackey et al. 2013) become inefficient to the point of being misleading at the dimensionality that we consider here. Our model requires the use of other sampling techniques such as Gibbs, nested, or slice sampling for full posterior sampling. We simplify the task by using Expectation-Maximisation (EM) whereby the posterior is maximised instead of sampled.

4. We bootstrap our method across our data, whose uncertainties have been resampled and the starting positions for the EM randomised 15,000 times. From our suite of bootstrapped models, we can estimate the posterior distribution (albeit one with a width larger than if we had performed resampling at each EM step) and hence the posterior predictive distributions for a number of related quantities (such as luminosity functions).

5. We find that when we apply the selection effects present in our star-forming dataset, our model resembles the input dataset. However, we find a deviation from the Hardcastle et al. (2016) 150MHz luminosity function that we attribute to their larger redshift, their higher apparent *r*-band magnitude limit and the broadening of our posterior due to bootstrapping.

6. We find that the luminosity-SFR relation at 150 MHz depends on mass (2.9σ offset between high and low stellar masses of $0.5^{+0.3}_{-0.2}$ dex). This is in agreement with Gürkan et al. (2018). However, we do not find evidence for a difference in the slope of the relation at low star-formation rates.

7. We also perform a simple comparison with the Horizon AGN simulation, constructing an $L_{150\,\mathrm{MHz}} - E_{SNe} - M_*$ relation for both Type-Ia and Type-II supernovae. Whilst we find a strong mass dependency in the relation between injected energy and observed luminosities and star-formation rates, we leave detailed investigation of their differing responsibilities to a future work.

We conclude by stating that more work is needed to quantify the mass dependency of the luminosity-SFR relation at 150 MHz further. In particular, including the resampled measurement uncertainties within the EM algorithm will act as to shrink the width of the posterior predictive distribution and may also give less weight to low signal-to-noise galaxies.

However, we find that fitting the complete distribution of astrophysical quantities is both practical and desirable. It enables detailed and fast analysis of marginal and joint distributions of parameters whilst adjusting for selection effects in the dataset. We intend to improve the algorithm further and use it to assess the nature of the redshift evolution of the main sequence of galaxies and the $L_{150\,\mathrm{MHz}} -$ SFR relation. There is also scope for its use in the joint modelling of AGN and star-forming galaxies in the above parameter space at the same time. In addition, we have shown that it becomes very easy to construct a joint model between simulations and observations through the use of Gaussian mixture models.

Chapter 5

Summary and Future Work

5.1 Summary

In this work, we have discussed the reliability of current scaling relations and their applicability to large, previously unobserved, regions of parameter space. We have highlighted and quantified deviations from the assumptions that are regularly used to estimate star-formation rates and black-hole masses. We have showed that whilst selection effects, sample biases, and instrumental sensitivity limits contrive to interfere with the estimations of such relations, it is both possible and desirable to quantify these effects simultaneously with their estimation. Indeed, in the current era of large-scale surveys in radio (e.g. with the SKA and LOFAR), infrared (e.g. with JWST), and optical (e.g. with LSST) wavelengths, the production rate of observational data will be large enough to make techniques, such as those described in this thesis, both statistically powerful and desperately required.

5.1.1 The FIRC

First, we discussed the existence of the Far-Infrared Radio Correlation (FIRC) at low frequency and its variability over galaxy properties. Frequently used to bootstrap radio star-formation rates from known infrared scaling relations, the stability and predictability of the FIRC is vital to the estimation of star-formation rates using radio luminosity.

We show that the correlation, readily seen with high frequency observations, persists at low frequency when observed with LOFAR. However, we find that both the slope of the FIRC and

the ratio $q = \frac{L_{IR}}{L_{rad}}$ are different at 150 MHz, implying that simply extrapolating high frequency relations will result in incorrect estimations of star-formation rates. Furthermore, we found that the FIRC, varies dramatically as a function of mid-infrared colour. Using the WISE mid-infrared colours and the Wright et al. (2010) star-burst classification, it appears that star-forming galaxies exhibit more radio luminosity for a given infrared luminosity at higher SFR.

Upon further investigation, we find that the slope of the FIRC depends on redshift, stellar mass, and dust temperature. We attempt to quantify the responsibility of each of these factors for the variation observed across the mid-infrared diagram, showing that 16, 36, and 48 per cent of variation is due stellar mass, dust temperature, and redshift respectively (if we assume a linear dependence for each variable).

In conclusion, we find complex behaviour of the FIRC over normal star-forming galaxies (as a function of redshift, stellar-mass, and star-formation rate). This variation needs to be understood in order to use radio luminosity as a star-formation rate indicator. In the era of large radio surveys by the upcoming SKA and its pathfinders (such as LOFAR), the opportunities for a dust-impervious radio star-formation rate indicator are numerous. Indeed, this advantage becomes evermore important with higher redshift and deeper surveys where other photometric information becomes more sparsely available. We hope that the work done here lays the foundation for a more sophisticated radio star-formation rate indicator in the future.

5.1.2 Photometric Reverberation Mapping

In Chapter 3, we discuss a new technique for the reduction and analysis of reverberation mapping (RM) and the efficiency of photometric RM.

Established estimates of black-hole masses are distinctly biased to low-redshift objects. The vast majority of catalogued black hole masses were estimated using spectroscopic techniques. Past long-term spectroscopic observations have targeted the brightest QSOs in order to maximise signal-to-noise. Furthermore, when targeting higher redshift QSOs, their inherent optical variability becomes increasingly affected by cosmological time dilation, increasing both the required frequency of observations and total duration of the campaign. Therefore, the most reliable lag measurements that we do have, thanks to reverberation mapping (RM) campaigns, are also biased to shorter time-scales, for a given L_{5100}.

In Chapter 3, we propose and implement a campaign of photometric RM observations, whereby we achieve the same signal-to-noise, per target QSO, as the SDSS spectroscopic RM campaign (Grier et al., 2017) but with a quarter of the observation time. Using the robotic capabilities of the Liverpool Telescope, we observe 10 QSOs (at redshifts which align one of the available redshifted Hα photometric filters to the Hβ emission line of the QSOs) with only the broad *i*-band and narrow Hα photometric filters. For the target with best time-scale coverage, we create a suite of light-curve simulations based on the damped random walk model of QSO variability and based on the signal-to-noise and cadence of our observations for that target.

We test the efficacy of the `Javelin` (Zu et al., 2013, 2016) fitting procedure with those simulated light-curves of known lag. We find that `Javelin` can recover lags that are less than a third of the duration of the observing campaign. Characterising the distribution of artefacts in the lag distribution retrieved by `Javelin`, we increase the signal-to-noise of our lag detection by a factor of 3.

After mitigating the effects of artefacts and aliasing in the probability distributions that `Javelin` produces using a suite of simulated light-curves, we estimate a lag of 72^{+5}_{-1} days which is equivalent to a black hole mass of $10^{8.28^{+0.12}_{-0.07}}\mathrm{M}_{\odot}$ for the QSO `SDSS J144645.44 +625304.0`.

Finally, we estimate that the photometric RM methodology increases efficiency over the spectroscopic SDSS-RM campaign (Shen et al., 2015a; Grier et al., 2017) by 310 per cent. We propose that this efficient means of estimating black hole masses can be applied with future large-scale surveys such as JPAS and LSST.

5.1.3 The $L_{150\,\mathrm{MHz}} - \mathrm{SFR}$ relation quantified using `CANDID`

The previous two projects highlighted the problem of deriving complete distributions from noisy, biased, and codependent data in astronomy. For example, estimating the variation of the FIRC required quantifying the contribution of three other parameters, and current reverberation mapped black-hole masses are biased to lower lags due to the length of observational campaigns.

In Chapter 4 we construct a Gaussian mixture model fitting process called `CANDID` which can tackle the issues of multi-dimensional, noisy, incomplete, and non-Gaussian data *in general*. We incorporated the different approaches taken by Kelly et al. (2008); Bovy et al. (2011); Hinton et al. (2017); and Melchior and Goulding (2018) into our method so that we can infer the

complete distribution of galaxies from the observed data. Given a quantified analytical selection function, we can reconstruct the full distribution that would be seen in the absence of such obscuration. It can accomplish this even when the data are noisy and possess non-Gaussian uncertainties. We can reconstruct the full distribution of 150 MHz luminosity, stellar mass, star-formation rate, optical magnitude, and BPT emission lines over redshift for the new LoTSS DR1 dataset. This enables us to better account for incompleteness as well as known correlations in the data, such as Malmquist bias.

Having inferred the intrinsic distribution of galaxies in the absence of selection effects, we confirm the existence of a mass dependency in the $L_{150\,\mathrm{MHz}} -$ SFR relation as found by Gürkan et al. (2018). However, we find no evidence for an upturn in the $L_{150\,\mathrm{MHz}} -$ SFR relation at low luminosities. The upturn detected by Gürkan et al. (2018) is unexpected in the sense that the calorimetry model for radio synchrotron generation breaks down at low luminosity, reducing synchrotron luminosity. We find, however, that at low star-formation rates, galaxies do not exhibit any significant excess of radio luminosity for a given star-formation rate (extrapolating from higher star-formation rates). However, our model posterior distribution may have become broadened by our use of bootstrapping rather than incorporating the data uncertainties into each iterative step. This likely masks any effect that may be present at low star-formation rates and we plan to remedy this as discussed in Section 5.2.

If there is such an upturn, we propose that type-Ia supernovae may contribute to the excess of synchrotron emission seen by Gürkan et al. (2018) given that their frequency does not have as strong a dependence upon instantaneous star-formation rate as type-II supernovae have.

Given that we can construct very complicated models using a generalised Gaussian specification, it becomes trivial to join simulations and observations together, assuming that they attempt to describe the same distribution of real objects. We attempt to show that there exists a more complicated covariation with injected supernovae energy using a simplified joint distribution with the Horizon AGN simulation. We conclude that there is much promise in the application of this type of method in estimating incomplete distributions and joining observations to simulations.

5.2 Future Work

5.2.1 The Mass Dependency of the $L_{150\,\mathrm{MHz}} - \mathrm{SFR}$ relation using `CANDID`

Although we have been able to test for a mass dependency in the $L_{150\,\mathrm{MHz}}$-SFR relation, much work remains to done in order to decidedly retrieve the form of the mass dependence: Chapter 4 remains a preliminary work.

The next step in improving our technique is to include the resampled data in the Expectation-Maximisation (EM) iteration directly. Doing so would shrink the width of the posterior and would help to further pin down the characteristics of the low signal-to-noise regime. We outline the modified E and M steps in Appendix B and plan to adapt our method immediately.

There are a number of avenues that we wish to explore regarding the mass dependency of the $L_{150\,\mathrm{MHz}} - \mathrm{SFR}$ relation and using the large LoTSS DR1 dataset in general. They are as follows:

The size of the aperture we have used to extract LOFAR 150 MHz fluxes is large and so confusion with neighbouring sources could have an effect on the low luminosity end of the $L_{150\,\mathrm{MHz}} -$ SFR relation. It is vital that we perform our analysis again with a smaller aperture size to see if and how the $L_{150\,\mathrm{MHz}} - \mathrm{SFR}$ relation changes.

Our selection criteria in Chapter 4 were strong in order to avoid low-luminosity AGN contamination, yet we relied only on the BPT emission line information. Sabater et al. (2018) derived a composite classification method whereby BPT emission line ratios, D_{4000} strength, radio luminosity, and WISE colours are used to classify galaxies more robustly than with any one of those methods alone. Relaxing our signal-to-noise constraint on the BPT emission lines and adopting the Sabater et al. (2018) classification scheme would allow more sources to be used in the inference. Furthermore, by its component nature, our method is highly suited to modelling more than one distinct population at once. Indeed, without any modification, we are able to fit our model to both AGN and SFGs at the same time and classify the model *after* the fitting. This would allow detailed classification and the assignment of an AGN proportion over the entire model. Having access to such a bimodal model of local galaxies would allow us to probe the regions between the traditional discrete classifications. This method would be vital to understanding the distribution of low-luminosity AGN, if they are a continuation of the radio loud branch or a disjoint set within the parameter space. Indeed, using a multi-wavelength dataset, it is possible to isolate the AGN distribution from the SFGs using this method.

It is also worth noting that our method facilitates the extraction of luminosity and mass functions over redshift without further effort. Indeed, any marginal distribution can be extracted given that the parameter of interest was included in the model along with important covariates. We foresee using this technique to probe the luminosity distribution of low luminosity AGN across the whole parameter space.

Our method also allows the inclusion of non-detections in any parameter. We have already included such non-detections in LoTSS radio flux in our sample, but we could extend support to optical emission lines. Our significance cut in the BPT emission lines removes the most sources from our catalogue. Dealing with the noisiest data in a self-consistent way instead of removing them, may increase our sensitivity at low luminosity.

The forthcoming LoTSS DR2 includes many more sources ($\gtrsim 1,000,000$) with an increased sensitivity and wider area. Testing for the existence of the flattening of the $L_{150\,\mathrm{MHz}} - \mathrm{SFR}$ relation at low star-formation rates would be made easier with the inclusion of data from DR2.

We cannot extrapolate unobserved distributions that have no significantly observed components. However, in a future work, we could compare the recovered distribution we inferred in Chapter 4 to one inferred from deeper observations (i.e. from LoTSS DR2) in order to see if the reconstruction and imputation is accurate.

In Chapter 4 we produced a joint distribution between the Horizon AGN simulation and LoTSS observational data. This was a simple model, which we used to demonstrate the existence of a more complex relation between supernovae energy injection and radio luminosity. We will now seek to use our more advanced, imputed model to produce the joint distribution. This will provide us with a much more robust connection between observations and simulations. Indeed, we can apply this technique to any simulation and observational dataset that share the same output observables.

5.2.2 AGN in Dwarf Galaxies using `CANDID`

Imputed Gaussian mixture models are ideally suited to inferring total distributions from poorly sampled observational data. The Hyper-Suprime-Cam SSP survey (HSC-SSP, Aihara et al., 2018) surveyed 1400 deg^2 with a 5σ point source r-band depth of 26 mag, much deeper than SDSS (22 mag). This would make the HSC-SSP ideally suited to study the dwarf galaxy AGN

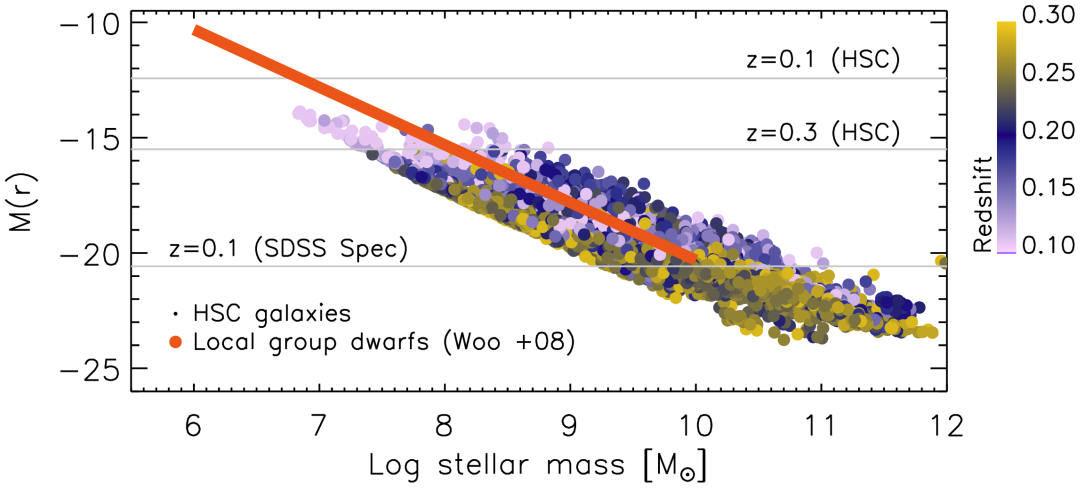

FIGURE 5.1: The HSC galaxy population coloured by redshift with the local group dwarfs represented by the thick red line (Woo et al., 2008). The limiting magnitudes for SDSS and HSC at $z = 0.1, 0.3$ are shown as grey lines.

fraction as a function of their stellar mass: a distribution that is sparsely investigated. Using cross-matched detections from WISE photometry together with optical r-band data from HSC-SSP, we can classify dwarf galaxies as AGN or star-forming using the Jarrett et al. (2011) classification seen in Chapter 2 and estimate the AGN fraction over stellar mass.

However, despite its superior optical depth, HSC-SSP rapidly becomes incomplete for stellar masses below $10^9\,M_\odot$, as shown in Figure 5.1. For given mass, only the brighter dwarfs will be detected, meaning that we would be biased to objects that are unusually bright for the dwarf regime. This could mean preferentially selecting galaxies who host a bright AGN or possess a high star-formation rate.

This is a very similar problem to that faced in Chapter 4. However, the use of WISE detections imparts a new bias towards bright mid-infrared galaxies. This multivariate covariation between different biases is precisely the domain of imputed Gaussian mixture models. Inferring the complete distribution in the space of M_r, $\log[M_*]$, $[4.6]-[12]$, and $[3.4]-[4.6]$ using the method detailed in Chapter 4 would enable us to mitigate the effects of being biased to brighter objects.

The more variables we have available about the observed population, the easier the imputation of missing data becomes. With HSC-SSP, we also have access to star-formation rates and spectroscopic redshifts. This would allow us to characterise a selection function which varies over those variables as well.

5.2.3 The covariation of the FIRC with intrinsic star-forming quantities

In Chapter 2, we described the variation of the Far-Infrared Radio Correlation (FIRC) over a few star-forming properties, namely dust temperature and stellar mass. If the mass dependency of the $L_{150\,\mathrm{MHz}} - \mathrm{SFR}$ relation is real, then the FIRC may exhibit a similar non-linearity. Not only do we now have the tools to probe such low-luminosity regions, but we are also able to disentangle covariances from multiple confounding variables. Building upon the analysis in Chapter 2, we can quantify the correlation of q_{250} with stellar mass, dust temperature, and redshift more accurately because `CANDID` does not assume a linear relation between them.

5.2.4 Reverberation Mapping

In Chapter 3 we estimated the black hole mass for `SDSS J144645.44 +625304.0` (one QSO out of ten observed). Having developed a methodology to reduce the impact of artefacts in the `Javelin` Gaussian process lag estimation, we can attempt to apply the same technique with other targets. However, these targets were not processed due to their low optical signal-to-noise. We can infer lags for these targets, not necessarily in order to estimate precise black-hole masses, but to model the $t - L_{5100}$ relation across the whole sample. We plan to submit Chapter 3 as soon as possible and then proceed with the analysis of the low signal-to-noise targets for which we already have data.

We also plan to submit another proposal to use the robotic Liverpool Telescope to observe more high redshift QSO targets, now that we have a greater understanding of how `Javelin` behaves as a function of Gaussian process parameters and light-curve signal-to-noise.

As previously discussed, photometric RM is ideally suited to upcoming large scale surveys. It seems desirable to select calibration fields based on the observability of suitable QSOs as well as other concerns. In this way we can build a large dataset of high redshift black hole masses for little extra effort using the latest upcoming large-scale surveys. The J-PAS and J-PLUS surveys are especially suited to this method since their instrument possesses 56 narrow-band filters, which are ideal for targeting a large range of high redshift QSOs.

In Chapter 3 we fit the $t - L_{5100}$ relation to QSO lags and optical luminosities. We discussed a bias in observability of lags that acts to reduce the number of observed lags with long time-scales. Based on an understanding of the artefacts produced by `Javelin`, cross-correlation

functions, and other tools such as `CREAM` (Starkey et al., 2016), we can build a selection function in the parameter space of lag and optical luminosity. Therefore, for each lag measurement in the literature, we could produce an individual selection probability for all known lag measurements and fit the $t - L_{5100}$ relation, accounting for biases. This type of approach is necessary to understand if the over-abundance of QSOs (offset below from the $t - L_{5100}$ as reported in Grier et al. 2017) is due to observational biases or an intrinsic accretion rate dependence (Du et al., 2016a). Indeed, about 20 per cent of QSOs that have been observed for RM campaigns do not possess a lag estimation (Grier et al., 2017). Including the non-detections and their prior selection probabilities will inform us as to whether there is a severe bias in the current distribution of black-hole masses and BLR lags.

5.3 Concluding Remarks

To conclude, I believe that the next few decades in the era of large-scale surveys will be filled with opportunities for the application of robust statistic methods. This thesis represents examples of such statistical techniques applied to relatively large datasets. The work described here is always ongoing but hopefully sets a foundation upon which future work can be based.

Appendix A

FIRC

A.1 FIRC relations with BPT-AGN

Further to the discussion in Section 2.4.5, we present versions of Figures 2.10, 2.11, and 2.14 which are generated from a sample of 4,541 sources formed by merging our star-forming sample with 447 BPT-classified AGN detected at 5σ in BPT emission lines. This material can be found online.

A.2 Supplementary figures

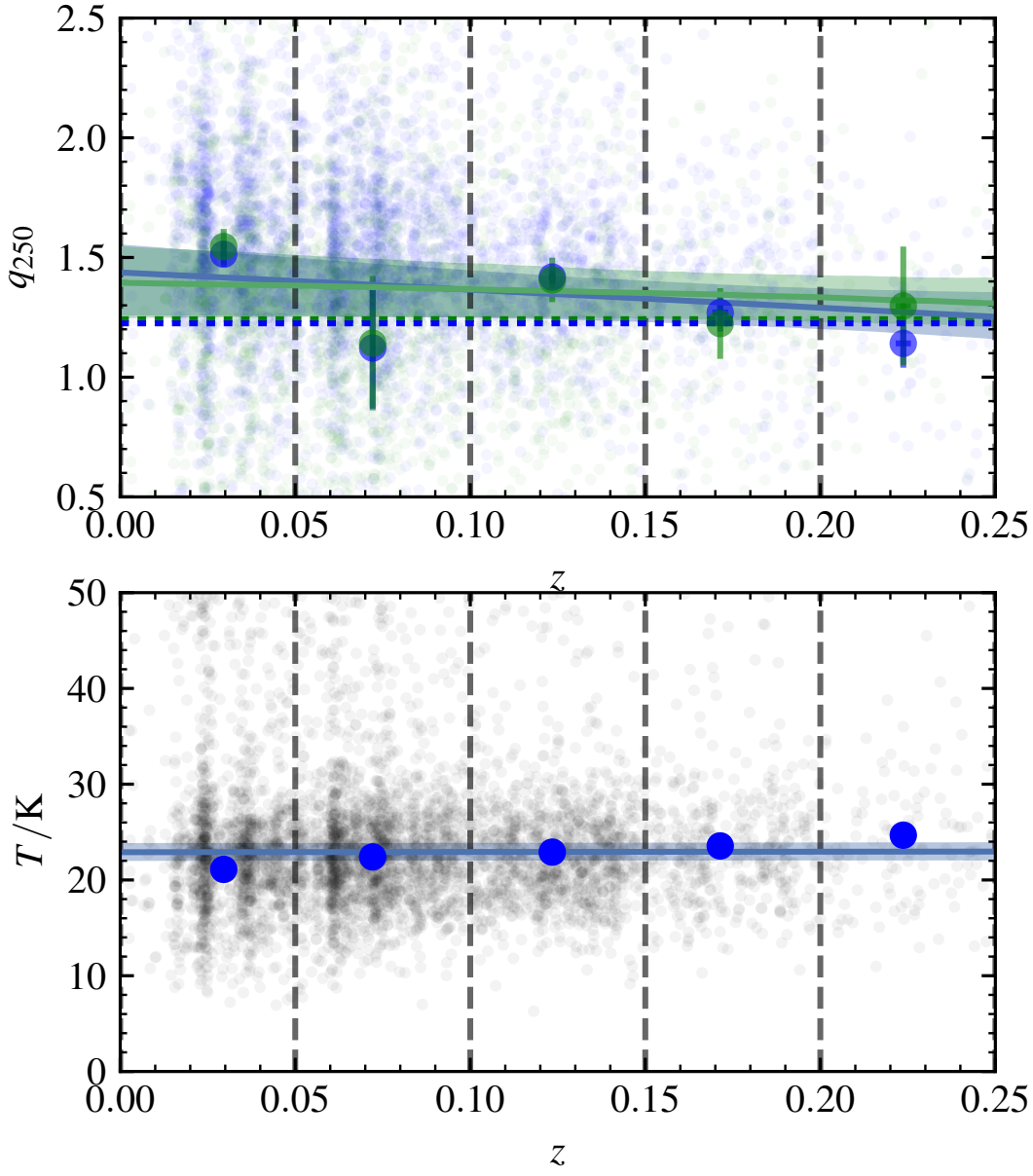

FIGURE A.1: **Top:** Evolution of q_{250} over redshift measured with LOFAR at 150 MHz (blue) and FIRST transformed to 150 MHz (green). This plot uses our star-forming sample merged with BPT-AGN whose emission lines are detected at 5σ . The dashed horizontal line in the upper plot is the mean-stacked q_{250} taken from Figure 2.8 for FIRST and LOFAR at 150 MHz. The coloured lines indicate the straight line fit to all galaxies in our sample binned in redshift for LOFAR and FIRST. **Bottom:** The temperature in each bin, calculated by constructing an infrared SED from the average K-corrected flux of each source in every band and fitting Equation 2.2 to the result. The temperature and uncertainties are overlaid with a straight line fit to the data. The vertical dashed lines represent bin edges.

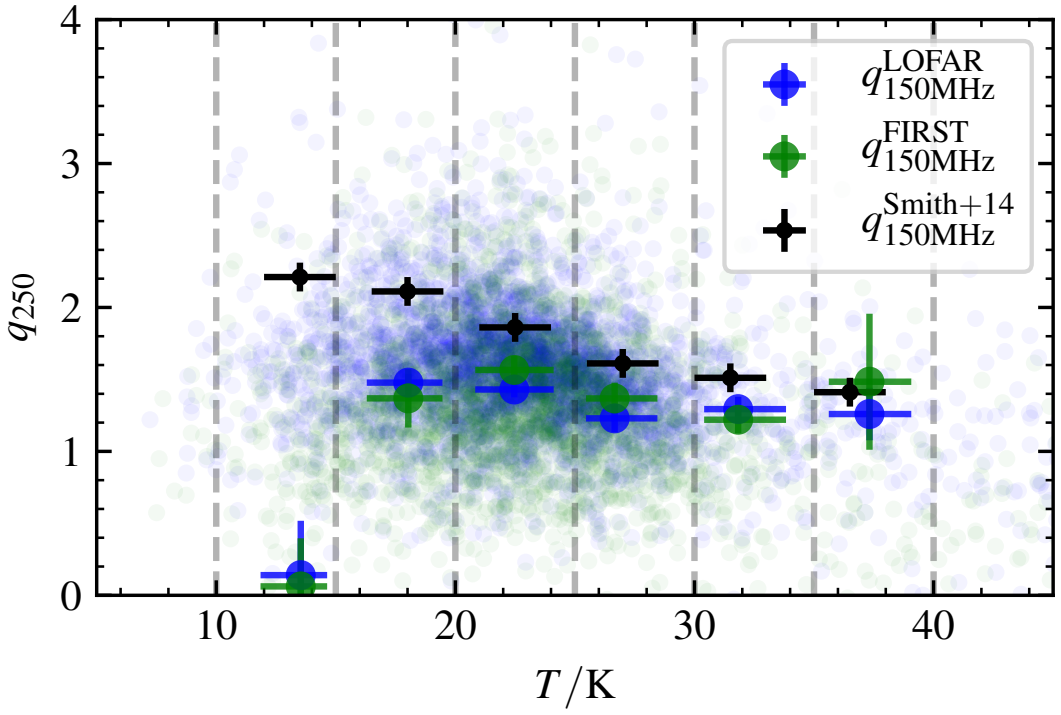

FIGURE A.2: The temperature dependence of q_{250} compared between high and low frequency using our star-forming sample merged with BPT-AGN whose emission lines are detected at 5σ . The background dots are the individual q_{250} calculated from the LOFAR 150 MHz (blue) and FIRST (green) luminosity densities. The q_{250} calculated from stacked LOFAR and SPIRE luminosity densities described earlier is plotted in bold points with errorbars derived from bootstrapping the luminosity densities within the depicted dashed bins 10,000 times. The temperature uncertainties in each bin are calculated from the 16th and 84th percentiles. The same calculation from Smith et al. (2014) is shown as the black errorbars for comparison.

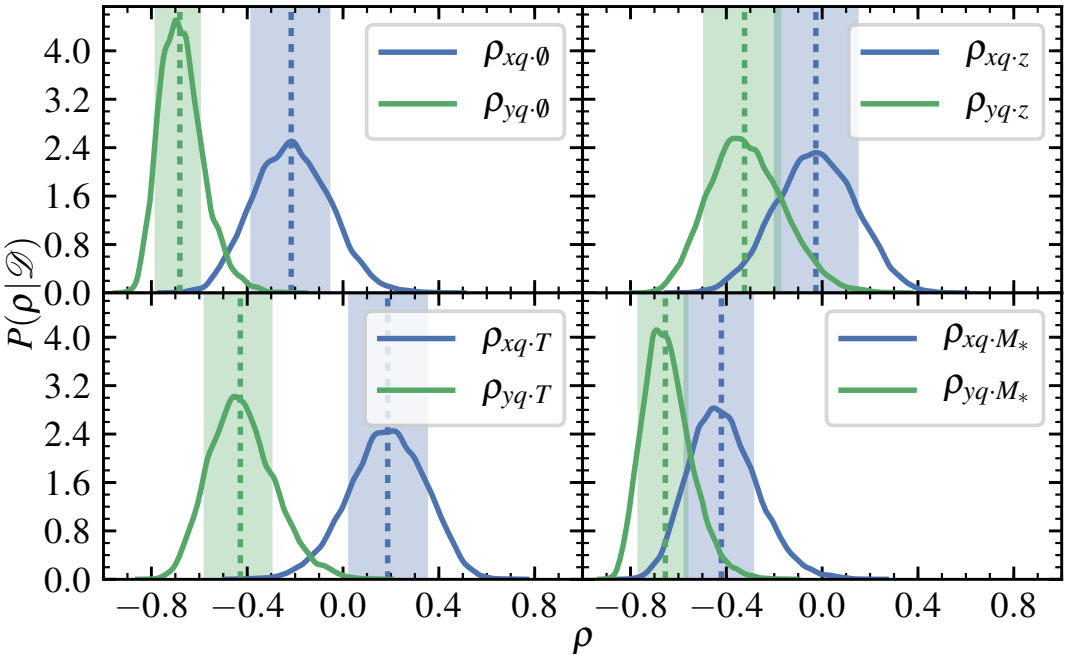

(a) Independent partial correlation coefficient PDFs

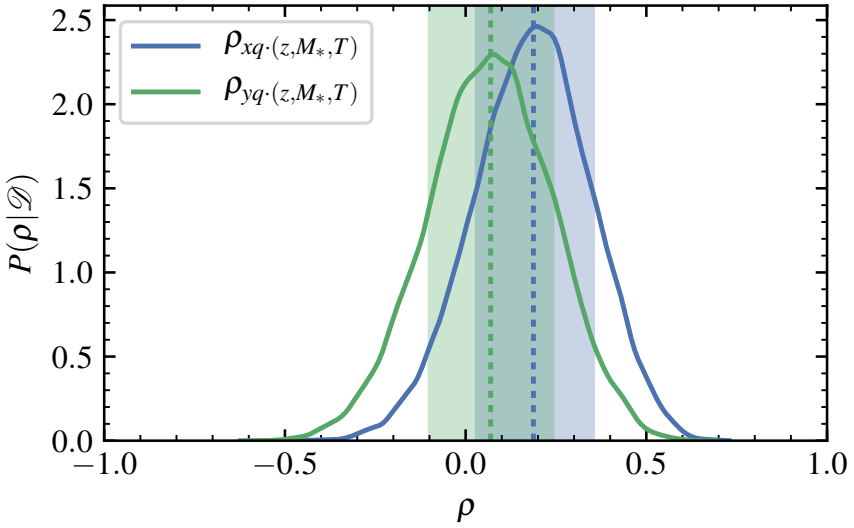

(b) Partial correlation coefficient PDF controlling for all variables at once.

FIGURE A.3: The marginalised probability density, $P(\rho|\mathscr{D})$, distributions for the correlation coefficients of $[4.6]-[12]$ (blue) and $[3.4]-[4.6]$ (green) against stacked q_{250}^{LOFAR} (using our star-forming sample merged with BPT-AGN whose emission lines are detected at 5σ). **Top left (a):** The correlation coefficient PDFs calculated assuming that q_{250}^{LOFAR} does not depend on other variables. **Top right (a):** The correlation coefficient PDFs after controlling for a linear dependence of q_{250}^{LOFAR} upon redshift. **Bottom left (a):** The correlation coefficient PDFs after controlling for a linear dependence of q_{250}^{LOFAR} upon effective temperature. **Bottom right (a):** The correlation coefficient PDFs after controlling for a linear dependence of q_{250}^{LOFAR} upon stellar mass. **Bottom panel (b):** The correlation distribution when controlling for all three parameters at once. The vertical lines mark the median value for the correlation coefficient with the shaded areas marking the $16-84$th percentile range. A Gaussian kernel was used to smooth the probability distributions.

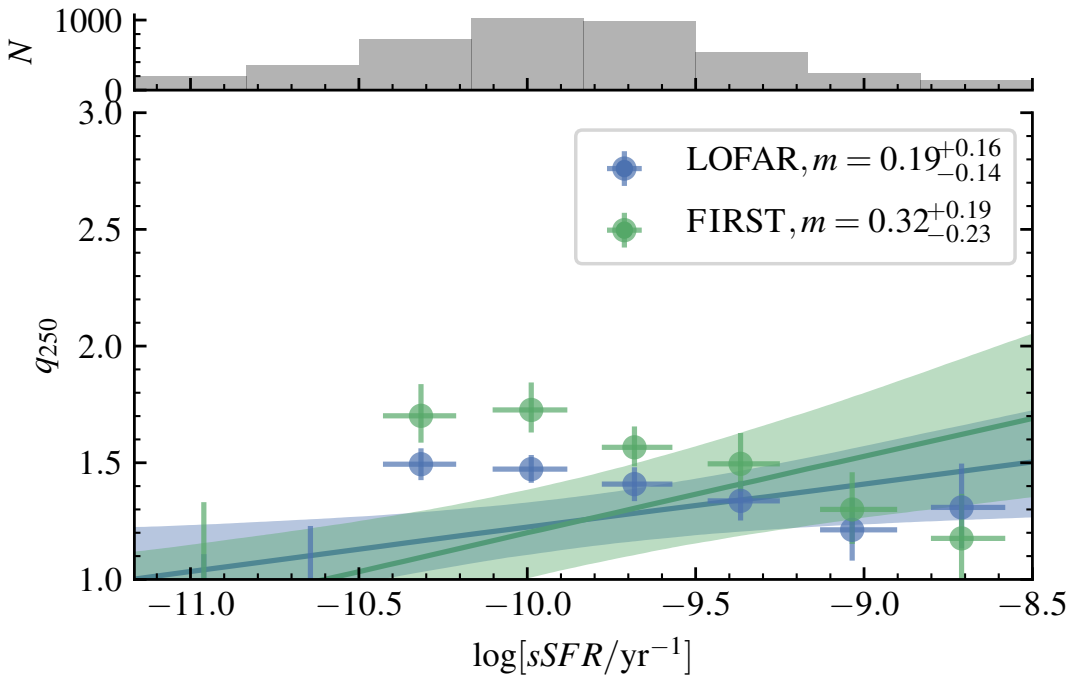

FIGURE A.4: q_{250} for LOFAR (blue) and FIRST (green) at 150 MHz against the specific star formation rate in 8 bins of width 0.3 dex. This plot uses our star-forming sample merged with BPT-AGN whose emission lines are detected at 5σ . The uncertainties on q_{250} are calculated via bootstrapping within each bin. The uncertainties on sSFR are calculated from the 16th and 84th percentiles in each bin. Straight line fits are shown as coloured lines with 1σ credible intervals shown as shaded regions. The top histogram shows the number of galaxies in each bin.

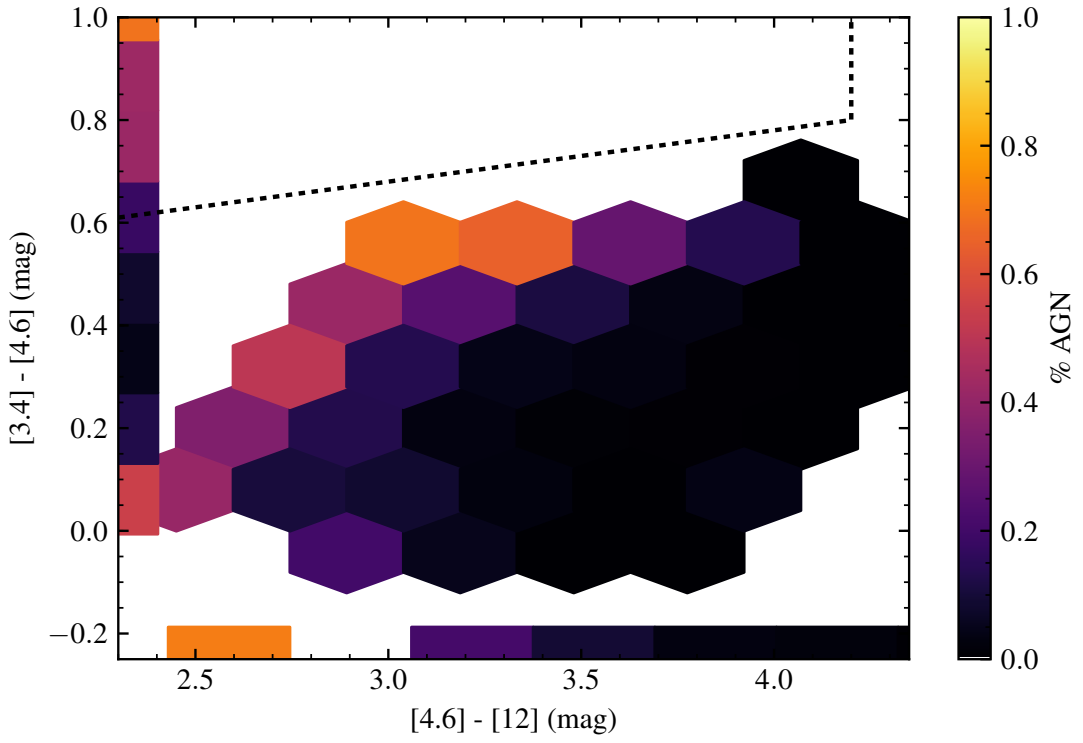

FIGURE A.5: Mean fraction of BPT-AGN across the Jarrett et al. (2011) MIRDD using our star-forming sample merged with BPT-AGN whose emission lines are detected at 5σ . Bins are hexagonal and are coloured linearly according to the scale shown on the right. All bins have an SNR in $q_{250\,\mu\mathrm{m}}^{\mathrm{LOFAR}} > 3$ and contain more than 50 galaxies each. Also plotted are the marginal bins summarising the horizontal and vertical slices of the entire plane. These slices also obey the two conditions set on the hexagonal bins. For reference, the box described by Jarrett et al. (2011) to contain mostly QSOs is marked by dotted lines.

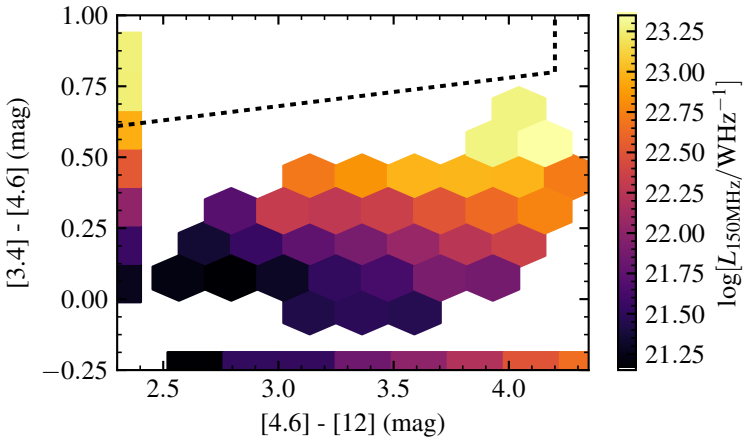

(a) LOFAR at 150 MHz

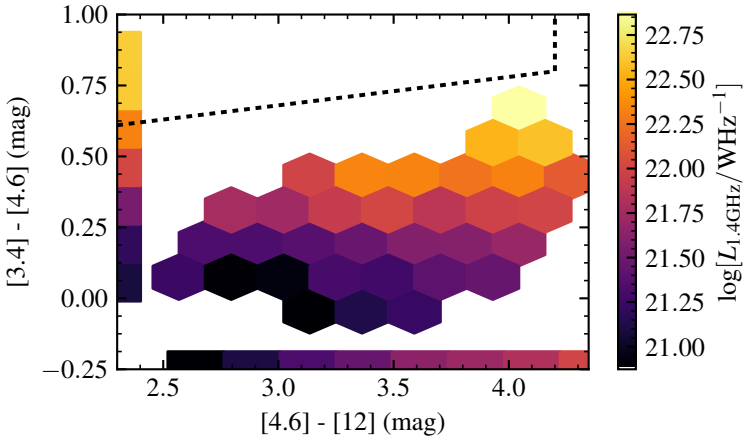

(b) FIRST at 1.4 GHz

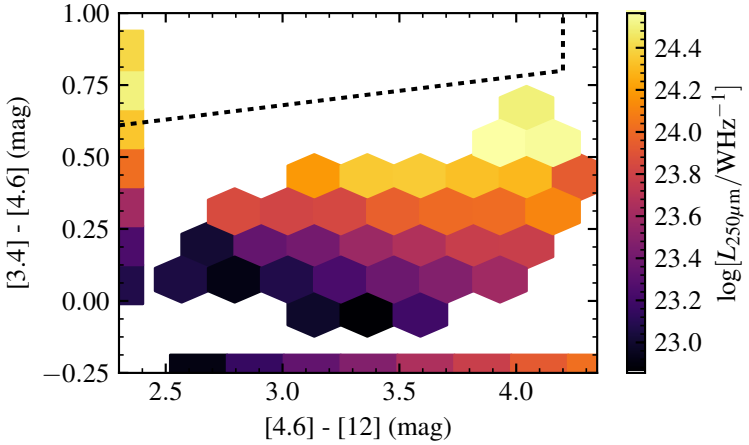

(c) 250 μm

FIGURE A.6: Mean luminosity density across the Jarrett et al. (2011) MIRDD. Bins are hexagonal and are coloured linearly according to the scale shown on the right. All bins have an SNR in $q_{250\,\mu\mathrm{m}}^{\mathrm{LOFAR}} > 3$ and contain more than 50 galaxies each. Also plotted are the marginal bins summarising the horizontal and vertical slices of the entire plane. These slices also obey the two conditions set on the hexagonal bins. For reference, the box described by Jarrett et al. (2011) to contain mostly QSOs is marked by dotted lines.

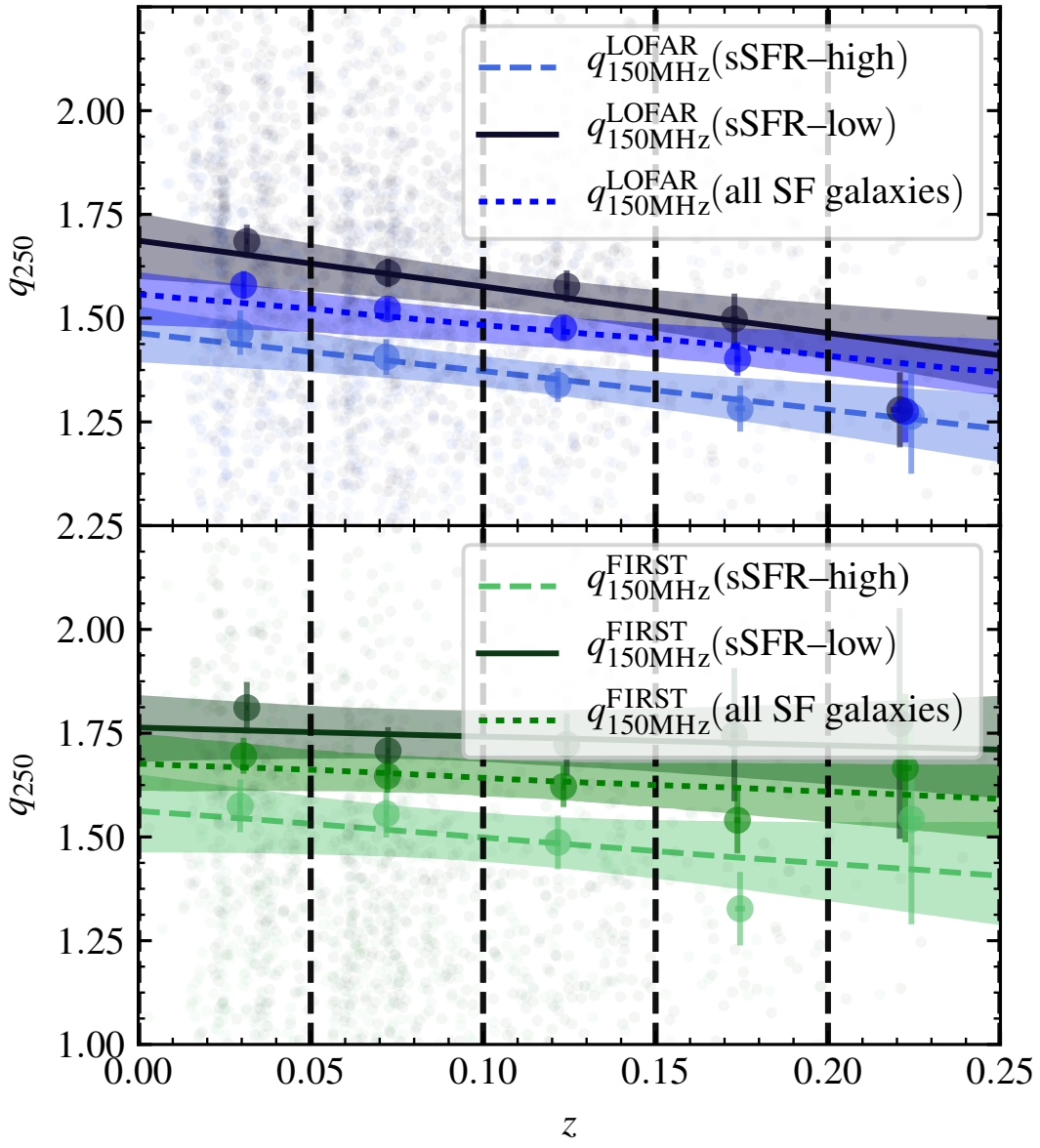

FIGURE A.7: Evolution of q_{250} over redshift for the high-sSFR (light points, dashed lines), low-sSFR (darker points, solid lines), and all star-forming galaxies (dotted line) measured with LOFAR at 150 MHz (blue) and FIRST transformed to 150 MHz (green). The coloured lines indicate the straight line fit to all galaxies in our sample binned in redshift for LOFAR and FIRST.

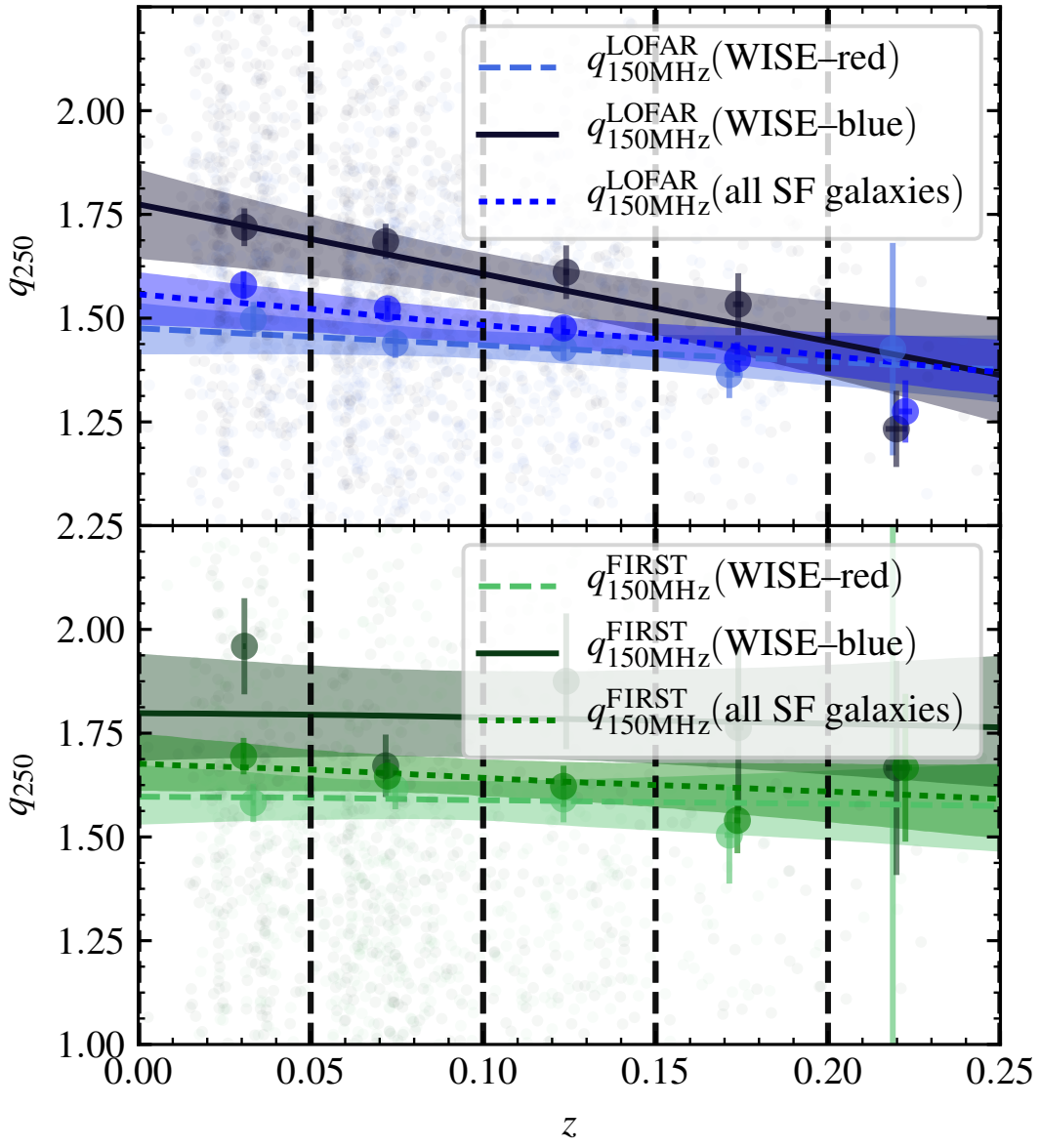

FIGURE A.8: Evolution of q_{250} over redshift for the WISE-red (light points, dashed lines), WISE-blue (darker points, solid lines), and all star-forming galaxies (dotted line) measured with LOFAR at 150 MHz (blue) and FIRST transformed to 150 MHz (green). The coloured lines indicate the straight line fit to all galaxies in our sample binned in redshift for LOFAR and FIRST.

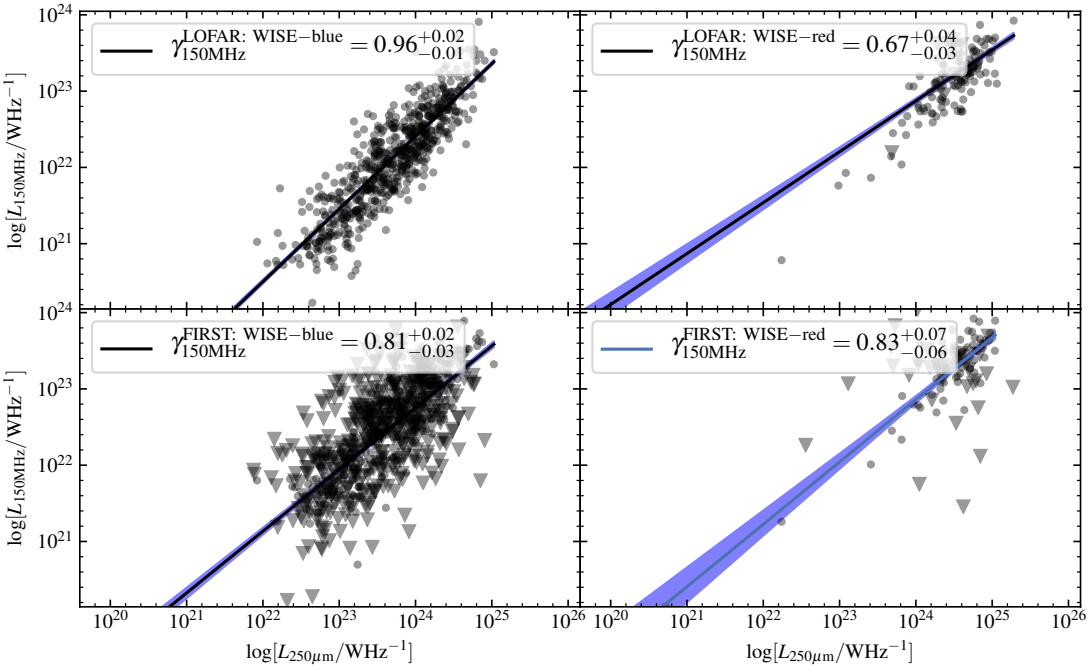

FIGURE A.9: Fits to the FIRC measured by LOFAR and FIRST for the WISE-red and WISE-blue sub-samples. 3σ detections are shown as black points. 3σ upper limits for sources for which there is not formal 3σ detection are shown as black triangles The fit lines are power-law fits to the all sources in our star-forming sample including non-detections. For the purpose of comparison the FIRST 1.4 GHz luminosity densities have been transformed to 150 MHz assuming a power law with spectral index from Mauch et al. (2013).

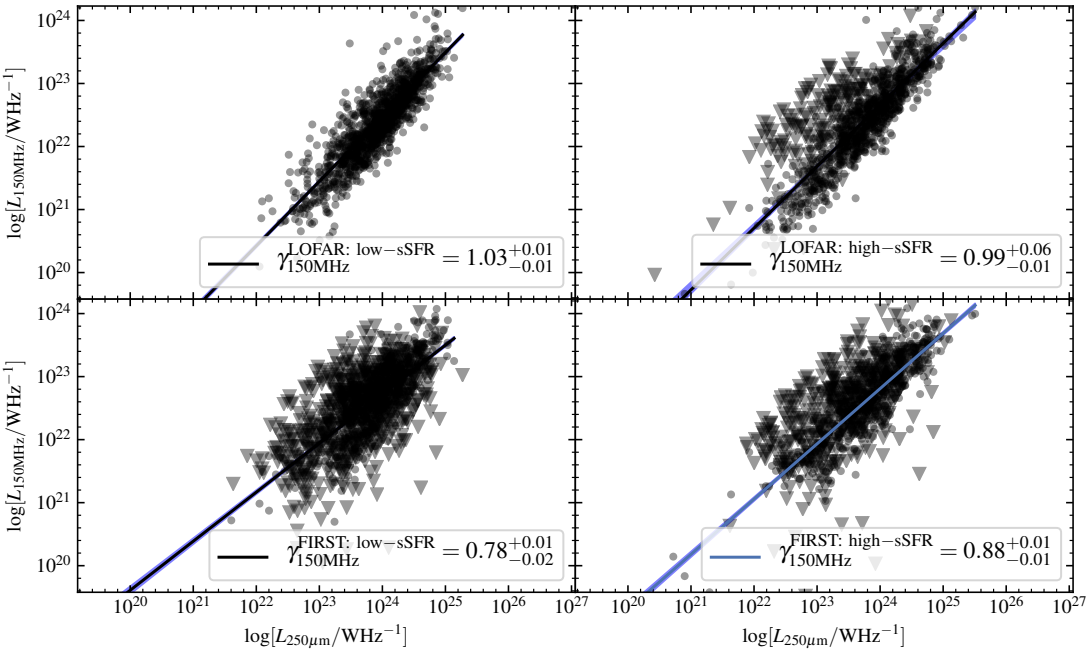

FIGURE A.10: Fits to the FIRC measured by LOFAR and FIRST for galaxies in our star-forming sample with MAGPHYS fit specific star-formation rates above $-9.75\mathrm{yr}^{-1}$ (high-sSFR) and below $-9.75\mathrm{yr}^{-1}$ (low-sSFR). 3σ detections are shown as black points. 3σ upper limits for sources for which there is not formal 3σ detection are shown as black triangles The fit lines are power-law fits to the all sources in each sample including non-detections. For the purpose of comparison the FIRST 1.4 GHz luminosity densities have been transformed to 150 MHz assuming a power law with spectral index from Mauch et al. (2013).

Appendix B

CANDID generalised to resampled non-Gaussian uncertainties

Following from Equation 4.18, we define the auxillary function $Q(\theta, \theta^{t-1})$ in terms of resampled data x_{ir}

$$Q(\theta, \theta^{t-1}) = E[l_c(\theta)|\mathscr{D}, \theta^{t-1}] \tag{B.1}$$

$$= \sum_{i=1}^{N}\sum_{k=1}^{K}\left[r_{ik}\log p(z_i = k|\theta) + r_{ik}\log p(x_i|z_i = k, \theta)\right] \tag{B.2}$$

$$= \sum_{i=1}^{N}\sum_{k=1}^{K}\left[r_{ik}\log \pi_k + r_{ik}\sum_{r=1}^{R}\log \mathscr{N}(x_{ir}|\mu_k, \Sigma_k)\right] \tag{B.3}$$

$$r_{ik} = p(z_i = k|x_i, \theta) = \frac{p(x_i|z_i = k, \theta)\cdot p(z_i = k)}{\sum_{j=1}^{K} p(x_i|z_i = j, \theta)\cdot p(z_i = j)} \tag{B.4}$$

$$= \frac{\mathscr{N}(x_i|\mu_k, \Sigma_k)\cdot \pi_k}{\sum_{j=1}^{K}\mathscr{N}(x_i|\mu_j, \Sigma_j)\cdot \pi_j} \tag{B.5}$$

$$= \frac{\prod_{r=1}^{R}\mathscr{N}(x_{ir}|\mu_k, \Sigma_k)\cdot \pi_k}{\sum_{j=1}^{K}\prod_{r=1}^{R}\mathscr{N}(x_{ir}|\mu_j, \Sigma_j)\cdot \pi_j} \tag{B.6}$$

where N is the number of data points, K is the number of components, and R is the number of resamples. Now taking the derivatives with respect to each Gaussian parameter, we can derive the M step updates.

Maximise Q for the means μ_k of the components:

$$\frac{\partial Q}{\partial \mu_k} = 0 \tag{B.7a}$$

$$= \sum_{i=1}^{N} r_{ik} \frac{1}{R} \sum_{r=1}^{R} \left[\frac{\partial}{\partial \mu_k} \log \mathcal{N}(x_{ir} | \mu_k, \Sigma_k) \right] = 0 \tag{B.7b}$$

$$= \sum_{i=1}^{N} r_{ik} \frac{1}{R} \sum_{r=1}^{R} \frac{\partial}{\partial \mu_k} \left[-\frac{1}{2} (x_{ir} - \mu_k)^T \Sigma_k^{-1} (x_{ir} - \mu_k) \right] = 0 \tag{B.7c}$$

Using

$$\frac{\partial}{\partial \mu_k} \left[-\frac{1}{2} (x_{ir} - \mu_k)^T \Sigma_k^{-1} (x_{ir} - \mu_k) \right] = \Sigma_k^{-1} (x_{ir} - \mu_k) \tag{B.8}$$

we can derive the update for the mean:

$$\cancel{-\frac{1}{2}} \sum_{i=1}^{N} \frac{1}{R} \sum_{r=1}^{R} r_{ik} \left[\cancel{\Sigma_k^{-1}} (x_{ir} - \mu_k) \right] = 0 \tag{B.9a}$$

$$\frac{\sum_{i=1}^{N} \sum_{r=1}^{R} x_{ik} r_{ik}}{\sum_{i=1}^{N} \sum_{r=1}^{R} r_{ik}} = \mu_k \tag{B.9b}$$

Maximise Q for the covariances Σ_k of the components:

$$\frac{\partial Q}{\partial \Sigma_k} = \sum_{i=1}^{N} r_{ik} \frac{1}{R} \sum_{r=1}^{R} \frac{\partial}{\partial \Sigma_k} \left[ln \frac{1}{\sqrt{|\Sigma_k|}} - \frac{1}{2} (x_{ir} - \mu_k)^T \Sigma_k^{-1} (x_{ir} - \mu_k) \right] \tag{B.10a}$$

$$= -\frac{1}{2} \sum_{i=1}^{N} r_{ik} \frac{1}{R} \sum_{r=1}^{R} \left[\frac{\partial \, ln \, |\Sigma_k|}{\partial \Sigma_k} + \frac{\partial}{\partial \Sigma_k} (x_{ir} - \mu_k)^T \Sigma_k^{-1} (x_{ir} - \mu_k) \right] \tag{B.10b}$$

$$\tag{B.10c}$$

Using

$$\frac{\partial ln \, |\Sigma_k|}{\partial \Sigma_k} = \frac{1}{|\Sigma_k|} \frac{\partial |\Sigma_k|}{\partial \Sigma_k} = \frac{1}{|\Sigma_k|} |\Sigma_k| (\Sigma_k^{-1})^T = \Sigma_k^{-1} \tag{B.11}$$

and

$$\frac{\partial}{\partial \Sigma_k} (x_{ir} - \mu_k)^T \Sigma_k^{-1} (x_{ir} - \mu_k) = -\Sigma_k^{-1} (x_{ir} - \mu_k)(x_{ir} - \mu_k)^T \Sigma_k^{-1} \tag{B.12}$$

we can derive the update for the covariances:

$$\frac{\partial Q}{\partial \Sigma_k} = -\frac{1}{2}\sum_{i=1}^{N} r_{ik}\frac{1}{R}\sum_{r=1}^{R}\left[\Sigma_k^{-1} - \Sigma_k^{-1}(x_{ir}-\mu_k)(x_{ir}-\mu_k)^T\Sigma_k^{-1}\right] \tag{B.13a}$$

$$= -\frac{1}{2}\sum_{i}^{m} r_{ik}\frac{1}{R}\sum_{r=1}^{R}\left[I - \Sigma_k^{-1}(x_{ir}-\mu_k)(x_{ir}-\mu_k)^T\right]\Sigma_k^{-1} = 0 \tag{B.13b}$$

$$\sum_{i=1}^{N} r_{ik}\frac{1}{R}\sum_{r=1}^{R}\left[\Sigma_k - (x_{ir}-\mu_k)(x_{ir}-\mu_k)^T\right] = 0 \tag{B.14a}$$

$$\frac{\sum_{i=1}^{N}\sum_{r=1}^{R} r_{ik}(x_{ir}-\mu_k)(x_{ir}-\mu_k)^T}{\sum_{i=1}^{N}\sum_{r=1}^{R} r_{ik}} = \Sigma_k \tag{B.14b}$$

The update for the weights, π_k remains the same, but now using the r_{ik} derived above.

$$\pi_k = \frac{\sum_{i=1}^{N} r_{ik}}{N} \tag{B.15}$$

Appendix C

Uncertainty expectation estimators for CANDID

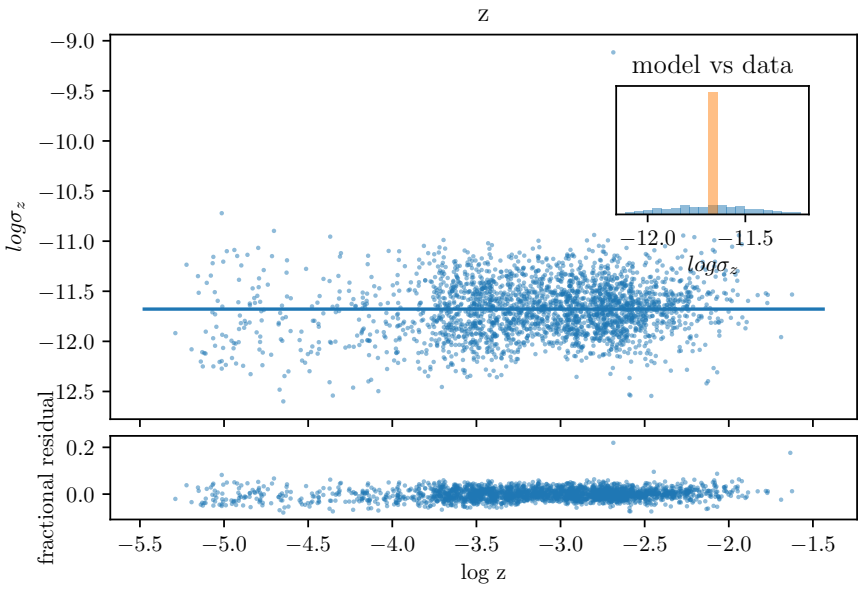

FIGURE C.1: The expected uncertainty model for a given redshift. The blue points are our star-forming sample, the blue line is the fit to the data, and its residuals are shown in the bottom panel. The inset axis shows the histogram for the data (blue) and the histogram for the predictions estimated from the model (orange).

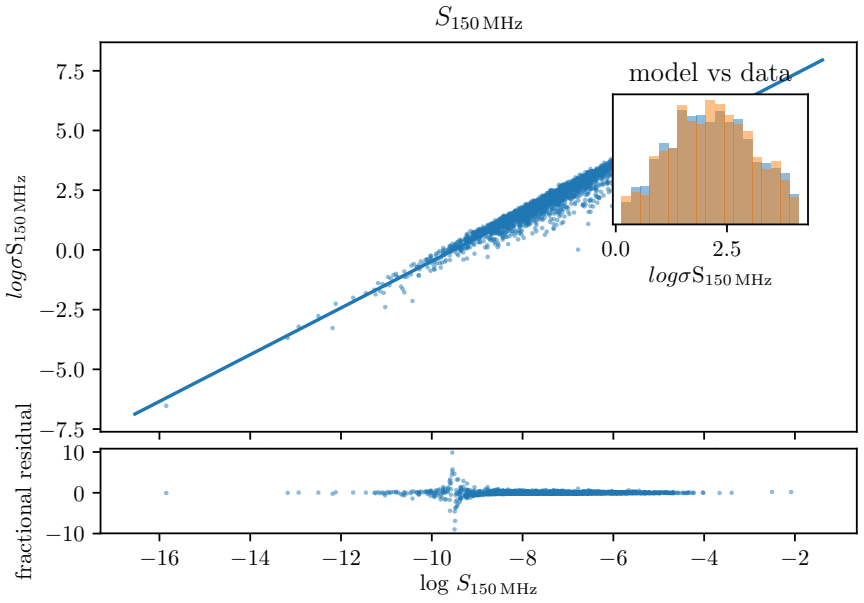

FIGURE C.2: The expected uncertainty model for a given radio flux. The blue points are our star-forming sample, the blue line is the fit to the data, and its residuals are shown in the bottom panel. The inset axis shows the histogram for the data (blue) and the histogram for the predictions estimated from the model (orange).

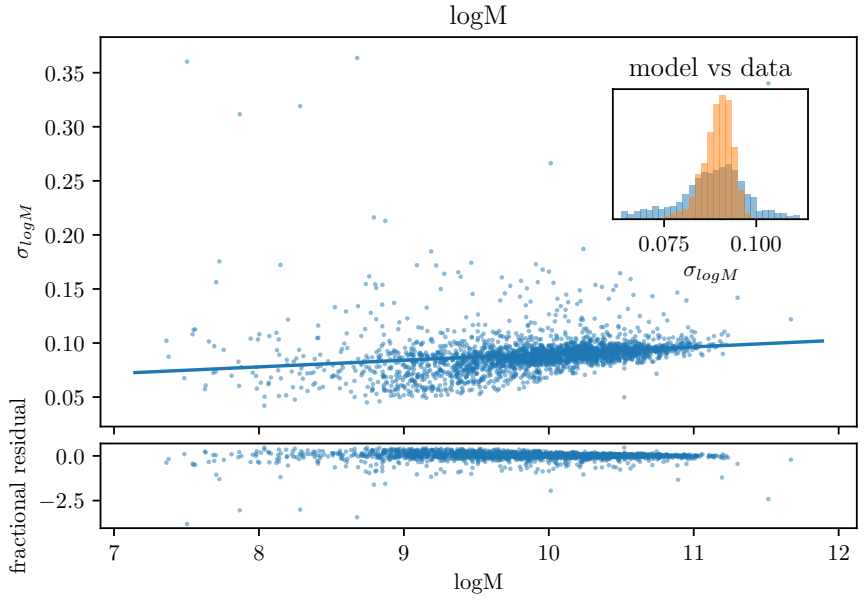

FIGURE C.3: The expected uncertainty model for a given stellar mass. The blue points are our star-forming sample, the blue line is the fit to the data, and its residuals are shown in the bottom panel. The inset axis shows the histogram for the data (blue) and the histogram for the predictions estimated from the model (orange).

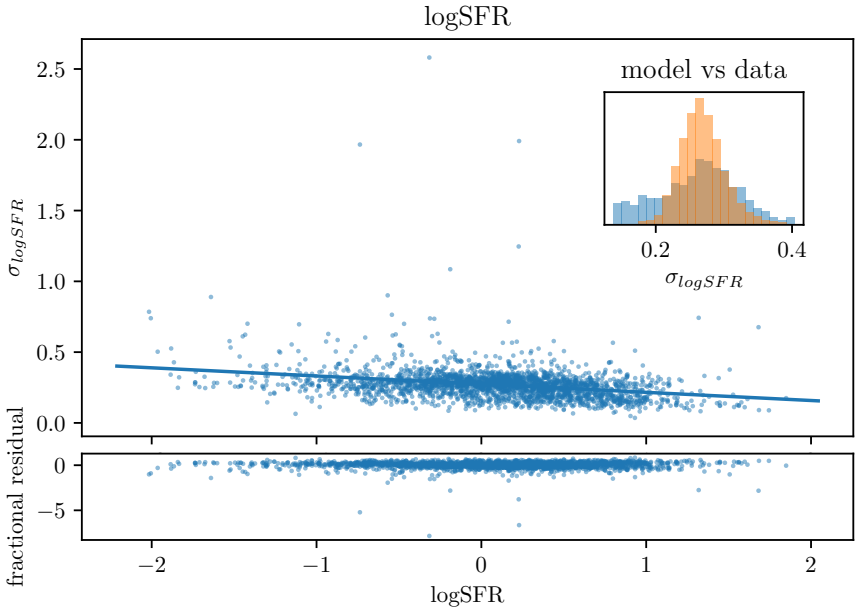

FIGURE C.4: The expected uncertainty model for a given star-formation rate. The blue points are our star-forming sample, the blue line is the fit to the data, and its residuals are shown in the bottom panel. The inset axis shows the histogram for the data (blue) and the histogram for the predictions estimated from the model (orange).

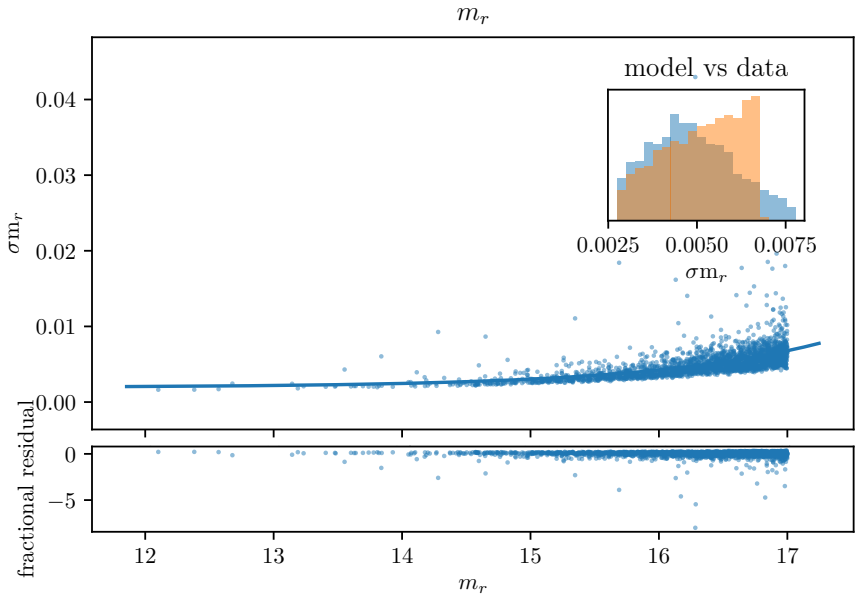

FIGURE C.5: The expected uncertainty model for a given apparent *r*-band magnitude. The blue points are our star-forming sample, the blue line is the fit to the data, and its residuals are shown in the bottom panel. The inset axis shows the histogram for the data (blue) and the histogram for the predictions estimated from the model (orange).

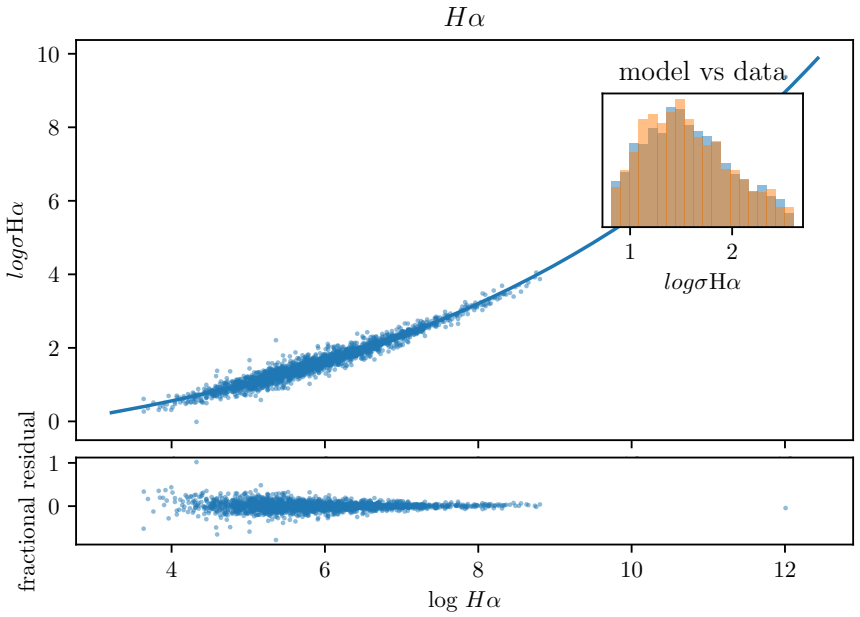

FIGURE C.6: The expected uncertainty model for a given Hα emission line flux. The blue points are our star-forming sample, the blue line is the fit to the data, and its residuals are shown in the bottom panel. The inset axis shows the histogram for the data (blue) and the histogram for the predictions estimated from the model (orange).

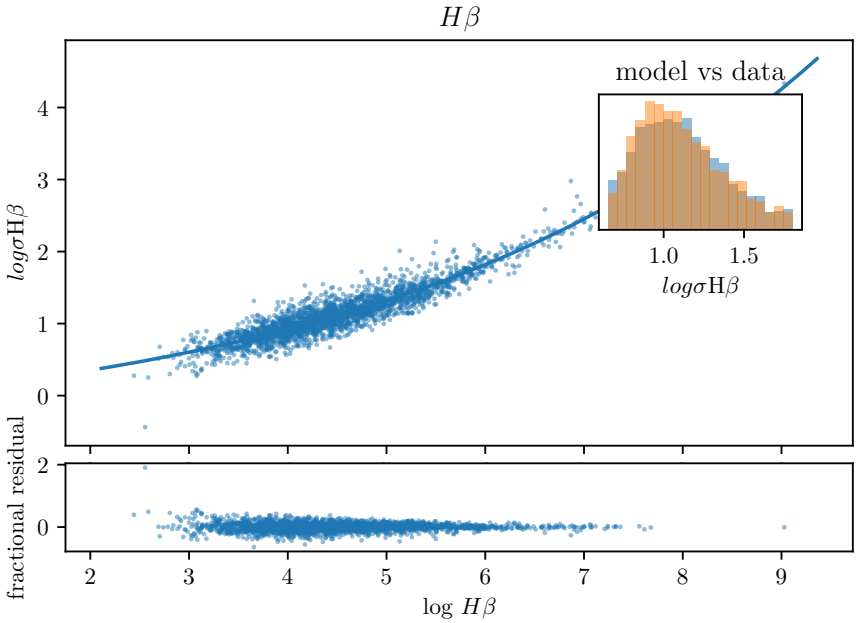

FIGURE C.7: The expected uncertainty model for a given Hβ emission line flux. The blue points are our star-forming sample, the blue line is the fit to the data, and its residuals are shown in the bottom panel. The inset axis shows the histogram for the data (blue) and the histogram for the predictions estimated from the model (orange).

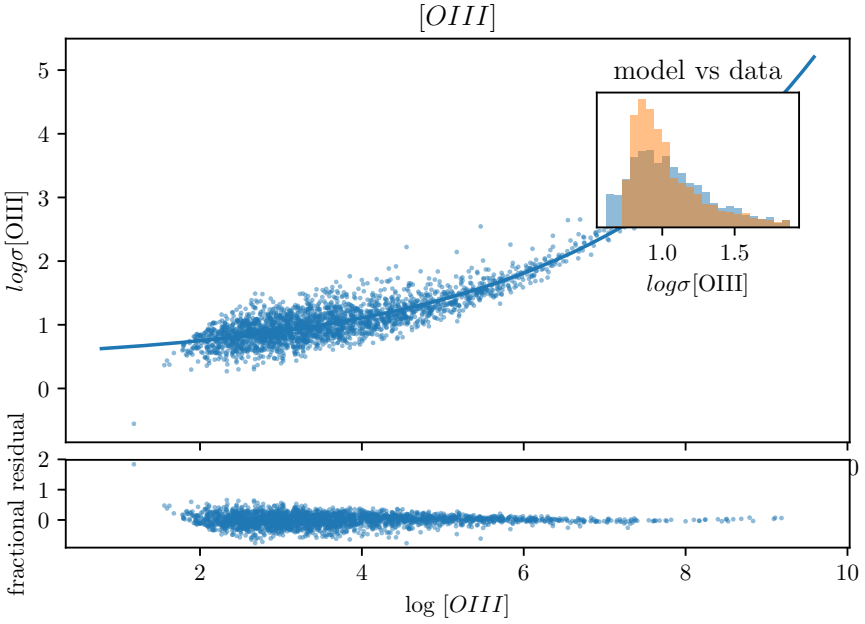

FIGURE C.8: The expected uncertainty model for a given [*OIII*] emission line flux. The blue points are our star-forming sample, the blue line is the fit to the data, and its residuals are shown in the bottom panel. The inset axis shows the histogram for the data (blue) and the histogram for the predictions estimated from the model (orange).

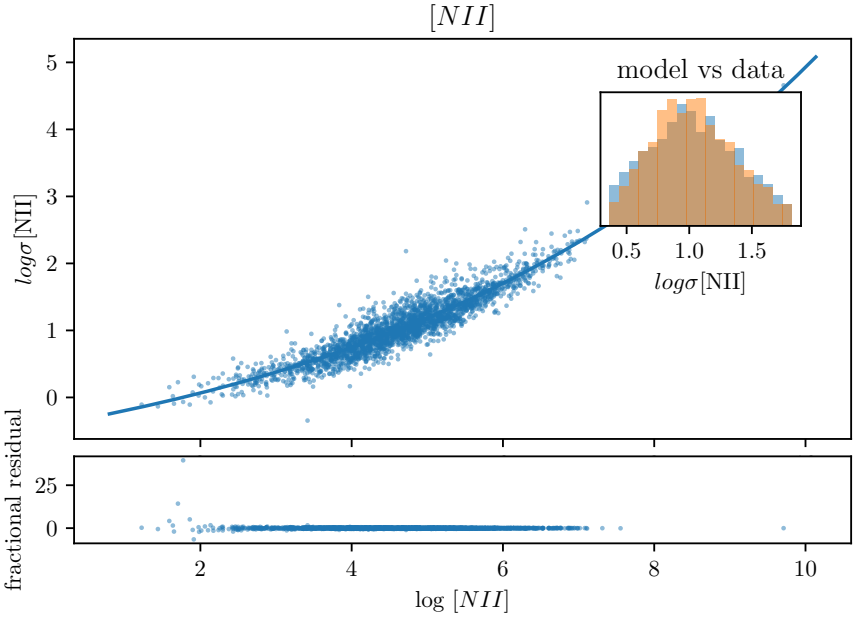

FIGURE C.9: The expected uncertainty model for a given [*NII*] emission line flux. The blue points are our star-forming sample, the blue line is the fit to the data, and its residuals are shown in the bottom panel. The inset axis shows the histogram for the data (blue) and the histogram for the predictions estimated from the model (orange).

Bibliography

Abazajian, K.N., Adelman-McCarthy, J.K., Agüeros, M.A., et al., 2009. The Seventh Data Release of the Sloan Digital Sky Survey. *The Astrophysical Journal Supplement Series*, 182:543.

Abraham, R.G. and van den Bergh, S., 2001. The Morphological Evolution of Galaxies. *Science*, 293(5533):1273.

Agertz, O., Teyssier, R., and Moore, B., 2011. The Formation of Disc Galaxies in a γCDM Universe. *Monthly Notices of the Royal Astronomical Society*, 410(2):1391.

Aihara, H., Arimoto, N., Armstrong, R., et al., 2018. The Hyper Suprime-Cam SSP Survey: Overview and Survey Design. *Publications of the Astronomical Society of Japan*, 70(SP1).

Antonucci, R., 1993. Unified Models for Active Galactic Nuclei and Quasars. *Annual Review of Astronomy and Astrophysics*, 31:473.

Antonucci, R.R.J., 1984. Optical Spectropolarimetry of Radio Galaxies. *The Astrophysical Journal*, 278:499.

Antonucci, R.R.J. and Miller, J.S., 1985. Spectropolarimetry and the Nature of NGC 1068. *The Astrophysical Journal*, 297:621.

Appleton, P.N., Fadda, D.T., Marleau, F.R., et al., 2004. The Far- and Mid-Infrared/Radio Correlations in the Spitzer Extragalactic First Look Survey. *The Astrophysical Journal Supplement Series*, 154(1):147.

Baade, W. and Minkowski, R., 1954. Identification of the Radio Sources in Cassiopeia, Cygnus A, and Puppis A. *The Astrophysical Journal*, 119:206.

Baba, K., Shibata, R., and Sibuya, M., 2004. Partial Correlation and Conditional Correlation as Measures of Conditional Independence. *Australian & New Zealand Journal of Statistics*, 46(4):657.

Babusiaux, C., van Leeuwen, F., Barstow, M.A., et al., 2018. Gaia Data Release 2. Observational Hertzsprung-Russell Diagrams. *Astronomy and Astrophysics*, 616:A10.

Baldry, I.K., 2008. Hubble's Galaxy Nomenclature. *Astronomy & Geophysics*, 49(5):5.25.

Baldry, I.K., Glazebrook, K., Brinkmann, J., et al., 2004. Quantifying the Bimodal Color-Magnitude Distribution of Galaxies. *The Astrophysical Journal*, 600(2):681.

Baldwin, J.A., Phillips, M.M., and Terlevich, R., 1981. Classification Parameters for the Emission-Line Spectra of Extragalactic Objects. *Publications of the Astronomical Society of the Pacific*, 93:5.

Balogh, M.L., Baldry, I.K., Nichol, R., et al., 2004. The Bimodal Galaxy Color Distribution: Dependence on Luminosity and Environment. *The Astrophysical Journal*, 615(2):L101.

Barišic, I., van der Wel, A., Bezanson, R., et al., 2017. Stellar Dynamics and Star Formation Histories of Z $\sim$ 1 Radio-Loud Galaxies. *The Astrophysical Journal*, 847(1):72.

Baron, D. and Netzer, H., 2019. DiscoveringAGN-Drivenwindsthroughtheirinfraredemission-I.Generalmethodandwindlocation. *Monthly Notices of the Royal Astronomical Society*, 482(3):3915.

Barth, A.J., Bennert, V.N., Canalizo, G., et al., 2015. The Lick AGN Monitoring Project 2011: Spectroscopic Campaign and Emission-Line Light Curves. *The Astrophysical Journal Supplement Series*, 217(2):26.

Basu, A., Wadadekar, Y., Beelen, A., et al., 2015. Radio-Far-Infrared Correlation in "Blue Cloud" Galaxies with 0 Extless Z Extless 1.2. *The Astrophysical Journal*, 803:51.

Baum, W.A., 1959. Population Inferences from Star Counts, Surface Brightness and Colors. *Publications of the Astronomical Society of the Pacific*, 71:106.

Becker, R.H., White, R.L., and Helfand, D.J., 1995. The FIRST Survey: Faint Images of the Radio Sky At Twenty Centimeters. *The Astrophysical Journal*, 450:559.

Beckmann, V. and Shrader, C.R., 2013. The AGN Phenomenon: Open Issues. *ArXiv:1302.1397 [Astro-Ph]*.

Begelman, M.C. and Cioffi, D.F., 1989. Overpressured Cocoons in Extragalactic Radio Sources. *The Astrophysical Journal*, 345:L21.

Behroozi, P.S., Wechsler, R.H., and Conroy, C., 2013. The Average Star Formation Histories of Galaxies in Dark Matter Halos from Z = 0-8. *The Astrophysical Journal*, 770:57.

Belfiore, F., Maiolino, R., Maraston, C., et al., 2017. SDSS-IV MaNGA - the Spatially Resolved Transition from Star Formation to Quiescence. *Monthly Notices of the Royal Astronomical Society*, 466(3):2570.

Bell, E.F., 2003. Estimating Star Formation Rates from Infrared and Radio Luminosities: The Origin of the Radio-Infrared Correlation. *The Astrophysical Journal*, 586(2):794.

Bell, E.F., Wolf, C., Meisenheimer, K., et al., 2004. Nearly 5000 Distant Early-Type Galaxies in COMBO-17: A Red Sequence and Its Evolution Since Z extasciitilde1. *The Astrophysical Journal*, 608:752.

Benitez, N., Dupke, R., Moles, M., et al., 2014. J-PAS: The Javalambre-Physics of the Accelerated Universe Astrophysical Survey. *ArXiv:1403.5237 [Astro-Ph]*.

Benson, A.J., Bower, R.G., Frenk, C.S., et al., 2003. What Shapes the Luminosity Function of Galaxies? *The Astrophysical Journal*, 599.

Bentz, M.C., Denney, K.D., Grier, C.J., et al., 2013. The Low-Luminosity End of the Radius-Luminosity Relationship for Active Galactic Nuclei. *The Astrophysical Journal*, 767(2):149.

Bentz, M.C., Horenstein, D., Bazhaw, C., et al., 2014. The Mass of the Central Black Hole in the Nearby Seyfert Galaxy NGC5273. *The Astrophysical Journal*, 796(1):8.

Bentz, M.C. and Katz, S., 2015. The AGN Black Hole Mass Database. *Publications of the Astronomical Society of the Pacific*, 127:67.

Bentz, M.C., Peterson, B.M., Netzer, H., et al., 2009a. The Radius-Luminosity Relationship for Active Galactic Nuclei: The Effect of Host-Galaxy Starlight on Luminosity Measurements. II. The Full Sample of Reverberation-Mapped AGNs. *The Astrophysical Journal*, 697(1):160.

Bentz, M.C., Walsh, J.L., Barth, A.J., et al., 2009b. The Lick AGN Monitoring Project: Broad-Line Region Radii and Black Hole Masses from Reverberation Mapping of Hβ. *The Astrophysical Journal*, 705(1):199.

Bernard, E.J., Ferguson, A.M.N., Richardson, J.C., et al., 2015. The Nature and Origin of Substructure in the Outskirts of M31 - II. Detailed Star Formation Histories. *Monthly Notices of the Royal Astronomical Society*, 446(3):2789.

Berta, S., Lutz, D., Santini, P., et al., 2013. Panchromatic Spectral Energy Distributions of Herschel Sources. *Astronomy & Astrophysics*, 551:A100.

Bertelli, G., Bressan, A., Chiosi, C., et al., 1994. Theoretical Isochrones from Models with New Radiative Opacities. *Astronomy and Astrophysics Supplement Series*, 106:275.

Bertelli, G., Mateo, M., Chiosi, C., et al., 1992. The Star Formation History of the Large Magellanic Cloud. *The Astrophysical Journal*, 388:400.

Bertin, E. and Arnouts, S., 1996. SExtractor: Software for Source Extraction. *Astronomy and Astrophysics Supplement Series*, 117:393.

Best, P.N., 2007. Radio-Loud AGN Feedback in Elliptical Galaxies. In *Cosmic Frontiers*, volume 379 of *Astronomical Society of the Pacific Conference Series*, page 213.

Best, P.N. and Heckman, T.M., 2012. On the Fundamental Dichotomy in the Local Radio-AGN Population: Accretion, Evolution and Host Galaxy Properties. *Monthly Notices of the Royal Astronomical Society*, 421(2):1569.

Best, P.N., Kauffmann, G., Heckman, T.M., et al., 2005. A Sample of Radio-Loud AGN in the Sloan Digital Sky Survey. *Monthly Notices of the Royal Astronomical Society*, 362(1):9.

Best, P.N., von der Linden, A., Kauffmann, G., et al., 2007. On the Prevalence of Radio-Loud Active Galactic Nuclei in Brightest Cluster Galaxies: Implications for AGN Heating of Cooling Flows. *Monthly Notices of the Royal Astronomical Society*, 379:894.

Biernacki, P. and Teyssier, R., 2018. The Combined Effect of AGN and Supernovae Feedback in Launching Massive Molecular Outflows in High-Redshift Galaxies. *Monthly Notices of the Royal Astronomical Society*, 475(4):5688.

Blandford, R.D. and McKee, C.F., 1982. Reverberation Mapping of the Emission Line Regions of Seyfert Galaxies and Quasars. *The Astrophysical Journal*, 255:419.

Blandford, R.D. and Rees, M.J., 1974. A ”twin-Exhaust” Model for Double Radio Sources. *Monthly Notices of the Royal Astronomical Society*, 169:395.

Blandford, R.D. and Znajek, R.L., 1977. Electromagnetic Extraction of Energy from Kerr Black Holes. *Monthly Notices of the Royal Astronomical Society*, 179:433.

Blumenthal, G.R. and Gould, R.J., 1970. Bremsstrahlung, Synchrotron Radiation, and Compton Scattering of High-Energy Electrons Traversing Dilute Gases. *Reviews of Modern Physics*, 42(2):237.

Blundell, K.M. and Rawlings, S., 2001. Spectral Ageing: a New Age Perspective. *Astronomical Society of the Pacific Conference Series*, 250:363.

Bosch, V.D., 2002. The Universal Mass Accretion History of Cold Dark Matter Haloes. *Monthly Notices of the Royal Astronomical Society*, 331(1):98.

Boselli, A., Eales, S., Cortese, L., et al., 2010. The Herschel Reference Survey. *Publications of the Astronomical Society of the Pacific*, 122(889):261.

Bouché, N., Dekel, A., Genzel, R., et al., 2010. The Impact of Cold Gas Accretion Above a Mass Floor on Galaxy Scaling Relations. *The Astrophysical Journal*, 718(2):1001.

Bourne, N., Dunne, L., Ivison, R.J., et al., 2011. Evolution of the Far-Infrared-Radio Correlation and Infrared SEDs of Massive Galaxies Over Z = 0 - 2. *Monthly Notices of the Royal Astronomical Society*, 410(2):1155.

Bovy, J., Hogg, D.W., and Roweis, S.T., 2011. Extreme Deconvolution: Inferring Complete Distribution Functions from Noisy, Heterogeneous and Incomplete Observations. *The Annals of Applied Statistics*, 5(2B):1657.

Brammer, G.B., Whitaker, K.E., van Dokkum, P.G., et al., 2009. The Dead Sequence: A Clear Bimodality in Galaxy Colors from Z = 0 to Z = 2.5. *The Astrophysical Journal*, 706(1):L173.

Bremer, M.N., Phillipps, S., Kelvin, L.S., et al., 2018. Galaxy and Mass Assembly (GAMA): Morphological Transformation of Galaxies Across the Green Valley. *Monthly Notices of the Royal Astronomical Society*, 476(1):12.

Bressan, A., Marigo, P., Girardi, L., et al., 2012. PARSEC: Stellar Tracks and Isochrones with the PAdova and TRieste Stellar Evolution Code. *Monthly Notices of the Royal Astronomical Society*, 427(1):127.

Brewer, B.J. and Elliott, T.M., 2014. Hierarchical Reverberation Mapping. *Monthly Notices of the Royal Astronomical Society*, 439:L31.

Bridle, A.H. and Perley, R.A., 1984. Extragalactic Radio Jets. *Annual Review of Astronomy and Astrophysics*, 22:319.

Brinchmann, J., Charlot, S., White, S.D.M., et al., 2004. The Physical Properties of Star Forming Galaxies in the Low Redshift Universe. *Monthly Notices of the Royal Astronomical Society*, 351(4):1151.

Brinchmann, J. and Ellis, R., 2000. The Mass Assembly and Star Formation Characteristics of Field Galaxies of Known Morphology.

Brown, A.G.A., Vallenari, A., Prusti, T., et al., 2018. Gaia Data Release 2 - Summary of the Contents and Survey Properties. *Astronomy & Astrophysics*, 616:A1.

Brown, M.J.I., Moustakas, J., Kennicutt, R.C., et al., 2017. Calibration of Ultraviolet, Mid-Infrared and Radio Star Formation Rate Indicators. *The Astrophysical Journal*, 847(2):136.

Bruzual, G., 2007. Stellar Populations: High Spectral Resolution Libraries. Improved TP-AGB Treatment. *From Stars to Galaxies: Building the Pieces to Build Up the Universe*, 374:303.

Bruzual, G. and Charlot, S., 2003. Stellar Population Synthesis At the Resolution of 2003. *Monthly Notices of the Royal Astronomical Society*, 344:1000.

Bruzual A., G. and Charlot, S., 1993. Spectral Evolution of Stellar Populations Using Isochrone Synthesis. *The Astrophysical Journal*, 405:538.

Burgarella, D., Buat, V., and Iglesias-Páramo, J., 2005. Star Formation and Dust Attenuation Properties in Galaxies from a Statistical Ultraviolet-To-Far-Infrared Analysis. *Monthly Notices of the Royal Astronomical Society*, 360:1413.

Burns, J.O., 1990. The Radio Properties of CD Galaxies in Abell Clusters. I. an X-Ray Selected Sample. *Astronomical Journal*, 99:14.

Böhringer, H., Chon, G., and Collins, C.A., 2014. The Extended ROSAT-ESO Flux Limited X-Ray Galaxy Cluster Survey (REFLEX II). IV. X-Ray Luminosity Function and First Constraints on Cosmological Parameters. *Astronomy and Astrophysics*, 570:A31.

Cackett, E.M., Chiang, C.Y., McHardy, I., et al., 2018. Accretion Disk Reverberation with Hubble Space Telescope Observations of NGC 4593: Evidence for Diffuse Continuum Lags. *The Astrophysical Journal*, 857(1):53.

Calistro-Rivera, G., Lusso, E., Hennawi, J.F., et al., 2016. AGNfitter: A Bayesian MCMC Approach to Fitting Spectral Energy Distributions of AGNs. *The Astrophysical Journal*, 833(1):98.

Calistro-Rivera, G., Williams, W.L., Hardcastle, M.J., et al., 2017. The LOFAR Window on Star-Forming Galaxies and AGN - Curved Radio SEDs and IR-Radio Correlation At 0*ExtlessZExtless*2.5. *ArXiv:1704.06268 [Astro-Ph]*.

Cao, X., 2009. An Accretion Disc-Corona Model for X-Ray Spectra of Active Galactic Nuclei. *Monthly Notices of the Royal Astronomical Society*, 394(1):207.

Caputi, K.I., Deshmukh, S., Ashby, M.L.N., et al., 2017. Star Formation in Galaxies At Z extasciitilde4-5 from the SMUVS Survey: a Clear Starburst/main-Sequence Bimodality for Halpha Emitters on the SFR-M* Plane. *ArXiv:1705.06179 [Astro-Ph]*.

Carroll, C.J. and Joner, M.D., 2015. Photometric Reverberation Mapping Using a Meter-Class Telescope. In *American Astronomical Society Meeting Abstracts #225*, volume 225 of *American Astronomical Society Meeting Abstracts*, page 144.08.

Castander, F.J., Ballester, O., Bauer, A., et al., 2012. The PAU Camera and the PAU Survey At the William Herschel Telescope. volume 8446, page 84466D.

Ceverino, D., Klypin, A., Klimek, E.S., et al., 2014. Radiative Feedback and the Low Efficiency of Galaxy Formation in Low-Mass Haloes At High Redshift. *Monthly Notices of the Royal Astronomical Society*, 442:1545.

Chabrier, G., 2003. GalacticStellarandSubstellarInitialMassFunction. *Publications of the Astronomical Society of the Pacific*, 115:763.

Chapman, S.C., Blain, A.W., Ivison, R.J., et al., 2003. A Median Redshift of 2.4 for Galaxies Bright At Submillimetre Wavelengths. *Nature*, 422(6933):695.

Charlot, S. and Fall, S.M., 2000. A Simple Model for the Absorption of Starlight by Dust in Galaxies. *The Astrophysical Journal*, 539(2):718.

Charlot, S. and Longhetti, M., 2001. Nebular Emission from Star-Forming Galaxies. *Monthly Notices of the Royal Astronomical Society*, 323(4):887.

Chelouche, D. and Daniel, E., 2012. Photometric Reverberation Mapping of the Broad Emission Line Region in Quasars. *The Astrophysical Journal*, 747(1):62.

Cicone, C., Maiolino, R., Sturm, E., et al., 2014. Massive Molecular Outflows and Evidence for AGN Feedback from CO Observations. *Astronomy and Astrophysics*, 562:A21.

Cid Fernandes, R., Gu, Q., Melnick, J., et al., 2004. The Star Formation History of Seyfert 2 Nuclei. *Monthly Notices of the Royal Astronomical Society*, 355(1):273.

Ciesla, L., Boselli, A., Elbaz, D., et al., 2016. The Imprint of Rapid Star Formation Quenching on the Spectral Energy Distributions of Galaxies. *Astronomy & Astrophysics*, 585:A43.

Ciesla, L., Charmandaris, V., Georgakakis, A., et al., 2015. Constraining the Properties of AGN Host Galaxies with Spectral Energy Distribution Modeling. *Astronomy & Astrophysics*, 576:A10.

Condon, J.J., 1992. Radio Emission from Normal Galaxies. *Annual Review of Astronomy and Astrophysics*, 30(1):575.

Condon, J.J., Anderson, M.L., and Helou, G., 1991. Correlations Between the Far-Infrared, Radio, and Blue Luminosities of Spiral Galaxies. *The Astrophysical Journal*, 376:95.

Condon, J.J., Cotton, W.D., Greisen, E.W., et al., 1998. The NRAO VLA Sky Survey. *The Astronomical Journal*, 115(5):1693.

Conselice, C.J., 2001. Morphological Evolution of Galaxies to Z $\sim$ 4. *Deep Fields*, page 91.

Conselice, C.J., Yang, C., and Bluck, A.F.L., 2009. The Structures of Distant Galaxies - III. The Merger History of Over 20000 Massive Galaxies At Z < 1.2. *Monthly Notices of the Royal Astronomical Society*, 394(4):1956.

Contini, M., Viegas, S.M., and Prieto, M.A., 2004. The Infrared Continuum of Active Galactic Nuclei. *Monthly Notices of the Royal Astronomical Society*, 348(3):1065.

Copperwheat, C.M., Steele, I.A., Bates, S.D., et al., 2014. Liverpool Telescope 2: a New Robotic Facility for Time Domain Astronomy in 2020+. page 914511. Montréal, Quebec, Canada.

Cortese, L., 2012. Are Passive Red Spirals Truly Passive?. The Current Star Formation Activity of Optically Red Disc Galaxies. *Astronomy and Astrophysics*, 543:A132.

Coziol, R., Torres-Papaqui, J.P., and Andernach, H., 2015. Comparing Narrow- and Broad-Line AGNs in a New Diagnostic Diagram for Emission-Line Galaxies Based on WISE Data. *The Astronomical Journal*, 149(6):192.

Crenshaw, D.M., Kraemer, S.B., and George, I.M., 2003. Mass Loss from the Nuclei of Active Galaxies. *Annual Review of Astronomy and Astrophysics*, 41:117.

Croston, J.H., Birkinshaw, M., Hardcastle, M.J., et al., 2004. X-Ray Emission from the Nuclei, Lobes and Hot-Gas Environments of Two FR II Radio Galaxies. *Monthly Notices of the Royal Astronomical Society*, 353:879.

Croton, D.J., Springel, V., White, S.D.M., et al., 2006. The Many Lives of Active Galactic Nuclei: Cooling Flows, Black Holes and the Luminosities and Colours of Galaxies. *Monthly Notices of the Royal Astronomical Society*, 365(1):11.

Croton, D.J., Stevens, A.R.H., Tonini, C., et al., 2016. Semi-Analytic Galaxy Evolution (SAGE): Model Calibration and Basic Results. *The Astrophysical Journal Supplement Series*, 222(2):22.

Curtis, H.D., 1918. Descriptions of 762 Nebulae and Clusters Photographed with the Crossley Reflector. *Publications of Lick Observatory*, 13:9.

Cutri, R.M., 2012. VizieR Online Data Catalog: WISE All-Sky Data Release (Cutri+ 2012). *VizieR Online Data Catalog*, 2311.

da Cunha, E., Charlot, S., Dunne, L., et al., 2011. MAGPHYS: a Publicly Available Tool to Interpret Observed Galaxy SEDs. *Proceedings of the International Astronomical Union*, 7(S284):292.

da Cunha, E., Charlot, S., and Elbaz, D., 2008. A Simple Model to Interpret the Ultraviolet, Optical and Infrared Emission from Galaxies. *Monthly Notices of the Royal Astronomical Society*, 388(4):1595.

Daddi, E., Alexander, D.M., Dickinson, M., et al., 2007. Multiwavelength Study of Massive Galaxies At Z extasciitilde2. II. Widespread Compton-Thick Active Galactic Nuclei and the Concurrent Growth of Black Holes and Bulges. *The Astrophysical Journal*, 670(1):173.

David, L.P., Nulsen, P.E.J., McNamara, B.R., et al., 2001. A High-Resolution Study of the Hydra A Cluster with Chandra: Comparison of the Core Mass Distribution with Theoretical Predictions and Evidence for Feedback in the Cooling Flow. *The Astrophysical Journal*, 557:546.

Davis, M., Faber, S.M., Newman, J., et al., 2003. Science Objectives and Early Results of the DEEP2 Redshift Survey. In *Discoveries and Research Prospects from 6- to 10-Meter-Class Telescopes II*, volume 4834 of *Society of Photo-Optical Instrumentation Engineers (SPIE) Conference Series*, pages 161–172.

Dawson, K.S., Schlegel, D.J., Ahn, C.P., et al., 2013. The Baryon Oscillation Spectroscopic Survey of SDSS-III. *The Astronomical Journal*, 145:10.

de Gouveia Dal Pino, E., Clavijo-Bohórquez, W., and Melioli, C., 2018. AGN and Star Formation Feedback in Galaxy Outflows. *ArXiv E-Prints*, page arXiv:1809.07588.

de Jong, T., Klein, U., Wielebinski, R., et al., 1985. Radio Continuum and Far-Infrared Emission from Spiral Galaxies - A Close Correlation. *Astronomy and Astrophysics*, 147:L6.

de Vaucouleurs, G., 1959. Classification and Morphology of External Galaxies. *Handbuch Der Physik*, 53:275.

Deeley, S., Drinkwater, M.J., Cunnama, D., et al., 2017. Galaxy and Mass Assembly (GAMA): Formation and Growth of Elliptical Galaxies in the Group Environment. *Monthly Notices of the Royal Astronomical Society*, 467(4):3934.

Dekel, A. and Birnboim, Y., 2006. Galaxy Bimodality Due to Cold Flows and Shock Heating. *Monthly Notices of the Royal Astronomical Society*, 368:2.

Delhaize, J., Smolčic, V., Delvecchio, I., et al., 2017. The VLA-COSMOS 3 GHz Large Project: The Infrared-Radio Correlation of Star-Forming Galaxies and AGN to $Z \lessapprox 6$. *Astronomy & Astrophysics*, 602:A4.

Delvecchio, I., Smolčic, V., Zamorani, G., et al., 2017. The VLA-COSMOS 3 GHz Large Project: AGN and Host-Galaxy Properties Out to $Z \lessapprox 6$. *Astronomy and Astrophysics*, 602:A3.

Dempster, A.P., Laird, N.M., and Rubin, D.B., 1977. Maximum Likelihood from Incomplete Data via the EM Algorithm. *Journal of the Royal Statistical Society. Series B (Methodological)*, 39(1):1.

Denney, K.D., Peterson, B.M., Pogge, R.W., et al., 2010. Reverberation Mapping Measurements of Black Hole Masses in Six Local Seyfert Galaxies. *The Astrophysical Journal*, 721(1):715.

Di Matteo, P., Combes, F., Melchior, A.L., et al., 2007. Star Formation Efficiency in Galaxy Interactions and Mergers: a Statistical Study. *Astronomy and Astrophysics*, 468(1):61.

Dolphin, A.E., 2002. Numerical Methods of Star Formation History Measurement and Applications to Seven Dwarf Spheroidals. *Monthly Notices of the Royal Astronomical Society*, 332(1):91.

Dolphin, A.E., Saha, A., Skillman, E.D., et al., 2003. Deep Hubble Space Telescope Imaging of Sextans A. III. The Star Formation History. *The Astronomical Journal*, 126(1):187.

Domingo-Santamaria, E. and Torres, D.F., 2005. High Energy Gamma-Ray Emission from the Starburst Nucleus of NGC 253. *Astronomy & Astrophysics*, 444(2):403.

Dressler, A., 1980. Galaxy Morphology in Rich Clusters: Implications for the Formation and Evolution of Galaxies. *The Astrophysical Journal*, 236:351.

Driver, S.P., Allen, P.D., Graham, A.W., et al., 2006. The Millennium Galaxy Catalogue: Morphological Classification and Bimodality in the Colour-Concentration Plane. *Monthly Notices of the Royal Astronomical Society*, 368:414.

Driver, S.P., Hill, D.T., Kelvin, L.S., et al., 2011. Galaxy and Mass Assembly (GAMA): Survey Diagnostics and Core Data Release. *Monthly Notices of the Royal Astronomical Society*, 413(2):971.

Drury, L., 1983. On Particle Acceleration in Supernova Remnants. *Space Science Reviews*, 36(1):57.

Du, P., Hu, C., Lu, K.X., et al., 2015. Supermassive Black Holes with High Accretion Rates in Active Galactic Nuclei. IV. Hβ Time Lags and Implications for Super-Eddington Accretion. *The Astrophysical Journal*, 806(1):22.

Du, P., Lu, K.X., Hu, C., et al., 2016a. Supermassive Black Holes with High Accretion Rates in Active Galactic Nuclei. VI. Velocity-Resolved Reverberation Mapping of the Hβ Line. *The Astrophysical Journal*, 820(1):27.

Du, P., Lu, K.X., Zhang, Z.X., et al., 2016b. Supermassive Black Holes with High Accretion Rates in Active Galactic Nuclei. V. A New Size-Luminosity Scaling Relation for the Broad-Line Region. *The Astrophysical Journal*, 825(2):126.

Duane, S., Kennedy, A., Pendleton, B.J., et al., 1987. Hybrid Monte Carlo. *Physics Letters B*, 195(2):216.

Dubois, Y., Pichon, C., Welker, C., et al., 2014. Dancing in the Dark: Galactic Properties Trace Spin Swings Along the Cosmic Web. *Monthly Notices of the Royal Astronomical Society*, 444(2):1453.

Duncan, K.J., Sabater, J., Röttgering, H.J.A., et al., 2018. The LOFAR Two-Metre Sky Survey IV. First Data Release: Photometric Redshifts and Rest-Frame Magnitudes. *ArXiv E-Prints*, page arXiv:1811.07928.

Dunn, R.J.H. and Fabian, A.C., 2006. Investigating AGN Heating in a Sample of Nearby Clusters. *Monthly Notices of the Royal Astronomical Society*, 373(3):959.

Dutton, A.A., van den Bosch, F.C., and Dekel, A., 2010. On the Origin of the Galaxy Star-Formation-Rate Sequence: Evolution and Scatter. *Monthly Notices of the Royal Astronomical Society*, 405:1690.

Eales, S., de Vis, P., Smith, M.W.L., et al., 2017. The Galaxy End Sequence. *Monthly Notices of the Royal Astronomical Society*, 465(3):3125.

Eales, S., Dunne, L., Clements, D., et al., 2010. The Herschel ATLAS. *Publications of the Astronomical Society of the Pacific*, 122(891):499.

Eales, S., Smith, D., Bourne, N., et al., 2018a. The New Galaxy Evolution Paradigm Revealed by the Herschel Surveys. *Monthly Notices of the Royal Astronomical Society*, 473(3):3507.

Eales, S.A., Baes, M., Bourne, N., et al., 2018b. The Causes of the Red Sequence, the Blue Cloud, the Green Valley, and the Green Mountain. *Monthly Notices of the Royal Astronomical Society*, 481(1):1183.

Edri, H., Rafter, S.E., Chelouche, D., et al., 2012. Broadband Photometric Reverberation Mapping of NGC 4395. *The Astrophysical Journal*, 756(1):73.

Eisenstein, D.J., Weinberg, D.H., Agol, E., et al., 2011. SDSS-III: Massive Spectroscopic Surveys of the Distant Universe, the Milky Way, and Extra-Solar Planetary Systems. *The Astronomical Journal*, 142:72.

Evans, D.A., Worrall, D.M., Hardcastle, M.J., et al., 2006. Chandra and XMM-Newton Observations of a Sample of Low-Redshift FRI and FRII Radio-Galaxy Nuclei. *The Astrophysical Journal*, 642(1):96.

Faber, S.M., Willmer, C.N.A., Wolf, C., et al., 2007. Galaxy Luminosity Functions to Z 1 from DEEP2 and COMBO-17: Implications for Red Galaxy Formation. *The Astrophysical Journal*, 665(1):265.

Fabian, A.C., 2012. Observational Evidence of AGN Feedback. *Annual Review of Astronomy and Astrophysics*, 50(1):455.

Fall, S.M. and Efstathiou, G., 1980. Formation and Rotation of Disc Galaxies with Haloes. *Monthly Notices of the Royal Astronomical Society*, 193:189.

Fath, E.A., 1909. The Spectra of Some Spiral Nebulae and Globular Star Clusters. *Lick Observatory Bulletin*, 5:71.

Fausnaugh, M.M., Grier, C.J., Bentz, M.C., et al., 2017. Reverberation Mapping of Optical Emission Lines in Five Active Galaxies. *The Astrophysical Journal*, 840(2):97.

Feng, H., Shen, Y., and Li, H., 2014. Single-Epoch Black Hole Mass Estimators for Broad-Line Active Galactic Nuclei: Recalibrating Hβ with a New Approach. *The Astrophysical Journal*, 794(1):77.

Fernandes, C.a.C., Jarvis, M.J., Martínez-Sansigre, A., et al., 2015. Black Hole Masses, Accretion Rates and Hot- and Cold-Mode Accretion in Radio Galaxies At Z $\sim$ 1. *Monthly Notices of the Royal Astronomical Society*, 447(2):1184.

Ferrarese, L. and Merritt, D., 2000. A Fundamental Relation Between Supermassive Black Holes and Their Host Galaxies.

Ferreras, I., Lisker, T., Pasquali, A., et al., 2009. On the Formation of Massive Galaxies: a Simultaneous Study of Number Density, Size and Intrinsic Colour Evolution in GOODS. *Monthly Notices of the Royal Astronomical Society*, 396(3):1573.

Fine, S., Shanks, T., Green, P., et al., 2013. Stacked Reverberation Mapping. *Monthly Notices of the Royal Astronomical Society*, 434:L16.

Fioc, M. and Rocca-Volmerange, B., 1997. PEGASE: a UV to NIR Spectral Evolution Model of Galaxies. Application to the Calibration of Bright Galaxy Counts. *Astronomy and Astrophysics*, 500:507.

Foreman-Mackey, D., Hogg, D.W., Lang, D., et al., 2013. Emcee: The MCMC Hammer. *Publications of the Astronomical Society of the Pacific*, 125:306.

Fraix-Burnet, D., 1990. Oblique Shocks in Extragalactic Jets. *Galactic and Intergalactic Magnetic Fields*, 140:437.

Fritz, J., Franceschini, A., and Hatziminaoglou, E., 2006. Revisiting the Infrared Spectra of Active Galactic Nuclei with a New Torus Emission Model. *Monthly Notices of the Royal Astronomical Society*, 366(3):767.

Furlanetto, C., Dye, S., Bourne, N., et al., 2018. The Second Herschel-ATLAS Data Release - III: Optical and Near-Infrared Counterparts in the North Galactic Plane Field. *Monthly Notices of the Royal Astronomical Society*.

Garrett, M.A., 2002. The FIR/Radio Correlation of High Redshift Galaxies in the Region of the HDF-N. *Astronomy & Astrophysics*, 384(3):4.

Gebhardt, K., Bender, R., Bower, G., et al., 2000. A Relationship Between Nuclear Black Hole Mass and Galaxy Velocity Dispersion.

Gelman, A. and Rubin, D.B., 1992. Inference from Iterative Simulation Using Multiple Sequences. *Statistical Science*, 7(4):457.

Geman, S. and Geman, D., 1984. Stochastic Relaxation, Gibbs Distributions, and the Bayesian Restoration of Images. *IEEE Transactions on Pattern Analysis and Machine Intelligence*, PAMI-6(6):721.

Gennaro, M., Tchernyshyov, K., Brown, T.M., et al., 2015. A New Method for Deriving the Stellar Birth Function of Resolved Stellar Populations. *The Astrophysical Journal*, 808(1):45.

Gillessen, S., Eisenhauer, F., Trippe, S., et al., 2009. Monitoring Stellar Orbits Around the Massive Black Hole in the Galactic Center. *The Astrophysical Journal*, 692:1075.

Girardi, L., Bressan, A., Bertelli, G., et al., 2000. Evolutionary Tracks and Isochrones for Low- and Intermediate-Mass Stars: From 0.15 to 7 $M_{\odot}$, and from Z=0.0004 to 0.03. *Astronomy and Astrophysics Supplement Series*, 141:371.

González Delgado, R.M., Cid Fernandes, R., Pérez, E., et al., 2016. Star Formation Along the Hubble Sequence. Radial Structure of the Star Formation of CALIFA Galaxies. *Astronomy and Astrophysics*, 590:A44.

Goodman, J. and Weare, J., 2010. Ensemble Samplers with Affine Invariance. *Communications in Applied Mathematics and Computational Science*, 5(1):65.

Gott, J. Richard, I., Vogeley, M.S., Podariu, S., et al., 2001. Median Statistics, H0, and the Accelerating Universe. *The Astrophysical Journal*, 549:1.

Graham, A.W., Driver, S.P., Petrosian, V., et al., 2005. Total Galaxy Magnitudes and Effective Radii from Petrosian Magnitudes and Radii. *The Astronomical Journal*, 130(4):1535.

Graham, A.W., Onken, C.A., Athanassoula, E., et al., 2011. An Expanded Mbh-σ Diagram, and a New Calibration of Active Galactic Nuclei Masses. *Monthly Notices of the Royal Astronomical Society*, 412:2211.

Grier, C.J., Martini, P., Watson, L.C., et al., 2013a. Stellar Velocity Dispersion Measurements in High-Luminosity Quasar Hosts and Implications for the AGN Black Hole Mass Scale. *The Astrophysical Journal*, 773:90.

Grier, C.J., Peterson, B.M., Horne, K., et al., 2013b. The Structure of the Broad-Line Region in Active Galactic Nuclei. I. Reconstructed Velocity-Delay Maps. *The Astrophysical Journal*, 764(1):47.

Grier, C.J., Peterson, B.M., Pogge, R.W., et al., 2012. Reverberation Mapping Results for Five Seyfert 1 Galaxies. *The Astrophysical Journal*, 755(1):60.

Grier, C.J., Trump, J.R., Shen, Y., et al., 2017. The Sloan Digital Sky Survey Reverberation Mapping Project: Hα and Hβ Reverberation Measurements From First-Year Spectroscopy and Photometry. *ArXiv:1711.03114 [Astro-Ph]*.

Griffin, M.J., Abergel, A., Abreu, A., et al., 2010. The Herschel-SPIRE Instrument and Its In-Flight Performance. *Astronomy and Astrophysics*, 518:L3.

Guo, Q., White, S., Boylan-Kolchin, M., et al., 2011. From Dwarf Spheroidals to CD Galaxies: Simulating the Galaxy Population in a ΛCDM Cosmology. *Monthly Notices of the Royal Astronomical Society*, 413(1):101.

Gurkan, G., Hardcastle, M.J., Jarvis, M.J., et al., 2015. Herschel-ATLAS:The Connection Between Star Formation and AGN Activity in Radio-Loud and Radio-Quiet Active Galaxies. *Monthly Notices of the Royal Astronomical Society*, 452(4):3776.

Gurkan, G., Hardcastle, M.J., Smith, D.J.B., et al., 2018. LOFAR/H-ATLAS: The Low-Frequency Radio Luminosity - Star-Formation Rate Relation. *Monthly Notices of the Royal Astronomical Society*.

Guzmán, R., Gallego, J., Koo, D.C., et al., 1997. The Nature of Compact Galaxies in the Hubble Deep Field (II): Spectroscopic Properties and Implications for the Evolution of the Star Formation Rate Density of the Universe.

Gültekin, K., Richstone, D.O., Gebhardt, K., et al., 2009. The M-σ and M-L Relations in Galactic Bulges, and Determinations of Their Intrinsic Scatter. *The Astrophysical Journal*, 698:198.

Gürkan, G., Hardcastle, M.J., Smith, D.J.B., et al., 2018. LOFAR/H-ATLAS: the Low-Frequency Radio Luminosity-Star Formation Rate Relation. *Monthly Notices of the Royal Astronomical Society*, 475(3):3010.

Haas, M., Chini, R., Ramolla, M., et al., 2011. Photometric AGN Reverberation Mapping - an Efficient Tool for BLR Sizes, Black Hole Masses and Host-Subtracted AGN Luminosities. *Astronomy & Astrophysics*, 535:A73.

Haering, N. and Rix, H.W., 2004. On the Black Hole Mass - Bulge Mass Relation. *The Astrophysical Journal*, 604(2):L89.

Halton, J.H., 1964. Algorithm 247: Radical-Inverse Quasi-Random Point Sequence. *Communications of the ACM*, 7(12):701.

Handley, W.J., Hobson, M.P., and Lasenby, A.N., 2015. POLYCHORD: Next-Generation Nested Sampling. *Monthly Notices of the Royal Astronomical Society*, 453(4):4384.

Hao, C.N., Kennicutt, R.C., Johnson, B.D., et al., 2011. Dust-Corrected Star Formation Rates of Galaxies. II. Combinations of Ultraviolet and Infrared Tracers. *The Astrophysical Journal*, 741:124.

Hardcastle, M.J., Evans, D.A., and Croston, J.H., 2006. The X-Ray Nuclei of Intermediate-Redshift Radio Sources. *Monthly Notices of the Royal Astronomical Society*, 370:1893.

Hardcastle, M.J., Gürkan, G., van Weeren, R.J., et al., 2016. LOFAR/H-ATLAS: A Deep Low-Frequency Survey of the Herschel-ATLAS North Galactic Pole Field. *Monthly Notices of the Royal Astronomical Society*, 462(2):1910.

Hardcastle, M.J., Williams, W.L., Best, P.N., et al., 2018. Radio-Loud AGN in the First LoTSS Data Release: The Lifetimes and Environmental Impact of Jet-Driven Sources. *ArXiv E-Prints*, page arXiv:1811.07943.

Hardcastle, M.J. and Worrall, D.M., 2000. The Environments of FRII Radio Sources. *Monthly Notices of the Royal Astronomical Society*, 319:562.

Harris, J. and Zaritsky, D., 2001. A Method for Determining the Star Formation History of a Mixed Stellar Population. *The Astrophysical Journal Supplement Series*, 136(1):25.

Hastings, W.K., 1970. Monte Carlo Sampling Methods Using Markov Chains and Their Applications. *Biometrika*, 57(1):97.

Hayward, C.C. and Smith, D.J.B., 2014. Should We Believe the Results of Ultraviolet-Millimetre Galaxy Spectral Energy Distribution Modelling? *Monthly Notices of the Royal Astronomical Society*, 446(2):1512.

Heavens, A., Panter, B., Jimenez, R., et al., 2004. The Star-Formation History of the Universe from the Stellar Populations of Nearby Galaxies. *Nature*, 428(6983):625.

Heckman, T. and Best, P., 2014. The Co-Evolution of Galaxies and Supermassive Black Holes: Insights from Surveys of the Contemporary Universe. *Annual Review of Astronomy and Astrophysics*, 52(1):589.

Heesen, V., Krause, M., Beck, R., et al., 2018. Radio Haloes in Nearby Galaxies Modelled with 1D Cosmic-Ray Transport Using SPINNAKER. *Monthly Notices of the Royal Astronomical Society*.

Helou, G., Soifer, B.T., and Rowan-Robinson, M., 1985. Thermal Infrared and Nonthermal Radio - Remarkable Correlation in Disks of Galaxies. *The Astrophysical Journal*, 298:L7.

Hernandez, X., Gilmore, G., and Valls-Gabaud, D., 2000a. Non-Parametric Star Formation Histories for Four Dwarf Spheroidal Galaxies of the Local Group. *Monthly Notices of the Royal Astronomical Society*, 317(4):831.

Hernandez, X., Valls-Gabaud, D., and Gilmore, G., 1999. Deriving Star Formation Histories: Inverting Hertzsprung-Russell Diagrams Through a Variational Calculus Maximum Likelihood Method. *Monthly Notices of the Royal Astronomical Society*, 304:705.

Hernandez, X., Valls-Gabaud, D., and Gilmore, G., 2000b. The Recent Star Formation History of the Hipparcos Solar Neighbourhood. *Monthly Notices of the Royal Astronomical Society*, 316(3):605.

Hernitschek, N., Rix, H.W., Bovy, J., et al., 2015. Estimating Black Hole Masses in Hundreds of Quasars. *The Astrophysical Journal*, 801(1):45.

Hertzsprung, E., 1911. Nachweis Der Veränderlichkeit Von α Ursae Minoris. *Astronomische Nachrichten*, 189:89.

Higson, E., Handley, W., Hobson, M., et al., 2019. NESTCHECK: Diagnostic Tests for Nested Sampling Calculations. *Monthly Notices of the Royal Astronomical Society*, 483(2):2044.

Hill, G.J., Gebhardt, K., Komatsu, E., et al., 2008. The Hobby-Eberly Telescope Dark Energy Experiment (HETDEX): Description and Early Pilot Survey Results. In *Panoramic Views of Galaxy Formation and Evolution*, volume 399 of *Astronomical Society of the Pacific Conference Series*, page 115.

Hiner, K.D., Cales, S., Calderon, P., et al., 2015. Probing the Non-Local M extlessSUB extgreaterBH extless/SUB extgreater-σ Relation: Spectroscopy of Narrow-Line Seyfert 1s. *American Astronomical Society Meeting Abstracts #225*, 225:432.09.

Hinton, S.R., Kim, A., and Davis, T.M., 2017. Accounting for Sample Selection in Bayesian Analyses. *ArXiv:1706.03856 [Astro-Ph]*.

Ho, L.C., 2008. Nuclear Activity in Nearby Galaxies. *Annual Review of Astronomy and Astrophysics*, 46:475.

Hogg, D.W., Blanton, M.R., Eisenstein, D.J., et al., 2003. The Overdensities of Galaxy Environments as a Function of Luminosity and Color. *The Astrophysical Journal*, 585(1):L5.

Hogg, D.W., Bovy, J., and Lang, D., 2010. Data Analysis Recipes: Fitting a Model to Data. *ArXiv:1008.4686 [Astro-Ph, Physics:physics]*.

Honeycutt, R.K., 1992. CCD Ensemble Photometry on an Inhomogeneous Set of Exposures. *Publications of the Astronomical Society of the Pacific*, 104:435.

Hood, C.E., Rivera, N.I., Thackeray-Lacko, B., et al., 2015. Photometric Reverberation Mapping with a Small Aperture Telescope. In *American Astronomical Society Meeting Abstracts #225*, volume 225 of *American Astronomical Society Meeting Abstracts*, page 144.11.

Hopkins, A.M. and Beacom, J.F., 2006. On the Normalisation of the Cosmic Star Formation History. *The Astrophysical Journal*, 651(1):142.

Hopkins, P.F., Cox, T.J., Younger, J.D., et al., 2009. How Do Disks Survive Mergers? *The Astrophysical Journal*, 691(2):1168.

Hu, J., 2008. The Black Hole Mass-Stellar Velocity Dispersion Correlation: Bulges Versus Pseudo-Bulges. *Monthly Notices of the Royal Astronomical Society*, 386:2242.

Hubble, E., Kirshner, R.P., and Carroll, S.M., 1958. *The realm of the nebulae*. Mrs. Hepsa Ely Silliman memorial lectures. Yale University Press, New Haven.

Hubble, E.P., 1925. NGC 6822, a Remote Stellar System. *The Astrophysical Journal*, 62:409.

Hubble, E.P., 1926. Extragalactic Nebulae. *The Astrophysical Journal*, 64.

Hubble, E.P., 1927. The Classification of Spiral Nebulae. *The Observatory*, 50:276.

Humason, M.L., 1932. The Emission Spectrum of the Extra-Galactic Nebula N. G. C. 1275. *Publications of the Astronomical Society of the Pacific*, 44:267.

Hwang, H.S., Elbaz, D., Magdis, G.E., et al., 2010. Evolution of Dust Temperature of Galaxies Through Cosmic Time as Seen by Herschel. *Monthly Notices of the Royal Astronomical Society*, 409(1):75.

Ibar, E., Ivison, R.J., Cava, A., et al., 2010. H-ATLAS: PACS Imaging for the Science Demonstration Phase. *Monthly Notices of the Royal Astronomical Society*, 409:38.

Ishibashi, W. and Fabian, A.C., 2015. AGNfeedback:galactic-Scaleoutflowsdrivenbyradiationpressureondust. *Monthly Notices of the Royal Astronomical Society*, 451(1):93.

Ivison, R.J., Magnelli, B., Ibar, E., et al., 2010. The Far-Infrared/radio Correlation as Probed by Herschel. *Astronomy and Astrophysics*, 518:L31.

Jackson, N. and Rawlings, S., 1997. Oiii 500.7 Spectroscopy of 3C Galaxies and Quasars At Redshift Z Extgreater 1. *Monthly Notices of the Royal Astronomical Society*, 286(1):241.

Jahnke, K., Sanchez, S.F., Wisotzki, L., et al., 2004. UV Light from Young Stars in GEMS Quasar Host Galaxies At 1.8 extlessz extless2.75. *The Astrophysical Journal*, 614(2):568.

Janssen, R.M.J., Rottgering, H.J.A., Best, P.N., et al., 2012. The Triggering Probability of Radio-Loud AGN: A Comparison of High and Low Excitation Radio Galaxies in Hosts of Different Colors. *Astronomy & Astrophysics*, 541:A62.

Jarrett, T.H., Cohen, M., Masci, F., et al., 2011. The Spitzer-WISE Survey of the Ecliptic Poles. *The Astrophysical Journal*, 735(2):112.

Jarvis, M.J., Smith, D.J.B., Bonfield, D.G., et al., 2010. Herschel-ATLAS: the Far-Infrared-Radio Correlation At Z Extless 0.5. *Monthly Notices of the Royal Astronomical Society*, 409(1):92.

Johnston, R., 2011. Shedding Light on the Galaxy Luminosity Function. *Astronomy and Astrophysics Review*, 19:41.

Kafka, P., 1967. How to Count Quasars. *Nature*, 213(5074):346.

Kaiser, C.R., Dennett-Thorpe, J., and Alexander, P., 1997. Evolutionary Tracks of FRII Sources Through the P-D Diagram. *Monthly Notices of the Royal Astronomical Society*, 292:723.

Kaiser, N., Aussel, H., Burke, B.E., et al., 2002. Pan-STARRS: A Large Synoptic Survey Telescope Array. In *Survey and Other Telescope Technologies and Discoveries*, volume 4836 of *Society of Photo-Optical Instrumentation Engineers (SPIE) Conference Series*, pages 154–164.

Kaiser, N., Burgett, W., Chambers, K., et al., 2010. The Pan-STARRS Wide-Field Optical/NIR Imaging Survey. In *Ground-based and Airborne Telescopes III*, volume 7733 of *Society of Photo-Optical Instrumentation Engineers (SPIE) Conference Series*, page 77330E.

Kaspi, S., Brandt, W.N., Maoz, D., et al., 2007. Reverberation Mapping of High-Luminosity Quasars: First Results. *The Astrophysical Journal*, 659(2):997.

Kaspi, S., Smith, P.S., Netzer, H., et al., 2000. Reverberation Measurements for 17 Quasars and the Size-Mass-Luminosity Relations in Active Galactic Nuclei. *The Astrophysical Journal*, 533(2):631.

Kauffmann, G., Heckman, T.M., Tremonti, C., et al., 2003a. The Host Galaxies of AGN. *Monthly Notices of the Royal Astronomical Society*, 346(4):1055.

Kauffmann, G., Heckman, T.M., White, S.D.M., et al., 2003b. Stellar Masses and Star Formation Histories for 105 Galaxies from the Sloan Digital Sky Survey. *Monthly Notices of the Royal Astronomical Society*, 341(1):33.

Kaviraj, S., Devriendt, J., Dubois, Y., et al., 2015. Galaxy Merger Histories and the Role of Merging in Driving Star Formation At Z > 1. *Monthly Notices of the Royal Astronomical Society*, 452(3):2845.

Kaviraj, S., Laigle, C., Kimm, T., et al., 2017. The Horizon-AGN Simulation: Evolution of Galaxy Properties Over Cosmic Time. *Monthly Notices of the Royal Astronomical Society*, 467(4):4739.

Keel, W.C., 1988. The Optical Continua of Extragalactic Radio Jets. *The Astrophysical Journal*, 329:532.

Kelly, B.C., Bechtold, J., and Siemiginowska, A., 2009. Are the Variations in Quasar Optical Flux Driven by Thermal Fluctuations? *The Astrophysical Journal*, 698:895.

Kelly, B.C., Fan, X., and Vestergaard, M., 2008. A Flexible Method of Estimating Luminosity Functions. *The Astrophysical Journal*, 682(2):874.

Kelvin, L.S., Bremer, M.N., Phillipps, S., et al., 2018. Galaxy and Mass Assembly (GAMA): Variation in Galaxy Structure Across the Green Valley. *Monthly Notices of the Royal Astronomical Society*, 477(3):4116.

Kelvin, L.S., Driver, S.P., Robotham, A.S.G., et al., 2012. Galaxy And Mass Assembly (GAMA): Structural Investigation of Galaxies via Model Analysis. *Monthly Notices of the Royal Astronomical Society*, 421:1007.

Kelvin, L.S., Driver, S.P., Robotham, A.S.G., et al., 2014a. Galaxy And Mass Assembly (GAMA): Stellar Mass Functions by Hubble Type. *Monthly Notices of the Royal Astronomical Society*, 444:1647.

Kelvin, L.S., Driver, S.P., Robotham, A.S.G., et al., 2014b. Galaxy And Mass Assembly (GAMA): UgrizYJHK Sérsic Luminosity Functions and the Cosmic Spectral Energy Distribution by Hubble Type. *Monthly Notices of the Royal Astronomical Society*, 439:1245.

Kennicutt, J., 1998a. The Global Schmidt Law in Star Forming Galaxies. *The Astrophysical Journal*, 498(2):541.

Kennicutt, J., 1998b. Star Formation in Galaxies Along the Hubble Sequence. *Annual Review of Astronomy and Astrophysics*, 36(1):189.

Kennicutt, Robert C., J., Hao, C.N., Calzetti, D., et al., 2009. Dust-Corrected Star Formation Rates of Galaxies. I. Combinations of Hα and Infrared Tracers. *The Astrophysical Journal*, 703:1672.

Kennicutt Jr, R.C. and Evans II, N.J., 2012. Star Formation in the Milky Way and Nearby Galaxies. *Annual Review of Astronomy and Astrophysics*, 50(1):531.

Kewley, L.J., Groves, B., Kauffmann, G., et al., 2006. The Host Galaxies and Classification of Active Galactic Nuclei. *Monthly Notices of the Royal Astronomical Society*, 372(3):961.

Kewley, L.J., Heisler, C.A., Dopita, M.A., et al., 2001. Optical Classification of Southern Warm Infrared Galaxies. *The Astrophysical Journal Supplement Series*, 132(1):37.

Khachikian, E.Y. and Weedman, D.W., 1974. An Atlas of Seyfert Galaxies. *The Astrophysical Journal*, 192:581.

Kirkpatrick, A., Pope, A., Sajina, A., et al., 2015. The Role of Star-Formation and AGN in Dust Heating of Z = 0.3-2.8 Galaxies - I. Evolution with Redshift and Luminosity. *ArXiv:1510.02806 [Astro-Ph]*.

Kocis, L. and Whiten, W.J., 1997. Computational Investigations of Low-Discrepancy Sequences. *ACM Transactions on Mathematical Software*, 23(2):266.

Koleva, M., Prugniel, P., Bouchard, A., et al., 2009. ULySS: a Full Spectrum Fitting Package. *Astronomy and Astrophysics*, 501(3):1269.

Komatsu, E., Smith, K.M., Dunkley, J., et al., 2011. Seven-Year Wilkinson Microwave Anisotropy Probe (WMAP) Observations: Cosmological Interpretation. *The Astrophysical Journal Supplement Series*, 192(2):18.

Koratkar, A. and Blaes, O., 1999. The Ultraviolet and Optical Continuum Emission in Active Galactic Nuclei: The Status of Accretion Disks. *Publications of the Astronomical Society of the Pacific*, 111(755):1.

Kormendy, J. and Ho, L.C., 2013. Coevolution (Or Not) of Supermassive Black Holes and Host Galaxies. *Annual Review of Astronomy and Astrophysics*, 51(1):511.

Krajnovic, D., Alatalo, K., Blitz, L., et al., 2013. The ATLAS3D Project - XVII. Linking Photometric and Kinematic Signatures of Stellar Discs in Early-Type Galaxies. *Monthly Notices of the Royal Astronomical Society*, 432(3):1768.

Krislock, A. and Krislock, N., 2014. Resolving Histogram Binning Dilemmas with Binless and Binfull Algorithms. *ArXiv:1405.4958 [Hep-Ex, Physics:hep-Ph, Physics:physics]*.

Kristian, J., 1973. Quasars as Events in the Nuclei of Galaxies: the Evidence from Direct Photographs. *The Astrophysical Journal Letters*, 179:L61.

Kroupa, P., 2001. On the Variation of the Initial Mass Function. *Monthly Notices of the Royal Astronomical Society*, 322:231.

Kullback, S. and Leibler, R.A., 1951. On Information and Sufficiency. *The Annals of Mathematical Statistics*, 22(1):79.

Kurucz, R.L., 1979. Model Atmospheres for G, F, A, B, and O Stars. *The Astrophysical Journal Supplement Series*, 40:1.

Lacki, B.C. and Thompson, T.A., 2010. The Physics of the FIR-Radio Correlation: II. Synchrotron Emission as a Star-Formation Tracer in High-Redshift Galaxies. *The Astrophysical Journal*, 717(1):196.

Lacki, B.C., Thompson, T.A., and Quataert, E., 2010. The Physics of the Far-Infrared-Radio Correlation. I. Calorimetry, Conspiracy, and Implications. *The Astrophysical Journal*, 717(1):1.

Lacy, M., Storrie-Lombardi, L.J., Sajina, A., et al., 2004. Obscured and Unobscured Active Galactic Nuclei in the Spitzer Space Telescope First Look Survey. *The Astrophysical Journal Supplement Series*, 154(1):166.

Lamastra, A., Menci, N., Fiore, F., et al., 2013. The Interaction-Driven Starburst Contribution to the Cosmic Star Formation Rate Density. *Astronomy and Astrophysics*, 552:A44.

Lee, G. and Scott, C., 2012. EM Algorithms for Multivariate Gaussian Mixture Models with Truncated and Censored Data. *Computational Statistics & Data Analysis*, 56(9):2816.

Leitherer, C. and Heckman, T.M., 1995. Synthetic Properties of Starburst Galaxies. *The Astrophysical Journal Supplement Series*, 96:9.

Leitherer, C., Ortiz Otálvaro, P.A., Bresolin, F., et al., 2010. A Library of Theoretical Ultraviolet Spectra of Massive, Hot Stars for Evolutionary Synthesis. *The Astrophysical Journal Supplement Series*, 189:309.

Leitherer, C., Schaerer, D., Goldader, J.D., et al., 1999. Starburst99: Synthesis Models for Galaxies with Active Star Formation. *The Astrophysical Journal Supplement Series*, 123:3.

Lewandowski, D., Kurowicka, D., and Joe, H., 2009. Generating Random Correlation Matrices Based on Vines and Extended Onion Method. *Journal of Multivariate Analysis*, 100(9):1989.

Li, J.T., Beck, R., Dettmar, R.J., et al., 2016. CHANG-ES VI: Probing Supernova Energy Deposition in Spiral Galaxies Through Multi-Wavelength Relationships. *Monthly Notices of the Royal Astronomical Society*, 456(2):1723.

Lilly, S.J., Carollo, C.M., Pipino, A., et al., 2013. Gas Regulation of Galaxies: The Evolution of the Cosmic Specific Star Formation Rate, the Metallicity-Mass-Star-Formation Rate Relation, and the Stellar Content of Halos. *The Astrophysical Journal*, 772(2):119.

Lilly, S.J., Le Fevre, O., Hammer, F., et al., 1996. The Canada-France Redshift Survey: The Luminosity Density and Star Formation History of the Universe to Z Approximately 1. *The Astrophysical Journal*, 460:L1.

Lisenfeld, U., Voelk, H.J., and Xu, C., 1996a. The FIR/radio Correlation in Starburst Galaxies: Constraints on Starburst Models. *Astronomy and Astrophysics*, 314:745.

Lisenfeld, U., Voelk, H.J., and Xu, C., 1996b. A Quantitative Model of the FIR/radio Correlation for Normal Late-Type Galaxies. *Astronomy and Astrophysics*, 306:677.

Liu, F.K. and Xie, G.Z., 1992. A Finding List of Extragalactic Radio Jets and Statistical Results. *Astronomy and Astrophysics Supplement Series*, 95:249.

Liu, H.T., Feng, H.C., and Bai, J.M., 2017. A New Method to Measure the Virial Factors in the Reverberation Mapping of Active Galactic Nuclei. *Monthly Notices of the Royal Astronomical Society*, 466(3):3323.

Long, J.P. and de Souza, R.S., 2017. Statistical Methods in Astronomy. *ArXiv:1707.05834 [Astro-Ph, Physics:physics, Stat]*.

Longair, M.S., 1994. *High energy astrophysics. Volume 2. Stars, the Galaxy and the interstellar medium.*, volume 2. Cambridge Univ. Press, 2nd edition.

Longair, M.S., 2011. *High energy astrophysics*. Cambridge University Press, Cambridge ; New York, 3rd ed edition.

Lynden-Bell, D., 1969a. Galactic Nuclei as Collapsed Old Quasars. *Nature*, 223:690.

Lynden-Bell, D., 1969b. Galactic Nuclei as Collapsed Old Quasars. *Nature*, 223:690.

Madau, P. and Dickinson, M., 2014. Cosmic Star Formation History. *Annual Review of Astronomy and Astrophysics*, 52(1):415.

Madau, P., Ferguson, H.C., Dickinson, M.E., et al., 1996. High-Redshift Galaxies in the Hubble Deep Field: Colour Selection and Star Formation History to Z~4. *Monthly Notices of the Royal Astronomical Society*, 283:1388.

Madau, P., Pozzetti, L., and Dickinson, M., 1998. The Star Formation History of Field Galaxies. *The Astrophysical Journal*, 498:106.

Maddox, S.J., Valiante, E., Cigan, P., et al., 2018. The Herschel -ATLAS Data Release 2. Paper II. Catalogs of Far-Infrared and Submillimeter Sources in the Fields At the South and North Galactic Poles. *The Astrophysical Journal Supplement Series*, 236(2):30.

Magorrian, J., Tremaine, S., Richstone, D., et al., 1998. The Demography of Massive Dark Objects in Galaxy Centers. *The Astronomical Journal*, 115:2285.

Marshall, P., Clarkson, W., Shemmer, O., et al., 2017. Lsst Science Collaborations Observing Strategy White Paper: "Science-Driven Optimization Of The Lsst Observing Strategy.

Martin, D.C., Wyder, T.K., Schiminovich, D., et al., 2007. The UV-Optical Galaxy Color-Magnitude Diagram. III. Constraints on Evolution from the Blue to the Red Sequence. *The Astrophysical Journal Supplement Series*, 173(2):342.

Massey, P., Johnson, K.E., and Degioia-Eastwood, K., 1995. The Initial Mass Function and Massive Star Evolution in the OB Associations of the Northern Milky Way. *The Astrophysical Journal*, 454:151.

Mateos, S., Alonso-Herrero, A., Carrera, F.J., et al., 2012. Using the Bright Ultrahard XMM-Newton Survey to Define an IR Selection of Luminous AGN Based on WISE Colours. *Monthly Notices of the Royal Astronomical Society*, 426(4):3271.

Mauch, T., Klöckner, H.R., Rawlings, S., et al., 2013. A 325-MHz GMRT Survey of the Herschel-ATLAS/GAMA Fields. *Monthly Notices of the Royal Astronomical Society*, 435(1):650.

Mayall, N.U., 1934. The Spectrum of the Spiral Nebula NGC 4151. *Publications of the Astronomical Society of the Pacific*, 46:134.

Mayall, N.U., 1939. The Occurrence of [Lambda]3727 [OII] in the Spectra of Extragalactic Nebulae. *Lick Observatory Bulletin*, 19:33.

McConnell, N.J. and Ma, C.P., 2013. Revisiting the Scaling Relations of Black Hole Masses and Host Galaxy Properties. *The Astrophysical Journal*, 764(2):184.

McLure, R.J. and Dunlop, J.S., 2001. The Black Hole Masses of Seyfert Galaxies and Quasars. *Monthly Notices of the Royal Astronomical Society*, 327(1):199.

McLure, R.J. and Dunlop, J.S., 2004. The Cosmological Evolution of Quasar Black Hole Masses. *Monthly Notices of the Royal Astronomical Society*, 352(4):1390.

McLure, R.J. and Jarvis, M.J., 2002. Measuring the Black Hole Masses of High Redshift Quasars. *Monthly Notices of the Royal Astronomical Society*, 337(1):109.

McLure, R.J. and Jarvis, M.J., 2004. The Relationship Between Radio Luminosity and Black Hole Mass in Optically Selected Quasars. *Monthly Notices of the Royal Astronomical Society*, 353(4):L45.

Mejía-Restrepo, J.E., Trakhtenbrot, B., Lira, P., et al., 2016. Active Galactic Nuclei At Z $\sim$ 1.5 - II. Black Hole Mass Estimation by Means of Broad Emission Lines. *Monthly Notices of the Royal Astronomical Society*, 460(1):187.

Melchior, P. and Goulding, A.D., 2018. Filling the Gaps: Gaussian Mixture Models from Noisy, Truncated Or Incomplete Samples. *Astronomy and Computing*, 25:183.

Merritt, D., 2013. *Dynamics and Evolution of Galactic Nuclei*. Princeton University Press, Princeton, USA.

Merritt, D. and Ferrarese, L., 2001. Black Hole Demographics from the M-Sigma Relation. *Monthly Notices of the Royal Astronomical Society*, 320:L30.

Michałowski, M., Hjorth, J., and Watson, D., 2010a. Cosmic Evolution of Submillimeter Galaxies and Their Contribution to Stellar Mass Assembly. *Astronomy and Astrophysics*, 514:A67.

Michałowski, M.J., Watson, D., and Hjorth, J., 2010b. Rapid Dust Production in Submillimeter Galaxies At Z Extgreater 4? *The Astrophysical Journal*, 712:942.

Miller, G.E. and Scalo, J.M., 1979. Theinitialmassfunctionandstellarbirthrateinthesolarneighborhood. *Astrophysical Journal Supplement*, 41:513.

Molnár, D.C., Sargent, M.T., Delhaize, J., et al., 2018. The Infrared-Radio Correlation of Spheroid- and Disc-Dominated Star-Forming Galaxies to Z $\sim$ 1.5 in the COSMOS Field. *Monthly Notices of the Royal Astronomical Society*, 475(1):827.

Mudd, D., Martini, P., Zu, Y., et al., 2017. Quasar Accretion Disk Sizes With Continuum Reverberation Mapping From the Dark Energy Survey. *ArXiv:1711.11588 [Astro-Ph]*.

Murphy, E.J., 2009. The Far-Infrared-Radio Correlation At High Redshifts: Physical Considerations and Prospects for the Square Kilometer Array. *The Astrophysical Journal*, 706:482.

Murphy, E.J., Condon, J.J., Schinnerer, E., et al., 2011. Calibrating Extinction-Free Star Formation Rate Diagnostics with 33 GHz Free-Free Emission in NGC 6946. *The Astrophysical Journal*, 737(2):67.

Murphy, K.P., 2012. *Machine learning: a probabilistic perspective*. Adaptive computation and machine learning series. MIT Press, Cambridge, MA.

Mushotzky, R.F., Edelson, R., Baumgartner, W.H., et al., 2011. Kepler Observations of Rapid Optical Variability in Active Galactic Nuclei. *The Astrophysical Journal*, 743(1):L12.

Naab, T., Oser, L., Emsellem, E., et al., 2014. The ATLAS extlessSUP extgreater3D extless/-SUP extgreater Project - XXV. Two-Dimensional Kinematic Analysis of Simulated Galaxies and the Cosmological Origin of Fast and Slow Rotators. *Monthly Notices of the Royal Astronomical Society*, 444(4):3357.

Narayan, R. and Yi, I., 1995. Advection-Dominated Accretion: Underfed Black Holes and Neutron Stars. *The Astrophysical Journal*, 452:710.

Negroponte, J. and White, S.D.M., 1983. Simulations of Mergers Between Disc-Halo Galaxies. *Monthly Notices of the Royal Astronomical Society*, 205:1009.

Netzer, H., 2015. Revisiting the Unified Model of Active Galactic Nuclei. *Annual Review of Astronomy and Astrophysics*, 53(1):365.

Netzer, H., Lira, P., Trakhtenbrot, B., et al., 2007. Black Hole Mass and Growth Rate At High Redshift. *The Astrophysical Journal*, 671(2):1256.

Niklas, S. and Beck, R., 1997. A New Approach to the Radio-Far Infrared Correlation for Non-Calorimeter Galaxies. *Astronomy and Astrophysics*, 320:54.

Noeske, K.G., Faber, S.M., Weiner, B.J., et al., 2007a. Star Formation in AEGIS Field Galaxies Since Z = 1.1: Staged Galaxy Formation and a Model of Mass-Dependent Gas Exhaustion. *The Astrophysical Journal Letters*, 660(1):L47.

Noeske, K.G., Weiner, B.J., Faber, S.M., et al., 2007b. Star Formation in AEGIS Field Galaxies Since Z = 1.1: The Dominance of Gradually Declining Star Formation, and the Main Sequence of Star-Forming Galaxies. *The Astrophysical Journal Letters*, 660(1):L43.

Noeske, K.G., Weiner, B.J., Faber, S.M., et al., 2007c. Star Formation in AEGIS Field Galaxies Since Z=1.1 : The Dominance of Gradually Declining Star Formation, and the Main Sequence of Star-Forming Galaxies. *The Astrophysical Journal*, 660(1):L43.

Olsen, K.A.G., 1999. Star Formation Histories from Hubble Space Telescope Color-Magnitude Diagrams of Six Fields of the Large Magellanic Cloud. *The Astronomical Journal*, 117(5):2244.

Onken, C.A., Ferrarese, L., Merritt, D., et al., 2004. Supermassive Black Holes in Active Galactic Nuclei. II. Calibration of the Black Hole Mass-Velocity Dispersion Relationship for Active Galactic Nuclei. *The Astrophysical Journal*, 615:645.

Osterbrock, D.E., 1981. Seyfert Galaxies with Weak Broad H Alpha Emission Lines. *The Astrophysical Journal*, 249:462.

O'Brien, T.A., Collins, W.D., Rauscher, S.A., et al., 2014. Reducing the Computational Cost of the ECF Using a NuFFT: A Fast and Objective Probability Density Estimation Method. *Computational Statistics & Data Analysis*, 79:222.

O'Brien, T.A., Kashinath, K., Cavanaugh, N.R., et al., 2016. A Fast and Objective Multidimensional Kernel Density Estimation Method: FastKDE. *Computational Statistics & Data Analysis*, 101:148.

Padilla, C., Ballester, O., Cardiel-Sas, L., et al., 2016. The PAU Camera At the WHT. page 99080Z. Edinburgh, United Kingdom.

Pancoast, A., Brewer, B.J., and Treu, T., 2011. Geometric and Dynamical Models of Reverberation Mapping Data. *The Astrophysical Journal*, 730(2):139.

Pancoast, A., Brewer, B.J., and Treu, T., 2014. Modelling Reverberation Mapping Data - I. Improved Geometric and Dynamical Models and Comparison with Cross-Correlation Results. *Monthly Notices of the Royal Astronomical Society*, 445(3):3055.

Panter, B., Heavens, A.F., and Jimenez, R., 2003. Star Formation and Metallicity History of the SDSS Galaxy Survey: Unlocking the Fossil Record. *Monthly Notices of the Royal Astronomical Society*, 343(4):1145.

Park, D., Kelly, B.C., Woo, J.H., et al., 2012. Recalibration of the Virial Factor and M BH-σ* Relation for Local Active Galaxies. *The Astrophysical Journal Supplement Series*, 203:6.

Pascale, E., Auld, R., Dariush, A., et al., 2011. The First Release of Data from the Herschel ATLAS: the SPIRE Images. *Monthly Notices of the Royal Astronomical Society*, 415(1):911.

Patel, H., Clements, D.L., Vaccari, M., et al., 2013. Evolution of the Far-Infrared Luminosity Functions in the Spitzer Wide-Area Infrared Extragalactic Legacy Survey. *Monthly Notices of the Royal Astronomical Society*, 428(1):291.

Patton, D.R., Pritchet, C.J., Yee, H.K.C., et al., 1997. Close Pairs of Field Galaxies in the CNOC1 Redshift Survey. *The Astrophysical Journal*, 475(1):29.

Peng, Y., Lilly, S.J., Kovac, K., et al., 2010. Mass and Environment as Drivers of Galaxy Evolution in SDSS and ZCOSMOS and the Origin of the Schechter Function. *The Astrophysical Journal*, 721(1):193.

Peng, Y., Maiolino, R., and Cochrane, R., 2015. Strangulation as the Primary Mechanism for Shutting Down Star Formation in Galaxies. *Nature*, 521(7551):192.

Penny, S.J., Masters, K.L., Smethurst, R., et al., 2018. SDSS-IV MaNGA: Evidence of the Importance of AGN Feedback in Low-Mass Galaxies. *Monthly Notices of the Royal Astronomical Society*, 476(1):979.

Peterson, B.M., 1997. *An introduction to active galactic nuclei*. Cambridge Univ. Press, Cambridge.

Peterson, B.M., 2001. Variability of Active Galactic Nuclei. *ArXiv:astro-Ph/0109495*.

Peterson, B.M., 2004. Black Hole Masses from Reverberation Measurements. *Proceedings of the International Astronomical Union*, 2004(IAUS222):15.

Peterson, J.R., Kahn, S.M., Paerels, F.B.S., et al., 2003. High-Resolution X-Ray Spectroscopic Constraints on Cooling-Flow Models for Clusters of Galaxies. *The Astrophysical Journal*, 590:207.

Petrosian, V., 1976. Surface Brightness and Evolution of Galaxies. *The Astrophysical Journal*, 209:L1.

Pier, E.A. and Krolik, J.H., 1992. Infrared Spectra of Obscuring Dust Tori Around Active Galactic Nuclei. I. Calculational Method and Basic Trends. *The Astrophysical Journal*, 401:99.

Pierce, C.M., Lotz, J.M., Primack, J.R., et al., 2010. The Effects of an Active Galactic Nucleus on Host Galaxy Colour and Morphology Measurements. *Monthly Notices of the Royal Astronomical Society*, 405(2):718.

Poglitsch, A., Waelkens, C., Geis, N., et al., 2010. The Photodetector Array Camera and Spectrometer (PACS) on the Herschel Space Observatory. *Astronomy and Astrophysics*, 518:L2.

Polletta, M., Tajer, M., Maraschi, L., et al., 2007. Spectral Energy Distributions of Hard X-Ray Selected Active Galactic Nuclei in the XMM-Newton Medium Deep Survey. *The Astrophysical Journal*, 663(1):81.

Polletta, M., Wilkes, B.J., Siana, B., et al., 2006. Chandra and Spitzer Unveil Heavily Obscured Quasars in the SWIRE/Chandra Survey. *The Astrophysical Journal*, 642(2):673.

Pozo Nuñez, F., Haas, M., Ramolla, M., et al., 2014. Modelling Photometric Reverberation Data -- a Disk-Like Broad-Line Region and a Potentially Larger Black Hole Mass for 3C120. *Astronomy & Astrophysics*, 568:A36.

Pozo Nuñez, F., Ramolla, M., Westhues, C., et al., 2012. Photometric Reverberation Mapping of 3C 120. *Astronomy & Astrophysics*, 545:A84.

Pozo Nuñez, F., Ramolla, M., Westhues, C., et al., 2015. The Broad-Line Region and Dust Torus Size of the Seyfert 1 Galaxy PGC 50427. *Astronomy & Astrophysics*, 576:A73.

Pozzetti, L., Bolzonella, M., Zucca, E., et al., 2010. ZCOSMOS - 10k-Bright Spectroscopic Sample. The Bimodality in the Galaxy Stellar Mass Function: Exploring Its Evolution with Redshift. *Astronomy and Astrophysics*, 523:A13.

Prusti, T., de Bruijne, J.H.J., Brown, A.G.A., et al., 2016. The Gaia Mission. *Astronomy and Astrophysics*, 595:A1.

Ramolla, M., Pozo, F., Westhues, C., et al., 2014. Photometric Reverberation Mapping of Active Galactic Nuclei. *Revista Mexicana de Astronomia y Astrofisica Conference Series*, 45:79.

Rasmussen, C.E., 2000. The Infinite Gaussian Mixture Model. In *In Advances in Neural Information Processing Systems 12*, pages 554–560. MIT Press.

Read, S.C., Smith, D.J.B., Gürkan, G., et al., 2018. The Far-Infrared Radio Correlation At Low Radio Frequency with LOFAR/H-ATLAS. *Monthly Notices of the Royal Astronomical Society*, 480(4):5625.

Reichardt, C., Jimenez, R., and Heavens, A.F., 2001. Recovering Physical Parameters from Galaxy Spectra Using MOPED. *Monthly Notices of the Royal Astronomical Society*, 327(3):849.

Rigby, E.E., Maddox, S.J., Dunne, L., et al., 2011. Herschel-ATLAS: First Data Release of the Science Demonstration Phase Source Catalogues. *Monthly Notices of the Royal Astronomical Society*, 415(3):2336.

Roberts, M.S. and Haynes, M.P., 1994. Physical Parameters Along the Hubble Sequence. *Annual Review of Astronomy and Astrophysics*, 32:115.

Rodighiero, G., Daddi, E., Baronchelli, I., et al., 2011. The Lesser Role of Starbursts for Star Formation At Z=2. *The Astrophysical Journal*, 739(2):L40.

Rosario, D.J., Trakhtenbrot, B., Lutz, D., et al., 2013. The Mean Star-Forming Properties of QSO Host Galaxies. *Astronomy & Astrophysics*, 560:A72.

Rosenberg, H., 1910. Über Den Zusammenhang Von Helligkeit Und Spektraltypus in Den Plejaden. *Astronomische Nachrichten*, 186:71.

Rowlands, K., Dunne, L., Maddox, S., et al., 2012. H-ATLAS/GAMA: Dusty Early-Type Galaxies and Passive Spirals. *Monthly Notices of the Royal Astronomical Society*, 419(3):2545.

Runnoe, J.C., Brotherton, M.S., Shang, Z., et al., 2013. Rehabilitating C IV-Based Black Hole Mass Estimates in Quasars. *Monthly Notices of the Royal Astronomical Society*, 434(1):848.

Russell, H.N., 1914. Relations Between the Spectra and Other Characteristics of the Stars. *Popular Astronomy*, 22:275.

Rybicki, G.B. and Kleyna, J.T., 1994. Study of Reverberation Lags and Spreads in NGC 5548. volume 69, page 85.

Sabater, J., Best, P.N., Hardcastle, M.J., et al., 2018. The LoTSS View of Radio AGN in the Local Universe. The Most Massive Galaxies Are Always Switched on. *ArXiv:1811.05528 [Astro-Ph]*.

Sadler, E.M., McIntyre, V.J., Jackson, C.A., et al., 1999. Radio Sources in the 2dF Galaxy Redshift Survey. I. Radio Source Populations. *Publications of the Astronomical Society of Australia*, 16(03):247.

Salim, S., Charlot, S., Rich, R.M., et al., 2005. New Constraints on the Star Formation Histories and Dust Attenuation of Galaxies in the Local Universe from GALEX. *The Astrophysical Journal*, 619(1):L39.

Salim, S. and Rich, R.M., 2010. Star Formation Signatures in Optically Quiescent Early-Type Galaxies. *The Astrophysical Journal*, 714(2):L290.

Salpeter, E.E., 1955. The Luminosity Function and Stellar Evolution. *The Astrophysical Journal*, 121:161.

Salvatier, J., Wiecki, T.V., and Fonnesbeck, C., 2016. Probabilistic Programming in Python Using PyMC3. *PeerJ Computer Science*, 2:e55.

Sandage, A., 1965. The Existence of a Major New Constituent of the Universe: the Quasistellar Galaxies. *The Astrophysical Journal*, 141:1560.

Sandage, A., 1975. Classification and Stellar Content of Galaxies Obtained from Direct Photography. In A. Sandage, M. Sandage, and J. Kristian, editors, *Galaxies and the Universe. Edited by Allan Sandage, Mary Sandage, and Jerome Kristian, with an index prepared by Gustav A. Tammann. Published by the University of Chicago Press (Stars and Stellar Systems. Volume 9), Chicago, IL USA., 1975, p.1*, page 1.

Santini, P., Rosario, D.J., Shao, L., et al., 2012. Enhanced Star Formation Rates in AGN Hosts with Respect to Inactive Galaxies from PEP-Herschel Observations. *Astronomy and Astrophysics*, 540:A109.

Sargent, M.T., Schinnerer, E., Murphy, E., et al., 2010. The VLA-COSMOS Perspective on the IR-Radio Relation. I. New Constraints on Selection Biases and the Non-Evolution of the IR/Radio Properties of Star Forming and AGN Galaxies At Intermediate and High Redshift. *The Astrophysical Journal Supplement Series*, 186(2):341.

Sbarrato, T., Padovani, P., and Ghisellini, G., 2014. The Jet-Disc Connection in AGN. *Monthly Notices of the Royal Astronomical Society*, 445(1):81.

Schawinski, K., Urry, C.M., Simmons, B.D., et al., 2014. The Green Valley Is a Red Herring: Galaxy Zoo Reveals Two Evolutionary Pathways Towards Quenching of Star Formation in Early- and Late-Type Galaxies. *Monthly Notices of the Royal Astronomical Society*, 440(1):889.

Schaye, J., Crain, R.A., Bower, R.G., et al., 2015. The EAGLE Project: Simulating the Evolution and Assembly of Galaxies and Their Environments. *Monthly Notices of the Royal Astronomical Society*, 446(1):521.

Scheuer, P.A.G., 1974. Models of Extragalactic Radio Sources with a Continuous Energy Supply from a Central Object. *Monthly Notices of the Royal Astronomical Society*, 166:513.

Scheuer, P.A.G. and Williams, P.J.S., 1968. Radio Spectra. *Annual Review of Astronomy and Astrophysics*, 6:321.

Schleicher, D.R.G. and Beck, R., 2016. Star-Forming Dwarf Galaxies: the Correlation Between Far-Infrared and Radio Fluxes. *Astronomy and Astrophysics*, 593:A77.

Schlickeiser, R., 2002. *Cosmic Ray Astrophysics*.

Schmidt, M., 1959. The Rate of Star Formation. *The Astrophysical Journal*, 129:243.

Schober, J., Schleicher, D.R.G., and Klessen, R.S., 2017. Tracing Star Formation with Non-Thermal Radio Emission. *Monthly Notices of the Royal Astronomical Society*, 468(1):946.

Schreiber, C., Elbaz, D., Pannella, M., et al., 2016. Observational Evidence of a Slow Downfall of Star Formation Efficiency in Massive Galaxies During the Past 10 Gyr. *Astronomy and Astrophysics*, 589:A35.

Schwarz, G., 1978. Estimating the Dimension of a Model. *The Annals of Statistics*, 6(2):461.

Seyfert, C.K., 1943. Nuclear Emission in Spiral Nebulae. *The Astrophysical Journal*, 97:28.

Seymour, N., Huynh, M., Dwelly, T., et al., 2009. Investigating the Far-IR/Radio Correlation of Star Forming Galaxies to Z=3. *Monthly Notices of the Royal Astronomical Society*, 398(3):1573.

Shankar, F., Weinberg, D.H., and Miralda-Escudé, J., 2009. Self-Consistent Models of the AGN and Black Hole Populations: Duty Cycles, Accretion Rates, and the Mean Radiative Efficiency. *The Astrophysical Journal*, 690:20.

Shen, Y., Brandt, W.N., Dawson, K.S., et al., 2015a. The Sloan Digital Sky Survey Reverberation Mapping Project: Technical Overview. *The Astrophysical Journal Supplement Series*, 216(1):4.

Shen, Y., Greene, J.E., Ho, L.C., et al., 2015b. The Sloan Digital Sky Survey Reverberation Mapping Project: No Evidence for Evolution in the M• $-\sigma^*$ Relation to Z$\sim$ 1. *The Astrophysical Journal*, 805(2):96.

Shen, Y., Richards, G.T., Strauss, M.A., et al., 2011. A Catalog of Quasar Properties from SDSS DR7. *The Astrophysical Journal Supplement Series*, 194(2):45.

Shimwell, T.W., Röttgering, H.J.A., Best, P.N., et al., 2017. The LOFAR Two-Metre Sky Survey. I. Survey Description and Preliminary Data Release. *Astronomy and Astrophysics*, 598:A104.

Shimwell, T.W., Tasse, C., Hardcastle, M.J., et al., 2018. The LOFAR Two-Metre Sky Survey - II. First Data Release. *ArXiv E-Prints*, page arXiv:1811.07926.

Silk, J. and Rees, M.J., 1998. Quasars and Galaxy Formation. *ArXiv:astro-Ph/9801013*.

Silva, L., Granato, G.L., Bressan, A., et al., 1998. Modeling the Effects of Dust on Galactic Spectral Energy Distributions from the Ultraviolet to the Millimeter Band. *The Astrophysical Journal*, 509(1):103.

Skilling, J., 2004. Nested Sampling. In *AIP Conference Proceedings*, volume 735, pages 395–405. AIP, Garching (Germany).

Slipher, V.M., 1917. The Spectrum and Velocity of the Nebula N.G.C. 1068 (M 77). *Lowell Observatory Bulletin*, 3:59.

Smethurst, R.J., Lintott, C.J., Simmons, B.D., et al., 2015. Galaxy Zoo: Evidence for Diverse Star Formation Histories Through the Green Valley. *Monthly Notices of the Royal Astronomical Society*, 450:435.

Smith, D.J.B., Dunne, L., da Cunha, E., et al., 2012a. Herschel-ATLAS: Multi-Wavelength SEDs and Physical Properties of 250 Micron-Selected Galaxies At Z Extless 0.5. *Monthly Notices of the Royal Astronomical Society*, 427(1):703.

Smith, D.J.B., Dunne, L., Maddox, S.J., et al., 2011. Herschel-ATLAS: Counterparts from the Ultraviolet-Near-Infrared in the Science Demonstration Phase Catalogue. *Monthly Notices of the Royal Astronomical Society*, 416:857.

Smith, D.J.B., Hardcastle, M.J., Jarvis, M.J., et al., 2013. Isothermal Dust Models of Herschel-ATLAS Galaxies. *Monthly Notices of the Royal Astronomical Society*, 436(3):2435.

Smith, D.J.B. and Hayward, C.C., 2015. Deriving Star Formation Histories from Photometry Using Energy Balance Spectral Energy Distribution Modelling. *Monthly Notices of the Royal Astronomical Society*, 453(2):1597.

Smith, D.J.B. and Jarvis, M.J., 2007. Evidence for Cold Accretion Onto a Massive Galaxy At High Redshift? *Monthly Notices of the Royal Astronomical Society*, 378(1):L49.

Smith, D.J.B., Jarvis, M.J., Hardcastle, M.J., et al., 2014. The Temperature Dependence of the Far-Infrared-Radio Correlation in the Herschel-ATLAS. *Monthly Notices of the Royal Astronomical Society*, 445(3):2232.

Smith, M.W.L., Gomez, H.L., Eales, S.A., et al., 2012b. The Herschel Reference Survey: Dust in Early-Type Galaxies and Across the Hubble Sequence. *The Astrophysical Journal*, 748(2):123.

Smith, M.W.L., Ibar, E., Maddox, S.J., et al., 2017. The Herschel -ATLAS Data Release 2, Paper I. Submillimeter and Far-Infrared Images of the South and North Galactic Poles: The Largest Herschel Survey of the Extragalactic Sky. *The Astrophysical Journal Supplement Series*, 233(2):26.

Smolcic, V., 2009. The Radio AGN Population Dichotomy: Green Valley Seyferts Versus Red Sequence Low-Excitation AGN. *The Astrophysical Journal*, 699(1):L43.

Sparke, L.S. and Gallagher, J.S., 2007. *Galaxies in the universe: an introduction*. Cambridge University Press, Cambridge ; New York, 2nd ed edition.

Sparre, M., Hayward, C.C., Springel, V., et al., 2015. The Star Formation Main Sequence and Stellar Mass Assembly of Galaxies in the Illustris Simulation. *Monthly Notices of the Royal Astronomical Society*, 447(4):3548.

Speagle, J.S., Steinhardt, C.L., Capak, P.L., et al., 2014. A Highly Consistent Framework for the Evolution of the Star-Forming "Main Sequence" from Z Extasciitilde 0-6. *The Astrophysical Journal Supplement Series*, 214(2):15.

Spindler, A., Wake, D., Belfiore, F., et al., 2018. SDSS-IV MaNGA: the Spatial Distribution of Star Formation and Its Dependence on Mass, Structure, and Environment. *Monthly Notices of the Royal Astronomical Society*, 476(1):580.

Starkey, D.A., Horne, K., and Villforth, C., 2016. Accretion Disc Time Lag Distributions: Applying CREAM to Simulated AGN Light Curves. *Monthly Notices of the Royal Astronomical Society*, 456(2):1960.

Steele, I.A., Smith, R.J., Rees, P.C., et al., 2004. The Liverpool Telescope: Performance and First Results. volume 5489, pages 679–692.

Stern, D., Assef, R.J., Benford, D.J., et al., 2012. Mid-Infrared Selection Of Active Galactic Nuclei With The Wide-Field Infrared Survey Explorer. I. Characterizing Wise-Selected Active Galactic Nuclei In Cosmos. *The Astrophysical Journal*, 753(1):30.

Stern, D., Eisenhardt, P., Gorjian, V., et al., 2005. Mid-Infrared Selection of Active Galaxies. *The Astrophysical Journal*, 631:163.

Strateva, I., Ivezic, Z., Knapp, G.R., et al., 2001. Color Separation of Galaxy Types in the Sloan Digital Sky Survey Imaging Data. *Astrophysical Journal*, 122:1861.

Sutherland, W. and Saunders, W., 1992. On the Likelihood Ratio for Source Identification. *Monthly Notices of the Royal Astronomical Society*, 259:413.

Sánchez, S.F., Avila-Reese, V., Hernandez-Toledo, H., et al., 2018. SDSS IV MaNGA - Properties of AGN Host Galaxies. *Revista Mexicana de Astronomia y Astrofisica*, 54:217.

Tacchella, S., Dekel, A., Carollo, C.M., et al., 2016. The Confinement of Star-Forming Galaxies into a Main Sequence Through Episodes of Gas Compaction, Depletion and Replenishment. *Monthly Notices of the Royal Astronomical Society*, 457(3):2790.

Tadhunter, C., 2016. Radio AGN in the Local Universe: Unification, Triggering and Evolution. *The Astronomy and Astrophysics Review*, 24(1).

Tamura, T., Kaastra, J.S., Peterson, J.R., et al., 2001. X-Ray Spectroscopy of the Cluster of Galaxies Abell 1795 with XMM-Newton. *Astronomy and Astrophysics*, 365:L87.

Taranu, D.S., Dubinski, J., and Yee, H.K.C., 2013. Mergers in Galaxy Groups. I. Structure and Properties of Elliptical Remnants. *The Astrophysical Journal*, 778(1):61.

Tasse, C., 2014a. Applying Wirtinger Derivatives to the Radio Interferometry Calibration Problem. *ArXiv:1410.8706 [Astro-Ph]*.

Tasse, C., 2014b. Nonlinear Kalman Filters for Calibration in Radio Interferometry. *Astronomy and Astrophysics*, 566:A127.

Tasse, C., Hugo, B., Mirmont, M., et al., 2018. Faceting for Direction-Dependent Spectral Deconvolution. *Astronomy & Astrophysics*, 611:A87.

Team, T.D., 2016. Theano: A Python Framework for Fast Computation of Mathematical Expressions. *ArXiv E-Prints*, abs/1605.02688.

Teyssier, R., 2002. Cosmological Hydrodynamics with Adaptive Mesh Refinement. A New High Resolution Code Called RAMSES. *Astronomy and Astrophysics*, 385:337.

Tian, Z., Liu, X., Yuan, H., et al., 2018. Binary Star Fractions from the LAMOST DR4. *Research in Astronomy and Astrophysics*, 18(5):052.

Tolstoy, E. and Saha, A., 1996. The Interpretation of Color-Magnitude Diagrams Through Numerical Simulation and Bayesian Inference. *The Astrophysical Journal*, 462:672.

Toomre, A., 1977. Mergers and Some Consequences. *Evolution of Galaxies and Stellar Populations*, page 401.

Torres, D.F., 2004. Theoretical Modelling of the Diffuse Emission of Gamma-Rays from Extreme Regions of Star Formation: The Case of Arp 220. *The Astrophysical Journal*, 617(2):966.

Tosi, M., Greggio, L., and Focardi, P., 1989. Star Formation in Dwarf Irregular Galaxies - Preliminary Results. *Astrophysics and Space Science*, 156:295.

Tosi, M., Greggio, L., Marconi, G., et al., 1991. Star Formation in Dwarf Irregular Galaxies: Sextans B. *Astronomical Journal*, 102:951.

Towers, S., 2012. Potential Fitting Biases Resulting from Grouping Data into Variable Width Bins. *ArXiv:1209.2690 [Astro-Ph, Physics:hep-Ex, Physics:physics]*.

Trayford, J.W., Theuns, T., Bower, R.G., et al., 2016. It Is Not Easy Being Green: the Evolution of Galaxy Colour in the EAGLE Simulation. *Monthly Notices of the Royal Astronomical Society*, 460(4):3925.

Tremaine, S., Gebhardt, K., Bender, R., et al., 2002. The Slope of the Black Hole Mass Versus Velocity Dispersion Correlation. *The Astrophysical Journal*, 574:740.

Tremonti, C.A., Heckman, T.M., Kauffmann, G., et al., 2004. The Origin of the Mass-Metallicity Relation: Insights from 53,000 Star-Forming Galaxies in the Sloan Digital Sky Survey. *The Astrophysical Journal*, 613(2):898.

Trump, J.R., Hsu, A.D., Fang, J.J., et al., 2013. A Census of Broad-Line Active Galactic Nuclei in Nearby Galaxies: Coeval Star Formation and Rapid Black Hole Growth. *The Astrophysical Journal*, 763(2):133.

Tully, R.B., Mould, J.R., and Aaronson, M., 1982. A Color-Magnitude Relation for Spiral Galaxies. *The Astrophysical Journal*, 257:527.

Ueda, N., Nakano, R., Ghahramani, Z., et al., 2000. Split and Merge EM Algorithm for Improving Gaussian Mixture Density Estimates. *Journal of VLSI Signal Processing Systems for Signal, Image and Video Technology*, 26(1):133.

Urry, C.M. and Padovani, P., 1995. Unified Schemes for Radio-Loud Active Galactic Nuclei. *Publications of the Astronomical Society of the Pacific*, 107:803.

Valiante, E., Smith, M.W.L., Eales, S., et al., 2016. The Herschel-ATLAS Data Release 1 Paper I: Maps, Catalogues and Number Counts. *Monthly Notices of the Royal Astronomical Society*, 462(3):3146.

van der Kruit, P.C., 1971. Observations of Core Sources in Seyfert and Normal Galaxies with the Westerbork Synthesis Radio Telescope At 1415 MHz. *Astronomy and Astrophysics*, 15:110.

van Haarlem, M.P., Wise, M.W., Gunst, A.W., et al., 2013. LOFAR: The LOw-Frequency ARray. *Astronomy & Astrophysics*, 556:A2.

Veilleux, S. and Osterbrock, D.E., 1987. Spectral Classification of Emission-Line Galaxies. *The Astrophysical Journal Supplement Series*, 63:295.

Vestergaard, M., 2004. Early Growth and Efficient Accretion of Massive Black Holes At High Redshift. *The Astrophysical Journal*, 601(2):676.

Vestergaard, M. and Peterson, B.M., 2006. Determining Central Black Hole Masses in Distant Active Galaxies and Quasars. II. Improved Optical and UV Scaling Relationships. *The Astrophysical Journal*, 641(2):689.

Voelk, H.J., 1989. The Correlation Between Radio and Far-Infrared Emission for Disk Galaxies - A Calorimeter Theory. *Astronomy and Astrophysics*, 218:67.

Wada, K., Schartmann, M., and Meijerink, R., 2016. Multi-Phase Nature of a Radiation-Driven Fountain with Nuclear Starburst in a Low-Mass Active Galactic Nucleus. *The Astrophysical Journal*, 828(2):L19.

Walborn, N.R., 1971. Some Spectroscopic Characteristics of the OB Stars: an Investigation of the Space Distribution of Certain OB Stars and the Reference Frame of the Classification. *The Astrophysical Journal Supplement Series*, 23:257.

Walborn, N.R. and Fitzpatrick, E.L., 1990. Contemporary Optical Spectral Classification of the OB Stars: A Digital Atlas. *Publications of the Astronomical Society of the Pacific*, 102:379.

Walmswell, J.J., Eldridge, J.J., Brewer, B.J., et al., 2013. A Transdimensional Bayesian Method to Infer the Star Formation History of Resolved Stellar Populations. *Monthly Notices of the Royal Astronomical Society*, 435(3):2171.

Wandel, A., Peterson, B.M., and Malkan, M.A., 1999. Central Masses and Broad-Line Region Sizes of Active Galactic Nuclei. I. Comparing the Photoionization and Reverberation Techniques. *The Astrophysical Journal*, 526(2):579.

Wetzel, A.R., Tinker, J.L., and Conroy, C., 2012. Galaxy Evolution in Groups and Clusters: Star Formation Rates, Red Sequence Fractions and the Persistent Bimodality. *Monthly Notices of the Royal Astronomical Society*, 424(1):232.

Whitaker, K.E., Labbé, I., van Dokkum, P.G., et al., 2011. The NEWFIRM Medium-Band Survey: Photometric Catalogs, Redshifts, and the Bimodal Color Distribution of Galaxies Out to Z Extasciitilde 3. *The Astrophysical Journal*, 735(2):86.

White, R.J. and Peterson, B.M., 1994. Comments on Cross-Correlation Methodology in Variability Studies of Active Galactic Nuclei. *Publications of the Astronomical Society of the Pacific*, 106.

Williams, B.F., Dalcanton, J.J., Dolphin, A.E., et al., 2015. A Global Star-Forming Episode in M31 2-4 Gyr Ago. *The Astrophysical Journal*, 806(1):48.

Williams, P.R., Pancoast, A., Treu, T., et al., 2018a. The Lick AGN Monitoring Project 2011: Dynamical Modeling of the Broad-Line Region. *ArXiv:1809.05113 [Astro-Ph]*.

Williams, W.L., Hardcastle, M.J., Best, P.N., et al., 2018b. The LOFAR Two-Metre Sky Survey (LoTSS) III. First Data Release: Optical/IR Identifications and Value-Added Catalogue. *ArXiv E-Prints*, page arXiv:1811.07927.

Wolf, C., Meisenheimer, K., Rix, H.W., et al., 2003. The COMBO-17 Survey: Evolution of the Galaxy Luminosity Function from 25 000 Galaxies with 0.2< Z <1.2. *Astronomy and Astrophysics*, 401:73.

Wong, O.I., Koss, M.J., Schawinski, K., et al., 2016. Determining the Radio Active Galactic Nuclei Contribution to the Radio-Far-Infrared Correlation Using the Black Hole Fundamental Plane Relation. *Monthly Notices of the Royal Astronomical Society*, 460(2):1588.

Woo, J., Courteau, S., and Dekel, A., 2008. Scaling Relations and the Fundamental Line of the Local Group Dwarf Galaxies. *Monthly Notices of the Royal Astronomical Society*, 390(4):1453.

Woo, J.H., Schulze, A., Park, D., et al., 2013. Do Quiescent and Active Galaxies Have Different $M_BH - \sigma_*$ Relations? *The Astrophysical Journal*, 772:49.

Wright, E.L., Eisenhardt, P.R.M., Mainzer, A.K., et al., 2010. The Wide-Field Infrared Survey Explorer (WISE): Mission Description and Initial On-Orbit Performance. *The Astronomical Journal*, 140:1868.

Wu, C.F.J., 1983. On the Convergence Properties of the EM Algorithm. *The Annals of Statistics*, 11(1):95.

Wyithe, J.S.B., 2006. A Log-Quadratic Relation Between the Nuclear Black Hole Masses and Velocity Dispersions of Galaxies. *Monthly Notices of the Royal Astronomical Society*, 365:1082.

Wyithe, J.S.B. and Padmanabhan, T., 2006. Properties of High-Redshift Quasars - I. Evolution of the Supermassive Black Hole to Halo Mass Ratio. *Monthly Notices of the Royal Astronomical Society*, 366:1029.

York, D.G., 2000. The Sloan Digital Sky Survey: Technical Summary. *The Astronomical Journal*, 120(3):1579.

Yu, S.Y. and Ho, L.C., 2019. On the Connection Between Spiral Arm Pitch Angle and Galaxy Properties. *The Astrophysical Journal*, 871:194.

Yuk, I.S. and Lee, M.G., 2007. Modeling Star Formation History and Chemical Evolution of Resolved Galaxies. *The Astrophysical Journal*, 668(2):876.

Yun, M.S., Reddy, N.A., and Condon, J.J., 2001. Radio Properties of Infrared-Selected Galaxies in the IRAS 2 Jy Sample. *The Astrophysical Journal*, 554(2):803.

Zhang, H., Yang, Q., and Wu, X.B., 2017. Broadband Photometric Reverberation Mapping Analysis on SDSS-RM and Stripe 82 Quasars.

Zhang, Z., Chen, C., Sun, J., et al., 2003. EM Algorithms for Gaussian Mixtures with Split-And-Merge Operation. *Pattern Recognition*, 36(9):1973.

Zolotov, A., Dekel, A., Mandelker, N., et al., 2015. Compaction and Quenching of High-Z Galaxies in Cosmological Simulations: Blue and Red Nuggets. *Monthly Notices of the Royal Astronomical Society*, 450(3):2327.

Zu, Y., Kochanek, C.S., Kozłowski, S., et al., 2013. Is Quasar Optical Variability a Damped Random Walk? *The Astrophysical Journal*, 765(2):106.

Zu, Y., Kochanek, C.S., Kozłowski, S., et al., 2016. Application of Stochastic Modeling to Analysis of Photometric Reverberation Mapping Data. *The Astrophysical Journal*, 819:122.

Zu, Y., Kochanek, C.S., and Peterson, B.M., 2011. An Alternative Approach To Measuring Reverberation Lags in Active Galactic Nuclei. *The Astrophysical Journal*, 735(2):80.